Endohedral fullerenes as standards for portable atomic clocks

Reuben Harding

Wadham College

University of Oxford

A thesis submitted for the degree of

Doctor of Philosophy

Hilary 2019

Abstract

Highly stable and accurate frequency sources underpin a wide range of modern technologies. For many applications, there is a need to develop clocks with low size, weight and power (SWaP). Significant effort has been expended in miniaturising existing atomic clock architectures, but the various limitations inherent to contemporary designs incentivise further exploration of novel architectures.

Here, I investigate endohedral fullerenes as possible frequency references in future portable atomic clocks. Firstly, I detail the instrumentation developed to acquire the low-field data presented in this thesis. I then show that the endohedral fullerene $^{15}N@C_{60}$ possesses a magnetic field-insensitive "clock transition" with $f_{\mathrm{clock}} \approx 38.6\,\mathrm{MHz}$ at a field $B_{\mathrm{clock}} \approx 0.8\,\mathrm{mT}$. This measurement is the first observation of a clock transition in a molecular spin system at room temperature, and it enables me to estimate the stability of an fullerene-based clock. The predicted performance is very poor, and I discuss potential strategies to address this problem.

I also investigate the hyperfine coupling as a function of pressure. The measured shift ($\mathrm{d}A/\mathrm{d}P \approx 3.5 \times 10^{-4}\,\mathrm{Hz\,Pa^{-1}}$) is too small to be a useful tunable parameter with which to offset the temperature coefficient of a fullerene-based atomic clock. However, it does ensure that such a clock would be reasonably insensitive to atmospheric pressure fluctuations. Using this datum I make the first experimental estimate of the compressibility of an isolated fullerene cage.

On the basis of the research performed in this thesis, I believe that the outlook for fullerene-based frequency standards is poor. They are fundamentally limited by their low frequency clock transitions and broad linewidths relative to the atomic frequency standards used in contemporary portable atomic clocks. This is due to their small hyperfine interaction and the coupling between the electron spin and degrees of freedom that are absent in atomic systems.

Declaration

Declaration

I confirm that this thesis is solely my own work, and no part of it has previously been submitted for examination at the University of Oxford or elsewhere. The copyright of this thesis rests with the author except where stated otherwise.

All experiments and data analysis presented in this thesis were performed by myself, with the exception of the high-pressure measurements presented in Chapter 4. The high-pressure data presented in this paper were obtained by Dr Andrea Folli in the Department of Chemistry at Cardiff University. I designed the experiments used to acquire these data and performed the data analysis.

Deoxygenation, using multiple cycles of freeze–pump–thaw, and flame sealing of both $N@C_{60}$ and lithium phthalocyanine (LiPc) samples was performed by Dr. William K. Myers at the Centre for Advanced Electron Spin Resonance (CAESR), Department of Chemistry, University of Oxford. Dr. Jennifer LeRoy helped to prepare the $^{15}N@C_{60}$ sample measured in the low-field spectrometer presented in Chapter 3. She redissolved a solid-state sample in deoxygenated CS_2 under an inert atmosphere, and the sample was subsequently flame-sealed by Dr. Myers. Throughout the course of my D. Phil, I have received assistance with sample preparation and chemistry-related lab work from Ms. Christina Foldbjerg–Holloway, Mr. James Zhou, and Dr. Shen Zhou.

Research outputs

Publications

- Spin resonance clock transition of the endohedral fullerene $^{15}N@C_{60}$ [**Har17**]
- High pressure electron spin resonance of the endohedral fullerene $^{15}N@C_{60}$ (in preparation)

Talks

- Observation of a clock transition in the EPR spectrum of $^{15}N@C_{60}$, *50*$^{\text{th}}$ *Annual International Meeting of the Electron Spin Resonance Group of the Royal Society of Chemistry*, 2$^{\text{nd}}$–6$^{\text{th}}$ of April 2017, Oxford, United Kingdom
- Endohedral fullerenes as frequency standards in portable atomic clocks, *American Physical Society March Meeting 2018*, 5$^{\text{th}}$–9$^{\text{th}}$ of March 2018, Los Angeles, United States of America

Relationship with thesis

This thesis and the associated appendices are heavily based on the papers listed above. Elements from these papers are interspersed throughout this paper. In particular:

- Chapter 3 and Appendix B are based on [**Har17**], and
- Chapter 4 and Appendix C are based on the as-yet unpublished paper on high pressure electron spin resonance measurements of $^{15}N@C_{60}$.

Acknowledgements

Firstly, I would like to express my gratitude to the Defence Science and Technology Laboratory (Dstl) for funding my D. Phil studies. Secondly, I would like to thank my supervisors (Professor G. Andrew D. Briggs, Dr. Edward A. Laird, and Dr. Jan A. Mol) for providing a well-equipped lab and setting the overall direction of the project. Edward in particular also read over many draft versions of papers and helped me improve and polish my work.

While the D. Phil. process is a solitary path, and often lonely, there are a great many people to whom I owe thanks. This acknowledgement section is, by necessity, nothing more than an outline; my apologies to those not named herein.

Dr. Junjie Liu was one of the greatest influences on my development as a scientist over the course of my D. Phil. due to his willingness to share knowledge, give help, and act as a sounding board for ideas. In addition to our productive discussions of physics, I always enjoyed our discussions of everything else besides—especially politics and current affairs. Sincere thanks also go to Professsor Arzhang Ardavan in the Department of Physics who gave me lab space in Clarendon 020. It was simultaneously a lab and a retreat from the outside world.

I would like to thank various people from office 40.12 in 12/13 Parks Road. While there will be nothing that I miss about the office itself, the conversations and cynicism are already sorely missed; Jake and Yutian in particular provided a steady stream of interesting topics at unsociable hours. Outside the office, but still in 12/13/14 P.R., thanks go to Sapna for conversations, life advice, a shared hatred of fullerenes, and regularly giving me a floor to crash on when I needed to do thesis work after having moved out of Oxford—I would have found it much harder to finish this thesis without her help.

Outside of work, Oxford University Cave Club gave me a much-needed escape from PhD life. In particular, I would like to thank Thomas and Rory for their enthusiasm for caving trips that allowed me to explore my personal limits. I would also like to express my deepest gratitude to Chi, who took the time to challenge the way I view myself, the world, and my place in it.

Outside of Oxford, there are many whom I wish to thank for their friendship and support. The list is long, but Canna and George rise to the top.

I thank my parents and maternal grandparents for always having given me easy access to books and the freedom to do what I wanted.

Contents

List of Figures

1 Introduction

Contents

In this chapter, I seek to give the motivation and context for this thesis: the search for novel frequency references for use in portable atomic clocks. To this end, I will provide a brief history of the development of portable atomic clocks. Secondly, I will introduce endohedral fullerenes. To allow for a fuller discussion of electron paramagnetic resonance (EPR) and instrumentation, the section of this chapter that would otherwise pertain to EPR has been incorporated into Chapter 2.

1.1 Motivation

Atomic clocks find use wherever there is a need to accurately measure time. This can range from fundamental science [**HK72b**; **HK72a**; **Ves80**; **PTM95**; **Phi01**; **Ash07**; **Rei07**] to industry [**KA99**; **Zha16**], with each application having its own specific requirements for accuracy and stability. In addition to these specifications,

there may be additional requirements pertaining to the maximum acceptable size, weight, and power (SWaP) [**Vig93**].

For example, contemporary atomic clocks have enabled placing stringent bounds on challenges to the theory of general relativity [**HK72b**; **HK72a**; **Ves80**; **PTM95**; **Phi01**; **Ash07**; **Rei07**]. In tests of fundamental physics, the figure of merit is stability and accuracy, with less consideration given to the SWaP of the complete atomic clock systems. These applications, in conjunction with the natural human desire to push the boundaries of what is achievable, have driven atomic clocks to the forefront of metrology, such that time is the physical quantity that we can measure most precisely. Caesium fountain frequency standards in national metrology institutes, such as the United Kingdom's National Physical Laboratory (NPL) and the National Institute of Standards and Technology (NIST) of the United States, have systematic uncertainties of approximately 2×10^{-16} [**LGS11**; **Hea14**]. This has since been exceeded by a variety of competing technologies, such as optical lattice clocks [**Lud08**; **Lem09**; **Hin13**; **Blo14**], and the field is in a state of constant improvement.

In addition to fundamental physics research, there are technological applications for atomic clocks. Precision timing has become an underpinning technology for many aspects of modern life, even while it remains invisible to the end user. For example, they are used in fields ranging from navigation [**Ril81**; **HLC01**] to telecommunications [**Vig93**; **KA99**], and seismic monitoring [**GC11**; **GC12**] to financial transactions [**Hic15**; **NPL16**]. Here, stability and accuracy remain important, but some performance can be sacrificed to achieve lower size weight and power. This has driven the development of ever smaller atomic clocks with lower power requirements suitable for use in portable applications.

Radio telecommunication requires accurate and stable frequency standards [**KA99**] for synchronisation and syntonisation, so atomic clocks based on sealed-cell rubidium standards are commonly employed in mobile telephony base stations due to their high stability [**BMM07**]. Stable clocks are a prerequisite for secure and jamming-resistant communication protocols such as frequency-hopping spread

spectrum [**Vig93**], in which the transmitted signal hops between carrier frequencies in some pre-arranged pseudorandom pattern that is known to both transmitter and receiver. The timing of the frequency shift is determined by a local clock on the transmitter and receiver. Synchronising the transmitter and the receiver, such that they switch frequencies at the same time and remain on the same frequency band as each other over the duration of the transmission, places stringent requirements on the clock stability.

Atomic clocks are essential to global navigation satellite systems (GNSS) such as the Global Positioning System (GPS) [**HLC01**]. Each satellite in the constellation broadcasts a unique time-stamped signal [**HLC01**]. In conjunction with orbital data, these time-stamped signals allow the receiver unit to fomulate a set of simultaneous equations that can be solved to determine the user's position and local time. The satellites have very stable and accurate frequency standards in order to generate the timestamped signals, a capability which is provided using multiple rubidium clocks for redundancy [**EFR04**]. However, these are not portable clocks in the sense that I consider in this thesis; the relevant clock system for this thesis is that of the receiver unit.

The requirements of the clock in the receiver unit are less stringent than those of the clocks on board the satellite. However, stable frequency standards can be used to improve the receiver's holdover performance and ability to cope with non-ideal rf environments [**BR14**; **CF15**], which may be due to obstruction of the field of view of the receiver antenna, such as would be experienced in urban terrain, or contested electromagnetic spectrum, such as may be experienced in a battle. A stable local time reference in the receiver allows finding position when only three satellites are in view of the receiver, because the fourth simultaneous equation required to constrain the time parameter is redundant [**Stu83**]. Even if four or more satellites are visible, atomic clock-enabled receivers may also provide better positional accuracy since it can be used to overconstrain the problem and minimise the effect of errors in the apparent time. It also allows locking onto the pseudorandom signal used as the data carrier more rapidly after signal loss, since the receiver does not have to search

over such a wide range of possible times [**CF15**]. This is particularly advantageous if one wishes to acquire the encrypted P(Y) code without first locking onto the C(A) code to find an approximate time and narrow the search region [**ND95**]. The P(Y) code gives greater positional accuracy than the C/A code. Furthermore, it is transmitted at a higher bit rate than the C/A code, which spreads the signal over a larger spectral bandwidth and makes it harder to jam with a given jammer power [**Wol98**]. Here, the clock is necessary because the pseudorandom sequence used as the carrier for the P(Y) code is very long, and the probability of matching the correct portion by chance is very small. While improved holdover performance and better reliability in adverse environments such as cities are of considerable interest in the civilian market, the development of portable atomic clocks suitable for use in GPS receivers is largely driven by military requirements.

In addition, many timing solutions rely on the signal emitted from the GPS satellites [**BR14**]. For example, many telecommunication protocols require accurate timestamping of packets of information, and hence use GPS-disciplined oscillators (GPSDOs) [**Ave93**; **Wal01**]. This makes a wide variety of infrastructure vulnerable to attacks on GPS jamming or spoofing the signal [**Nar12**; **BR14**]. For this reason, complete systems often include a high-performance clock capable of giving good holdover performance until the GPS signal is reacquired [**Wal01**].

Concerns over the vulnerability of GPS to disruption, either accidental or intentional, has given rise to the field of "alternative PNT", where PNT stands for precision navigation and timing. The aim of alternative PNT is to obtain GPS-level position and timing accuracy without relying on external signals in small packages comparable to existing GPS modules. This will be achieved by developing highly accurate, low SWaP accelerometers and clocks. Since it falls outside of the field of interest for this thesis, I will not discuss further the components, such as accelerometers, necessary for implementing navigation. I will focus solely on the timing aspects of alternative PNT and the search for highly stable and accurate portable atomic clocks with low SWaP.

The majority of atomic frequency standards designed for portable or low SWaP applications are based on the use of alkali metal vapours. The reference frequency is provided by hyperfine transitions in the ground state manifold of the atom. The use of all-optical interrogation of the clock transition [**CTB93**] and the development of microfabricated vapour cells [**Lie04**] has permitted the development of ultraportable chip-scale atomic clocks (CSACs) [**Kna04**]. However, CSACs have some limitations inherent to the vapour cell technology. The vapour cell needs to be heated to increase the optical density of the alkali metal vapour in order to increase the signal to noise ratio of the transition, which requires electrical power. This power consumption can be mitigated by packaging the vapour cell within a vacuum chamber [**Lut04**; **MLV05**], but the suspension of the cell may introduce mechanical weakness [**Lut07**]. Secondly, the frequency is affected by the pressure of the buffer gas in the vapour cell [**Ril92**]. This is problematic because barium left over from the cell filling process acts as a getter for the nitrogen buffer gas [**Kna05b**; **Kna05a**]. These residual chemical reactions in the cell lead to changes in the buffer gas pressure and cause significant long term drifts in the CSAC's output frequency [**Kna04**]; however, this can be mitigated by using a noble gas as the buffer gas [**Kna05b**; **Kna05a**]. Despite these limitations, they are already commercially available in packages that occupy volumes of approximately $10\,\mathrm{cm}^3$ [**MSC17**].

Although many of these problems have been addressed to a certain extent, there remains an interest in developing alternative architectures [**Lut16**]. This includes the use of different vapour cell designs, such as hollow-core photonic crystal fibres [**RU18**]. Less conservatively, this may include cold atom clocks [**FZA10**] or miniaturised ion trap clocks [**Jau12**]. However, it is worth investigating radically different approaches to implementing an atomic frequency standard. For this reason, there has been a long-standing interest in atomic clocks using condensed matter systems as frequency standards. Several different systems have been proposed as frequency standards: these include NV centres in diamond [**Hod13**], vanadium ions doped into magnesium oxide [**WH05**; **Whi05**], endohedral fullerenes [**HB06**; **BA12**], and spin donors in silicon [**Kar14**; **Kar15**].

In this thesis, I investigate the potential use of endohedral fullerenes as a frequency standard. The EPR spectra of the endohedral fullerenes, particularly the spectrum of $N@C_{60}$, display properties that make them attractive for implementing atomic frequency standards, such as sharp resonances [**Mor06**]. The fullerene cage shields the electronic spin of $N@C_{60}$ from environmental perturbations that would otherwise cause decoherence [**Kna97**; **Din00a**; **Mor06**]. The coherence lifetime of $N@C_{60}$ is therefore the longest of any known molecular system at room temperature [**Zad15**], with consequently narrow linewidths due to suppression of lifetime broadening. Calculations suggest that the species $^{15}N@C_{60}$ exhibits a dipole-forbidden clock transition, thereby shielding it against small perturbations in the magnetic field and further suppressing lifetime broadening [**BA12**; **Har17**].

Using endohedral fullerenes in solution or solid state may enable high spin densities without needing to heat the cell, thereby minimising power consumption. Moreover, the chemical stability of the endohedral fullerene may eliminate the linear drift caused by cell aging observed in CSACs. Furthermore, it may be possible to package the complete fullerene clock onto a single integrated circuit following the approach used to implement "1-chip NMR" previously [**Sun11**; **Wu14**; **GGB15**]. If it is also possible to integrate the magnet onto the same chip using the MEMS fabrication techniques outlined in [**AN09**] it will be possible to build not only a chip-scale atomic clock, but a true single-chip atomic clock.

1.2 Atomic clocks: a basic guide

The reference frequency in an atomic clock is provided by an atomic resonance [**AV76**; **Rie04**]. This provides a frequency that is set by physical constants rather than manufacturing tolerances. Since all atoms of a given isotope are alike, this reference frequency is, in principle, fundamentally reproducible barring frequency shifts due to interactions with the external environment, such as the Zeeman effect, that perturb the energy levels of the atom. By picking a resonance that is minimally sensitive by environmental perturbations, it is possible to to achieve a highly stable reference frequency. However, the means by which the atomic reference frequency is converted

into a useful signal differs greatly between the various types of atomic clock. For example, atomic clocks may be either passive or active frequency standards. In a passive standard, a local oscillator is locked to an atomic resonance via a feedback loop. In an active frequency standard, such as an active hydrogen maser, the atomic system itself behaves as a local oscillator and the signal is given by the frequency of emitted radiation. A further distinction can be made by dividing atomic clocks into primary and secondary standards. A primary standard is one that, in principle, does not require calibration against another standard. The systematic uncertainty of a primary standard's frequency accuracy is evaluated from first principles by considering the internal environment of the atomic clock, such as the electric and magnetic fields at the location of the atoms, and the physical properties of the reference atoms. The systematic uncertainty parameterises the how uncertainty in these factors propagates through to a systematic uncertainty in the output caused by frequency shifts due to interactions between the atoms and the environment. The statistical uncertainty is measured using a "three-cornered hat" method, in which three or more standards are compared against one another to extract the stability of each separately [**GA74**]. In contrast, a secondary standard requires calibration against a primary standard, since its output frequency depends sensitively on factors that are not known *ab initio*. For example, vapour-cell based atomic clocks require calibration, since the output frequency depends sensitively on factors such as the pressure and composition of the buffer gas in the vapour cell, which may be affected by imperfections in the manufacturing process, residual chemical interactions within the cell, or by the temperature and pressure of the external environment.

	Primary standard	Secondary standard
Active		Active hydrogen maser
Passive	Caesium beam	Rubidium atomic frequency standard (RAFS)

Table 1.1: Table summarising types of atomic frequency standard.

The performance of an atomic clock is typically measured using the Allan deviation [**All66**; **Bar71**; **Ril94**]. The Allan deviation, and related metrics, measure

the fractional frequency instability of the clock's output. It is desirable to maximise the clock's stability, and hence minimise the Allan deviation. In addition to stability, the output of the frequency standard can be assessed for accuracy and reproducibility. Accuracy reflects how well the standard's output matches the design frequency output determined by the transition frequency of an unperturbed atom, and reproducibility reflects the degree of similarity between nominally identical frequency standards. Other figures of merit are the physical size, weight, and electrical power required to operate the complete clock system [**Vig93**].

1.2.1 Portable atomic frequency standards

An atomic frequency standard used in portable applications must satisfy various criteria in addition to achieving the necessary frequency stability. For example, it must be sufficiently small and low-weight [**Vig93**]. This is particularly important for man-portable systems, such as field radios, and for airborne applications where payload may be limited. Furthemore, the frequency standard should have low power requirement in order to permit long mission duration where battery capacity is limited by size and weight considerations.

Most portable atomic frequency standards are based on vapour cell designs. Here, the reference frequency is provided by transitions in the ground state of an alkali metal atom, typically rubidium (6.8 GHz) or caesium (9.2 GHz) [**AV76**]. These resonances modulate the absorption of light passing through the vapour cell [**AFI59**]. The resonance is interrogated using either an optical–RF double resonance technique [**AFI59**] or using all-optical techniques [**CTB93**].

The original designs were lamp-pumped double resonance designs [**AFI59**; **Car60**]. Here, a discharge lamp is used to optically pump the vapour, and the absorption of the cell is measured as a function of the applied RF frequency. The main limitation on power consumption is the power consumed by the discharge lamp and the oven used to maintain the vapour cell at a constant temperature. This is necessary to maximise the SNR of the transition and maintain a constant output frequency. One limitation on size is the RF cavity surrounding the vapour

cell [**CTB93**], which is necessary to enhance the RF magnetic field to drive the transitions. Both aspects have been improved, such that the vapour cell and resonator packages occupy a total volume less than $1\,\mathrm{cm}^3$ [**Vio14**].

The next major step forward to developing miniaturised frequency standards was the proposal to implement all-optical interrogation of the alkali metal vapour [**CTB93**]. In this approach, two phase-coherent electromagnetic waves are used to drive transitions between different sub-levels in the atomic ground state via an excited state. When the frequency difference between the two light sources is equal to the resonant frequency of the transition, a superposition of the two ground states is formed. This superposition does not couple to the electromagnetic field of the light sources. Therefore, the superposition does not absorb the input light and is hence a "dark state", which shows up as a decrease in absorption. By generating the frequency difference between the light sources from the local oscillator and measuring the absorption it is possible to determine the oscillator's frequency offset from the transition's centre frequency and adjust it accordingly.

The advantage of all-optical interrogation is that it obviates the need for a resonant cavity surrounding the vapour cell, thereby permitting a significant reduction in size compared to traditional RAFS designs [**Kna04**]. Furthermore, since the power consumption of the laser diodes used to drive the transitions is considerably less than that of the discharge lamp used previously to pump the vapour [**MLV05**]. In 2004, Knappe et al. introduced the chip-scale atomic clock (CSAC) architecture [**Kna04**] that forms the conceptual basis of most contemporary miniaturised atomic clocks. Here, the alkali metal vapour that serves as the frequency reference is confined in a microfabricated vapour cell. The physics package of the first generation CSAC occupied a volume $9.5\,\mathrm{mm}^3$ and consumed a power $P < 75\,\mathrm{mW}$ while achieving an fractional frequency instability $\sigma_y = 2.5 \times 10^{10}$ over a duration 1 s.

Nevertheless, the first generation CSACs suffered from some notable flaws. The output frequency was not constant over long time periods due to residual chemical interactions shifting the buffer gas pressure within the cell [**Kna04**]. Furthermore, the temperature of the cell must be relatively high to ensure sufficient vapour

density to achieve a high SNR and hence the power budget of the physics package was therefore dominated by thermal losses [**Kna04**]. Subsequent generations of CSAC have ameliorated, if not eliminated, these problems by improved cell fabrication [**Kna05b**] and placing the vapour cell inside a vacuum package [**Lut04**; **MLV05**]. However, the power consumption for the complete clock system remains high (0.1W) [**Lut07**], which is primarily due to the power consumption of the local oscillator and phase-locked loop control circuitry. Recently, this power consumption problem has been addressed by synthesising the local oscillator signal using a thin film bulk acoustic resonator voltage-controlled oscillator (FBAR-VCO) [**Har18**]. The FBAR-VCO consumes only 9 mW, and occupies a volume approximately 2 mm^3, which represents a highly significant improvement relative to the previous state-of-the art.

Despite the vast improvements in CSAC technology since they were introduced in 2004, their limitations have fuelled interest in developing alternative architectures for atomic clocks [**Lut16**]. One very exciting proposal is the use of carbonyl sulfide [**Wan18**], due to its high clock transition frequency, relative insensitivity to external perturbations, and potential for integration of a complete system onto a single chip. This has been experimentally demonstrated at a benchtop scale, but considerable further development work is required. However, in this thesis I am focusing on $N@C_{60}$, a condensed matter system, whereas the carbonyl sulfide frequency reference is gaseous. As such, I intend to focus on comparing it against other proposed condensed matter frequency standards for portable atomic clocks.

The use of condensed matter systems as atomic frequency standards may increase robustness and potential for miniaturisation. In common with the proposed carbonyl sulfide frequency standard, some of the proposed standards eliminate optical interrogation. In turn, this removes the need to integrate optical components into the clock system, and may permit the development of true single chip atomic clocks. If the system can be operated at room temperature, without need for ovenization of the frequency reference to maintain temperature, this may permit a reduction in power consumption. Furthemore, eliminating the vacuum packaging necessary to

maintain the temperature of the frequency reference would permit miniaturisation of the complete clock system. There have been several proposals, including using NV centres in diamond [**Hod13**] as atomic frequency standards, vanadium ions doped into magnesium oxide crystals [**WH05**; **Whi05**], and endohedral fullerenes [**HB06**; **BA12**].

The proposed NV center frequency standard would use the negative N-V^- defect in a a diamond lattice as the frequency reference [**Hod13**]. The defect comprises a lattice vacancy paired with a nitrogen atom, which substitutes for a carbon atom. The vacancy possesses an effective electron spin $S = 1$ with a large zero field splitting $D = 2.87\,\mathrm{GHz}$ between the $|0\rangle$ and $|\pm1\rangle$ energy levels of the ground state manifold that define the clock transition. It is an attractive candidate for a frequency standard due to its long coherence times even at room temperature [**Gae06**], which would lead to narrow linewidths in the absence of inhomogeneous broadening. The proposed frequency standard interrogates the clock transition using the spin-state dependent fluorescence signal resulting from optically pumping the transition. The frequency of the local oscillator used to generate the rf that manipulates the spin state is stabilised using feedback from the fluorescence signal, thereby achieving clock operation. The spin state can be measured using pulsed or continuous wave operation, and the sample may comprise either an ensemble of NV centres or a single, individually-addressed defect. The highest predicted stability would be for an ensemble sample interrogated using pulsed rf, with a predicted Allan deviation $\sigma_y = 10^{-7}\,\tau^{-1/2}$, or $\sigma_y \sim 10^{-12}\,\tau^{-1/2}$ if the lattice strains that broaden the resonance could be eliminated [**Hod13**]. In the latter case, an NV-based clock is predicted to achieve good stabilities considerably greater than that of current miniaturised atomic clock technologies. Furthermore, it would in principle be amenable to extreme miniaturisation and ruggedness. However, the long-term stability would be severely compromised by the temperature-dependence of the zero field splitting that defines the reference frequency. This dependence is due to strain within the crystal lattice, which may also lead to broadening of the resonance and hence reduced clock

stability. Despite these limitations, it is an attractive proposal and merits further development to take it from a theoretical proposal to a realised system.

To the best of my knowledge, the only previous experimental attempt at implementing a condensed matter atomic clock used the zero-field splitting of vanadium ions doped into magnesium oxide (V^{++}:MgO) to define the clock frequency [**WH05**; **Whi05**]. Here, the clock transition frequency $f_{\text{clock}} \sim 1\,\text{GHz}$. Similarly to the NV-based frequency standard, the clock is predicted to have a large temperature dependence due to lattice strains. However, it uses solely rf to interrogate the clock transition, without any optical components, which may permit development of single chip atomic clocks using the spectrometer-on-a-chip platforms developed for NMR and EPR. In practice, the authors managed to lock an oscillator to the resonance for short periods of time, though considerable drift in the frequency was observed over a period of only twenty minutes. They estimate that with improvements it may be possible to achieve short-term fractional frequency instabilities in the range 10^{-7} to 10^{-9}. However, as with NV centres in diamond, broadening due to interactions with the crystal lattice pose a significant challenge to developing it into a useful frequency standard.

Another proposal, and the one which this thesis aims to investigate, is the use of endohedral fullerenes as a frequency reference [**BA12**]. As will be discussed in detail in Section 1.3, endohedral fullerenes such as $N@C_{60}$ have long coherence times at room temperature, leading to narrow lines. In contrast to the previous two proposals for condensed matter atomic systems, the endohedral fullerenes can be used as solution samples. These solution samples are not subject to the limitations of solid state samples, such as strains in a crystal lattice that can lead to inhomogeneous broadening or temperature dependent resonance frequencies. In principle, the fact that all molecules are the same ensures that the frequency of the reference should remain constant. However, a very significant limitation is the low frequency clock transition due to the small hyperfine coupling in the endohedral nitrogen atoms. This low frequency can impair the achievable stability by limiting the transition quality factor, which parameterises the ratio of clock frequency to transition frequency,

and the SNR of the resonance signal due to the small Boltzmann factor. However, in common with the V^{++}:MgO-based frequency standard, the all-rf interrogation scheme potentially allows for ultra-miniaturised and ultra-rugged atomic clocks.

1.3 Fullerenes

Carbon is a highly versatile element, not simply in terms of its rich chemistry, but also the great variety of its allotropes. While diamond and graphite have been known since antiquity, in recent years additional allotropes have been discovered and have become the focus of intense study. Notable among these are graphene [**Nov04**], fullerenes [**Kro85**], and carbon nantotubes [**Iij91**]. These provide excellent systems for investigating fundamental physics, but they also hold out the possibility of technological application due to their unique electronic properties. Graphene, discovered in 2004 by Novoselov et al. [**Nov04**], is a two-dimensional sheet of carbon atoms arranged in a hexagonal lattice. Fullerenes and carbon nanotubes are three-dimensional structures. Fullerenes are typically "ball-shaped", whereas nanotubes are rolled-up sheets of graphene capped with fullerenes. This thesis focuses on fullerenes, and, specifically, endohedral fullerenes: fullerenes with an atom inside [**Bet93**].

There exists a diverse array of endohedral fullerenes, with a correspondingly diverse range of of chemical and physical properties. In this thesis, I am primarily interested in $N@C_{60}$ and $P@C_{60}$, which are referred as "Group V" endohedral fullerenes [**Bel02**]. This is a holdover from previous naming conventions, where the pnictogens (N, P, As, Sb, Bi, Uup) were placed in "group V" due to their pentavalency. This naming convention has since been replaced by group 15 in International Union of Pure and Applied Chemistry (IUPAC) conventions [**Flu88**]. However, I keep the name "group V" for consistency with previous literature. I also briefly discuss metallofullerenes, such as $Sc@C_{82}$ and $Y@C_{82}$, which are fullerenes with an encapsulated metal atom. Both families of fullerenes are of interest due to their spin properties: they are EPR spin active, with narrow linewidths [**Bro10**], and possess clock transitions at low fields.

For each of these families of fullerenes, there are different degrees of interactions between the endohedral species and the fullerene cage. The endohedral atoms of the group V endohedral fullerenes behave almost like free atoms trapped at the cage centre [**Alm96**; **Kna97**; **Pie98**; **Jak03**], with which they interact only weakly, whereas the metal atoms form charge transfer complexes with the fullerene cage [**Shi00**]. This leads to different spin properties in each case; the charge transfer fullerenes more sensitive to the external environment [**Zak10**].

For group V atoms, the cage is sometimes described as a "chemical Faraday cage" [**Pie97**] due to its protection of the highly reactive nitrogen atom from chemical reactions. While this chemical protection is clear, it is less clear that it "protects" the spin system from decoherence due to interaction with the environment. While it presumably shields the spin from short-ranged interactions, such as Heisenberg spin exchange [**Din00a**], the cage may not protect against long range forces, such as dipolar coupling between spins. However, it is certainly true that the spin has a much longer coherence time than most molecular spin systems [**Mor06**; **Zad15**]. Indeed, to the best of my knowledge, $N@C_{60}$ has the longest electron spin coherence time of any molecular spin system at room temperature. This long coherence time has led to suggestions for the use of endohedral fullerenes such as $N@C_{60}$ as spin qubits for use in quantum information processing [**Har02b**; **Ben06**]. At low temperatures, the spin coherence time has been exceeded by vanadium-based spin qubits [**Zad15**], where the spin coherence lifetime has been extended by using ligands without spins.

Endohedral fullerenes are reasonably stable under adverse environmental conditions, which is important because the stability of the clock will depend on the SNR of the resonance and hence the spin density in the ensemble. For example, they are stable up to high temperatures [**Wai01**], which is compatible with the anodic bonding temperatures used to fabricate sample chambers in MEMS devices [**Sha14**]. However, $N@C_{60}$ is photosensitive and decays under UV illumination [**Liu11**; **EWH15**]. This decay leads to a decrease in EPR signal intensity that is undesirable because it will reduce the SNR of the resonance signal, which in turn reduces the stability of the frequency standard's output. However, this should not pose a

problem for clocks implemented using $N@C_{60}$ because the sample will be stored in a hermetically-sealed, light-tight enclosure. Nonetheless, it is advisable to minimise the fullerene sample's exposure to light during the initial characterisation of the low-field behaviour of fullerenes in the home-built EPR spectrometer.

$N@C_{60}$ is not the only fullerene of interest: other fullerenes, such as the metallofullerenes, also demonstrate long coherence times [**Bro10**] and narrow linewidths [**Shi00**]. High purity samples are feasible due to the relatively large difference in retention time for the metallofullerene samples and the empty cage fullerene [**Lu12**]. Therefore, in contrast to the relatively low purity of $N@C_{60}$ available, it is relatively easy to obtain pure metallofullerene samples with a commensurate increase in spin density. This is desirable to increase the EPR signal intensity and improve SNR; as such, the metallofullerenes should not be excluded from further consideration. However, dipolar coupling in spin-concentrated samples leads to line broadening [**Jak03**; **Zak10**] that may place limits on the possible degree of spin-concentration in the sample.

The metallofullerenes have the disadvantage of a high nuclear spin quantum number and small hyperfine coupling. For example, the fullerenes of most interest due to their long coherence times and narrow linewidths are $Sc@C_{82}$ and $Y@C_{82}$ [**Bro10**], which have nuclear spins $I = 7/2$ and $I = 1/2$, respectively. The hyperfine coupling of $Sc@C_{82}$ is anisotropic, with $A = [15.5,\ 7.8,\ 7.3]\,\mathrm{MHz}$ [**Mor05b**], whereas the yttrium hyperfine coupling is approximately isotropic, with $A = 1.4\,\mathrm{MHz}$ [**Suz92**]. The large nuclear spin number increases the number of energy levels in the hyperfine manifold. Therefore, since the spin population is split between more levels, the change in population and hence power absorbed by the spin ensemble on resonance is less, which leads to a smaller signal amplitude and signal to noise ratio. This is compounded by the small hyperfine coupling, which further reduces the population difference between the clock transition energy levels.

The most promising endohedral fullerene other than $N@C_{60}$ is $P@C_{60}$. These two fullerenes are chemically very similar, since phosphorous is also a group V atom. As such, like $N@C_{60}$, it does not interact strongly with the cage and hence

is reasonably well isolated from the environment, leading to long coherence times and narrow linewidths [**Kna98**; **Wei98b**]. Most importantly for the purpose of using P@C_{60} as a frequency reference, it has a large hyperfine coupling $A \approx 138\,\mathrm{MHz}$ [**Kna98**]. This will increase the transition Q factor, a key figure of merit for use as a frequency reference.

One potential limitation of an endohedral fullerene frequency standard is the temperature-dependent hyperfine coupling [**Pie02**]. At room temperature, the shift $\mathrm{d}A/\mathrm{d}T \sim 2\,\mathrm{kHz\,K^{-1}}$. From the perspective of developing an atomic clock, this is a significant flaw since it reduces long term stability by introducing sensitivity to environmental perturbations. This is particularly significant for portable atomic clocks that may be used in environments with poor control of temperature. Temperature sensitivity is, of course, a problem common to many frequency standards, and may be overcome by temperature compensation or stabilization. Such approaches require some form of temperature monitoring that can be used as an input to compensation or feedback circuity. In this thesis, I show that it is feasible in principle to use auxiliary transitions for monitoring temperature. This is better than using an external sensor, such as a thermistor, because this approach measures the temperature of the sample itself, without any offset, and is not susceptible to drifts in the calibration of the external sensor [**Hod13**]. However, it is always preferable to find a working point at which the sensitivity to external perturbations is minimised in order to minimise the requirements of the compensation or stabilization hardware. This is possible within vapour cells by altering the buffer gas pressure and composition and choosing a tradeoff between pressure shift, light shift, and temperature shift of the reference frequency. Without finding such a point for N@C_{60}, the long-term stability of miniaturised frequency standards based on N@C_{60} may remain poor, due to the difficulty of maintaining a fixed temperature without using an oven with significant power consumption.

I tried to find a parameter by which the hyperfine coupling could be tuned to offset the temperature shift, as was proposed for NV centres in diamond [**Hod13**].

However, the pressure shift measured in Chapter 4 is too small to offset the temperature shift, since it would require a change in pressure of approximately $100\,\mathrm{atm\,K^{-1}}$. However, the small magnitude of the pressure shift ensures that a fullerene-based atomic clock would not be sensitive to atmospheric pressure fluctuations.

1.3.1 Production of endohedral fullerenes

Fullerenes were first synthesised by pulsed laser ablation of a carbon target [**Kro85**]. As the carbon-rich plasma cools, the carbon atoms form a variety of molecules including fullerene cages and nanotubes. The fullerenes can be extracted from the soot using appropriate solvents, which dissolve the fullerenes but not the amorphous carbon soot [**Dor94**].

Endohedral fullerenes can be produced either in a single-step process, wherein the endohedral fullerene is synthesised directly, for example [**Cha91**], or a two-step process in which the empty cage is synthesised prior to implantation of the endohedral species such as is used to synthesise $N@C_{60}$ [**Alm96**]. The one-step process is commonly used in metallofullerene production: a metal-doped carbon sample is vaporised in a laser furnace [**Cha91**] or dc arc furnace [**Shi92**], which directly produces a metallofullerene-containing soot. The metallofullerenes can be extracted from the soot with an appropriate solvent. The solution can then be purified using high-performance liquid chromatography (HPLC) to isolate the desired metallofullerene [**Shi93**; **Dor94**].

The endohedral fullerene $N@C_{60}$ is typically synthesised by implanting nitrogen ions into empty fullerene cages [**Wei98a**]. The empty fullerene cages are synthesised using dc arc discharge, as explained above, and are commercially available in high purity. A solid sample of empty fullerenes is then sublimed by heating in a vacuum chamber under high vacuum. An ion source generates nitrogen ions by breaking down N_2 feed gas. These ions are accelerated and directed perpendicular to the flux of sublimed fullerenes. Collisions between the endohedral fullerene and ions may result in implantation of nitrogen atom inside the fullerene cage. Since the collision cross section for the fullerene cage and ion is very low, the probability

of a successful implantation is small—the majority of cages remain empty. The soot deposited on the copper target thus contains a mixture of endohedral nitrogen fullerenes, empty-cage fullerenes, and amorphous carbon due to breakdown of the nanostructures. The isotopic distribution of the implanted fullerenes is controlled via the isotopic distribution of the feed gas.

The fullerenes are extracted from the soot using solvents, and the ion-implanted fullerenes are then separated from the remaining empty cages using HPLC [**Jak03**]. The development of high-throughput processing techniques [**PP14**] ensures the availability of sufficient quantities of endohedral fullerenes for development work on the atomic clock. Large-scale production of endohedral fullerenes is yet to be established but it seems possible that the development of fullerene-based technologies may provide sufficient impetus to develop new approaches to mass production.

The synthesis of P@C_{60} is performed in the same way, except the nitrogen gas used in the ion implantation procedure is replaced by phosphine (PH_3) [**Sch06**]. Synthesis has previously been performed, and EPR studies performed on P@C_{60} [**Kna98**; **Wei98b**]. Furthermore, the P@C_{60} should benefit from easier purification than N@C_{60}, due to the significant difference in retention time in an HPLC column for P@C_{60} and empty cage C_{60} [**Sch06**]. EPR studies of P@C_{60} indicate that it may be more suitable than N@C_{60} due to its larger hyperfine coupling, and hence higher clock transition frequency. However, P@C_{60} was not used in this thesis. Phosphine gas is toxic, and handling it was outside of the capabilities of the chemistry lab that synthesised the N@C_{60} used in this thesis. However, future efforts to developing fullerene clocks may wish to invest effort in finding ways to overcome these problems, due to the potential advantages of P@C_{60} over N@C_{60}.

2

EPR: Theory and instrumentation

Contents

2.1 Electron paramagnetic resonance

For this thesis, I designed and built low-frequency ($f < 100\,\mathrm{MHz}$) cw and pulsed EPR spectrometers. In this chapter, I discuss the theory and practice of EPR, with a focus on instrumentation and in particular how this applies to the low-frequency cw spectrometer I built. A schematic diagram of this spectrometer is given in Figure 2.1. In Chapter 3, I report on the experimental observation of the clock transition in N@C_{60}, which was achieved using the low-frequency cw spectrometer.

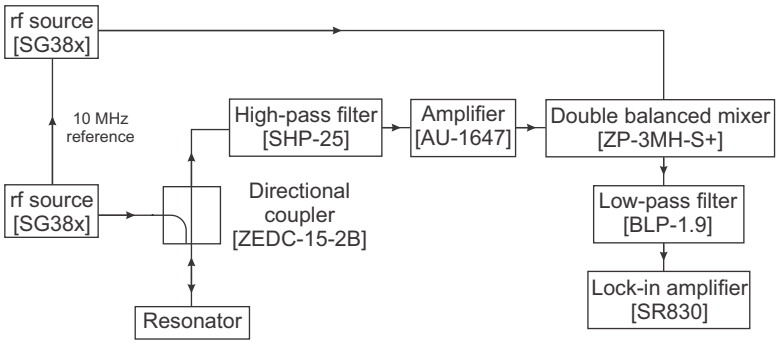

Figure 2.1: Schematic circuit diagram of the cw EPR spectrometer used at frequencies between 30 and 100 MHz. The label in square brackets corresponds to the part number of each component. With the exception of the rf amplifier (L3 Narda-MITEQ), the rf components were purchased from Mini-Circuits, Inc. The rf source and lock-in amplifier are from Stanford Research Systems, Inc.

Unfortunately, I was not able to acquire a signal from N@C_{60} using the pulse spectrometer during my PhD. For this reason, the design is detailed in Appendix D rather than the main text of this thesis. The results presented in Chapter 4 were obtained using a commercial spectrometer operating at the X band.

2.1.1 A brief history of electron paramagnetic resonance

Electron paramagnetic resonance was first observed by Zavoisky in 1944 [**Zav45**]. Zavoisky observed the paramagnetic resonance of various transition metal ion solutions probed using low-frequency radiation with a wavelength $\lambda = 25\,\mathrm{m}$, which corresponds to a frequency of approximately 10 MHz. The sample was placed in a tuned coil that served as the tank for an electrical oscillator. The response of the spin ensemble was measured via the electrical current flowing in the oscillator circuitry. The low frequencies employed in these spectrometers, which resulted in a small spin polarization, coupled with the broad linewidth, resulted in low sensitivity. At a similar time, EPR was independently discovered by Cummerow and Halliday at the University of Pittsburgh [**CH46**] and the group of Bleaney *et al.* at the Clarendon Laboratory, University of Oxford [**BG47**; **BP48**].

The early attempts at EPR spectroscopy were limited by the sophistication, or lack thereof, of the available equipment and poor choice of sample. Since the pioneering days of EPR spectroscopy, instrument development has been key to

opening up new avenues for discovery. After this initial period, the availability of war-surplus radar equipment operating at microwave frequencies enabled the rapid development of EPR spectroscopy. Rapidly, the frequency of the applied radiation increased [**Whi48**]. This choice of frequency has since become locked in, and X-band (ca. 9–10GHz) is still the most widely available frequency band.

In addition to the increase in frequency, the means of detection rapidly improved in sensitivity. The first attempts at detecting magnetic resonance used calorimetric measurement of the sample [**Gor36b**; **Gor36c**; **Gor36a**; **GB42**], to detect an increase in temperature as the spin ensemble absorbed rf power and transferred to the crystal lattice. Later, the absorption of rf power was detected as a change in grid current in an oscillating circuit [**Zav45**]. Most EPR spectrometers now operate by using separate rf sources and detectors [**Poo83**]. These detectors may be power (square-law) detectors, voltage (linear) detectors, or, more rarely, bolometric detectors. These detect the transmission of rf power through a structure, such as a waveguide or coaxial transmission line, containing the sample or, more commonly, the transmission or reflection of radiation from a resonant structure, such as a microwave cavity, containing the sample. The sensitivity of detectors has improved over time [**Mis11**], presumably due to improved semiconductor processing and device fabrication technologies. In particular, this has reduced low-frequency noise such as $1/f$ noise and "popcorn noise". Furthermore, lock-in detection to shift the detection frequency away from the low-frequency components of the noise is now standard [**Poo83**]. This is by no means an exhaustive list of improvements, but provides a brief illustrative guide.

As well as measuring the absorption of power by the spin ensemble, it is possible to measure a time-dependent magnetization of the spin ensemble by the voltage it induces in a conductor. Initially, the net magnetization is aligned with the static magnetic field. Following a classical picture, it can be tilted by driving transitions between different spin states using a pulse of rf radiation resonant with the transition. The magnetization now precesses about the static magnetic field, which can be detected by measuring the voltage induced by the changing

magnetic flux. This was one of the early approaches to detecting CW magnetic resonance [**BHP46**]. This approach is now rarely used for cw experiments, but it now forms the foundation of pulse EPR [**SJ01**].

Pulse techniques involve measuring the free induction decay or spin echoes [**SJ01**]. The free induction decay measures directly the decaying voltage induced by the precession of the magnetization vector directly after a pulse of rf radiation. The existence of spin echoes was discovered by Erwin Hahn in 1950 [**Hah50**], and they are the result of the time evolution of the spin state refocusing dephasing of a free induction decay. Pulsed magnetic resonance allows more direct access to physical parameters such as relaxation times and spin-spin couplings than can be achieved with continuous wave experiments, at the cost of increased complexity. The development of pulsed EPR hardware has been slower than that of pulsed NMR due to the higher frequencies. In addition, the much shorter relaxation times of EPR-active samples compared to NMR-active samples further increases the difficulty of performing pulsed EPR.

Despite this, pulsed EPR has a long history. The earliest report on pulsed EPR in the literature dates from 1958 [**Blu58**], where Blume measured the relaxation times of solvated sodium ions in ammonia. This was achieved by measuring the free induction decay and Hahn spin echo from the sample. Since then, the sophistication of EPR pulse experiments has dramatically increased, and a great variety of different pulse sequences has been developed to extract different information and account for imperfections of the experimental equipment [**EE95**; **SJ01**].

The development of theory and instrumentation over the last 70 years has brought EPR from being a scientific curiosity to a highly developed tool. While EPR remains less prevalent than NMR, it is a key underpinning technology for fields ranging from quantum information processing [**WM16**] to biology [**Ber17**]. With further effort, it may one day permit the development of a new generation of miniaturised atomic clocks.

2.2 Electron paramagnetic resonance theory

Electron paramagnetic resonanace is analogous to nuclear magnetic resonance (NMR), but rather than measuring the resonance of nuclear spins, one measures the resonance of electron spins as they interact with an oscillating magnetic field. It is less widely applicable than NMR due to the relative paucity of materials with unpaired electron spins, but it is more sensitive than NMR [**DG15**]. This is because the greater magnetic moment of the electron compared to nuclear spins gives a stronger coupling to the rf magnetic field.

The resonance condition of the spin system can be changed by either adjusting its Hamiltonian to change the splitting of the energy levels, or by altering the frequency of the applied radiation such that it coincides with the energy splitting of the levels. From this, it is possible to deduce the structure of the Hamiltonian, and determine the numerical value of the coefficients describing the various interactions. This can be used to shed light on the physical reality of the spin system in question, such as the molecular structure, physical dynamics, and chemical reaction pathways [**PRM01**; **RS18**]. It can also be used to investigate the behaviour of electrons in semiconductor systems, with application to device physics, and controlling spin qubits [**Bro77**; **Wat99**].

2.2.1 The terms in the spin Hamiltonian

The energy levels of the spin system are given by the eigenvalues of the spin Hamiltonian, and energy level corresponds to a specific eigenstate. In this section, I discuss the interactions that make up the Hamiltonian that describes the N@C_{60} spin system.

Electrons, being charged particles with angular momentum, possess a spin magnetic moment $\boldsymbol{\mu}$. The spin magnetic moment may be either that of a single unpaired electron, or a group of unpaired electrons. For example, in the N@C_{60} molecule investigated in this thesis, the unpaired p orbital electrons give the electron configuration ${}^4S_{3/2}$, with spin magnetic moment $S = 3/2$ and orbital

angular momentum $L = 0$. This spin magnetic moment interacts with magnetic fields $\boldsymbol{B}$, which is described by the Zeeman interaction

$$H = -\boldsymbol{\mu} \cdot \boldsymbol{B}. \tag{2.1}$$

This can either be a static magnetic field or radio frequency magnetic field. Static magnetic fields are used to split the energy levels, and radio frequency magnetic fields are used to drive transitions between the energy levels.

In addition to the Zeeman interaction there are many interactions that also affect the energy levels. However, for the purposes of this thesis, I will focus on relatively few: due to the high symmetry and simplicity of the N@C60 spin system, only a small number of interactions modify the energy levels of the spin system. Indeed, the spin Hamiltonian for the $N@C_{60}$ spin system given in the literature includes only the Zeeman interaction and hyperfine coupling [**Alm96**]. However, other interactions [**Kna97**; **Mor06**] are relevant for decoherence processes, so I will also discuss them.

The $N@C_{60}$ spin system posesses both electronic and nuclear spins, which are coupled by spin-orbit and hyperfine coupling. The spin-orbit coupling

$$\hat{\mathcal{H}}_{LS} \propto \boldsymbol{L} \cdot \boldsymbol{S}, \tag{2.2}$$

and hence does not contribute to the spin Hamiltonian, since the total orbital angular momentum L of the unpaired $2p^3$ orbital electrons is zero. However, the hyperfine coupling between the spins is significant, and understanding it is a major focus of this thesis.

The hyperfine coupling between the electronic spin and nuclear spin is described by the Hamiltonian

$$\hat{\mathcal{H}}_{\text{hf}} = \boldsymbol{S} \cdot \hat{\boldsymbol{A}} \cdot \boldsymbol{I}, \tag{2.3}$$

where the hyperfine coupling tensor $\hat{\boldsymbol{A}} = \hat{\boldsymbol{A}}_{\text{F.c.i.}} + \hat{\boldsymbol{A}}_{\text{dip.}}$ includes contributions from the Fermi contact interaction $\hat{\boldsymbol{A}}_{\text{F.c.i.}}$ and from the magnetic dipole coupling $\hat{\boldsymbol{A}}_{\text{dip.}}$.

The Fermi contact interaction is an isotropic interaction proportional to the overlap between the electronic wavefunction and the nucleus [**Fer30a**; **Fer30b**]. The

nucleus is taken to be a point-like particle, such that the Fermi contact interaction is only non-zero for wavefunctions that are non-zero at $r = 0$, where r is the radial coordinate of the wavefunction, such as s orbitals. Electronic wavefunctions with nodes at $r = 0$, such as the $2p$ orbitals relevant for N@C_{60}, should not give rise to a Fermi contact interaction.

The dipolar coupling gives rise to an anisotropic hyperfine coupling described by a traceless matrix [**BG09**]. However, unlike the Fermi contact interaction, the dipolar coupling is a long range interaction. Therefore, it gives a non-zero hyperfine coupling even for wavefunctions with nodes at the nucleus.

The hyperfine coupling for N@C_{60} is taken to be isotropic [**Alm96**; **Kna97**] yet the unpaired electrons are in p orbitals and the spherical symmetry of the N@C_{60} spin system precludes a dipolar hyperfine. Taken together, these facts imply that N@C_{60} should not have a hyperfine coupling. I discuss possible reasons for this in Chapter 4, with particular focus on the factors that could lead to spin polarisation of the s orbitals.

In addition to terms coupling the electronic and nuclear spin, there are terms coupling each spin to itself. The self-coupling of the electron spin is termed the zero-field splitting, and is described by the Hamiltonian

$$\hat{\mathcal{H}}_{\mathrm{hf}} = \boldsymbol{S} \cdot \hat{\boldsymbol{D}} \cdot \boldsymbol{S}, \tag{2.4}$$

where $\hat{\boldsymbol{D}}$ is a traceless matrix describing magnetic dipolar coupling. The self-coupling of the nucleus to itself is termed quadrupolar coupling, and is described by the Hamiltonian

$$\hat{\mathcal{H}}_{\mathrm{hf}} = \boldsymbol{I} \cdot \hat{\boldsymbol{Q}} \cdot \boldsymbol{I}, \tag{2.5}$$

where $\hat{\boldsymbol{Q}}$ is the quadrupolar coupling matrix. The quadrupolar coupling is only active for nuclear spins with a non-spherical charge distribution, which requires $I > 1/2$. It is therefore not present for the ^{15}N@C_{60} molecules investigated in this thesis, since for ^{15}N the nuclear spin $I = 1/2$. Secondly, the quadrupolar coupling requires an electric field gradient at the location of the nucleus. Since the

$N@C_{60}$ molecule posesses spherical symmetry, there is no electric field gradient and the quadrupolar coupling is zero even for $^{14}N@C_{60}$, which has a nuclear spin $I = 1$.

While the zero-field splitting and quadrupolar terms are negligible, up to the precision of the experiment, solvent molecule collisions may break the symmetry of the cage. This could lead to a time-dependent perturbation to the Hamiltonian, thereby causing spin-lattice relaxation [**Kna97**]. Another interaction that is relevant for the the $N@C_{60}$ molecule is coupling between mechanical excitations of the fullerene cage and the spin system [**Mor06**]. Analysis of the relaxation time as a function of temperature indicates that the relaxation time is governed by an Orbach process where phonons corresponding to cage vibrations excite the electron to a higher-energy state, which leads to spin relaxation and decoherence. The Orbach mechanism was found to fit the data more convincingly than the previously proposed fluctuating zero-field splitting. The relaxation rate due to the Orbach mechanism $\Gamma_{\text{Orb.}} \propto \omega^{-2}$, where ω is the resonant angular frequency of the transition [**Atk67**]. Given that the Orbach mechanism should be unaffected by the clock transition's insensitivity to field fluctuations, which only protects against dipolar decoherence, it may severely limit the maximum achievable coherence time and hence minimum achievable linewidth of the low-frequency clock transition.

2.2.2 Selection rules

In a magnetic resonance experiment, such as the EPR experiments detailed in this thesis, the transitions between energy levels obey certain "selection rules". These selection rules are based on the symmetry of the system and the interaction coupling the two energy levels. For a transition to be allowed, the interaction $\hat{\boldsymbol{I}}$ operating on the initial state $|i\rangle$ must give a state $|i'\rangle = \hat{\boldsymbol{I}}\,|i\rangle$ that is not orthogonal to the final state $|f\rangle$, such that the transition probability $P = |\langle f|\,\hat{\boldsymbol{I}}\,|i\rangle|^2 \neq 0$. These selection rules are important for this thesis because they govern whether or not it will be possible to observe the EPR signal from the clock transition, as will be shown in Chapter 3.

For EPR experiments, the selection rules governing magnetic dipole transitions between the different spin states depend on the orientation of the oscillating drive field $\boldsymbol{B_1}$ relative to $\boldsymbol{B_0}$. The transitions are driven by the Zeeman interaction

$$\hat{\mathcal{H}} = -\boldsymbol{\mu} \cdot \boldsymbol{B_1} \tag{2.6}$$

between the rf magnetic field $\boldsymbol{B_1}$ and the spin magnetic moment $\boldsymbol{\mu}$. For an electron, the spin magnetic moment $\boldsymbol{\mu} = g_e \mu_B \boldsymbol{S}$. The expression for a nuclear magnetic moment is similar, with the electron g factor, magneton, and electron spin operator replaced by the nuclear equivalents. The transition matrix element $V_{ij} = \langle j | \hat{\mathcal{H}} | i \rangle$, with initial state $|i\rangle$ and final state $|j\rangle$ in the $|S, m_s\rangle$ basis, for this transition are therefore given by

$$g\mu_B B_1 \langle j | \boldsymbol{S} \cdot \boldsymbol{x} | i \rangle \qquad (\boldsymbol{B_1} = B_1 \boldsymbol{x}) \tag{2.7}$$

$$g\mu_B B_1 \langle j | \boldsymbol{S} \cdot \boldsymbol{y} | i \rangle \qquad (\boldsymbol{B_1} = B_1 \boldsymbol{y}) \tag{2.8}$$

$$g\mu_B B_1 \langle j | \boldsymbol{S} \cdot \boldsymbol{z} | i \rangle \qquad (\boldsymbol{B_1} = B_1 \boldsymbol{z}). \tag{2.9}$$

The minus sign has been neglected due to the convention of giving the electron g factor as a positive quantity. The projection of the spin operators onto the axes give

$$g\mu_B B_1 \langle j | \frac{1}{2}(S_+ + S_-) | i \rangle \qquad (\boldsymbol{B_1} = B_1 \boldsymbol{x}) \tag{2.10}$$

$$g\mu_B B_1 \langle j | \frac{1}{2i}(S_+ + S_-) | i \rangle \qquad (\boldsymbol{B_1} = B_1 \boldsymbol{y}) \tag{2.11}$$

$$g\mu_B B_1 \langle j | S_z | i \rangle \qquad (\boldsymbol{B_1} = B_1 \boldsymbol{z}), \tag{2.12}$$

where S_+ and S_- are the spin raising and lowering operators respectively. With the oscillating magnetic drive field $\boldsymbol{B_1}$ oriented along the $\boldsymbol{x}$ or $\boldsymbol{y}$ axes, perpendicular to the static magnetic field $\boldsymbol{B_0} = B_0 \boldsymbol{z}$, the magnetic dipole transitions therefore couple spin states with the projection of spin along the $\boldsymbol{z}$ axis differing by one. This corresponds to a selection rule $\Delta m_s = \pm 1$ for perpendicular mode transitions. In contrast, for parallel mode transitions, with the oscillating magnetic drive field $\boldsymbol{B_1}$ oriented along the $\boldsymbol{z}$ axis, the selection rule is $\Delta m_s = 0$.

The clock transition of the endohedral fullerene $\Delta m_S = 0$, which requires driving the transition by setting $\boldsymbol{B_1} \parallel \boldsymbol{B_0}$, or by driving the transition indirectly via an auxiliary level as illustrated in Figure 3.2.

2.2.3 Two-level systems and the Bloch sphere

In a magnetic resonance experiment, one wishes to excite transitions between energy levels. One can therefore pick the upper and lower energy levels as a pair of basis states $|u\rangle$ and $|l\rangle$, respectively. Applying a rf pulse to the ground state gives the state

$$|\psi\rangle = \frac{1}{\sqrt{\alpha^2 + \beta^2}} \left(\alpha |l\rangle + \beta |u\rangle\right), \tag{2.13}$$

where the coefficients α and β depend on the duration and phase of the pulse, and the magnitude of the rf field B_1. The state ψ is conveniently represented using a Bloch sphere [**NC00**], as shown in Figure 2.2. Using the Bloch sphere representation, the state

$$|\psi\rangle = cos(\frac{\theta}{2}) |l\rangle + \sin\left(\frac{\theta}{2}\right) \mathrm{e}^{i\phi} |u\rangle, \tag{2.14}$$

where the angles θ and ϕ give the relative proportion of the states and relative phase between the basis states, respectively. This vector, which has unit length, describing the location of the spin state on the Bloch sphere is known as the Bloch vector.

The Bloch sphere representation is only valid for a pure state, whereas in reality we are concerned with a physically measurable quantity. For the EPR experiment, this quantity is the net magnetization of the spin ensemble. The magnetization is given by the average over the magnetization of each spin in the ensemble. As such, the magnetization is calculated by taking the trace of the magnetization operator on a mixed state, rather than a pure state.

For simple spin systems, such as a single spin-1/2 particle, there is a natural overlap between the Bloch sphere picture and the magnetization in the rotating frame. Here, a $\pi/2$ pulse puts the spin into a superposition of the two states, which naturally corresponds to rotating the magnetization vector into the xy plane such that it precesses about the magnetic field along the z axis. For higher-spin and coupled spin systems, this correspondence breaks down. The Bloch sphere picture, though more abstract, should be preferred.

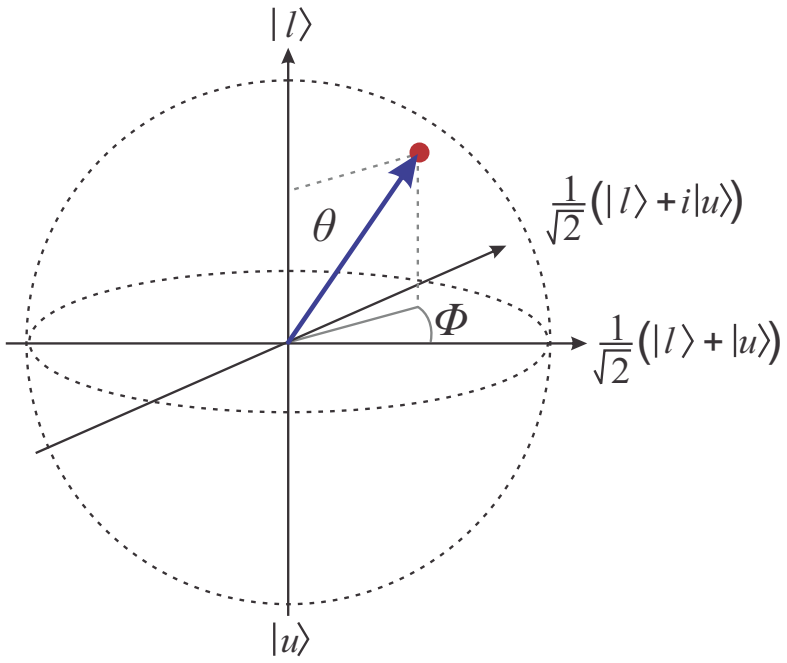

Figure 2.2: The Bloch sphere allows for a convenient representation of a two-level system. The basis states used here are the ground state $|l\rangle$ and excited state $|u\rangle$. The pure state $|\psi\rangle$ corresponds to a point on the surface of a sphere with unit radius. The vector linking this point to the origin is parameterised by the polar angle θ, which gives the relative proportion of the ground and excited states, and the azimuthal angle ϕ, which gives the phase between the two basis states.

A specific example of this breakdown is at the clock transition in N@C_{60}. At the clock field, the basis states for the Bloch sphere are

$$|l\rangle = \frac{1}{\sqrt{2}}\left(+ \left|-\frac{1}{2}, -\frac{1}{2}\right\rangle - \left|-\frac{3}{2}, \frac{1}{2}\right\rangle \right) \tag{2.15}$$

$$|u\rangle = \frac{1}{\sqrt{2}}\left(- \left|-\frac{1}{2}, -\frac{1}{2}\right\rangle - \left|-\frac{3}{2}, \frac{1}{2}\right\rangle \right), \tag{2.16}$$

in the $|m_S, m_I\rangle$ basis [**Lin15**]. By considering the selection rules given in Section 2.2.2, it can easily be seen that the clock transition is an allowed transition in parallel mode, but forbidden in perpendicular mode. The expected magnetic moment of an arbitrary spin state ψ is given by

$$\boldsymbol{M} = \langle\psi|\, g_{\mathrm{e}}\mu_{\mathrm{B}}\hat{\boldsymbol{S}} + g_{\mathrm{N}}\mu_{\mathrm{N}}\hat{\boldsymbol{I}}\,|\psi\rangle\,, \tag{2.17}$$

where $g_{\mathrm{e(N)}}$ and $\mu_{\mathrm{e(N)}}$ are the electron(nuclear) g factor and electron(nuclear) magnetic moment, respectively. The magnetic moment along each axis can be found by decomposing the spin operator into its vector components. Assuming

thermal equilibrium, the net magnetization of the spin ensemble can be calculated from the expected magnetic moment and the population of each spin state, which is determined by the Boltzmann factor. By considering the M_x and M_y components of the magnetization, it can be seen that the magnetization in the xy plane is always zero regardless of the angles θ and ϕ on the Bloch sphere. Here, a $\pi/2$ pulse rotates the spin on the Bloch sphere, but does not tilt the magnetization vector. One can see why this is physically: since the magnetic fields B_0 and B_1 are coaxial along the $\boldsymbol{z}$ axis, there is no preferred axis and hence the magnetization vector of the spins in the ensemble would be equally distributed in the xy plane. Since the magnetization vector is not tilted, it does not precess around the static magnetic field $\boldsymbol{B} = B_0\boldsymbol{z}$. However, the difference in energy between the basis states $|l\rangle$ and $|u\rangle$ lead to a time varying phase ϕ. By calculating the magnetization of the state, one can see that this phase leads to an oscillating magnetization along the $\boldsymbol{z}$ axis. Therefore, this signal can be detected despite the fact that there is no precessing magnetization vector.

The Bloch sphere also gives a natural picture for understanding pulse sequences, which can be seen as a series of transformations of the Bloch vector on the Bloch sphere [**VC05**]. However, the Bloch sphere picture is unhelpful for visualising spin relaxation and dephasing, since the unit-length Bloch vector only represents pure states. This is better represented by the "Bloch ball", where the vector can have non-unit length. The length of the vector depends on the degree of dephasing and decoherence, since the vector is the sum of all the spin vectors in the sample. The effect of spin-lattice relaxation and spin-spin decoherence is discussed in Section 2.2.4.

2.2.4 Spin relaxation and decoherence on the Bloch sphere

The Bloch sphere does not provide a good picture for spin relaxation and spin decoherence because a state vector on the surface of the sphere, with unit length, describes a pure state. When the spin relaxes, it moves back to the ground state. The relaxation time is the characteristic timescale for the spin to relax. For a single spin, as is described by the Bloch sphere, this would be a discontinuous jump. However, when talking about the spin relaxation of the sample in this

thesis, I am primarily interested in the collective behaviour of all the spins in the sample. Therefore, the Bloch sphere picture with a single spin does not provide an intuitive physical picture of how the spin ensemble behaves. Furthermore, spin-spin dephasing specifically relates to how the phase of a given spin evolves relative to another spin in the ensemble; as such, the single spin picture is deficient.

The spin-lattice relaxation time T_1 and spin-spin dephasing time T_2 are traditionally derived with regards to the Bloch equations [**Sli90**], which describe the evolution of the magnetization of an ensemble of uncoupled spins in response to an rf field. However, as discussed above, this magnetization-based picture is deficient for the parallel mode transitions investigated in this thesis. It is therefore instructive to see how this picture can be converted to a picture based on the spin state. Figure 2.3 gives a Bloch ball diagram. Here, the Bloch vector used in the original Bloch sphere picture is replaced by a vector that is the sum of the Bloch vectors for each spin in the ensemble. Now, the length of the vector is not fixed and may change in response to spin relaxation and dephasing. Spin-lattice relaxation corresponds to an increasing projection of the vector onto the $\boldsymbol{z}$ axis as the spin ensemble returns to equibibrium. Spin-spin dephasing corresponds to a decreasing projection of the spin vector onto the xy plane.

The T_2 time is the characteristic timescale for dephasing of spins due to physical processes inherent to the spin system itself, and its interactions with the environment. In practice, spin-spin dephasing typically occurs faster than the characteristic T_2 time due to field inhomogeneities over the sample [**Sli90**]. This field inhomogeneity leads to different Zeeman energies, and hence different energy splittings, at different points in the sample. The rate of change of the spin state's quantum mechanical phase is therefore position dependent, and hence the effective dephasing rate over the whole sample is greater than that for an individual spin in the ensemble. The characteristic timescale for the spin-spin dephasing after including the effect of field inhomogeneity is denoted by T_2^*.

Various mechanisms can cause spin-lattice relaxation and spin-spin dephasing, as will be discussed later. Given sufficient signal-to-noise ratio on a signal, it may

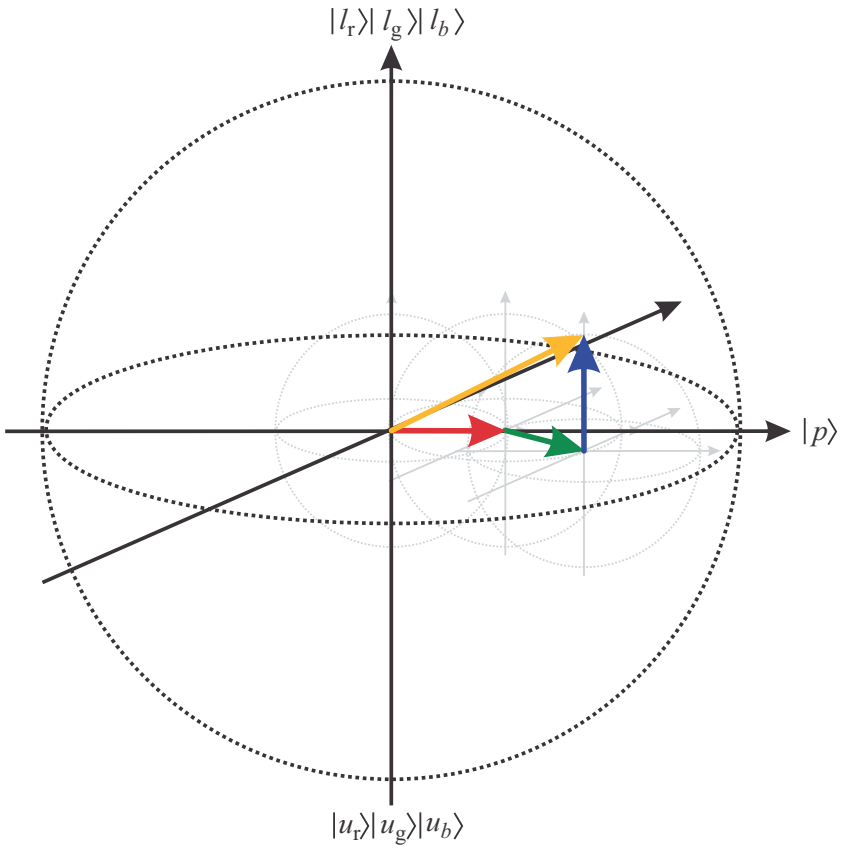

Figure 2.3: The Bloch ball allows for a convenient representation of an ensemble of two-level systems. Here, I am showing a simple ensemble of three uncoupled spins to illustrate dephasing and spin relaxation, and their effect on the mixed state. The state vectors of the three spins are displayed as red, green, and blue arrows; the vector describing the mixed state of the ensemble is displayed as a yellow arrow. The spins start in the ground state $|l\rangle$, and are put in prepared state $|p\rangle$ using an rf pulse. Initially, the prepared state $|p\rangle$ is a pure state and the state vector of the ensemble falls on the surface of the Bloch sphere. Here, however, I have illustrated dephasing (changing angle ϕ of green state vector) and relaxation (blue state vector returning to ground state), such that the total state vector (yellow) falls within the volume of the Bloch sphere. The point is not uniquely described; for example, it could be that the blue spin had dephased and the green spin relaxed. The ensemble is therefore described by a mixed state.

be possible to deduce information about the decoherence or relaxation process by considering the lineshape of the resonance [**PF99**]. Lorentzian lineshape functions are typically associated with homogeneous broadening processes that affect all spins within the ensemble in the same way. In contrast, inhomgeneously broadened resonances signals give a Gaussian lineshape. In practice, the lineshape function may be described by a convolution of the two.

The relaxation and coherence lifetimes can be deduced from cw experiments

probing the linewidth and power saturation behaviours of the transition [**Por53**; **Cas59**]. However, it is hard to extract separately the spin–lattice relaxation time and spin–spin decoherence time, and the requirements on the SNR of the resonance and the instrumentation are severe. For this reason, pulse EPR spectroscopy has become popular: furthermore, it permits extracting far more information about the spin system than can be deduced from cw measurements, and instrumental imperfections can be mitigated by judicious choice of pulse sequence [**SJ01**].

2.3 Electron paramagnetic resonance instrumentation

In this thesis, I designed and built a low-frequency continous wave EPR spectrometer that operated at frequencies ranging from $\mathcal{O}(10)\,\mathrm{MHz}$ to $\mathcal{O}(100)\,\mathrm{MHz}$. This spectrometer will be the focus of the remainder of this chapter and Chapter 3. I also designed and built a low-frequency pulse EPR spectrometer presented in Appendix D.

In continuous wave mode, the spectrometer detects a change in reflection coefficient of a tuned circuit containing the sample when the applied rf magnetic field is resonant with a magnetic dipole transition between spin states. This change in reflection coefficient leads to a change in the amount of rf power reflected from the circuit. In pulse mode, the spectrometer detects the rf voltage induced in the tuned circuit by the oscillating magnetization of the spin ensemble. In both cases, the rf voltage was measured using a double-balanced mixer as a homodyne detector. The amplified signal rf is mixed with a local oscillator, and the output is low-pass filtered to remove the sum frequencies. The output from the detector is thus a voltage linearly proportional to the signal amplitude. This baseband signal can be digitised directly, as is the case for the pulse spectrometer, or measured using a lock-in amplifier, as is the case for the cw spectrometer.

The sample is placed into a tuned circuit, which may be modelled as an effective inductance L, capacitance C, and resistance R as shown in Figure 2.4. The

impedance of the bare resonator, without the sample inserted, is given by

$$Z = \left[i\omega C_0 + \frac{1}{i\omega L_0 + R_0} \right]^{-1}, \tag{2.18}$$

where ω is the angular frequency, and the capacitance, inductance, and resistance are denoted by C_0, L_0, and R_0, respectively. The resonant angular frequency ω_0 of the bare resonator is determined by finding the frequency at which the imaginary impedance tends to zero, and is given by

$$\omega_0 = \frac{1}{\sqrt{L_0 C_0}} \left(1 - \frac{R_0^2 C_0}{L_0} \right). \tag{2.19}$$

The inductance of of the resonator, and hence its impedance, is modified by the magnetic susceptibility of the sample $\chi(B_0, f)$, which itself depends on the static magnetic field B_0 and the frequency f of applied radiation. The magnetic susceptibility $\chi = \chi' - i\chi''$ perturbs the inductance of the resonator such that

$$L_0 \to L_0(1 + \eta\chi' - i\eta\chi''), \tag{2.20}$$

where the the filling factor η parameterises how much of the resonator volume is filled by the sample [**Sli90**]. Near resonance, the real part of the sample's magnetic susceptibility modifies the inductance of the resonator, and hence the resonant frequency of the tuned circuit. The imaginary part of the sample's magnetic susceptibility leads to an imaginary inductance, which behaves like a resistance. These effects can be modelled by taking the inductance and resistance of the resonator as

$$L = L_0(1 + \eta\chi') \tag{2.21}$$

$$R = R_0(1 + \omega L_0 \eta\chi''), \tag{2.22}$$

where the second equation is derived by noting that the since $Z_L = i\omega L$, the imaginary inductance leads to a real impedance that is formally similar to a resistance. This resistance corresponds to the energy absorbed by the spin ensemble, and changes the quality factor of the tuned circuit. In principle, this resistance

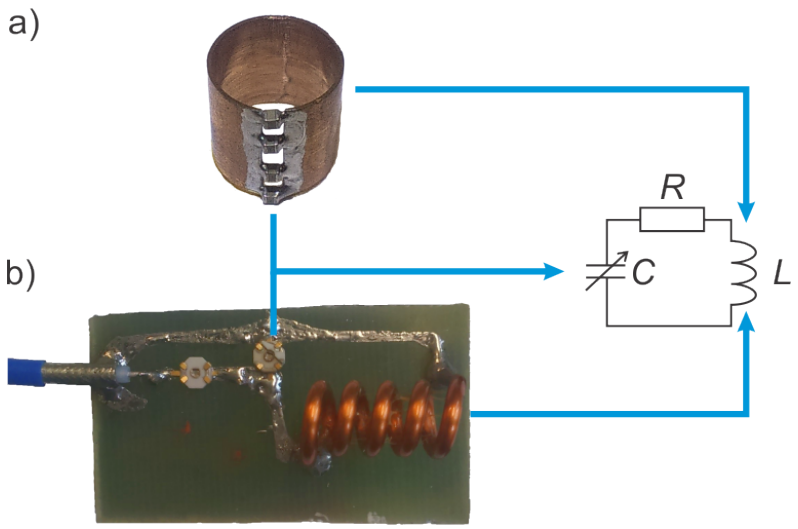

Figure 2.4: The resonator can be described by a lumped element LCR circuit. The copper loop is the inductive element of the loop-gap resonator (a). The resonant frequency is tuned using the chip capacitors soldered across the gap. In circuit (b), the solenoid is modelled as an inductance, and the resonant frequency is tuned using a trimmer capacitor. Losses in the circuit are modelled as a resistance R. The trimmer capacitor on the left of the circuit board is for matching the solenoid resonator impedance to the characteristic impedance of the transmission line (see Section 2.8).

also changes the frequency, but as a second-order perturbation it is ignored. The frequency, impedance, and Q factor of the resonator changes on resonance.

The resonator, with the sample inserted, is initially impedance matched to the spectrometer transmission line with the magnetic field set such that the spin system is far from resonance. This ensures that minimum power is reflected from the resonance; in principle, it should be possible to eliminate any reflected power, but in practice leakage and imperfect impedance matching lead to a finite reflected power. On resonance, the impedance of the resonator changes due to the change in the magnetic susceptibility of the sample. The resonator is no longer impedance matched to the transmission line, and the impedance mismatch leads to an increase in the rf power reflected from the resonator, and a change in the phase of the reflected rf signal. The frequency of the resonator also changes, because the frequency is pulled towards the resonant frequency of the spin system. In fact, in the experiments I performed, it was this frequency shift that I measured. This is discussed in detail in Appendix B.

By selecting suitable excitation frequencies relative to the resonator frequency, and by selecting the appropriate local oscillator phase, it is possible to observe either the phase or the absorption component of the spin ensemble's magnetic susceptibility. In commercial EPR spectrometers one typically only observes the absorption component due to the automatic frequency control (AFC), which locks the frequency of the excitation source to the cavity frequency [**BG09**]. However, the spectrometer detailed in this thesis possesses no AFC and care must be taken to ensure that the measured signal is not a mixture of phase and dispersion components.

2.3.1 Radio frequency source

The source provides the rf energy used to drive the transitions and provide the local oscillator signal to the rf mixer used to detect the EPR signal. The source typically contributes a significant portion of the system's total noise budget, so it is highly desirable to choose the lowest-noise rf source available to maximise the sensitivity of the spectrometer [**Rin04**].

The noise of a source is typically evaluated using the phase noise, which measures the noise power relative to the carrier within a given bandwidth at a specified frequency offset from the carrier. An example of phase noise is given in Figure 2.5. Phase noise is problematic since it may be demodulated to amplitude noise by the resonator and the detection scheme, if one is using a phase-sensitive detector such as a double-balanced mixer. It is important for the lock-in detection scheme used in this thesis, since the spin ensemble converts the field modulation into a sideband on the carrier signal offset by the modulation frequency. The phase noise at the modulation offset therefore contributes directly to noise on the measurement. Fortunately, at the low frequencies measured in this thesis, very low phase noise sources are available. Furthermore, the low Q resonators employed in the spectrometer are not such significant sources of demodulation.

The rf sources must also provide the local oscillator signal for the double-balanced mixer that I use to detect spin resonance. The local oscillator signal can be at the same frequency as the rf used to excite the transitions (homodyne detection) or

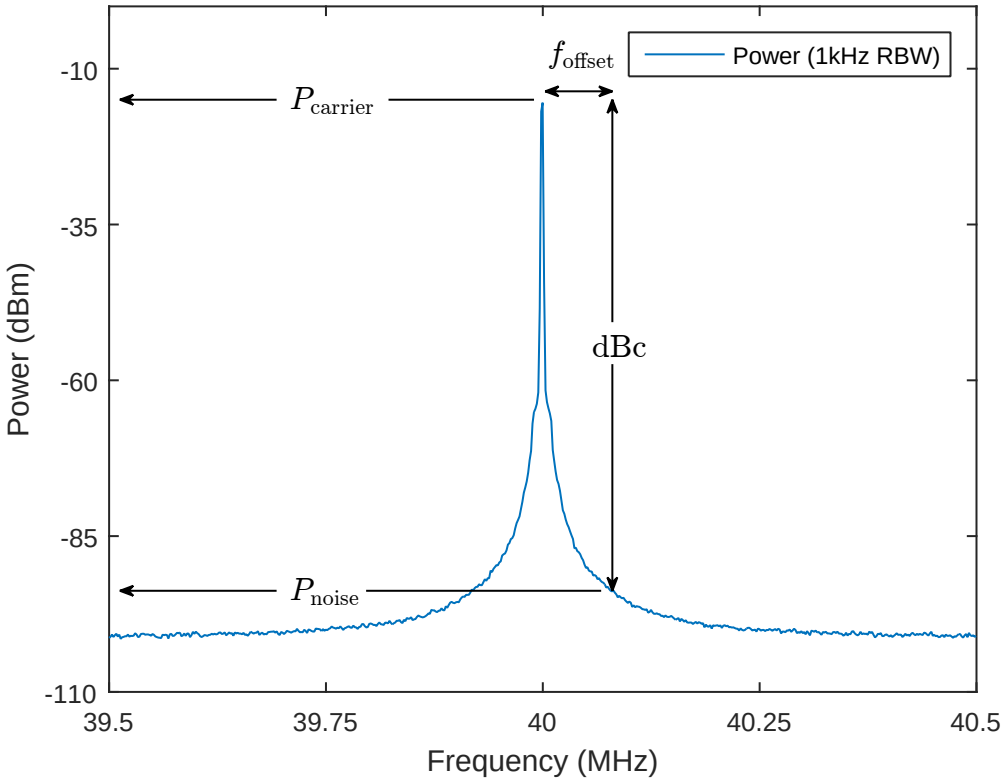

Figure 2.5: The phase noise of Stanford Research Systems SR382 signal generator measured using a Rigol DSA815 spectrum analyser.

offset by some known amount (heterodyne detection). In the spectrometers detailed in this thesis, I used homodyne detection due to to its simplicity. In both cases, it is desirable to adjust the relative phase of the rf and local oscillator signals to measure either the absorption or phase response of the spin ensemble to the applied rf radiation. In addition, the amplitude of the local oscillator must remain fixed in order to drive the double-balanced mixer at its optimal level, whereas it is desirable to adjust the excitation source amplitude to optimise the EPR signal.

The cw spectrometer uses separate Stanford Research Systems SG380 series rf signal generators for excitation source and local oscillator to permit convenient adjustment of relative phase and amplitude. The signal generators were phase locked using a 10 MHz reference frequency to ensure that they remain coherent. A periodic relative phase oscillation was observed as shown in Figure 2.6. This oscillation is related to how the oscillator inside the slaved source is locked to the

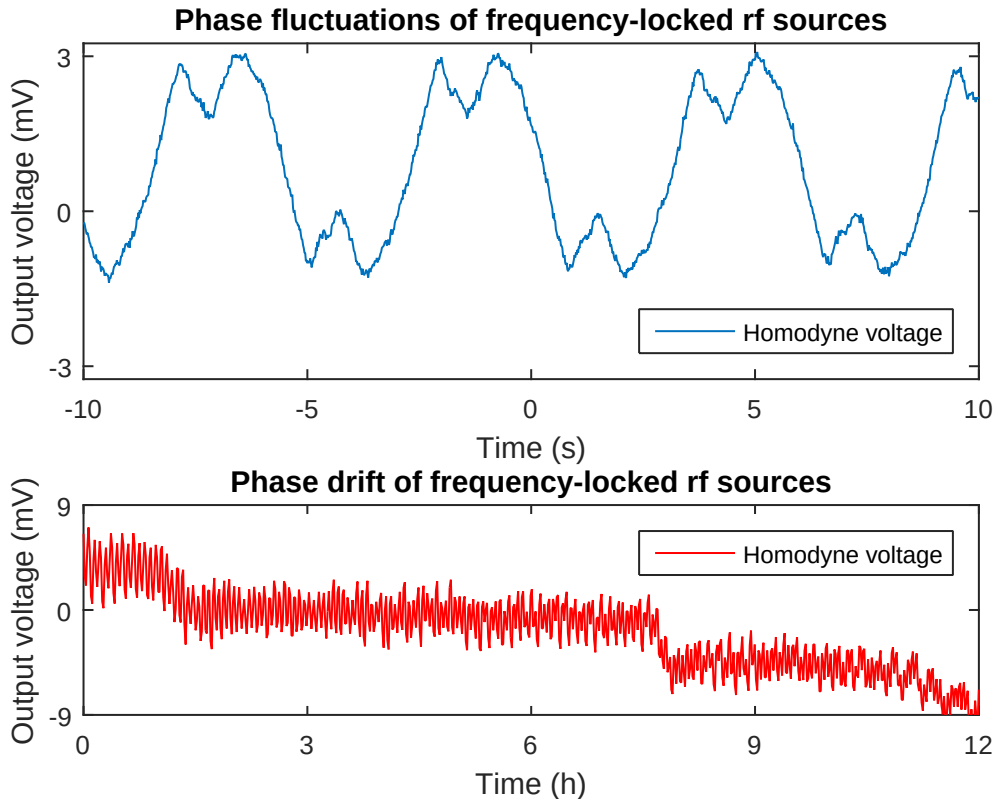

Figure 2.6: (a) shows a periodic oscillation in the relative phase for two locked oscillators. (b) shows a long term drift in the the relative phase.

10 MHz external reference signal. This observation is concerning, but probably not significant: when the relative phase of the signal and local oscillator are adjusted to maximise the amplitude sensitivity, the detector's phase sensitivity is minimised. However, phase drifts over long duration measurements (see Figure 2.6b) are of concern. As such, it is likely preferable to use a single source with separate amplitude and phase adjustment where feasible.

2.3.2 Resonator design

For maximum sensitivity, one wishes to maximise the coupling of the spin system to the spectrometer circuitry. Following the "principle of reciprocity" argument given by Hoult and Richards [**HR76**], this corresponds to maximising the conversion of rf power to ac magnetic field, which is achieved using a resonator. The resonator enhances the magnetic field, and hence the sensitivity, by a factor proportional

to the quality factor Q of the resonator.

The performance of a resonator can therefore be parameterised by how efficiently it converts rf energy into magnetic field, which depends on:

- the mode volume of the resonator,
- the filling factor of the resonator,
- and the quality factor of the resonator.

The mode volume of the resonator is the volume of the standing wave magnetic and electric fields excited by the applied rf signal. The filling factor η parameterises the overlap of the magnetic field with the sample and hence the fraction of the energy stored in the magnetic field that is used to excite transitions, as discussed in Section 2.2. The quality factor measures the rate of energy loss from the em mode of the resonator due to dissipation, either within the sample or the resonator itself, and due to energy coupled out to the spectrometer itself. There are also secondary considerations, such as optimising the homogeneity of the rf B_1 field. This is particularly important for pulse spectrometers, to ensure that all the spins in the sample are manipulated in the same way [**Mor05c**]. Furthermore, it is also important to consider the effect of the resonator on B_0 field homogeneity via the magnetic susceptibility of the materials used in its construction in order to avoid field inohomogeneities that broaden the EPR linewidth [**HR76**].

While developing the spectrometers used in this thesis, I investigated solenoidal coil resonators [**HR76**] and loop-gap resonators (LGRs) [**HW81**; **FH82**]. Most EPR spectrometers operate at microwave frequencies, and hence use cavity resonators [**Poo83**]. Here, the capacitance and inductance are distributed through the cavity and the size of the cavity is dictated by the desired cavity mode and resonant frequency. Cavity resonators are therefore unsuitable for use at low frequencies, since a resonator with a sufficiently low frequency would be very large; in the sample-limited case, such as is true given the small amounts of N@C_{60} available, this would lead to a poor filling factor [**EE04**]. At the low frequencies used in

this paper, is therefore desirable to use resonators whose size is not directly linked to the resonant frequency. The resonant frequency of both solenoids and LGRs can be tuned using additional capacitance.

For the purposes of driving the forbidden clock transition via auxiliary transitions, I considered double-tuned resonators. Such resonators have two separate resonant frequencies that can be tuned separately to the resonant frequency of each auxiliary transition. However, this line of enquiry was not pursued further, since directly driving the transition in parallel mode proved satisfactory, and the experimental apparatus required for direct drive is simpler.

Quality factor

The efficiency of the resonator is measured by the Q factor, which parameterises the rate of energy dissipation such that

$$Q \equiv 2\pi \frac{E}{E_{\text{cyc.}}} \tag{2.23}$$

where E is the energy stored in the resonator and $E_{\text{cyc.}}$ is the energy dissipated per cycle [**Poo83**]. In the high-Q regime, with $Q \gg 1$, the value of Q is given by

$$Q = \frac{f}{\Delta f}, \tag{2.24}$$

where f is the resonant frequency of the resonator and Δf is the bandwidth between the $-3\,\text{dB}$ points of the resonance. This measurement is shown in Figure 2.7, and is justified in Appendix A.

The quality factor can be the loaded or unloaded quality factor. The unloaded quality factor is the quality factor of the bare resonator, and is determined solely by the energy dissipated in the electrical resistance of the resonator itself. The loaded quality factor has more than one possible definition: it may be the quality factor of the resonator when it is critically coupled to a transmission line or the quality factor once a sample is loaded into the resonator. Both definitions correspond to "loading" the resonator with external losses. The first definition of loaded quality factor accounts for the fact that energy is coupled out of the resonator; the second

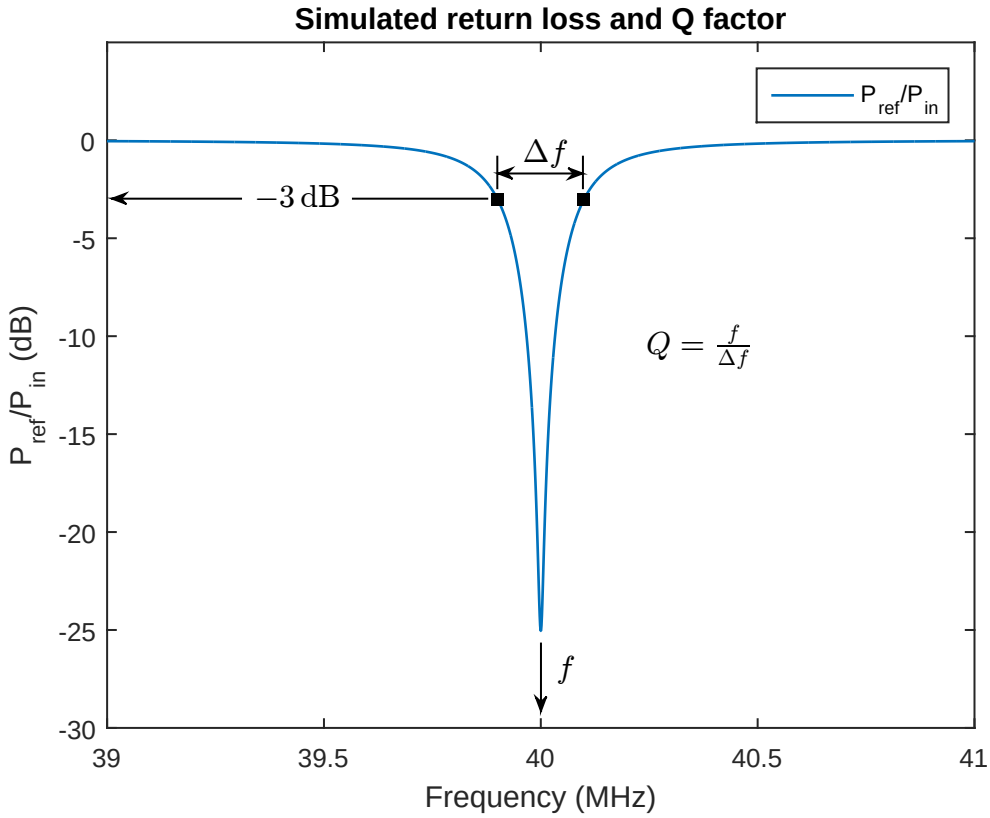

Figure 2.7: The loaded quality factor can be determined from the −3 dB points of the reflected power from the resonator. The resonator is matched to near critical coupling and the bandwidth Δf is measured between the points at which the reflected power is 3 dB less than the reflected power at points far from the resonant frequency f. Assuming that the circuit is not highly lossy, and hence $\Delta f << f$, the loaded quality factor $Q = f/\Delta f$.

definition accounts for losses within the sample. In this thesis, the reported quality factors Q are the quality factors for the resonator at or near critical coupling. For the low frequency experiments using the LGRs, the Q factors are approximately the same regardless of whether or not the sample is present in the resonator because the frequency is low and E field is small, leading to small dielectric losses. For experiments at X band, any Q factors reported in this thesis are at critical coupling with the sample present in the resonator.

To maximise the Q factor of the resonator, it is necessary to minimise the power dissipated by minimising the effective resistance. Moreover, the Johnson–Nyquist thermal noise across the resonator, which in an ideal case determines the noise level of the measurement, is determined by the resistance. Minimising the

resonator resistivity therefore maximises the SNR, and hence the sensitivity, of the experiment [**HR76**]. For this reason, the resonator was fabricated from copper due to its low resistivity. Using the geometry of the resonator, the frequency of the rf current, and the materials properties, it is possible to estimate the resistance of the resonator and hence its Q factor [**HR76**; **HW81**; **FH82**]. However, the Q factors I measured are much lower than the predicted values. This implies that energy is being dissipated in some lossy component, which, in this case, is likely the capacitors used to tune the frequency (see Section 2.3.2), since the formulae used to estimate the Q factor assume that the capacitive element is a parallel-plate air-gap capacitor.

Tuning

The resonators used in the spectrometer presented in this thesis fall within the domain of "lumped element models", since they can be treated as systems built from discrete components. As such, it is possible to select the resonant frequency by altering the values of the components. In a lumped element resonator, the inductance and capacitance are treated as separate elements that can be individually tuned while, in principle, not affecting the other parameter.

Both the LGR and solenoid require capacitors to tune the frequency of the resonator. It is important to use non-magnetic capacitors to minimise field inhomogeneity. Since the capacitors are very close to the sample, the effect of any magnetic components leads to significant field inhomogeneity [**HR76**]. I tuned the frequency of the LGRs using chip capacitors. These are small form-factor, surface mount capacitors ("chip capacitors"). The capacitors are formed by interleaved metal plates in a solid ceramic dielectric. Non-magnetic chip capacitors are available, where the metal plates are made of low-susceptibility metal. The ceramic dielectrics come in different variants, such as C0G, X7R, and NP0, with different dielectric lossses and temperature coefficient.

The capacitors have a Q factor, that, as with the resonator, parameterises the rate of energy loss. The capacitor Q factor depends on frequency [**PP19**]. At high frequencies, the dielectric losses are high, which corresponds to a low capacitor Q

factor and high equivalent series resistance (ESR). The ESR of the capacitor shifts the impedance of the resonator assembly. For high ESR, the impedance cannot be transformed to the impedance of the transmission line and hence cannot be matched to the spectrometer. I found this to be a problem for capacitors using X7R dielectric, whereas the dielectric loss of NP0 dielectric capacitors was sufficiently low to allow matching over the frequency range of resonators used in this thesis. These dielectric problems would be eliminated by using air gap capacitors, which typically have a much higher Q since less energy is dissipated in air than in the dielectric. However, due to the lower dielectric constant of air compared to that of the dielectric, the size necessary to achieve a certain capacitance is much larger. This makes them impractical for tuning the LGRs down to the frequencies used in this thesis: the LGRs have very small inductance. Therefore, given that the resonant frequency $\omega = 1/\sqrt{LC}$, it is necessary to use very large capacitances, which are typically $\mathcal{O}(1000)$ pf. The quality factor of the resonator was better if I used multiple low capacitance chip capacitors in parallel than a single, large-capacitance chip capacitor. This is probably because the effective resistance of the capacitances is in parallel, resulting in a smaller total resistance. Furthermore, it has the advantage that the field homogeneity is likely better, since the rf current is more evenly distributed along the vertical extent of the resonator.

Dielectric loss presented a less significant problem for resonators using solenoidal coils, due to their large inductance, which places less severe requirements on the total capacitance necessary to bring the resonant frequency to the desired low frequency. Here, I used trimmer capacitors and piston capacitors. The trimmer capacitors have metal rotor and stator plates, with a dielectric in between. The overlap of the plates, and hence the capacitance, is altered by turning the rotor. While the dielectric was not sufficiently lossy to cause problems, axial pressure from the tuning tool reduces electrode spacing, and hence capacitance. It was therefore difficult to accurately and precisely alter the frequency of the resonators using trimmer capacitors. Piston capacitors, in which the capacitance is tuned using a screw thread mechanism to adjust the spacing of the capacitor plates, allow for precise and stable capacitance

adjustment. However, the form-factor of the piston capacitors is inconvenient: the piston capacitors are quite large and it is hard to install the capacitor on the resonator. In view of this, the LGR frequency was tuned using chip capacitors.

Matching

In order to be useful, the resonators must be coupled to the spectrometer circuitry. While there are exceptions (for example, [**TJ10**]), solenoidal coils are typically capacitively coupled, whereas loop-gap resonators are more commonly inductively coupled [**RE99**]. While developing the spectrometer detailed in this thesis, I used solenoidal coils with an "L-section" impedance matching network and LGRs inductively coupled to the transmission line using an electrically shorted pick-up loop. These two setups are shown in Figure 2.8. Coaxial cable, as is used to connect components in the spectrometer, is an unbalanced transmission line, where the outer sheath is maintained at the ground potential. For the solenoidal coils, the high voltage across the resonator on resonance leads to rf voltages on the outer sheath of the transmission line. The rf voltages on the outer sheath of the coaxial cable capacitively couple to the external environment, and introduce parasitic capacitances into the lumped element picture of the resonant system. This can lead to "hand-waving effects", where changes in the external environment, such as the experimentalist moving their hands, change the tuning and matching of the resonator. The parasitic capacitances lead to drifts in the spectrometer and spurious noise by introducing coupling to the external environment. This can be avoided by winding the coaxial cable through a ferrite ring, which acts as a choke and attenuates the rf currents flowing on the sheath of the coaxial cable. In contrast, the inductively-coupled loop gap resonator is not susceptible to hand-waving effects.

Prior to performing an EPR experiment, the LGR is tuned to the desired frequency and mounted in the EPR probe before being impedance matched to the transmission line. However, inductive coupling between resonator and cryostat used to support the resonator upon installing the probe between the electromagnet pole pieces increased the effective inductance of the LGR. This decreases the resonant

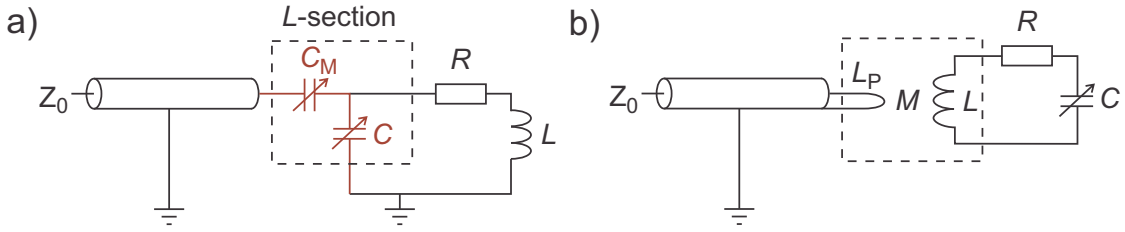

Figure 2.8: Tuning and matching circuits for solenoidal coils and loop-gap resonators. The solenoidal coil is matched to the transmission line using an "L-section" capacitive impedance matching network (a) formed from the tuning capacitor C and the matching capacitor C_{M}. The loop-gap resonator is inductively matched (b) to the transmission line by adjusting the mutual inductance M between the resonator inductance L and an electrically short pickup loop used to terminate the transmission line, which behaves as an inductance L_{P}. The mutual inductance is changed by physically translating the L relative to L_{P} by mounting the LGR on a screw thread. The losses in the circuit are modelled by a resistance R in series with the inductor.

frequency of the resonator, and brings it out of match. This problem was solved by installing a metal-foil Faraday cage around the resonator. The resonator no longer couples to the cryostat, and the frequency and matching remains unchanged when placing the probe in the resonator.

2.3.3 Amplification

The signal from the resonator must be amplified before digitization to boost it over the quantization limit of the digitizer. While practical amplifiers always contribute some noise and reduce SNR, it is necessary in order to boost the signal over the noise floor set by subsequent stages in the detection chain.

The performance of an amplifier is parameterised by its noise factor F [**Poz12**]. The noise factor measures the change in signal-to-noise ratio for signals amplified by the amplifier, such that $F = \frac{\mathrm{SNR_{in}}}{\mathrm{SNR_{out}}}$, where $\mathrm{SNR_{in}}$ and $\mathrm{SNR_{out}}$ are the SNR of the signal input to the amplifier and the signal output from the amplifier, respectively. The values of SNR are the signal-to-noise ratio with respect to power rather than voltage. In amplifier specification sheets, the noise factor is often quoted in terms of the noise figure N.F., where

$$\mathrm{N.F.(dB)} \equiv \log_{10}(F) = \log_{10}\left(\frac{\mathrm{SNR_{in}}}{\mathrm{SNR_{out}}}\right). \tag{2.25}$$

The noise figure is practically useful since the noise figure is additive. The noise factor of a chain of amplifiers is given by Friis' noise formula, which states that the total noise factor

$$F = F_1 + \frac{F_2 - 1}{G_1} + \frac{F_3 - 1}{G_2} + \ldots, \tag{2.26}$$

where G_i and F_i are the power gain and noise factor of the i^{th} amplifier in the chain, respectively [**Poz12**]. The practical consequence of Friis' noise formula is that the noise factor of the first amplifier, given sufficient gain, dominates the noise factor of the complete amplifier chain. Therefore, it is highly desirable that the first amplifier in the chain should have the lowest noise figure possible.

The noise factor also applies to passive components, such as attenuators. Assuming an isothermal system, passive attenuation reduces the input signal and input noise equally, without decreasing the noise floor. The noise figure of an attenuator is therefore equal to its attenuation. Friis' noise formula therefore implies that any attenuation, such as cable loss, prior to the first amplifier sets the minimum achievable noise factor of the detection system. This means that first amplifier should be as close to the resonator as possible, and the cable joining the amplifier to the resonator should be as low-loss as possible.

The voltage noise of the complete detection system was measured using a lock-in amplifier or oscilloscope. The root mean square noise of this signal gives the noise voltage, which can be used to calculate the noise in $\text{nV}/\sqrt{\text{Hz}}$ given the bandwidth of the lock-in measurement. By measuring the total gain in the system prior to the lock-in amplifier, it is possible to take this noise voltage and convert it into an input-referred voltage. This input-referred voltage noise can be compared to the expected Johnson–Nyquist noise of the $50\,\Omega$ characteristic impedance of the system to estimate the noise factor of the complete detection system.

2.3.4 Detection schemes

After amplifying the signal, it is necessary to translate it from the rf domain to a frequency suitable for digitising and processing. This frequency may either be

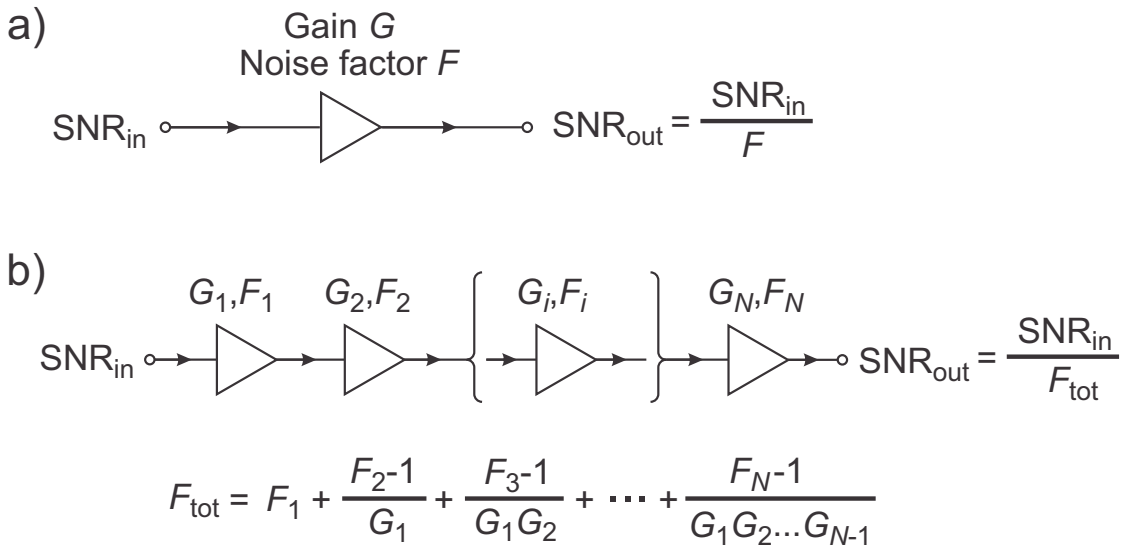

Figure 2.9: (a) The noise factor F measures how much the amplifier degrades the SNR of an input signal. (b) Friis' noise formula gives the total noise factor F_{tot} for a chain of amplifiers $1, \ldots, N$. The gain and noise factor of the i^{th} amplifier in the chain are given by G_i and F_i respectively. Attenuation due to cable losses or attenuators can be treated as amplifiers with $G = 1/A$ and $F \approx A$, where A is the power attenuation factor of the passive component.

at a sufficiently low intermediate frequency (IF) that direct digitisation of the IF waveform is feasible, or the rf input signal may be mixed down to dc baseband. Either approach requires a device capable of translating the frequency. There are a number of different schemes [**Poo83**], but I will focus on diode detectors and double-balanced mixers.

A diode detector measures the incident rf power by using a diode to rectify the E field of the applied radiation and convert it to an electrical current [**Poz12**]. This current passes through a resistor, and the voltage is measured. The diode can be biased by applying a voltage. By adjusting this bias voltage, it is possible to operate the diode in either linear or non-linear regimes. At low bias voltages, the diode is a non-linear square law or power detector, for which the output voltage is proportional to the power incident on the detection. The disadvantage of this approach is that the diode detector is not sensitive to the phase of the incident radiation and measures solely the incident power, which leads to wasted information.

The double-balanced mixers used in the spectrometers detailed in this thesis are formed from four diodes arranged in a ring. The mixer provides phase-sensitive

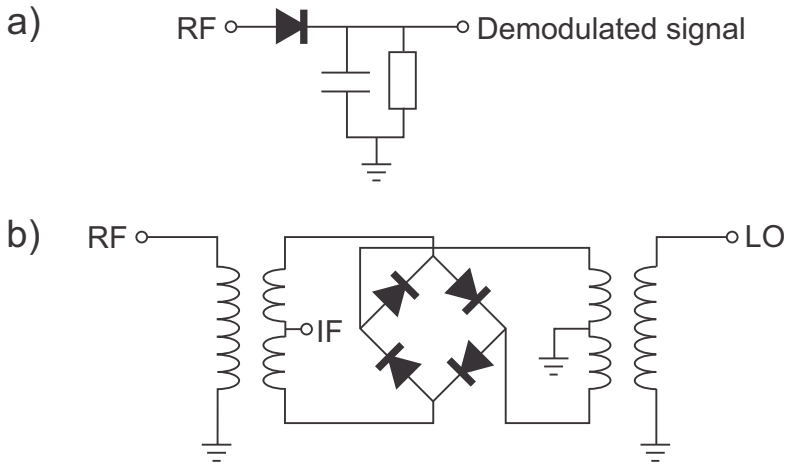

Figure 2.10: Schematic diagram showing (a) simple diode detector and (b) double-balanced mixer. The diode detector circuit (a) rectifies the input rf signal and, for low rf powers, produces a voltage output proportional to the input rf power at the demodulated signal output. The passive, double-balanced, diode ring mixer circuit shown in (b) can be used a phase sensitive detector. For large amplitude local oscillator signals, such that the diodes are either fully conducting or reverse biased into the off state, the double-balanced mixer produces a signal at the IF port proportional to the product of the rf voltages at the RF and LO ports. The IF signal therefore contains components at the sum and difference frequencies of the RF and LO signals; after suitably adjusting the relative phase between the rf and LO signals, and low-pass filtering to remove the sum frequency, the output voltage is proportional to the input rf voltage. Alternatively, the relative phase can be adjusted to set the output voltage proportional to the relative phase between the rf and LO signals.

detection such that, after low-pass filtering, the output only includes contributions from input signals that have a fixed phase relationship with the local oscillator signal [**Rub06**]. While this requires a local oscillator signal that remains phase locked to the rf source used to excite the transitions, it enables selective detection of the phase and amplitude signal. The diodes are driven using a local oscillator with sufficient amplitude that they saturate, and switch the input rf signal such that the output at the IF port is the product of the signals at the RF and LO ports.

In this thesis, I use the mixer as a homodyne detector and low-pass filter the IF output to remove the component at the sum of the local oscillator frequency ω_{LO} and rf signal frequency ω_{RF}. The output signal at baseband after filtering $v_{\mathrm{b}}(t)$ is therefore

$$v_{\mathrm{b}}(t) = \frac{1}{2V_1} V_{\mathrm{LO}} V_{\mathrm{RF}}(t) \Big[\cos\left[(\omega_{\mathrm{LO}} - \omega_{\mathrm{RF}})t - \Delta\phi(t)\right] \Big] \tag{2.27}$$

where V_{LO} is the amplitude of the local oscillator signal, $V_{\mathrm{RF}}(t)$ is the amplitude of the rf carrier as a function of time t, and $V_1 = 1\,\mathrm{V}$ is a normalising factor with the dimension of volts [**Rub06**]. The relative phase between the local oscillator phase ϕ_{LO} and the rf input phase $\phi_{\mathrm{RF}}(t)$ is given by $\Delta\phi(t) = \phi_{\mathrm{RF}}(t) - \phi_{\mathrm{LO}}(t)$.

It is possible to maximise amplitude or phase sensitivity by adjusting the local oscillator phase to set $\Delta\phi_0 = n\pi$ or $\Delta\phi_0 = (n + 1/2)\pi$, respectively, where $n = 0, 1, 2, 3, \ldots$. Here, $\Delta\phi_0$ is the phase difference between the LO and the RF carrier far from resonance, such that the spin ensemble does not modify the phase of the rf signal. The use of a mixer thus enables detection of either imaginary or real components of the spin ensemble's complex magnetic susceptibility. Furthermore, higher sensitivity is possible for phase sensitive detection using a mixer than for a diode detector [**Poo83**].

The diodes used in the mixer are subject to electronic noise. In addition to Johnson–Nyquist thermal noise and shot noise, which are inevitable and unavoidable features of electronic devices, semiconductors may experience, for example, "pink" noise with a $1/f$ power spectral density and "popcorn" noise [**Mis11**]. In early spectrometers, spurious noise in the microwave detectors significantly impaired the maximum achievable spectrometer sensitivity [**Wil67**; **Poo83**]. However, the noise level has decreased with time as semiconductor fabrication processes have improved.

Lock-in detection

Often, noise can be mitigated by averaging for long periods to reduce the measurement bandwidth. However, while this approach may be satisfactory for white noise, the power spectral density as a function of frequency means that one cannot eliminate $1/f$ noise by averaging for arbitrarily long periods. This is because the low-frequency components of the noise become significant and exceed the improvements in SNR achieved by averaging out white noise. However, it can be minimised by using modulation to shift the demodulated signal away from dc baseband toward higher frequencies. The $1/f$ noise has a corner frequency above which it is less significant than the white noise. By selecting a modulatation frequency above the

corner frequency, it contributes minimally to the total electronic noise of the system. Lock-in detection makes it possible to achieve very narrow measurement bandwidths while moving the signal away from the noisy, low-frequency baseband.

A schematic diagram of a simple lock-in amplifier is given in Figure 2.11. Using a lock-in amplifier, one only detects signals at the same frequency and with a fixed phase relative to the applied modulation [**SRS11**]. The lock-in amplifier achieves improved sensitivity by reducing the measurement bandwidth and hence the noise on the signal. This bandwidth reduction is achieved by phase-synchronous detection to mix the modulated signal down to dc, which is subsequently low-pass filtered. Filtering at low frequencies allows for narrow pass bands, even when using filters with low quality factors. The time constant and number of filters is user adjustable to set the measurement bandwidth. In the SR830 amplifier, each stage provides filtering with 8 dB/octave, with up to three stages. However, increasing the number or stages increases the settling time, which means that one must not sweep through the resonance line too fast lest it distort the apparent lineshape of the resonance.

To use lock-in detection, one must modulate the signal from the spin ensemble. Amplitude modulation of the applied rf excitation can be used, but although it does allow for narrowband detection, any fluctuation in the coupling of the resonator to the transmission line gives rise to noise or a baseline drift [**HSF89**]. Instead, one should find a modulation that satisfies the "transfer of modulation" principle. This is a modulation for which the spin system itself converts the applied modulation into a modulation of the rf signal. The most common approaches are modulation of the static magnetic field used to split the energy levels or frequency modulation of the applied radiation to bring the spin system into and out of resonance. In this thesis, I have used field modulation in preference to frequency modulation. This is because, with frequency modulation, one observes a background signal from the resonator since the reflection coefficient is frequency-dependent. This background signal reduces the dynamic range of the experiment and can lead to increased noise levels.

Field modulation is the most common approach to cw EPR. While this can lead to problems with microphonic signals and mechanical vibrations, I have suppressed

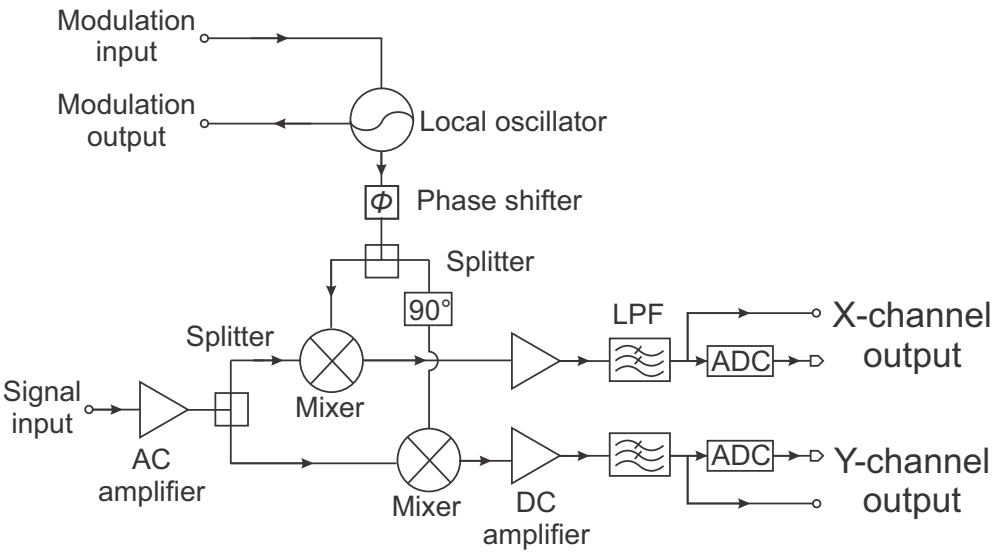

Figure 2.11: Diagram indicating the principle of operation of a lock-in amplifier. The input signal is amplified using an ac-coupled amplifier before being mixed with a local oscillator signal. The phase of the local oscillator signal can be adjusted using a phase shifter to put the output signal in either the X- or Y- output channels. This accounts for phase shifts in the response of the measured system relative to the applied modulation. The output from the mixer is low-pass filtered and amplified using a dc-coupled amplifier prior to digitization. The phase of the input signal relative to the local oscillator can be adjusted using the phase shifter. The dynamic range or noise performance are optimimised by changing the gain balance between the ac- and dc-coupled amplifiers. If the modulation applied to the sample is generated by an external source, the local oscillator of the lock-in amplifier can be locked to the source via the modulation input channel.

these such that I can successfully detect the small signal from the N@C_{60} sample. Modulation of the magnetic field brings the spin system in and out of resonance, thereby modulating the signal from the spectrometer. An intuitive picture is given in Figure 2.12. For small modulation amplitudes, the lock-in signal amplitude is proportional to the modulation amplitude. The signal strength can be improved by increasing the modulation amplitude, but this leads to distortion of the lineshape. Furthermore, large modulation amplitudes can cause increased microphonic noise.

The modulation frequency ω_{mod} is selected to avoid mechanical resonances of the EPR probe and spurious noise sidebands on the carrier frequency. In addition, the noise spectrum of the spectrometer system typically includes low-frequency components. As such, there is an advantage in using higher modulation frequencies to shift the signal away from the low-frequency noise. However, it is not possible to

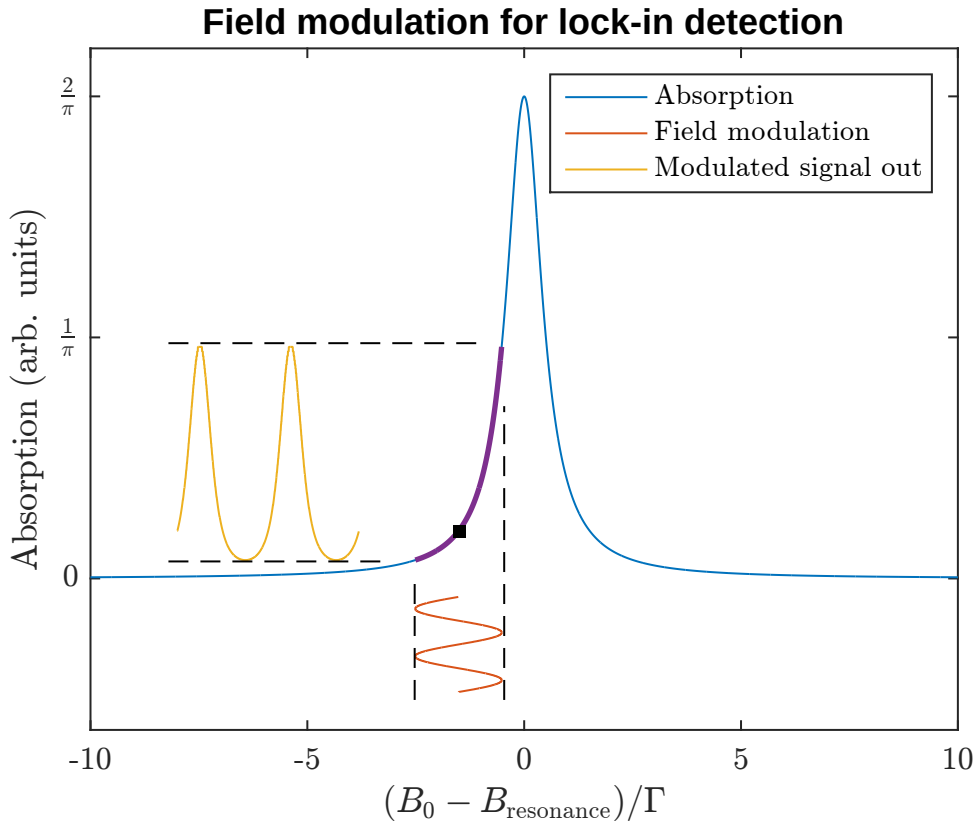

Figure 2.12: The magnetic field is modulated, which brings the spin system in and out of resonance, thereby modulating the signal output from the resonator. This modulated signal is measured using a lock-in amplifier synchronised with the modulation field.

measure narrower linewidths than the modulation frequency because the amplitude modulation leads to broadening in the frequency domain. This can be a problem for samples with very narrow spin linewidths; for example, the 100 kHz modulation frequency used in many commercial EPR spectrometers can lead to modulation sidebands that distort the observed lineshape [**Poo83**]. It is also desirable to avoid harmonics of 50 Hz to avoid pick up from the mains electricity. The modulation frequency I used in this paper was typically about 5 kHz.

The formers for the field modulation coils were designed using Autodesk Inventor, and fabricated from acrylonitrile butadiene styrene (ABS) using a MakerBot Replicator 3d printer. The coils are circular, but are not Helmholtz coils due to the spatial constraints imposed on the probe head by the cryostat used to support it. The coils were wound using enamelled copper wire, which was subsequently

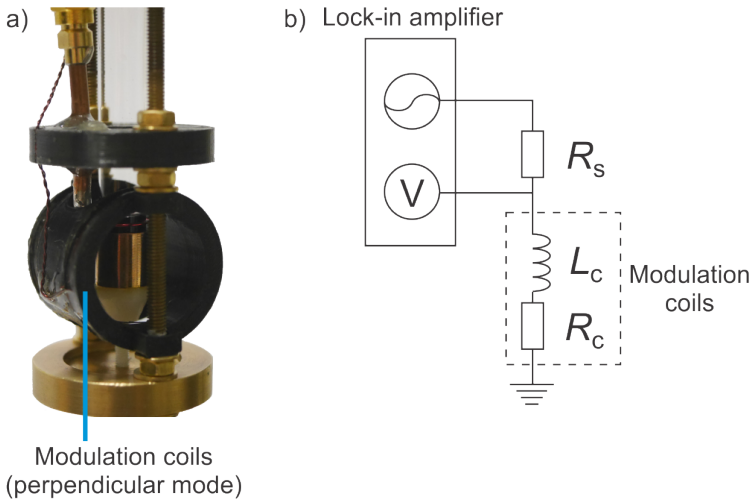

Figure 2.13: (a) Photograph of probe head set up for perpendicular mode measurements. The modulation coils coils are wound on the black structure surrounding the LGR and pickup coil. (b) The impedance of the modulation coils is measured using a lock-in amplifier. The coils form a potential divider with a large resistance R_S, and the voltage across the coils is measured as a function of frequency in order to deduce the inductance L_c and resistance R_c of the coils.

potted in epoxy resin to eliminate high frequency motion of the wire. The relatively large mass of the probe head, which is mounted on the end of a long cantilever with small effective spring constant, ensures that the mechanical resonance of the system is at low frequencies far from the modulation frequency. A photo of the complete probe head and modulation coils is given in Figure 2.13.

The modulation coils are driven with an Agilent 3300 series signal generator. The coils must be calibrated to calculate the modulation field for a given modulation voltage. The modulation coil is modelled with an impedance

$$Z_{\text{coil}}(\omega_{\text{mod}}) = R_c + j\omega_{\text{mod}}L_c, \tag{2.28}$$

with R_c and L_c the resistance and inductance of the coil respectively, and ω_{mod} the modulation angular frequency. The resistance and inductance are measured using the potential divider setup given in Figure 2.13(b). The modulation coil is put in series with a large resistor R_s such that the current flowing in the circuit $I_c \approx V_{\text{mod}}/R_s$, since $|R_s| \gg \sqrt{R_c^2 + \omega_{\text{mod}}^2 L_c^2}$, where V_{mod} is the modulation voltage output by the

lock-in amplifier. The magnitude of the measured lock-in voltage across the coil

$$V \approx V_{\mathrm{mod}} \frac{\sqrt{R_{\mathrm{c}}^2 + \omega_{\mathrm{mod}}^2 L_{\mathrm{c}}^2}}{R_{\mathrm{s}}}. \tag{2.29}$$

Using this data, it is possible to deduce L_{coil} by looking at how the voltage changes with frequency and R_{coil} from the voltage as the modulation frequency tends to zero.

The modulation field for a given current is estimated by treating the coils as Helmholtz coils. The appropriate modulation voltage V_{mod} is set by considering the desired modulation field, and hence necessary modulation current I_{mod}, at the modulation frequency using the expression $V = I_{\mathrm{mod}}|Z_{\mathrm{coil}}(\omega_{\mathrm{mod}})|$. Since the modulation coils are not perfect Helmholtz coils, and hence the validity of the predicted magnetic field is questionable, this is confirmed by measuring the magnetic field with a pickup coil. The pickup coil is placed in the centre of the modulation coil, and the voltage induced by the modulation field is measured using an oscilloscope. The position and orientation of the pickup coil and the reference phase of the lock-in amplifier are both adjusted to maximise the induced voltage, from which it is possible to calculate the magnitude of the modulation field.

The disadvantage of field modulation is that it results in mechanical force on the resonator and probe head, which may manifest itself as microphonic noise. Secondly, the modulation field may itself induce a voltage in the detection circuitry. Since the resulting signal is coherent with the modulation it therefore gives rise to a background signal, and may overload the amplifiers in the detection chain.

Mechanical vibrations of the EPR probe can lead to spurious electrical noise by, for example, leading to fluctuating parasitic capacitances and modulating the resonator–transmission line impedance matching condition. However, the modulation coils may themselves act as a motor within the static magnetic field B_0 and generate a microphonic signal. In addition, the modulation coils induce eddy currents in the copper walls of the resonator such that the resonator itself experiences a Lorentz force. Since both these motor effects are at the modulation frequency, they are not eliminated by the lock-in detection and give rise to a background signal. Any fluctuations in the microphonic background signal are picked up as noise on the

trace. The microphonic signal is most significant near mechanical resonances of the system. Therefore, the noise was measured for different modulation frequencies and a frequency was selected to reduce the noise. Due to the care taken in constructing the probe, selecting a suitable modulation frequency, and the small modulation fields employed, microphonic noise caused by field modulation did not significantly contribute to the overall noise of the spectrometer.

Secondly, the mutual inductance between the field modulation coils and the pickup loop used to couple the LGR resonator to the spectrometer circuitry leads to an oscillating current flowing in the pickup coil, which can saturate the amplifiers in the detection chain. Therefore I adjusted the orientation of the pickup coil to minimise its mutual inductance with the modulation coil by setting the normal of the modulation and pickup coils perpendicular to one another. However, this does not completely eliminate the modulation pickup. High-pass filters are used to filter out the low-frequency ($f_{\mathrm{mod}} < 100\,\mathrm{kHz}$) modulation pickup, while passing the rf signal from the resonator. Alternatively the effect of modulation pickup can be eliminated by using bisymmetric modulation [**Rob80**]. Here, the response from the spin signal is present at the second harmonic, whereas the modulation pickup is only present at odd harmonics. However, this would be unsatisfactory for clock operation, since the observed signal peaks at resonance and hence does not encode information about whether the applied radiation is above or below the transition frequency. Secondly, the error signal is insensitive to small perturbations about the transition frequency because the peak is a stationary point. This could limit the stability of the clock system.

3

The clock transition of $^{15}N@C_{60}$

Contents

3.1 Introduction

In order for endohedral fullerenes to be viable as frequency references in highly stable atomic clocks, they must possess certain properties. One of these criteria is insensitivity of the transition used as a reference frequency to environmental perturbations [**AV76**]. If the energy levels of the selected transition are susceptible to external influences, environmental fluctuations will be coupled to the output

frequency of the atomic clock and will degrade the stability of the atomic clock over timescales comparable to the characteristic timescale of the fluctuations. This often limits the clock stability over long measurement durations, in addition to reducing the accuracy at any given point in time.

For example, magnetic field noise is ubiquitous in the natural environment. The Earth has a non-negligible geomagnetic field, which can fluctuate over time due to solar effects [**Gon94**]. Moreover, the geomagnetic field is not constant regardless of position: its magnitude and direction vary depending on one's geographical location. Local spatial variations may also occur due to magnetically permeable materials in the vicinity of the clock system, such as steel [**Yam03**]. Finally, electromagnetic interference (EMI) due to electric power distribution and machinery can generate significant field fluctuations [**BY02**; **Liu15**].

This magnetic field noise is relevant because spins with magnetic moment $\boldsymbol{\mu}$ couple to the magnetic field $\boldsymbol{B}$ by the Zeeman interaction $\hat{\mathcal{H}}_{\mathrm{Z}} = -\boldsymbol{\mu} \cdot \boldsymbol{B}$. The energy splitting, and hence the transition frequency, therefore depends on the magnetic field, the magnetic moment of the spin, and their relative orientation. The magnetic moment of the electron spin $\mu = \gamma \mathbf{S}$, where γ is the gyromagnetic ratio of the spin, and $\mathbf{S}$ is the spin angular momentum. Since electrons have a large gyromagnetic ratio, a small shift in magnetic field is sufficient to greatly change the resonance frequency.

To avoid this, the frequency reference could be passively [**Ril90**] or actively shielded [**Mor14**; **Li16**] from magnetic field fluctuations. However, both these approaches minimise the magnetic field noise rather than completely eliminate it. Therefore, to achieve highly stable clock operation it is essential to suppress the reference's intrinsic sensitivity to ambient magnetic field fluctuations by selecting a transition that is inherently insensitive to any fluctuations. Certain atoms and molecules, such as N@C_{60}, possess such clock transitions. Clock transitions are transitions in which the change of frequency with respect to magnetic field is zero at a given field, which is termed the "clock field". The clock transition in ^{15}N@C_{60} is a first-order clock transition, where the first derivative of the transition frequency $\mathrm{d}f/\mathrm{d}B_0 = 0$ at the clock field. However, higher-order terms such as

the second-order Zeeman shift ($\mathrm{d}^2 f/\mathrm{d}^2 B_0 \neq 0$) also give rise to frequency shifts. Achieving the best possible frequency accuracy and stability therefore requires one to account for these effects.

Clock transitions find broader application than clocks alone. For example, they are attractive for use in quantum information processing: a clock transition can shield a spin qubit against dipolar decoherence by eliminating the matrix element for magnetic dipole transitions [**Wol13**; **Shi16**; **Col19**]. This allows for high concentrations of spins without reducing the coherence times, thereby improving the signal-to-noise-ratio of the experiment.

The existence of the clock transition is predicted by the spin Hamiltonian of the endohedral fullerene, which has previously been deduced from high-field EPR experiments [**Alm96**]. Here, I show that the spin Hamiltonian is also valid at low fields and verify the existence of the clock transition in the low field spectrum of $N@C_{60}$. To the best of my knowledge, this is the first observation of a clock transition at room temperature in a molecule.

I estimate the stability of an atomic clock based on the endohedral fullerene $^{15}N@C_{60}$, and compare it with the stabilities of existing atomic clocks. The stability of an atomic clock is commonly paramaterised using the Allan deviation, or two-sample variance of the clock's output frequency, to evaluate the fractional frequency stability of an atomic clock. I estimate the Allan deviation of a $^{15}N@C_{60}$-based atomic frequency standard for short measurement durations, such that the dominant noise sources are white-noise, using the experimental data for signal-to-noise ratio, linewidth, and transition frequency presented in this chapter. The predicted stability for a clock based on endohedral fullerenes is very low, and not competitive with existing portable atomic frequency standards. I make suggestions for improving the performance by optimising the conditions under which the experiment is performed.

In addition to magnetic field fluctuations, a $^{15}N@C_{60}$ frequency reference would also be susceptible to temperature fluctuations due to the temperature dependence of the isotropic hyperfine coupling constant [**Pie02**]. While this effect is small, it is sufficient to significantly impair the long-term stability of a fullerene-based

clock. I discuss the possible approaches for monitoring temperature to implement a thermal stabilization or compensation protocol. In particular, I show that it is possible in principle to monitor multiple transitions in the EPR spectrum to extract information about temperature and magnetic field in addition to the local oscillator frequency. This approach has the advantage that temperature is monitored directly at the frequency reference itself, and the calibration will not drift.

3.2 Spin Hamiltonian of N@C_{60}

The endohedral fullerene ^{15}N@C_{60} comprises a nitrogen atom encapsulated within a carbon cage [**Alm96**], as is depicted in the inset of Figure 3.1(a). The nitrogen, located at the cage centre, retains its ground state electronic configuration $^4S_{3/2}$ [**Lip00**], with spin quantum numbers $S = 3/2$ for the electron and $I = 1/2$ for the nucleus. The energy levels of this molecule in a magnetic field $\boldsymbol{B_0} = B_0\,\hat{\boldsymbol{z}}$ are described by the Hamiltonian

$$\mathcal{H} = g_\mathrm{e}\mu_\mathrm{B}S_zB_0 - g_\mathrm{N}\mu_\mathrm{N}I_zB_0 + A\hat{\boldsymbol{S}}\cdot\hat{\boldsymbol{I}}, \tag{3.1}$$

where g_e (g_N) is the g-factor of the electron (nucleus), μ_B (μ_N) is the Bohr (nuclear) magneton and A is the isotropic hyperfine constant [**Mor06**]. The electron and nuclear spin operators are denoted by $\hat{\boldsymbol{S}}$ and $\hat{\boldsymbol{I}}$ respectively. Zero-field splitting is neglected due to the near-spherical symmetry of the system [**Mor05a**]. This Hamiltonian has previously been verified by numerous measurements at X-band ($\sim$ 10 GHz), for example [**Alm96**], in addition to at higher frequencies [**Wei00**; **Wit18**].

Early literature value for the N@C_{60} give $g_e = 2.003$. However, since these reports significant effort has been expended to accurately determine the g factor of N@C_{60}, given its potential for use as a g value standard. The current most accurate value of $g = 2.00204(4)$, which was achieved using a quasi-optical EPR setup operating at $f \sim 300$ GHz [**Wit18**]. The high degree of precision was achieved by measuring the nuclear magnetic resonance signal from solvent protons to precisely and accurately determine the magnetic field at the location of the sample.

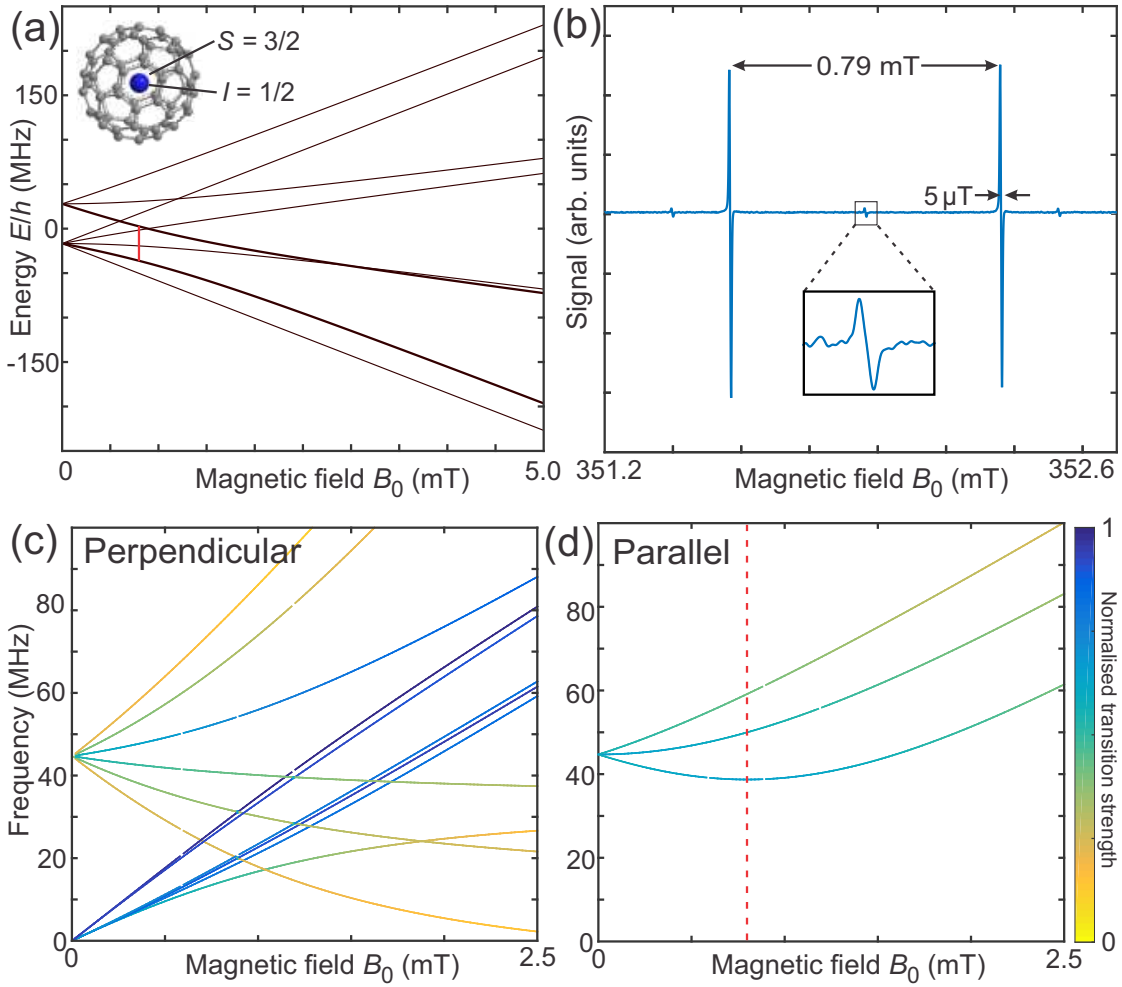

Figure 3.1: (a) Simulated energy levels of $^{15}N@C_{60}$ as a function of magnetic field. The clock transition is denoted by a vertical red line. Inset: molecular structure, labelled with electron (S) and nuclear (I) spins. (b) EPR spectrum of $^{15}N@C_{60}$ measured at X-band ($f = 9.86\,\mathrm{GHz}$). The zoom-in highlights the contribution of residual $^{14}N@C_{60}$. (c) and (d): Simulated frequencies of allowed transitions for driving magnetic field applied perpendicular (c) and parallel (d) to the static magnetic field B_0. Traces are colored according to transition intensity. The clock field is marked with a dashed line. (Reproduced with minor modification from [**Har17**], © American Physical Society, 2017.)

Figure 3.1(a) shows simulated energy eigenstates of Hamiltonian (3.1) as a function of magnetic field. The eigenenergies were simulated by diagonalising the Hamiltonian at discrete magnetic fields in Matlab. This gives the energy eigenvalues and eigenvectors in the $|SIm_Sm_I\rangle$ basis for each value of magnetic field. The simulation parameters are $g_e = 2.00204$ and $|A|/h = 22.35\,\mathrm{MHz}$ [**Pie98**], with $g_N = -0.566$ [**Bal62**; **Sto05**]. The negative nuclear g-factor leads to a negative value of A, leading to an inverted energy level manifold [**VA89**].

Near zero field, the eigenstates form a pair of hyperfine-split multiplets labelled by quantum numbers $|F, m_F\rangle$, where $\hat{\boldsymbol{F}} = \hat{\boldsymbol{I}} + \hat{\boldsymbol{S}}$. At high fields, where the Zeeman interaction dominates, the level diagram simplifies to four doublets labelled by $|m_S, m_I\rangle$. Between these limits lies a crossover region in which the eigenstates are mixed in either basis.

In a magnetic resonance experiment, the allowed transitions between energy levels depend on the orientation of the oscillating drive field $\boldsymbol{B_1}$ relative to $\boldsymbol{B_0}$, as shown in Section 2.2. The frequency of the allowed transitions as a function of magnetic field is plotted in Fig. 3.1(c) and (d) for perpendicular mode ($\boldsymbol{B_1} \perp \boldsymbol{B_0}$) and parallel mode ($\boldsymbol{B_1} || \boldsymbol{B_0}$) respectively. To indicate the strength of each transition, traces are colored according to the magnitude of the transition matrix element $\langle f | \, g_{\mathrm{e}} S_{x(z)} + g_{\mathrm{N}} I_{x(z)} \, | i \rangle$ for perpendicular- (parallel-) mode transitions between initial state $|i\rangle$ and final state $|f\rangle$.

The clock transition occurs at an anticrossing between two levels that are mixed by the hyperfine interaction (Fig. 3.1(a)). At the clock field, the transition frequency is insensitive to magnetic field ($\mathrm{d}f/\mathrm{d}B = 0$). This clock transition occurs at a field

$$B_{\mathrm{clock}} = |A|/(g_{\mathrm{e}}\mu_{\mathrm{B}} + g_{\mathrm{N}}\mu_{\mathrm{N}}) \approx 0.8\,\mathrm{mT}, \tag{3.2}$$

and the clock transition frequency

$$f_{\mathrm{clock}} = \sqrt{3}|A|/h \approx 39\,\mathrm{MHz}. \tag{3.3}$$

These equations are derived by diagonalising the spin Hamiltonian [**Lin15**]. The selection rules for magnetic dipole radiation means that this is a forbidden transition for $\boldsymbol{B_1} \perp \boldsymbol{B_0}$, since $\Delta m_S = 0$. However, the transition can be directly driven by setting $\boldsymbol{B_1} || \boldsymbol{B_0}$, as can be seen in Fig. 3.1(d).

Alternatively, the forbidden transition can be driven indirectly via an intermediate level [**BA12**]. This technique is commonly used in atomic clocks; for example, phase-locked lasers can be used to interrogate the clock transition via coherent population trapping [**CTB93**]. A typical such experiment is Λ-scheme coherent population trapping, so named because the transitions between different energy

levels look like a "Λ" when represented on an energy level diagram (Figure 3.2) When the frequency difference between the two electromagnetic radiation fields used to interrogate the transtion is equal to that of the energy splitting between the two transitions, the lower energy levels of each forbidden transition are put into a coherent superposition that no longer couples to the applied electromagnetic field—a "dark state". This dark state is observed as increased transmission of laser light through the vapour cell. In principle, an analogous effect should be observed for N@C_{60}. Here, sweeping the frequency of one radiation source (rf signal generator) would allow one to observe the change in energy absorbed. Such an approach was considered for this work. However, the contrast achieved in double resonance experiments is necessarily less than the signal amplitude of a single resonance and it introduces extra experimental complexity. For example, it is necessary to use either a resonator with very large bandwidth to accommodate both transition frequencies, or a double-tuned resonator that resonates at both frequencies simultaneously. Therefore, I decided to use single resonant excitation in the parallel mode to measure the clock transition of N@C_{60}.

3.3 The use of endohedral fullerenes as standards in portable atomic clocks

To understand the performance of a fullerene-based atomic clock, it is helpful to first discuss in more detail how such a clock could operate, and how its performance may be benchmarked. In this section, I discuss a potential architecture for a fullerene clock and how the stability of a clock can be parameterised using the Allan deviation. I also show how the sample temperature could be monitored using additional transitions. This approach could be used to provide feedback to some means of stabilizing the temperature of the fullerene sample. Such temperature stabilization would likely be necessary to mitigate the effect of temperature fluctuations on the long-term stability of the clock.

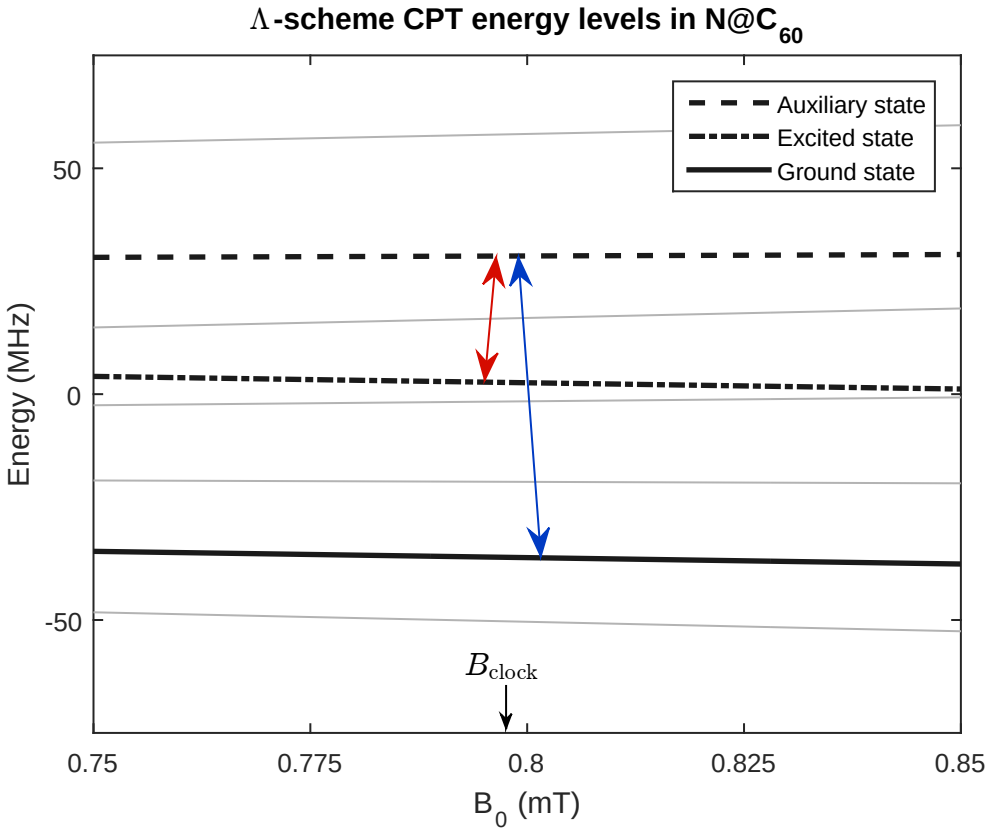

Figure 3.2: Energy level diagram showing the relevant levels for implementing a Λ-scheme coherent population trapping experiment in ^{15}N@C$_{60}$, showing the ground (solid black line) and excited (dash-dot black line) energy levels that define the clock transition. The auxiliary state can be reached via a magnetic dipole-allowed transition from either state. The lower-frequency (red arrow) and higher frequency (blue arrow) transitions both occur at the same magnetic field, and their apparent separation in the field domain is simply for illustrative purposes.

3.3.1 Clock operation

In common with other highly portable atomic clocks, the proposed endohedral fullerene clock would be a passive atomic clock suitable for use as a secondary frequency standard. The local oscillator would be disciplined to the clock transition via a feedback loop. At the clock field, where the transition frequency is stationary with respect to magnetic field, $f_{\text{clock}} = \sqrt{3}|A|/h$ [**Lin15**]. The local oscillator operates at a frequency f_{osc}. This frequency is multiplied by some constant C_1 before being output as the excitation signal to the sample, such that the frequency of radiation interrogating the clock transition is $f_{\text{rad}} = C_1 f_{\text{osc}}$. This constant is selected such that, at the clock field, $f_{\text{clock}} = C_1 f_{\text{osc}}$. Therefore, if the local oscillator deviates

from its desired frequency $f_{\rm set}$ by some amount $\Delta f_{\rm osc}$ such that $f_{\rm osc} = f_{\rm set} + \Delta f_{\rm osc}$, the transition will be subject to an excitation frequency $C_1(f_{\rm set} + \Delta f_{\rm osc})$. By measuring the absorption of the applied radiation, it is possible to measure the offset frequency using the known lineshape and linewidth of the resonance, which is assumed to have a fixed resonant frequency. This assumption is made for the purposes of discussing the process of locking an oscillator to the atomic resonance; in practice, the transition frequency will be shifted by environmental perturbations, thereby degrading the accuracy and stability of the standard's output frequency.

Any deviation from the set frequency can be measured from the change in absorption of the EPR resonance. By measuring the first derivative signal, a voltage proportional to the frequency difference may be observed for small frequency differences that fall within the capture region. The error signal

$$\epsilon_1 = f_{\rm clock} - C_1(f_{\rm set} + \Delta f_{\rm osc}) = C_1 \Delta f_{\rm osc} \tag{3.4}$$

can then be used as input to, for example, a proportional-integral-derivative (PID) controller. The output signal from this PID controller can be used as an input to the local oscillator to discipline it and maintain the oscillator frequency at the set point.

The set point is therefore referenced to the atomic transition, which I initially assume to be immune to environmental perturbations. Assuming that the resonance remains stable in time, the stability of the local oscillator will depend on how well it is locked to the resonance. This is affected by the linewidth of the resonance and the signal-to-noise ratio of the resonance, assuming that the feedback loop is itself noiseless. The importance of these factors can be seen from Figure 3.4. Assuming the lineshape can be described by a Lorentzian, the capture region in the frequency domain $\delta f_{\rm cap} \lessapprox \frac{\sqrt{3}}{3}\delta f$, which is determined by the inflection points of the Lorentzian lineshape. Within this region, the error signal ϵ is proportional to the first derivative of the absorption response such that

$$\epsilon = CS, \tag{3.5}$$

where S is the measured signal amplitude of the first-derivative signal and C is some proportionality constant. Noise on the observed signal $\Delta S_{\rm noise}$ due to, for

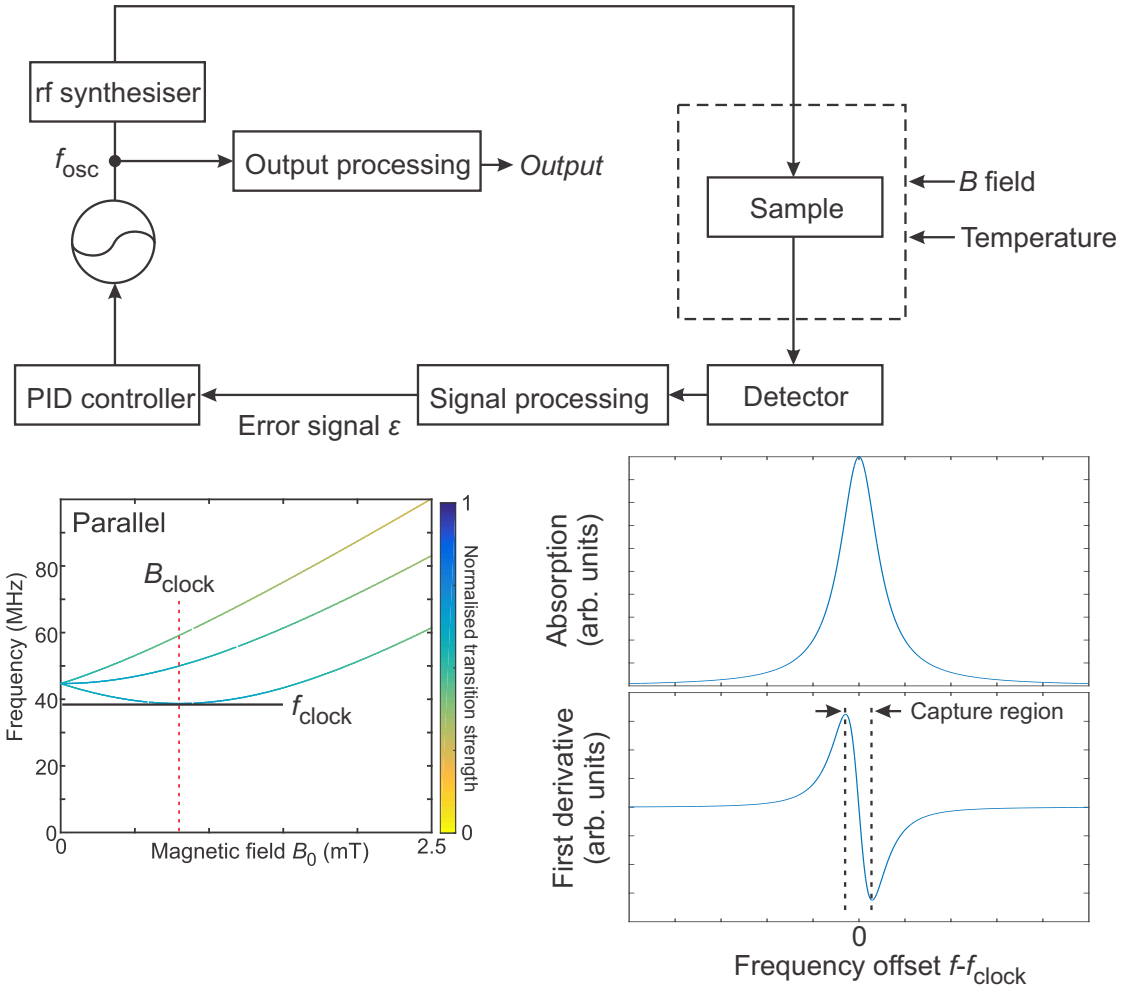

Figure 3.3: Simplified schematic of a passive atomic clock, showing the feedback loop that locks the local oscillator to the clock transition in the sample. The output from the local oscillator is buffered and converted to a useful output, such as a 1 pulse-per-second (pps) time signal, by the output electronics. The lower panels show the parallel mode transitions and the expected resonance signals. The first derivative signal has a region in which the response is proportional to the offset, and can be used to derive a suitable error signal ϵ. (Bottom left panel adapted from [**Har17**], © American Physical Society, 2017.)

example, electronic noise in the spectrometer, leads to noise of the error signal $\Delta\epsilon_{\text{noise}} = C\Delta S_{\text{noise}}$. This noise on the error signal $\Delta\epsilon_{\text{noise}}$ is coupled to the local oscillator frequency by the feedback loop, and hence contributes to instability of the local oscillator. The resulting frequency noise

$$\Delta f_{\text{noise}} = \frac{\mathrm{d}f}{\mathrm{d}\epsilon}\frac{\mathrm{d}\epsilon}{\mathrm{d}S}\Delta S_{\text{noise}} = C\frac{\mathrm{d}f}{\mathrm{d}\epsilon}\Delta S_{\text{noise}} \tag{3.6}$$

of the local oscillator leads to fluctuations in the output frequency of the atomic clock system, thereby reducing its stability. Improving the stability of the atomic

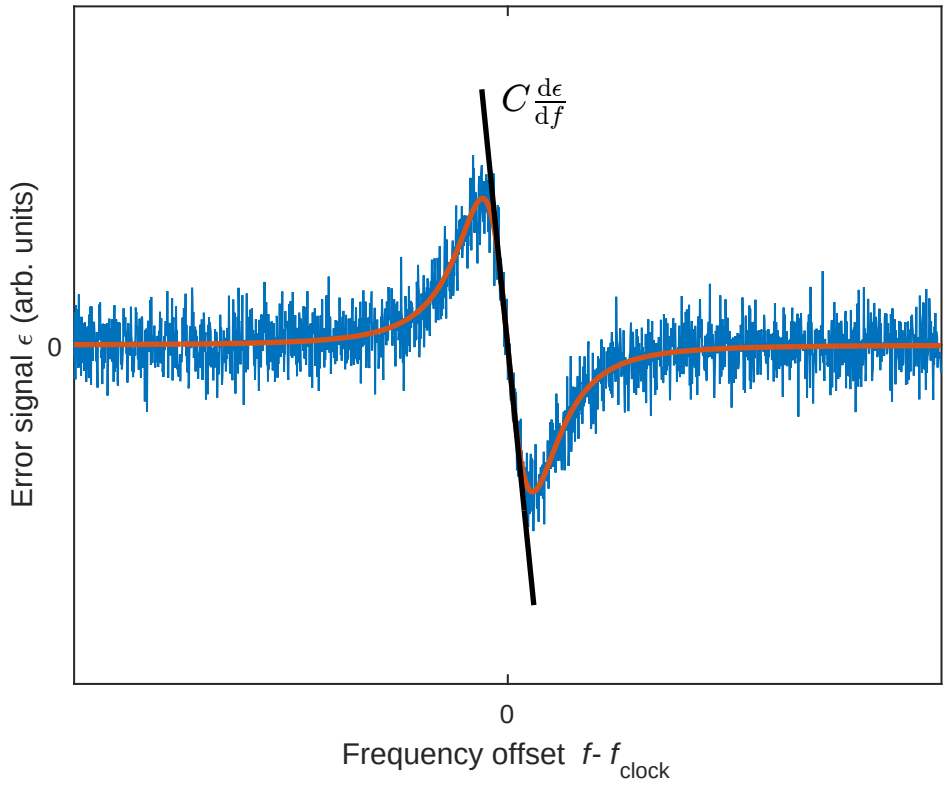

Figure 3.4: Plot of simulated resonance signal as function of frequency. The resonance is assumed to have a Lorentzian lineshape. The ideal signal measured by the spectrometer (solid orange line) is assumed to have a Lorentzian derivative lineshape. In practice, a realistic signal (blue line) includes electronic noise. Within the capture region, the error signal can be approximated by a straight line with gradient $\mathrm{d}\epsilon/\mathrm{d}f$

clock system therefore requires minimising the linewidth and maximising the signal amplitude, which corresponds to minimising the product of $\mathrm{d}f/\mathrm{d}\epsilon$ and $\mathrm{d}\epsilon/\mathrm{d}S$, and minimising the measured noise, which corresponds to minimising $\Delta S_{\mathrm{noise}}$. This relationship is valid assuming that the transition frequency itself is not noisy, and that the frequency locking protocol does not introduce additional noise.

If the energy levels that define the clock transition are sensitive to the external environment, noise and drifts in the external environment will cause instability in the clock frequency. For example, the hyperfine coupling at room temperature is approximately linearly temperature dependent such that $A(T) = A_0 + A_1\Delta T$. Since the clock transition frequency depends on the hyperfine coupling, external temperature fluctuations lead to a time-dependent clock frequency, which may

be a significant source of error over long timescales. The error signal will now have two unknown factors: oscillator frequency error and temperature error. The error signal is now

$$\epsilon_1 = \sqrt{3}|A_1|\Delta T - C_1 \Delta f_{\text{osc}} \tag{3.7}$$

Since this is a single linear equation for two unknown parameters ΔT and f_{osc}, the problem is underconstrained: it is not possible to extract separately the temperature and frequency errors. However, by monitoring suitable auxiliary transitions it would be possible to acquire sufficient information. Futhermore, other environmental perturbations such as pressure could also shift the transition frequency. I will discuss how suitable error signals could be provided for temperature and field feedback in section 3.3.2.

3.3.2 Monitoring multiple transitions for field and temperature stabilisation

Temperature compensation a requires a temperature-sensing element to measure the temperature of the frequency reference. This requirement is also necessary for temperature stabilisation using an oven, where the temperature sensor is necessary to implement a feedback loop. Thermistors have insufficient long-term stability to permit stable clock operation [**Hod13**]. However, suitable temperature monitoring could in principle be achieved by measuring simultaneously the three parallel-mode low-field transitions shown schematically in Figure 3.5. Measuring these transition frequencies allows one to formulate a set of linear equations, which may be solved to deduce the frequency, magnetic field, and temperature. This information may then be used to stabilize these parameters at the desired setpoint.

As with the error signal for the frequency error, I start by considering a local oscillator with frequency f_{osc}. In this case, the circuitry is modified to synthesise three separate excitation signals at frequencies $C_1 f_{\text{osc}}$, $C_2 f_{\text{osc}}$, and $C_3 f_{\text{osc}}$ derived from this local oscillator signal. The frequency of these excitation signals corresponds to the frequency of the clock transition and two auxiliary transitions, respectively.

I consider small perturbations to the temperature and magnetic field about the set point, given by ΔT and ΔB, respectively. At room temperature, the hyperfine coupling has a linear dependence on temperature. The hyperfine coupling may therefore be approximated as

$$A = A_0 + A_1 \Delta T, \tag{3.8}$$

where A_0 is the hyperfine coupling at the set temperature T_0 and $A_1 = (\partial A/\partial T)_{T_0}$. The magnetic field set point is assumed to be the clock field B_{clock}.

By linearising the equations for the transitions about the set point, I get

$$f_1 = \sqrt{3}(|A_0 + A_1 \Delta T|), \tag{3.9}$$

$$f_2 = k_1(|A_0 + A_1 \Delta T|) + k_2 B_{\text{clock}} + k_3 \Delta B, \tag{3.10}$$

$$f_3 = k_4(|A_0 + A_1 \Delta T|) + k_5 B_{\text{clock}} + k_6 \Delta B, \tag{3.11}$$

where f_1 is the frequency of the clock transition, and frequencies f_2 and f_3 are the frequencies of the auxiliary transition. The transitions and the linearised approximations are plotted in Figure 3.5. The constants $k_{1\ldots6}$ are determined from the spin Hamiltonian and the physical parameters of the endohedral fullerene system. The magnetic field perturbations are assumed to be sufficiently small that second-order and higher terms are negligible.

In addition to these temperature and field errors, I assume that the oscillator frequency has some error Δf_{osc}. The difference in frequency between the transitions and the corresponding excitation signal are therefore given by

$$\epsilon_1 = \sqrt{3}|A_1|\Delta T - C_1 \Delta f_{\text{osc}}, \tag{3.12}$$

$$\epsilon_2 = k_1|A_1|\Delta T + k_3 \Delta B - C_2 \Delta f_{\text{osc}}, \tag{3.13}$$

$$\epsilon_3 = k_4|A_1|\Delta T + k_6 \Delta B - C_3 \Delta f_{\text{osc}}. \tag{3.14}$$

As before, the frequency differences $\epsilon_{1\ldots3}$ can be detected as an error signal by measuring the power absorbed by the ensemble of endohedral fullerene spins.

The set of equations listed above is a set of three linear equations in three unknowns; as such, it completely constrains the problem. It is therefore possible

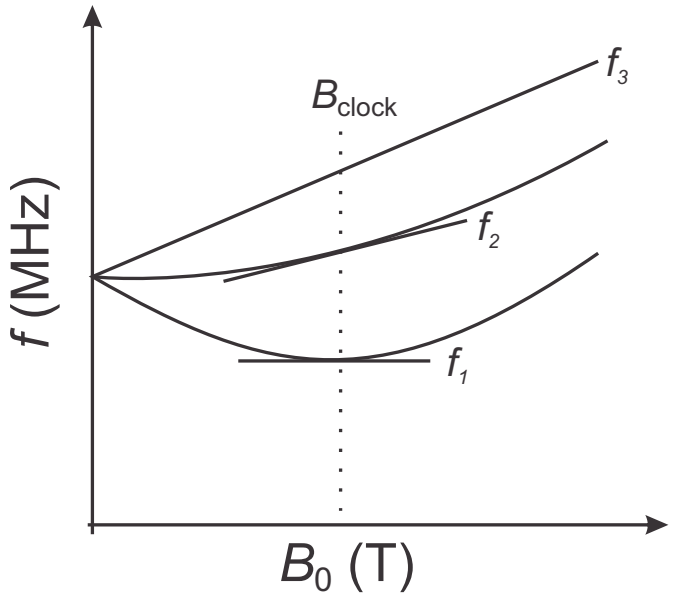

Figure 3.5: Plot of parallel mode transitions near the clock field. Sufficiently near the clock field, the transitions may be accurately approximated by linear functions (solid black lines). The range of fields for which this approximation is valid is smaller than the extent of the lines plotted in the graph, which are for illustrative purposes only.

to deduce the frequency offset of the local oscillator, the temperature offset, and the field offset. Using this information, one could implement compensation for such offsets in the signal conditioning circuitry used to translate the local oscillator frequency to the desired output signal to the end use. Alternatively, it could be used to generate a control signal. This control signal could be used as an input to a PID loop controlling the power supply of an electrogmagnet used to adjust the magnetic field, or of an oven used to stabilise the temperature.

3.3.3 Parameterising stability

The performance of an atomic clock can be parameterised in the frequency domain or the time domain [**All66**]. In the frequency domain, the stability can be parameterised using the spectral density $S_y(f)$ of the frequency standard's output signal to measure its instantaneous frequency stability. However, the spectral density is directly affected by amplitude fluctuations in the signal being measured, and the spectrum does not uniquely characterise the nature of the frequency

fluctuations. For clocks, therefore, time-domain characterisation of the output stability is preferred [**Bar71**].

Following Barnes et al. ([**Bar71**]), I discuss the "Allan variance", a time-domain measure of frequency stability originally proposed by Allan in 1966 [**All66**].

Time-domain characterisation involves measuring the fractional frequency instability y over a measurement of duration τ. The instantaneous fractional frequency instability at time t is defined as

$$y(t) \equiv (f(t) - f_0)/f_0, \tag{3.15}$$

where f is the output frequency and f_0 is the desired output frequency. The average frequency instability $\bar{y}_k$ over the k^{th}time period between time t_k and time t_{k+T} is given by

$$\bar{y}_k \equiv \frac{1}{\tau}\int_{t_k}^{t_k+\tau} y(t)\mathrm{d}t. \tag{3.16}$$

The stability of a frequency standard can be parameterised using the variance of these fractional frequency fluctuations in the standard's output signal. The general measure of stability in this framework is defined by

$$\left\langle \sigma_y^2(N,T,\tau)\right\rangle \equiv \left\langle \frac{1}{N-1}\sum_{n=1}^{N}\left(\bar{y}_n - \frac{1}{N}\sum_{k=1}^{N}\bar{y}_k\right)^2\right\rangle, \tag{3.17}$$

where $\left\langle \sigma_y^2(N,T,\tau)\right\rangle$ denotes the infinite time average of the N-sample variance of the fractional frequency deviation over measurements of duration τ taken at intervals spaced by time T.

The Allan variance $\sigma_y^2(\tau)$ is defined by taking the number of samples $N = 2$ and $T = \tau$, such that there is no dead-time between measurements of the average fractional frequency deviation. Formally, the Allan variance

$$\sigma_y^2(\tau) \equiv \left\langle \sigma_y^2(2,\tau,\tau)\right\rangle. \tag{3.18}$$

When taking the variance of a quantity, one would typically wish to have $N \to \infty$ in order that the sample variance should better approximate the population variance. However, for the purposes of characterising a frequency reference, this is undesirable:

low-frequency noise processes can lead to divergent $\left\langle \sigma_y^2(N,\tau,\tau) \right\rangle$ for $N \to \infty$ whereas $\left\langle \sigma_y^2(2,\tau,\tau) \right\rangle$ remains convergent.

The Allan variance can therefore be written as

$$\sigma_y^2(\tau) = \left\langle \frac{(\bar{y}_{k+1} - \bar{y}_k)^2}{2} \right\rangle. \tag{3.19}$$

While this measure is an expectation value and is, in principle, an average over infinitely many measurements, the Allan variance is estimated from a finite number of measurements. Various modifications of the Allan deviation exist, to make more efficient use of data or to ensure convergence for different noise processes. However, the Allan variance $\sigma_y^2(\tau)$ or, as it is more commonly reported, the Allan deviation $\sigma_y(\tau) = \sqrt{\sigma_y^2(\tau)}$, remains one of the most widely used estimates of stability.

3.4 Methods

3.4.1 Sample preparation

A $^{15}N@C_{60}$ sample was prepared by ion implantation of C_{60} using $^{15}N_2$ (isotopic purity 98%) [**Alm96**]. The crude sample was dissolved in toluene and purified by high performance liquid chromatography to a purity ($^{15}N@C_{60}$:C_{60}) of $\sim$ 6000 ppm [**Kan04**]. The sample was characterised at X-band (Fig. 3.1(b)), showing a pair of narrow spin resonances corresponding to the $m_I = \pm 1/2$ projections of the nuclear spin I, as is to be expected from hyperfine interaction in $^{15}N@C_{60}$ [**Alm96**]. For low-field experiments, the sample was redissolved in deoxygenated CS_2 under N_2 atmosphere (< 0.01 ppm O_2) and flame sealed in a Suprasil tube.

The carbon disulfide solvent was selected to minimise the influence of nuclear spins on coherence times, and hence linewidth, of the spin states [**Mor07**]. Carbon disulfide is comprised of carbon and sulfur, for which most nuclei are spin free. Both carbon and sulfur have only one isotope with a nuclear spin: ^{13}C and ^{33}S, respectively, each with a natural abundance of approximately 1%. In contrast, toluene, with chemical formula C_7H_8, is comprised of carbon and hydrogen. The large magnetic dipole moment of hydrogen atoms give rise to a significant fluctuating nuclear spin bath. Therefore, spin-spin and spin-lattice relaxation rates due to

dipolar coupling between the endohedral fullerene spin and the nuclear spin bath resulting from magnetic nuclei in the solvent are reduced for samples dissolved in CS_2 compared to that observed for toluene.

It is important to optimise the spin density in the resonator. To first order, neglecting spin-spin interactions between endohedral fullerenes that could broaden the resonance, the signal amplitude is proportional to the number of spins in the resonator. Therefore, it is desirable to maximise the spin number to maximise the signal-to-noise ratio of the experiments. In addition to being relatively free of nuclear spins, a further advantage of carbon disulfide is that it is a good solvent for endohedral fullerenes. The saturation concentration at room temperature (293–298 K) of C_{60} in CS_2 is $7.9\,\mathrm{mg\,mL^{-1}}$ compared to $2.8\,\mathrm{mg\,mL^{-1}}$ for toluene [**Ruo93**]. The use of CS_2 therefore allows for a higher spin density and higher signal strength than would be possible using toluene. The total spin number of the final sample is $N_{\mathrm{spin}} \approx 1.4 \times 10^{16}$ in a volume $0.55\,\mathrm{cm^3}$.

3.4.2 Experimental setup

To measure the low-field EPR spectrum and characterise the clock transition, I performed swept-field continuous-wave spin resonance measurements over a range of frequencies using the spectrometer detailed in Fig. 3.6.

The swept magnetic field $\boldsymbol{B}_{\mathrm{coil}}$ was generated using an air-cored Helmholtz coil electromagnet. The absence of a highly-permeable core material limits the achievable magnetic field strength, but ensures that there is no remnant field. A non-negligible remnant field, such as would be found using an iron-cored electromagnet, would prevent performing the near zero-field measurements that are necessary for this work. The Helmholtz configuration allows one to achieve a homogeneous field over the sample region. The magnetic field was set solely by adjusting the current I_{coil} flowing through the electromagnet, without using a feedback circuit, such as could be implemented using a Hall sensor. The electromagnet was powered by a Keithley K2280 power supply, which allows for precise control over the current flowing through the coil. The coil constant k, which parameterises the relationship between the

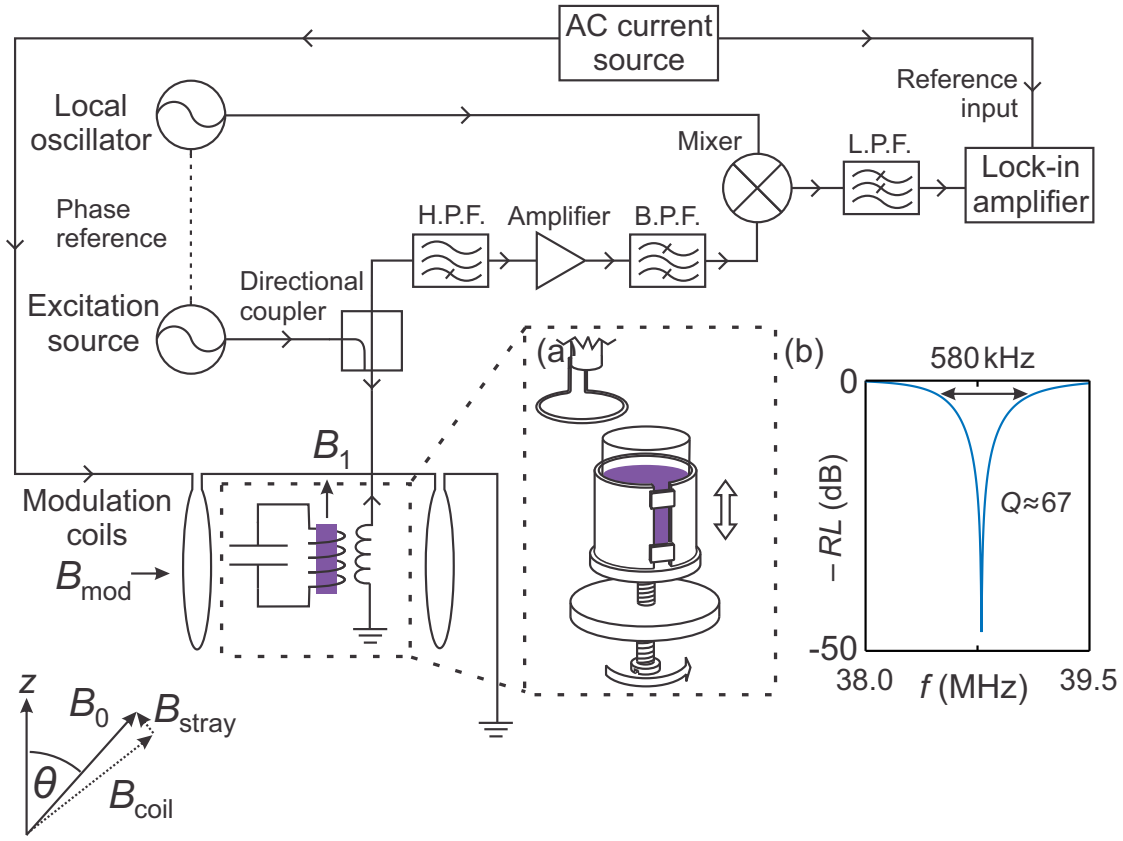

Figure 3.6: Measurement setup. An excitation source and local oscillator are implemented using two phase-locked synthesisers. The signal reflected from the resonator is high-pass filtered (H.P.F.) before amplification, in order to suppress inductive pickup of the modulation field. The signal is subsequently band-pass filtered (B.P.F.) and mixed down to baseband, before being low-pass filtered (L.P.F.) and measured using a lock-in amplifier synchronised with the modulation field. Inset (a): Loop-gap resonator with sample (purple). Adjustable coupling between antenna and resonator is achieved by mechanical displacement of the resonator (vertical block arrow) via a screw-thread mechanism. Inset (b): Reflection from the resonator, demonstrating near-critical coupling and good return loss RL for maximum sensitivity. For this particular resonator, $Q \approx 67$. (Adapted from [**Har17**], © American Physical Society, 2017.)

current and the magnetic field such that $B_{\text{coil}} = kI_{\text{coil}}$, was calibrated by measuring the resonant field and frequency for a sample of 2,2-diphenyl-1-pricrylhydrazyl (DPPH) radical, which is an organic stable free-radical molecule with spin $S = 1/2$ and $g = 2.0036$. The resonant frequency was plotted as a function of current, and the data were fitted using a first-order polynomial. From the fit coefficient, I deduce that the coil constant $k = 4.07\,\text{mT}\,\text{A}^{-1}$. This value is consistent with the value predicted by considering the geometry of the coil.

The sample and resonator are fixed such that the axis of the resonator, and

hence the B_1 field, are parallel to the local gravity vector. This is necessary in order to ensure that the liquid sample remains at the bottom of the EPR tube and within the oscillating magnetic field of the resonator, as is desired. Therefore the Helmholtz coil itself can be reoriented to select either perpendicular or parallel mode operation. The spectrometer was not shielded from stray magnetic fields $\boldsymbol{B}_{\text{stray}}$, which have the effect of slightly shifting the true magnetic field $\boldsymbol{B}_0$ at the location of the sample away from the nominal value set by $\boldsymbol{B}_{\text{coil}}$. This leads to systematic errors when fitting the resonances, which is accounted for by including free parameters to account for the effect of the stray field, which is assumed to be constant over the duration of the experiment.

To obtain each spectrum, the sample was loaded into one of a series of interchangeable loop-gap resonators (LGRs) [**FH82**] spanning the range 38–70 MHz. The LGRs were fabricated by boring and lathing a solid copper rod to form a tube with internal diameter 10.5 mm and external diameter 11.5 mm. The gap was formed by cutting the tube wall using a rotary cutter and abrasive cut-off wheel. The resonant frequency of each LGR was adjusted using capacitors soldered across the gap.[1] Due to the fixed value of the capacitances, the frequency could only be adjusted in discrete steps. It was not possible to use a tunable capacitor because of insufficient space around the resonator.

The resonator was inductively coupled to the spectrometer circuitry using a loop antenna formed from an electrical short at the end of a length of semi-rigid coaxial cable. The coupling between the resonator and the spectrometer circuitry depends on the mutual inductance between the loop and the resonator, which can be altered by changing the relative displacement of the resonator and antenna since this affects the overlap of the magnetic fields. In the setup detailed here, the loop was fixed and the coupling was adjusted by displacing the resonator. The resonator was mounted on a screw thread to facilitate precise and stable adjustment of the coupling. The resonator was impedance matched to the 50 ohm characteristic impedance of the transmission line using a directional coupler and scalar network

[1] 0505C series non-magnetic high-Q, low ESR (NP0 TC) capacitors, Passive Plus, Inc., New York, USA

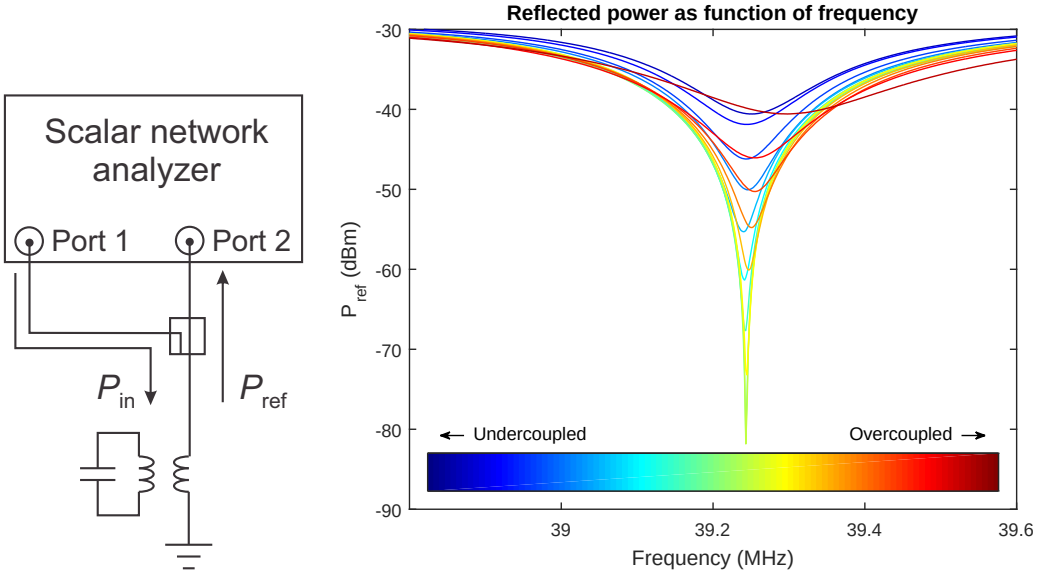

Figure 3.7: The apparatus used for tuning and impedance matching of the resonators used in the spin resonance experiments.

analyzer, as shown in Figure 3.7. The reflection coefficient was measured while sweeping the frequency, and the coupling was adjusted to minimise the reflected power on resonance. The minimum reflected power corresponds to optimal matching of the resonator to the 50 ohm characteristic impedance.

It was possible to achieve a return loss of ∼60 dB by carefully adjusting the resonator position. The loaded quality factor $Q = f/\Delta f$ was estimated by taking the frequency width Δf equal to the frequency-domain separation of the -3 dB points, as shown in Figure 3.7(b). The -3 dB points are the points at which the reflected power drops to 3 dB less than the off-resonance reflected power, where it is assumed that no power is coupled into, and dissipated in, the resonator and sample. This is at best a rough estimate, since the background reflected power is not flat, so one must exercise discretion to select a suitable reference point. A typical trace over a wide frequency range is shown in Figure 3.7(c).

The resonance signal was detected by monitoring the sample-loaded resonator's radio-frequency (rf) reflection coefficient as a function of magnetic field [**Whi48**]. On resonance, power is absorbed by the spin system, which changes the matching of the resonator to the transmission line, and hence the reflection coefficient. The

LGR was probed via a coupling antenna as described above, with the separation adjusted mechanically to achieve near-critical coupling (return loss $RL > 50\,\mathrm{dB}$. For typical resonators, the loaded quality factor $Q \sim 70$).

The EPR resonance is detected using a single-stage homodyne receiver. The rf signal reflected from the resonator was filtered and amplified before being mixed with a local oscillator signal using a double balanced mixer. The local oscillator signal is at the same frequency as the excitation source, and the output from the mixer is low pass filtered to generate a homodyne voltage. The phase between the local oscillator and the excitation source was chosen to maximise the dc component of this voltage, which maximises sensitivity to the amplitude of the reflected signal as discussed in Section 2.3.4. The homodyne voltage is therefore proportional to the rf voltage of the signal reflected from the resonator.

The sign of the change in reflected voltage on resonance depends on the coupling of the resonator to the spectrometer circuitry [**Poo83**]. For undercoupled resonators the sign is negative and for overcoupled resonators the sign is positive. It is desirable that the resonator remains either under- or overcoupled throughout the experiment. If the resonator coupling fluctuates over long-duration experiments, or if sweeping through the resonance changes whether the cavity is under- or overcoupled, the change in sign could lead to distortions of the observed signal. An alternative is to detune the frequency of applied radiation. The excitation frequency was set 3 kHz above the LGR frequency. Here, resonance is detected by the spin ensemble pulling the resonant frequency of the of cavity on resonance, which changes the reflection coefficient of the radiation applied with a fixed frequency.

For improved sensitivity, a small modulation field $\boldsymbol{B}_{\mathrm{mod}}$ was applied parallel to $\boldsymbol{B}_0$ at a frequency $f_{\mathrm{mod}} \approx 5\,\mathrm{kHz}$. The modulation amplitude, measured using a search coil, was $B_{\mathrm{mod}} \approx 1.1 \times 10^{-5}\,\mathrm{T}$. The magnetic field modulation brings the spin system into and out of resonance, thereby modulating the reflected power and hence the dc homodyne voltage. The homodyne voltage is measured using a lock-in amplifier synchronised with this modulation. The lock-in amplifier permits very narrow measurement bandwidths, thereby reducing the noise on the measurement.

However, the oscillating modulation field induces a current in the loop antenna, which leads to spurious background signals. The loop antenna was therefore mechanically adjusted to minimise its mutual inductance with the modulation coils. This is achieved by setting the normal of the loop antenna to be perpendicular to the magnetic field generated by the modulation coil. This minimises inductive coupling between the modulation coils and the antenna, and reduces the spurious background signals. I also use high-pass filter before the first preamplifier to attenuate any remaining modulation pickup.

Optimising the sensitivity of the experiment requires optimising the magnitude of the rf magnetic field used to drive the transitions. For small rf magnetic fields, the signal strength S is proportional to the B_1 drive field, and hence $S \propto \sqrt{P}$. However, at too high powers the transition saturates as the spin temperature increases, which reduces the difference in population between the two energy levels that define the transition. In extreme cases, and for homogeneously broadened resonances, this can decrease the signal amplitude. Furthermore, the linewidth increases as the transition saturates. Figure 3.8 shows resonance signals for different applied powers, and Figure 3.9 plots the signal amplitude as a function of power, demonstrating a peak near $P = -21\,\mathrm{dBm}$. This power was therefore selected as the optimal power for the spin resonance measurements.

3.5 Results and analysis

Low-field EPR spectra obtained using the spectrometer are shown in Fig. 3.10. The resonant fields are extracted by fitting the peaks with the second derivative of a Lorentzian. The observed lineshape is explained in Appendix B. The resonant fields for each measured frequency match well the predictions of Fig. 3.1(c-d), as can be seen from visual inspection. For quantitative analysis, the resonant field-frequency combinations are fitted to the theoretical values calculated from the spin Hamiltonian given in Eq. (3.1). The Hamiltonian was diagonalised [**Lin15**] to give an closed-form expression for each energy level, and the transition frequency as a function of magnetic field is calculated from the difference of these energy levels.

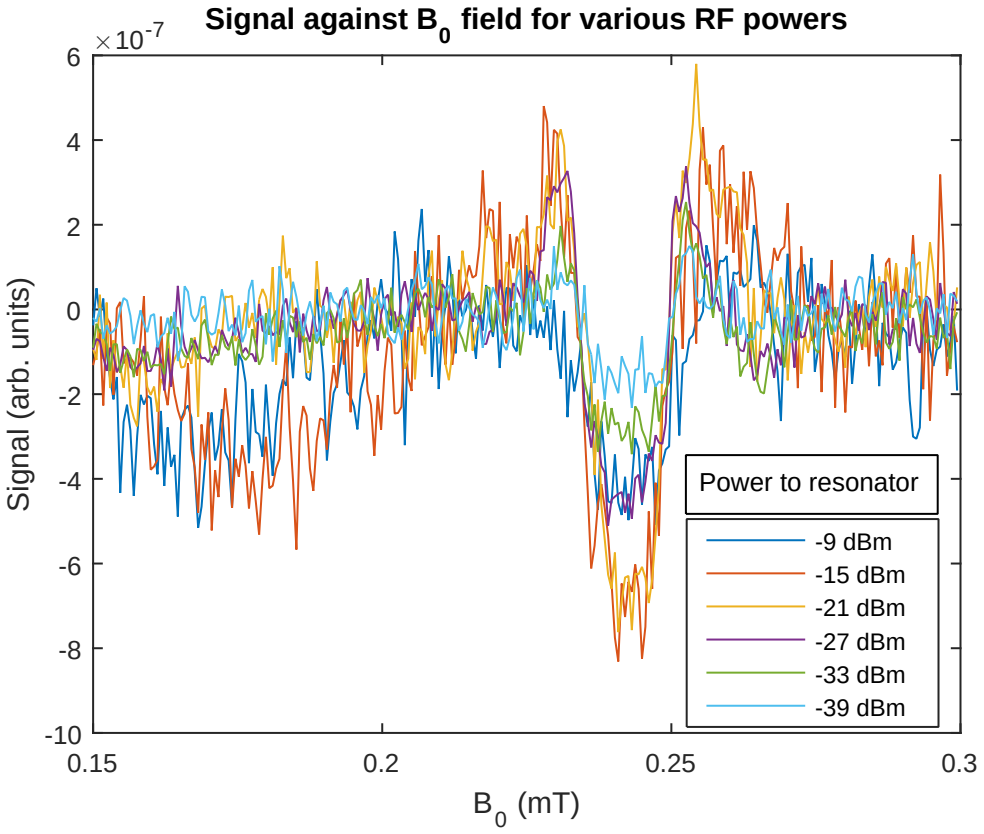

Figure 3.8: Plot of resonance signals as a function of magnetic field for different input powers to the resonator.

I account for small differences between the nominal field B_{coil} and the true field B_0 at the sample by fitting the data using

$$B_0 = \alpha B_{\text{coil}} + B_{\text{offset}}, \tag{3.20}$$

where α is a correction parameter, reflecting sample misalignment and uncertainty in the calculated coil constant, and B_{offset} is an environmental offset field. Fitting parallel and perpendicular datasets simultaneously using A, α, and B_{offset} as fit parameters, while fixing $g_{\text{e}} = 2.00204$ and $g_{\text{N}} = -0.566$, I extract $|A|/h = 22.30 \pm 0.02\,\text{MHz}$, $\alpha = 1.024 \pm 0.003$, and $B_{\text{offset}} = -28 \pm 4\,\mu\text{T}$. The quoted errors are one standard deviation intervals derived from the 95% confidence interval of the fit returned by the MATLAB fitting procedure. The one standard deviation error σ is computed from this confidence interval as $\sigma = \text{C.I.}_{95}/4$. The extracted α and B_{offset} are used to plot the data in terms of B_0 rather than B_{coil}.

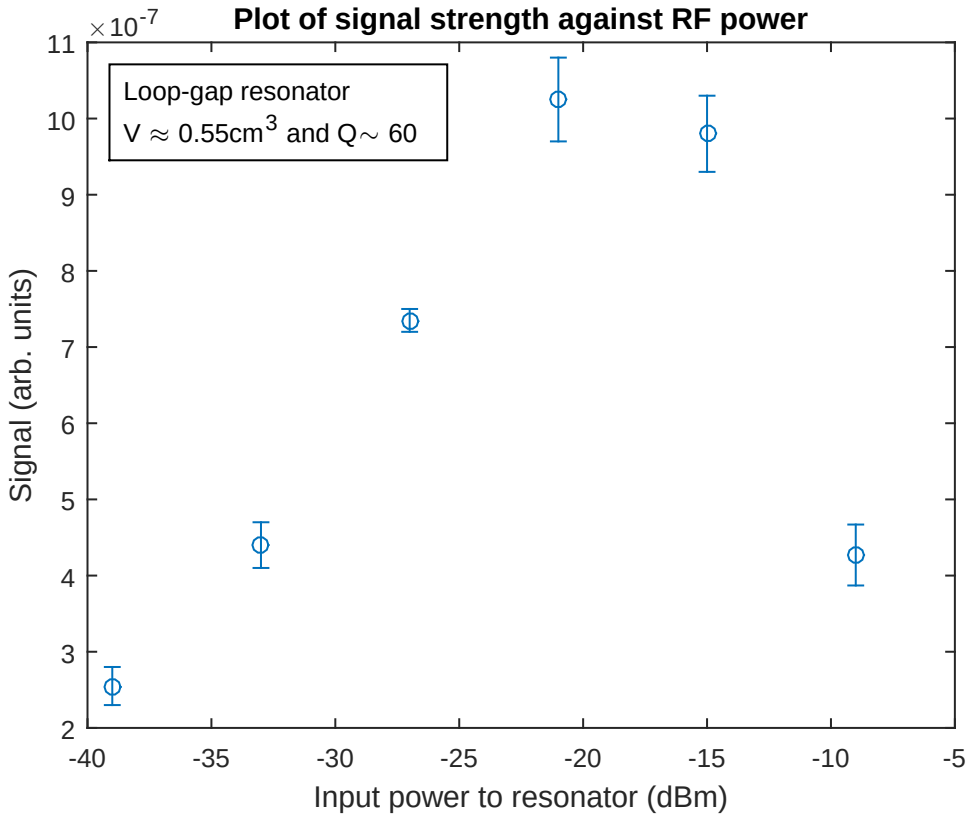

Figure 3.9: Plot of signal amplitude as a function of input power to the resonator.

To characterise the clock transition in detail, Fig. 3.11 shows the parallel-mode spectra near the clock field. Fitting these data as in Fig. 3.10, I extract $|A|/h = 22.277 \pm 0.001\,\mathrm{MHz}$, $\alpha = 1.0257 \pm 0.0005$, and $B_{\mathrm{offset}} = -12.1 \pm 0.5\,\mu\mathrm{T}$. The value of A is consistent between Fig. 3.10 and Fig. 3.11, and lies within the range of previous X-band measurements [**Har02a**; **Pie98**]. The values obtained for B_{offset} are much smaller than B_{coil}, and are consistent with the geomagnetic field.

Measuring near the clock field reduces the sensitivity of the transition frequency to magnetic field fluctuations. To quantify this, I extract field-domain linewidths δB from the spectra of Fig. 3.11 by fitting the resonances to the second derivative of a Lorentzian. As a function of the deviation from the clock field $\Delta B_{\mathrm{C}} = |B_0 - B_{\mathrm{clock}}|$, the field-domain linewidth δB increases towards the clock field (Fig. 3.12). However, when this field-domain linewidth is converted to a frequency-domain linewidth

$$\delta f = \left|\frac{\mathrm{d}f}{\mathrm{d}B_0}\right| \delta B, \tag{3.21}$$

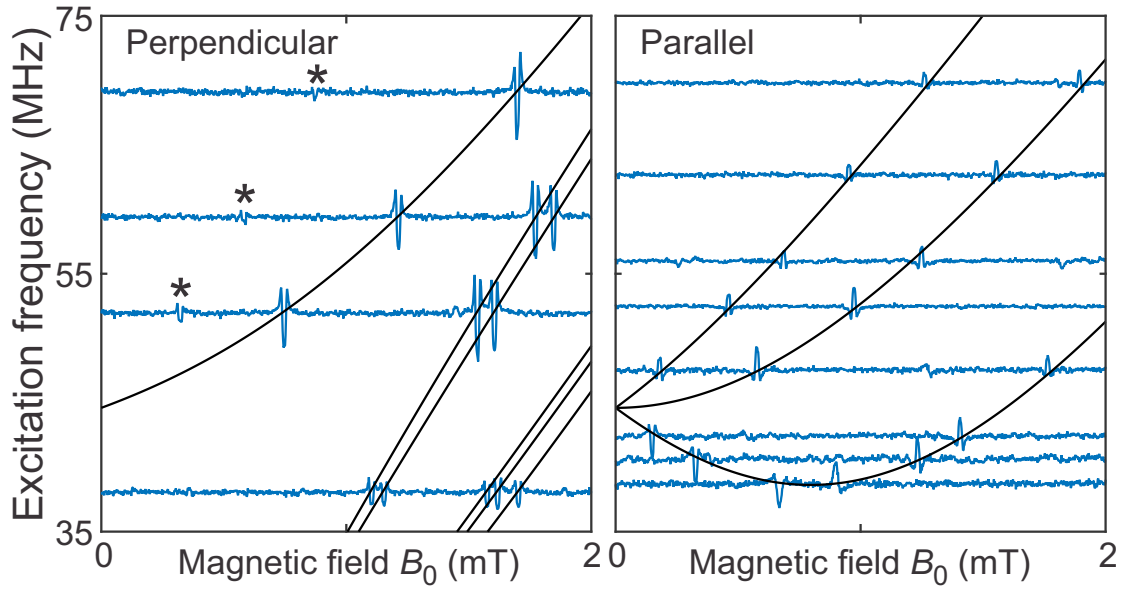

Figure 3.10: Perpendicular- and parallel-mode EPR spectrum of $^{15}N@C_{60}$ at selected excitation frequencies. Blue: Lock-in signal (arbitrary units) as a function of rescaled magnetic field B_0, offset such that the baseline of each trace aligns with the corresponding excitation frequency. Each trace is an average of up to 100 sweeps. Black: fit to resonant fields using exact solutions to the Hamiltonian given in Eq. (3.1). In perpendicular mode, it is possible to observe resonances (marked by $\star$) that were not fitted due to low signal-to-noise ratio. (Reproduced from [**Har17**], © American Physical Society, 2017.)

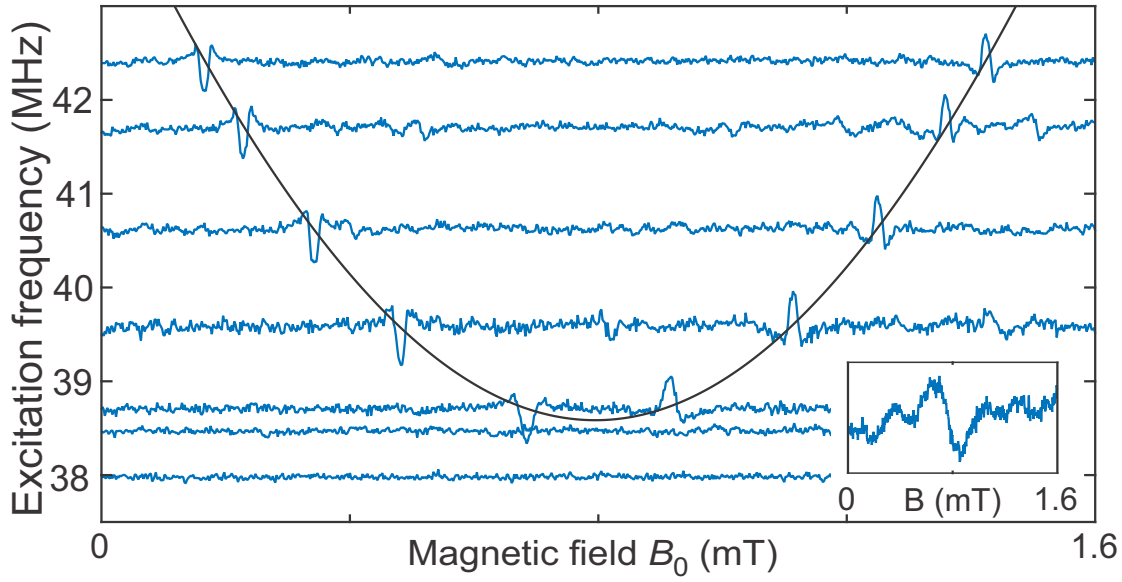

Figure 3.11: Parallel-mode EPR spectrum of the clock transition near the clock field at selected excitation frequencies. Blue: Lock-in signal (arbitrary units) as a function of rescaled magnetic field at each frequency. Black line: fit to resonant fields. Inset: spectrum measured at 38.474 MHz, cutting near the tip of the parabola. A larger modulation amplitude was necessary to detect the nearly field-independent transition. (Reproduced from [**Har17**], © American Physical Society, 2017.)

the resonance sharpens toward the clock transition as expected. Although the field-swept configuration precludes directly measuring the linewidth at the clock field, I estimate the corresponding dephasing time T_2^* by assuming that an intrinsic linewidth set by T_2^* adds in quadrature with broadening due to magnetic field fluctuations of strength B_{var}:

$$(\delta f(\Delta B_{\text{C}}))^2 = \left(\frac{1}{\pi T_2^*}\right)^2 + \left(\frac{\mathrm{d}f(\Delta B_{\text{C}})}{\mathrm{d}B} \cdot B_{\text{var}}\right)^2 . \tag{3.22}$$

Here B_{var} accounts for line-broadening due to both the modulation field and environmental field noise. Field noise could, for example, arise from the power supply used to energize the electromagnet or other electrical machinery in the immediate vicinity. Fitting with this model (Fig. 3.12) gives $T_2^* = 3.0 \pm 0.4\,\mu\text{s}$ at the clock field and $B_{\text{var}} = 26.2 \pm 0.9\,\mu\text{T}$, including the contribution of the modulation field. For comparison, a coherence time $T_2 = 80\,\mu\text{s}$ was attained in a carefully prepared $^{14}\text{N@C}_{60}$ sample measured at X-band at room temperature [**Mor06**], which is a significant improvement over the T_2^* value measured here.[2] Since T_2 represents an upper bound on T_2^* in the absence of dephasing due to inhomogenous local magnetic fields, it is not unreasonable to believe that T_2 and T_2^* should be similar at the clock field due to the transition's field insensitivity. The low value of T_2^* is therefore surprising and may indicate a field-dependent relaxation mechanism.

3.6 Implications for endohedral fullerene clocks

These measurements of the linewidth at the clock transition enable an assessment of the feasibility of an endohedral fullerene frequency standard. For short measurement times τ such that the noise spectrum is approximately white, the Allan deviation

[2] I have no directly comparable data, i.e. dilute samples measured at X-band at room temperature. However, measurements of a concentrated samples at 200 K ($0.67\,\text{mg}\,\text{ml}^{-1}$) give $T_1 = 186 \pm 7\,\mu\text{s}$ and $T_2 = 60 \pm 2\,\mu\text{s}$. Although this is less than values for dilute samples [**Mor06**], this is not surprising given the increased spin density. X-band data for measurements of samples dissolved in toluene made at 200 K ($T_1 = 151.6 \pm 0.5\,\mu\text{s}$ and $T_2 = 8.0 \pm 0.2\,\mu\text{s}$) are similar to the literature values [**Mor07**], and hence provide evidence to support the goodness of the sample preparation. I made no measurements of T_2^* at X-band.

can be estimated as [**Rie04**]:

$$\sigma_y(\tau) \approx \frac{1}{\mathrm{SNR} \cdot Q_A}\sqrt{\frac{1}{\tau}}, \tag{3.23}$$

where SNR and Q_A are the signal-to-noise ratio and quality factor of the clock transition resonance signal respectively. The signal-to-noise ratio $\mathrm{SNR} = S_0/\delta S$, where S_0 is the signal amplitude and δS is the root mean square noise per $\sqrt{\mathrm{Hz}}$ bandwidth; the transition quality factor is defined by $Q_A \equiv f_{\mathrm{clock}}/\delta f$.

Considering the experimentally measured parameters, with signal amplitude $S_0 \approx 5\,\mathrm{nV}$, input-referred noise voltage $\delta S \approx 2.5\,\mathrm{nV\,Hz^{-1/2}}$, clock frequency $f_{\mathrm{clock}} = \sqrt{3}|A|/h \approx 38.6\,\mathrm{MHz}$, and resonance linewidth $\delta f \approx 100\,\mathrm{kHz}$, Eq. (3.23) predicts a short-term Allan deviation $\sigma_y \approx 1.3 \times 10^{-3}\,\tau^{-1/2}$, where the numerical prefactor has units $\mathrm{s}^{1/2}$, such that σ_y is dimensionless.

To improve the performance, it is apparent from Equation 3.23 that it will be necessary to optimise both SNR and Q_A. Improvements to the signal strength could come from increased spin density, achieved by using higher-purity material and by choosing a solvent that allows for a higher molecular concentration, or even a powder sample. Further improvements to SNR could be achieved with a larger sample volume to increase the spin number and hence signal amplitude, or by reducing electronic noise. To increase Q_A, the linewidth should be reduced below the value measured here, the origin of which is currently unknown. There are other molecular species with clock transitions at higher frequencies [**Shi16**], but these do not benefit from the fullerene cage to protect the spin states from environmental decoherence.

I now consider what would be necessary to make an endohedral fullerene clock competitive with existing miniature atomic clocks, which achieve short-term Allan deviations $\sigma_y \leq 3\times10^{-10}$ for $\tau = 1\,\mathrm{s}$ [**MSC17**]. These improvements are summarised in Table 3.1. Firstly, I consider how to increase the SNR. The spin density in the sample ($n \approx 2.5 \times 10^{22}\ \mathrm{m^{-3}}$) approaches the limit set by the saturation concentration of C_{60} in CS_2 ($7.9\,\mathrm{mg\,ml^{-1}}$) [**Ruo93**] given the sample purity. Using pure material would increase the spin density by a factor of 170, while using 1-chloronaphthalene solvent (saturation concentration $51\,\mathrm{mg\,ml^{-1}}$) would permit

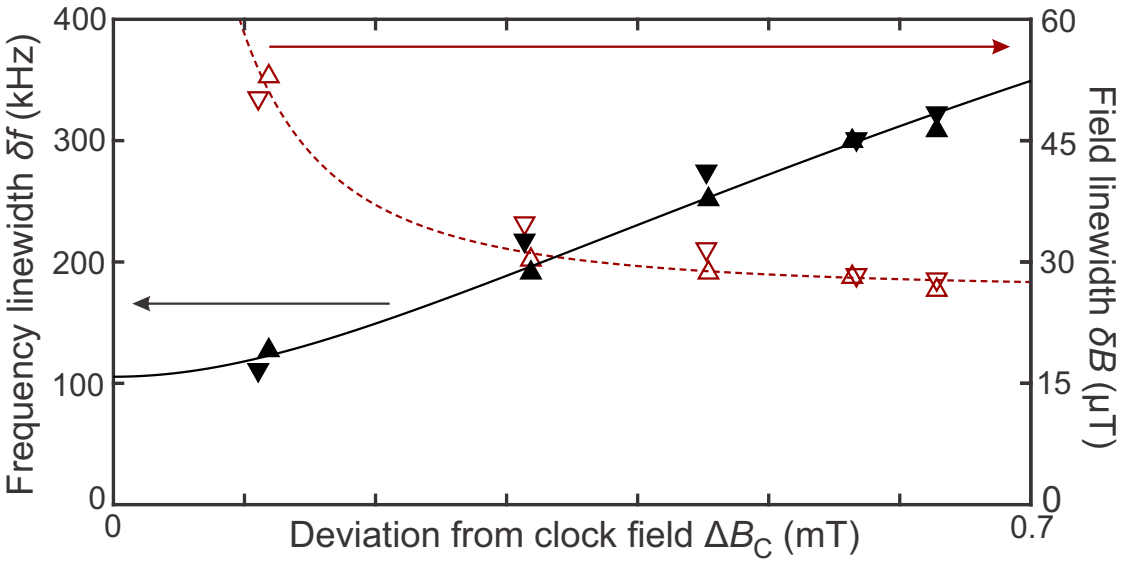

Figure 3.12: Linewidth as a function of deviation from the clock field. Left axis: frequency-domain linewidth δf above (▲) and below (▼) the clock field. Right axis: field-domain linewidth δB above (△) and below (▽) the clock field. Solid black line: fit to the frequency-domain linewidth generated using Eq. (3.22). Dashed red line: the same fit mapped to the field domain. Arrows indicate the relevant axes for the fits. (Reproduced from [**Har17**], © American Physical Society, 2017.)

an additional factor of 10. The LGR could be replaced by a solenoid with a similar filling factor and improved rf quality factor $Q \approx 200$ [**HR76**], giving a roughly three-fold increase in signal. Furthermore, there is scope to reduce voltage noise from $\delta S \approx 2.5\,\mathrm{nV\,Hz^{-1/2}}$ to the room-temperature Johnson-Nyquist limit $\delta S \approx 0.9\,\mathrm{nV\,Hz^{-1/2}}$ characteristic of a $50\,\Omega$ system. Combining all these improvements multiplicatively, while maintaining the sample volume, would lead to a short-term Allan deviation $\sigma_y \sim 1 \times 10^{-7}\tau^{-1/2}$ given the measured linewidth.

An endohedral fullerene-based atomic clock with this stability would still not be competitive with existing miniaturised atomic clocks. Furthermore, it is far from clear that such multiplicative combination of improvements is feasible; for example, it is likely that significantly increasing the spin density would increase the decoherence rate due to spin-spin interactions. The resultant increase in linewidth may offset any improvement in SNR and lead to negligible, or possibly negative, improvements to the Allan deviation. However, the scope for extreme miniaturisation using single-chip spectrometer technologies pioneered for on-chip NMR may permit the

Limiting factor	Change	Relative improvement
Purity (%)	$0.6 \to 100$	170
Concentration ($\mathrm{mg\,ml^{-1}}$)	$5 \to 51$	10
Resonator Q-factor	$70 \to 200$	2.9
Electronic noise ($\mathrm{nV\,Hz^{-1/2}}$)	$2.5 \to 0.9$	2.8
Linewidth (Hz)	$10^5 \to 10^2$	1000
	Product	1.4×10^7

Table 3.1: Summary of potential improvement factors such that a $^{15}N@C_{60}$-based frequency standard could achieve a short-term Allan deviation $\sigma_y(\tau = 1\,\mathrm{s}) \sim 1 \times 10^{-10}$. (Reproduced from [**Har17**], © American Physical Society, 2017.)

development of a true single-chip atomic clock. The advantages of reduced size, weight, and power (SWaP) may outweigh the disadvantages of reduced stability.

Secondly, I consider improvements in linewidth at the clock transition. If the linewidth could be reduced to $\delta f \sim 100\,\mathrm{Hz}$, a demanding requirement, the Allan deviation would be $\sigma_y \sim 1 \times 10^{-10}\,\tau^{-1/2}$. It is hard to see where this improvement could come from, given the $\sim 100\,\mathrm{kHz}$ linewidth measured in this study.

Alternatively, using a powder sample ($n \approx 1.4 \times 10^{27}\ \mathrm{m^{-3}}$) instead of a solution would allow the same performance to be achieved with the larger linewidth $\delta f \sim 4\,\mathrm{kHz}$. However, in both powder and high-density solution, it is critical that dipolar coupling does not broaden these linewidths. Fortunately, such broadening is typically suppressed at the clock field [**Wol13**; **Shi16**] because of the spin system's reduced coupling to the magnetic field.

For large τ, the Allan deviation $\sigma_y(\tau)$ will be greater than that predicted by Eq. (3.23) because of drifts in the experimental conditions and low-frequency noise, e.g. $1/f$ noise. For example, thermal drift enters via the temperature dependence of the hyperfine constant [**Pie02**], known from $^{14}N@C_{60}$ measurements to be $\frac{1}{A}\frac{dA}{dT} = 89\,\mathrm{ppm/K}$. Since the clock transition frequency is proportional to the hyperfine coupling, any temperature fluctuations will be directly transferred to the output frequency of the clock and reduce its stability. This is in contrast to RAFSs, where it is usually possible to adjust the buffer gas pressure and composition to find

a working point where the transition frequency is minimally sensitive to temperature fluctuations. Even here, though, it is necessary to ensure that the system is shielded from temperature fluctuation in the external environment. The development of a stable fullerene-based frequency standard will therefore require thermal isolation, temperature stabilisation, compensation or a combination of all three at the cost of increased SWaP of the complete clock system.

As a route to improving both short- and long-term stability, the endohedral fullerene $^{31}P@C_{60}$, with the same spin quantum numbers as $^{15}N@C_{60}$ but larger hyperfine coupling ($A \approx 138\,\mathrm{MHz}$ [**Kna98**]), offers a clock frequency $f_{\mathrm{clock}} \approx 240\,\mathrm{MHz}$. Given a linewidth $\delta f \approx 350\,\mathrm{kHz}$ [**Kna98**], the predicted transition quality factor $Q_A \approx 700$ for $^{31}P@C_{60}$ compares favourably to the measured value $Q_A \approx 400$ for $^{15}N@C_{60}$. The $^{31}P@C_{60}$-based frequency standard would also benefit from an approximately twenty-fold improvement due to the frequency-dependent SNR scaling, where $\mathrm{SNR} \propto f_{\mathrm{clock}}^{7/4}$ [**HR76**]. Assuming the same sample volume, concentration and purity as considered above, the improved SNR and Q_A would lead to a forty-fold improvement of the predicted short-term Allan deviation relative to that of a $^{15}N@C_{60}$-based standard, such that $\sigma_y \sim 3 \times 10^{-9}\,\tau^{-1/2}$ might be achieved in solution without further improvements in linewidth compared to the literature value. To achieve $\sigma_y \sim 1 \times 10^{-10}\,\tau^{-1/2}$ would require a linewidth $\delta f \sim 10\,\mathrm{kHz}$. Furthermore, $^{31}P@C_{60}$ exhibits a marginally weaker temperature dependence $\frac{1}{A}\frac{dA}{dT} = 74\,\mathrm{ppm/K}$ [**Pie02**].

3.7 Conclusions

I have demonstrated that $^{15}N@C_{60}$ possesses a spin resonance clock transition and therefore fulfils one of the requirements for a condensed matter atomic clock. The data presented here do not yet demonstrate clock operation, which would require a swept-frequency measurement at the clock field, but do provide the first step toward molecule-based atomic clocks: this is the first observation of a magnetic field-insensitive clock transition in a molecular system at room temperature.

In addition to posessing a clock transition, the molecular nature of the $^{15}N@C_{60}$ spin system ensures the reproducibility of the transition frequency since, in principle, all molecules are alike and have identical spin properties. However, the linewidth and the SNR are currently not favourable for using endohedral fullerenes as frequency standards in portable atomic clocks. The predicted stability of the clock on the basis of the experimental data presented in the chapter is $\sigma_y \approx 1.3 \times 10^{-3}\tau^{-1/2}$, though I identify factors that may permit significant improvement such that it could approach the stability of existing miniaturised atomic clocks.

Successful use of endohedral fullerenes in an atomic clock would require significant improvement. In particular, the development of an endohedral fullerene frequency standard would require achieving a much narrower linewidth than is measured in this work. This is particularly stringent demand, because the condensed-matter environment introduces spin relaxation mechanisms that will likely limit the minimum achievable linewidth at the clock transition [**Mor06**]. The clock transition protects against decoherence mediated by the magnetic field, but not other interactions that do not couple directly to the magnetic moment of the spins.

Furthermore, one of the most significant limitations preventing the use of endohedral fullerenes in atomic clocks is the weak hyperfine coupling. Neglecting the endohedral metallofullerenes, which transfer charge to the cage, and hence typically have broader lines, I focus on group V endohedral fullerenes: those that contain atoms from group five of the periodic table. The only known group V endohedral fullerenes are $N@C_{60}$, $N@C_{70}$ and $P@C_{60}$. In these molecules, the encapsulated atom has a half-filled outer shell with electrons in the p orbital such that the electronic ground state has term symbol $^4S_{3/2}$. To a first-order approximation, therefore, the spin systems should have zero hyperfine coupling: the p orbitals have zero spin density at the nucleus, which precludes a Fermi contact interaction, and the spherical symmetry of the electron wavefunction ensures that the electron-nuclear dipolar hyperfine coupling averages to zero. The observed hyperfine coupling is due to spin polarisation of the s orbitals due to exchange interactions with the outer shell electrons, or mixing of electronic configurations with non-zero hyperfine

coupling [**HLN62**]. However, this is much weaker than the hyperfine couplings arising directly from unpaired s shell electrons that are observed for the alkali metal atoms. The clock transition frequency is therefore much lower for the endohedral fullerenes than for the alkali metal atoms. The equation for Allan deviation (Equation 3.23) indicates that a high clock transition frequency is important for achieving good stability. While it may be possible to offset some deficiency in the clock transition frequency by achieving a narrower linewidth, the weak hyperfine coupling and low clock transition frequency will always impair the suitability of endohedral fullerenes for use as the frequency reference of an atomic clock.

For these reasons, the maximum quality factor of the clock transition Q_A will likely be less than is achieved in vapor-based clocks, which are capable of achieving both very narrow linewidths and high transition frequencies. To compensate for this, it will be necessary to improve the SNR of the spin resonance signal. This could be achieved by further engineering of the spectrometer, to reduce electronic noise and increase sensitivity, or increasing the spin density of the sample within the resonator. Increasing the spin density within the resonator should increase signal amplitude. However, this is likely a trade-off between signal amplitude and linewidth, since increased spin density may broaden the line due to spin-spin interactions and further reduce Q_A.

However, the low-frequency solid-state approach could eliminate the complexity of vapor-based clocks in favor of a single radio-frequency circuit packaged on the same chip as the sample. This would enable further miniaturisation, robustness, and ease of manufacture, leading to a wider range of application of atomic clocks.

4
High pressure EPR

Contents

4.1 Introduction

As shown in the previous chapters, the clock transition frequency depends on the hyperfine coupling between the incarcerated nitrogen atom's nuclear and electron spins. However, the temperature sensitivity of this coupling introduces a mechanism by which the environment may perturb the clock frequency, leading to long term drifts. This is a problem common to other atomic frequency standards [**Ril92**; **Hod13**], which has led to a range of mitigation strategies. For example, for frequency standards based on NV centres, it has been proposed to tune the clock

frequency using pressure in order to offset the effect of temperature [**Hod13**]. Such an approach could be implemented using entirely passive components by enclosing the sample within a holder possessing the appropriate thermal expansion coefficient. In this chapter, I investigate the sensitivity of the hyperfine coupling to pressure, in search of a experimental "knob" with which to tune the hyperfine coupling and find a strategy to ameliorate the temperature sensitivity. Furthermore, the pressure sensitivity is itself an important factor to consider; for example, the resonance frequency of some atomic frequency standards are sensitive to changes in barometric pressure [**Ril92**].

The EPR signal of $^{15}N@C_{60}$ in solution was measured at X-band over a range of pressures from atmospheric pressure to 0.25 GPa, or approximately 2500 times atmospheric pressure. The hyperfine coupling was observed to depend weakly on pressure, with $\mathrm{d}|A|/\mathrm{d}P \approx 3.5 \times 10^{-4}\,\mathrm{Hz\,Pa^{-1}}$. I hypothesise that compression of the fullerene cage at high pressures increases the strength of the interactions between the electrons of the nitrogen atom and those of the cage, and leads to increased spin polarization of the nitrogen atom's s orbital electrons, which in turn increases the isotropic hyperfine coupling.

I consider various models of the nitrogen–cage interaction to interpret the pressure dependence. These models are based on either dispersive interactions (van der Waals forces), caused by fluctuating polarizations of the electron clouds of the nitrogen and the cage or "squeezing" of atomic orbitals [**Wei00**]. The former model is justified by the importance of dispersive interactions in the the binding energy of the endohedral fullerene system [**Par02**], and its use in explaining the increased hyperfine coupling for nitrogen atoms trapped in a matrix of inert gas atoms [**Adr62**]. The latter model is preferred within the fullerene community [**Wei00**], though, to the best of my knowledge, has never been evaluated against a dispersive interaction model.

I use these models to estimate the bulk modulus of the fullerene cage from the pressure dependence. While the bulk modulus has previously been measured for fullerene crystals [**Duc91**; **LS94**; **Pin99**; **Lev00**], this is the first experimental

estimate of the bulk modulus for an individual molecule—prior measurements reflect the strength of the intermolecular bonds rather than the rigidity of the cage itself. This estimate of the molecule's bulk modulus is compared against theoretical predictions in the literature that were made using molecular dynamics simulations and density functional theory calculations [**RR91**; **Woo92**; **AM09**; **Kau10**; **Peó14**]. The agreement between the theoretical predictions and the experimental value is poor: the measured hyperfine shift indicates a more compressible cage than is predicted by theory, and is far closer to the literature values for fullerene crystals.

I also take a purely empirical approach, by considering the hyperfine coupling for $^{14}N@C_{60}$ and $^{14}N@C_{70}$. The radius of these two molecules differs, giving experimental data points for the hyperfine coupling as a function of cage radius. By assuming a function joining these two points in the radius–hyperfine coupling plane, it is possible to estimate the bulk modulus. The estimates of bulk modulus obtained using this approach are in closer agreement with the other experimental values deduced using the dispersive model detailed above than the theoretical estimates made using density functional theory (DFT) and molecular dynamics.

In addition to a pressure dependent hyperfine coupling, I also observe an apparent pressure dependent g factor and linewidth. The shift in g factor is the same for the $^{15}N@C_{60}$ sample, which is pressurised, and a lithium phthalocyanine (LiPc) sample used as a g marker, which is not pressurised. This indicates that the g factor shift is not due to pressurisation of the sample. Instead, the observed effect could plausibly arise from a pressure-dependent shift in the B_0 field. However, it is hard to know where such a field could come from, since the experimental apparatus was designed to minimise the magnetic susceptibility of any parts within the region of high magnetic field between the pole pieces. Furthermore, particular care was used to ensure that any moving parts were removed from the region of high magnetic field, and were fabricated from low magnetic susceptibility materials.

I investigate various potential line broadening mechanisms. I consider models based on the translational diffusion of protons on the solvent molecules and the rotation of fullerene clusters containing more than one endohedral fullerene, both of

which lead to fluctuating local magnetic fields. The effect of a pressure-dependent field inhomogeneity is considered but discounted, since any moving parts are fabricated from low-permeability materials.

The data are well fitted by the rotating cluster model, and the postulated fullerene clusters are consistent with fullerence aggregation in high concentration samples. At low pressure, the solvent is sufficiently non-viscous that anisotropic interactions that broaden the resonance, such as dipole-dipole coupling between spins, are averaged out by rotation of the cluster. At high pressure, the solvent viscosity increases, leading to incomplete averaging and an increase in the linewidth towards the rigid lattice limit [**BPP48**]. I found that although the rotating cluster model fits the data extremely well, the implied spin density appears too low relative to the purity of the sample as measured using UV-Vis spectroscopy and quantitative EPR spectroscopy.

4.2 Methods

As given in the previous chapter, the energy levels of the $^{15}N@C_{60}$ spin system are described by the Hamiltonian

$$\mathcal{H} = g_e \mu_B S_z B_0 - g_N \mu_N I_z B_0 + A \hat{\boldsymbol{S}} \cdot \hat{\boldsymbol{I}}, \tag{4.1}$$

where the first two terms parameterise the Zeeman interaction of the electron spin $S = 3/2$ and nuclear spin $I = 1/2$ with the static magnetic field B_0. The electronic and nuclear g factors are denoted by g_e and g_N, respectively. The final term describes the hyperfine interaction, with coupling strength A. At high fields, where the Zeeman interaction dominates, the energy levels are labelled by the quantum numbers m_S and m_I, which give the projection of the relevant spin onto the axis defined by the direction of B_0. In this regime, the EPR spectrum measured as a function of magnetic field at a fixed frequency f exhibits a pair of spin resonances corresponding to the two states of the ^{15}N nuclear spin, as shown in the upper inset of Fig. 3.1. These resonances are split in the frequency domain by A, and in the field domain by $\Delta B = A/(g\mu_B)$.

Measurements of the EPR spectrum of a $^{15}N@C_{60}$ sample were performed at the X band (frequency $f \sim 9.5\,\mathrm{GHz}$) using a Bruker EMXmicro spectrometer and Bruker ER 4122 ST cavity resonator. All measurements were performed at room temperature, with sufficient time between increasing the pressure and performing the measurement to allow thermal equilibriation. The EPR signal at each pressure is fitted using the first derivative of a Lorentzian to extract the field-domain linewidth δB and the resonant field of each resonance.

The resonant fields and frequencies are then fitted using an analytical expression obtained by diagonalising the spin Hamiltonian. The fit parameters for this equation are the isotropic hyperfine coupling A and electron g factor g_J. Each of the two resonances in the spectrum is the sum of three unresolved resonances split by the second-order terms in the hyperfine coupling. I fit the resonant field using the expression for the resonant field of the central resonance in the triplet.

To fit the data, it is necessary to know precisely the frequency at which the spectrum is measured. The frequency of the microwave radiation used to drive the EPR transitions is set to match the resonant frequency of the cavity, which depends weakly on pressure via the dielectric constant of the toluene solvent [**SCF68**; **Mop69**]. The frequency of applied radiation is therefore measured automatically at each pressure by a microwave frequency counter built into the spectrometer itself.

The sample used for high-pressure measurements had a fullerene concentration of about $1\,\mathrm{mg\,mL^{-1}}$. This was necessary because the small sample volume of the pressure cell leads to a low resonator filling factor, which reduces the signal-to-noise ratio (SNR) of the measurement. This sample was then injected into an yttria-stabilised zirconia cell attached to a barocycler [**Ler15**]. The solvent used in these experiments was toluene rather than carbon disulfide (CS_2), as was used for the measurements in the previous chapter. While this adversely affects the minimum achievable linewidth [**Mor07**], toluene was selected due to its low volatility in comparison with CS_2. The cell filling procedure is sufficiently delicate and time consuming, that, if CS_2 were used, it would evaporate before the sample chamber could be sealed. In addition to toluene, the EPR spectrum of the sample was also

measured in deuterated toluene to investigate the effect of translational diffusion of proton spins on the linewidth, which is detailed in Section 4.3.2.

The pressure was applied to the sample using a HUB440 pressure amplifier, which amplified and converted pneumatic pressure to hydraulic pressure. The working fluid of the pressure amplifier is water. The working fluid acts on a moving piston that separates the working fluid and the sample, thereby pressurising the sample.

4.2.1 High-pressure setup

A schematic diagram of the experimental setup is given in Figure. 4.1. Fig. 4.1(a) shows the apparatus as it was initially configured, and Fig. 4.1(b) shows the apparatus with the addition of a non-magnetic spacer between the yttria-stabilized zirconia (YSZ) sample cell and the stainless steel pressure vessel. The piston inside the pressure vessel separates the fullerene-containing toluene sample from the aqueous working fluid by which the barocycler applies pressure. As the toluene sample is compressed under pressure, this piston moves.

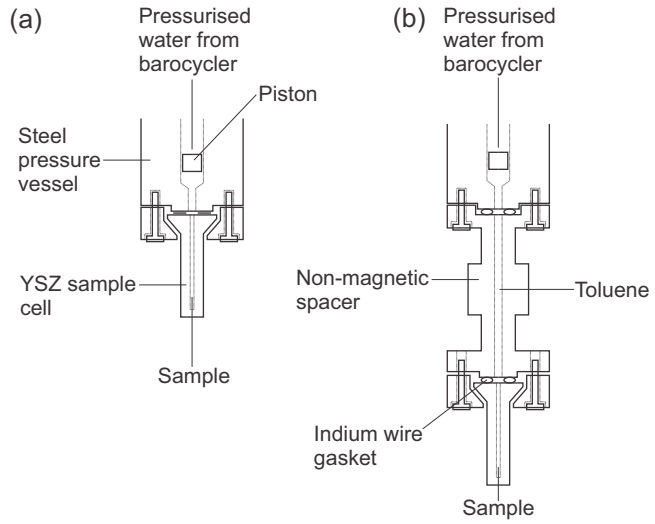

Figure 4.1: Schematic diagram of the high-pressure EPR apparatus. (a) shows the original setup, in which the yttria-stabilized zirconia (YSZ) cell containing the sample is mated directly to the stainless steel pressure vessel that serves as the interface with the barocycler. (b) shows the new setup, in which a non-magnetic spacer is placed between the stainless steel pressure vessel and the sample cell. The flat kapton washer is replaced by indium wire gaskets, and the original steel screws are replaced with non-magnetic titanium alloy screws.

Samples measured in the high pressure setup initially exhibited an EPR linewidth of approximately 200 mG, which is an order of magnitude larger than linewidths previously reported in the literature for both solution [**Kna97**] and dilute solid-state samples [**Din00b**]. Furthermore, the lineshape was notably asymmetric in contrast to previous measurements of N@C60 in solution [**Kna97**]. This increased linewidth and poor lineshape was observed even at atmospheric pressure, where the experimental conditions should be similar to previous measurements. Reducing the modulation amplitude and applied rf power did not correct these problems. To ensure that sample contamination was not responsible for the increased linewidth, the sample was removed from the YSZ pressure cell and measured in a conventional EPR setup. Under these conditions, the resonance has a narrow linewidth consistent with a modulation amplitude-limited linewidth of ∼20 mG.

Experimentally achieving an EPR linewidth that accurately represents the narrow intrinsic linewidth of the $N@C_{60}$ sample requires a highly homogeneous magnetic field B_0, in addition to careful sample preparation and optimisation of experimental parameters such as applied microwave power, field modulation amplitude, and field modulation frequency [**Mor06**; **Mor07**]. The magnetic field generated by the electromagnet satisfies the homogeneity requirement, but the field is perturbed by the presence of magnetic objects, whether paramagnetic, diamagnetic, or ferromagnetic. The resulting field inhomogeneities lead to broadening and distortion of the observed resonance signal.

The linewidth and lineshape of the resonances observed for $N@C_{60}$ samples measured in the high pressure setup are consistent with an inhomogeneous static magnetic field. The magnetic field inhomogeneity was caused by the stainless steel pressure vessel used to mate the YSZ sample cell to the barocycler. The pressure vessel is located between the pole pieces of the electromagnet that produces the static magnetic field B_0. The pressure vessel has a non-zero magnetic susceptibility, and hence becomes magnetized, thereby generating a spatially inhomogeneous magnetic field. The sum of the static B_0 field and this inhomogeneous field leads to inhomogeneous broadening of the EPR resonance. This inhomogeneous broadening

was not previously observed for the apparatus, because it is typically used with spin-labelled proteins [**Ler15**]. These samples typically have very broad linewidths due to the short spin–lattice relaxation and spin–spin decoherence times. The measurements are therefore not particularly sensitive to small distortions of the B_0 field. However, this broadening is significant for the N@C_{60} samples measured in this thesis due to their sharp resonances.

4.2.2 Simulated EPR resonance signal with inhomogeneity

To estimate the field inhomogeneity and simulate the EPR resonance signal, I model the steel pressure vessel as a cylinder-shaped linear paramagnet with susceptibility χ in a uniform magnetic field B_0. The cylinder is split into cube-shaped volume elements with a magnetization $M = \chi B_0/\mu_0$. The demagnetizing field $B_{\text{inh.}}$ due to these magnetic dipole elements is regularly sampled at points along a line coaxial with the sample, and the magnetic field between these points is interpolated by fitting the simulated values with a fifth-order polynomial.

The first-derivative EPR signal is first simulated in the absence of perturbing magnetic field at equally spaced points along the sample. The spectrum at each point is then shifted in the field domain by the perturbing field calculated for the point. The inhomogeneously broadened EPR spectrum is calculated by summing the field-shifted spectra for all points along the sample. The simulated peak-to-peak linewidth is determined by visual inspection. Some typical lineshapes are shown in Fig. 4.2 for a range of magnetic susceptibilities.

Since the contribution to the total signal from a given point is proportional to the B_1 field, the B_0 field inhomogeneity must be weighted by the B_1 field distribution to determine the magnitude of the inhomogeneous broadening. This is because the contribution of a given volume to the overall signal is proportional to the magnitude of the RF field at that particular volume. Assuming that the sample is coaxial with the resonator, the expectation value of the demagnetizing field due to the pressure vessel is therefore given by

$$\int_{x_{\min}}^{x_{\max}} B_{\text{inh}}(x) B_1(x)\,\mathrm{d}x \Big/ \int_{x_{\min}}^{x_{\max}} B_1(x)\,\mathrm{d}x, \tag{4.2}$$

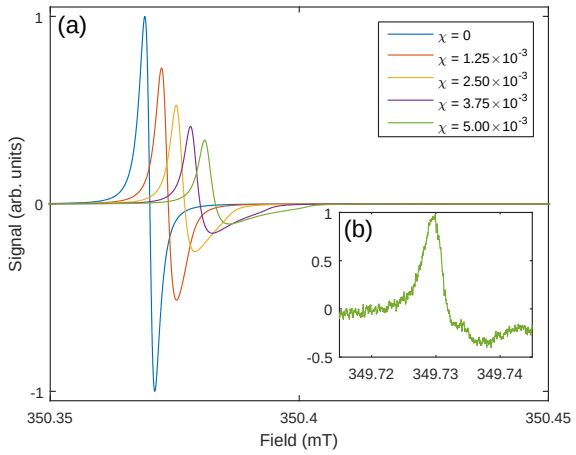

Figure 4.2: Plot of simulated lineshapes accounting for pressure vessels with different magnetic susceptibilities. The linewidth, lineshape, and resonant field are all affected by the demagnetizing field of the pressure vessel. The inset (b) shows experimental data for the initial magnetic setup as a comparison, demonstrating clearly the line broadening and asymmetry.

where $x_{\min}$ and $x_{\max}$ are the minimum and maximum extent of the sample, respectively. The B_0 magnetic field is most inhomogeneous near the pressure vessel, and hence near the wall of the cavity. However, the excited electromagnetic mode in the Bruker ER 4122 SHQ-E resonator is a cylindrical TE_{011} mode, which is described by a sinusoid with nodes in the B_1 field at the cavity walls such that $B_1(x) = B_1 \sin(x)$. This reduces the influence of the region of strong spatial inhomogeneity near the pressure vessel.

I model the pressure vessel as a cylinder with diameter 16 mm and height 50 mm, and susceptibility $\chi = 0.003$ [**KL95**]. The static magnetic field is assumed to be constant over the pressure vessel and resonator, with magnitude $B_0 \approx 0.35$ T. For the initial setup without the non-magnetic spacer, the pressure vessel is approximately 20 mm above the top of the resonator, and the sample cell is inserted into resonator by approximately 10 mm. The field inhomogeneity over the resonator, which is assumed to have a height of 25 mm, is 15 μT, and the B_1 field-weighted inhomogeneity over the sample is 3.6 μT. Visual inspection of the simulated resonance indicates that an initial peak-to-peak linewidth of 2 μT, which is deduced from later experiments using the non-magnetic spacer, would be inhomogeneously broadened to approximately

4 μT. This is less than the experimental value of 7 μT, but the simulation reproduces the observed lineshape reasonably well. The discrepancy may be due to the steel screws used in the original setup, which had a high magnetic permeability and consequently had a significant effect on the magnetic field. Furthermore, the exact lineshape and linewidth depends sensitively on the pressure vessel–resonator distance and amount of sample inserted into the resonator.

4.2.3 Non-magnetic spacer

To mitigate the inhomogeneous broadening caused by the field inhomogeneity due to the steel pressure vessel, I designed a non-magnetic spacer to go between the steel pressure vessel and the sample cell as shown in Fig. 4.1(b). The spacer removes the pressure vessel from the region of high magnetic field between the pole pieces and increases the separation of the magnetized pressure vessel from the sample. This has the dual effect of reducing the magnetization of the pressure vessel and increasing the distance between the magnetized pressure vessel and the sample, both of which reduce the magnitude of the field inhomogeneity at the location of the sample. The use of this spacer enabled the measurement of EPR resonance linewidths for the fullerene samples that were comparable with literature values. The lineshape distortion was also reduced, such that the EPR resonance as well fitted by the derivative of a Lorentzian, as is typical for homogeneously broadened resonances. Figure 4.3 displays an EPR resonance signal obtained after installing the non-magnetic spacer, demonstrating a narrow resonance and symmetric lineshape.

Fig. 4.4(a) is a photograph of the finished spacer, and Fig. 4.4(b) is a photograph of the complete assembly installed in the magnet. The spacer was machined from a single billet of a low susceptibility, high tensile strength titanium alloy. The spacer has a hexagonal cross-section that is gripped by a mechanical support shown in Fig. 4.4 to ensure that the sample does not move when the system is pressurised. A detailed account of the mechanical aspects of the spacer design is given in Appendix C.

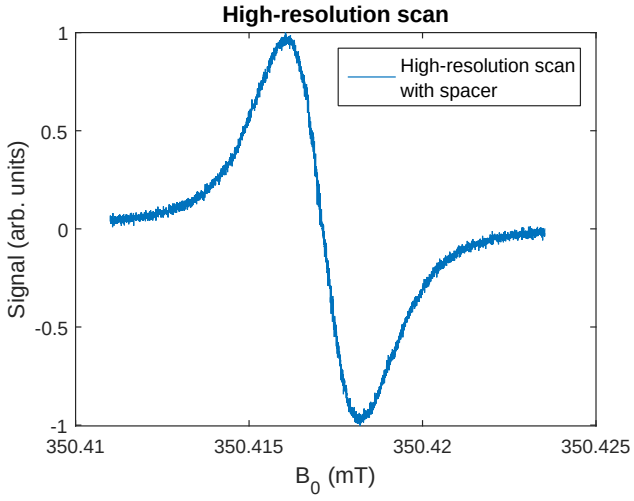

Figure 4.3: High-resolution scan of $^{15}N@C_{60}$ EPR signal after installing the non-magnetic spacer. The lineshape is highly symmetric, which contrasts strongly with the distorted signal obtained using the original setup without the spacer (see inset (b) of Figure 4.2).

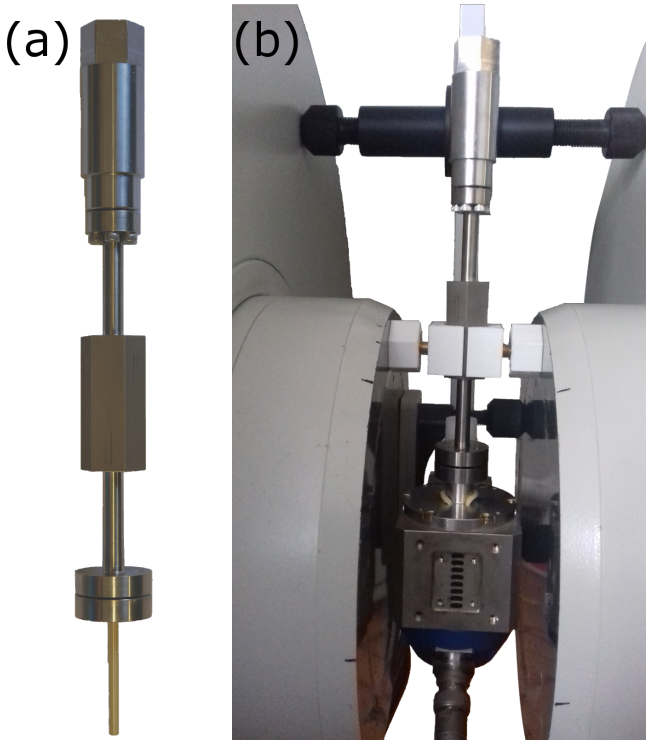

Figure 4.4: Photographs of the spacer assembly and magnet. (a) shows the pressure vessel, non-magnetic extender, and sample cell. (b) shows the setup installed in the electromagnet used to apply the static B_0 field. The spacer is clamped between the pole pieces to prevent movement of the sample that could give rise to spurious shifts in the apparent resonant field.

The spacer introduces a substantial volume that must be filled with fluid, but that does not contribute to the EPR signal. However, only a small quantity of

endohedral fullerene sample is available. The fullerene sample dissolved in toluene is therefore loaded into the YSZ cell as previously, and the dead volume in the spacer itself is filled with a toluene blank. During the measurement, $N@C_{60}$ diffuses from the sample cell into the spacer, which reduces the concentration of the $N@C_{60}$ sample within the microwave resonator. This is observed as a reduction in the signal amplitude. However, the signal-to-noise ratio remains adequate over the sequence of measurements.

It is not possible to replace the toluene blank with an air column. By considering Boyle's law and assuming that the sample is initially at atmospheric pressure, one can calculate that the volume of the air column would decrease to 0.04% of its initial value upon pressurising the sample to 0.25 GPa. However, the piston used to apply pressure to the sample has limited travel due to the design of the stainless steel pressure vessel, which would prevent it from pressurising the sample to the pressures necessary to observe the small pressure effects presented here. Secondly, it is highly likely that the much lower viscosity of air compared to toluene would render the seals between the pressure vessel, extender, and sample cell ineffective. Thirdly, by considering Henry's law, one can see that the concentration of oxygen in the sample would increase at high pressures as oxygen from the air column dissolves in the sample. This is problematic since dissolved oxygen may broaden the EPR resonance due to spin–spin interactions between endohedral fullerenes and the paramagnetic triplet state of oxygen. For these reasons, an air column is not a feasible replacement for the toluene blank as a means of transmitting pressure to the sample.

Field inhomogeneity simulations for setup incorporating non-magnetic spacer

To validate the spacer design, I estimate the expected inhomogeneous broadening of the EPR resonance measured using the setup incorporating the non-magnetic spacer. The field inhomogeneity is estimated using the same method presented in Section 4.2.2. The total length of the spacer is $L = 112\,\mathrm{mm}$. Neglecting any magnetization of the titanium spacer, due to its low magnetic susceptibility $\chi = 1.8 \times 10^{-4}$ [**Suy11**], and considering only the steel pressure vessel, the field

inhomogeneity over the resonator is approximately 90 nT and the inhomogeneity over the sample is approximately 40 nT. The B_1 field-weighted inhomogeneity over the sample is approximately 10 nT, and the observed broadening is negligible to within the precision of the simulation. Moreover, these figures overestimate the broadening since the pressure vessel is outside the pole pieces, and hence is in a lower magnetic field than the assumed 0.35 T.

In addition to the line broadening caused by the pressure vessel, it is also necessary to consider the effect of the piston that separates the toluene sample and aqueous pressurising fluid. The original steel piston was appreciably magnetic, with a magnetic susceptibility $\chi \approx 25$ at an applied field $H = 3300$ Oe, and hence would cause a substantial inhomogeneous field. By considering the compressibility of the toluene and the sample volume, I estimate the piston moves a distance $d \sim 2$ cm over the 0.25 GPa range of applied pressure. If the field inhomogeneity is significantly affected by the magnetized piston, this displacement could give rise to an apparent pressure-dependent linewidth and lineshape. The piston was therefore replaced with a copper piston, with magnetic susceptibility $\chi = -9.7 \times 10^{-6}$ [**Hay14**].

The copper piston is modeled as a cylinder with diameter 4 mm and height 10 mm located 25 mm above the bottom of the pressure vessel. Using these parameters, the estimated field inhomogeneity due to the copper piston is neglibible to within the precision of the simulation. Simulating the EPR spectra for these condition indicates that the piston does not contribute to the linewidth of the resonance, and I conclude that motion of the piston is not responsible for the pressure-dependent hyperfine splitting of the resonances or line broadening.

From these simulations, I therefore conclude that the high pressure apparatus does not contribute to the linewidth after replacing the magnetic components with non-magnetic alternatives and moving the remaining magnetic components away from the sample.

4.2.4 Reliable g factor measurements

The g factor of $N@C_{60}$ deduced from the EPR measurements is very close to that of a free electron. However, it is slightly less, due to spin-orbit coupling of the unpaired p orbital electrons that give rise to the endohedral fullerene's EPR signal [**Wit18**]. I hypothesised that compression of the cage would distort the orbitals such that the spin-orbit coupling would change.

The g factor was determined from the analytical fit of the resonance fields previously used to determine the isotropic hyperfine coupling coefficient. However, the g factor determined from this fit is not reliable. This is because the Hall effect sensor used to measure the magnetic field is not calibrated to sufficient accuracy and precision to enable a reliable calculation of the g factor. Furthermore, the sensor is located on the pole pieces of the magnet and is therefore displaced from the sample location; as such, it may not accurately record the magnetic field value at the sample itself. Discrepancies may be due, for example, to field inhomogeneities caused by, for example, external fields or magnetization of the pole pieces.

The g factor is therefore measured relative to a standard sample with a known g factor. Such a measurement does not require such precise and accurate calibration of the field sensor. In this case, the EPR signal from the $^{15}N@C_{60}$ sample and a lithium phthalocyanine standard sample, which has a known g factor $g = 2.00214$ [**BA99**], are measured simultaneously. The sample was placed in a capillary in the same resonator as the pressurised sample, as shown in Figure 4.5.

Lithium phthalocynanine is a molecule in which a lithium atom is at the centre of a phthalocyanine deck [**Tur87**]. The EPR signal arises from the unpaired electron spin of the lithium atom. The sample is prepared electrochemically from dilithium phthalocyanine, and by tailoring the conditions, it is possible to achieve different crystal structures, with different magnetic properties. The x-form is of particular interest due to its very narrow EPR resonance under anoxic conditions [**BTA98**] which is caused by extreme exchange narrowing as the electrons are free to hop between spin sites. For the purposes of this experiment, the powder was placed in a fused quartz capillary, pumped under vacuum to remove oxygen, and flame

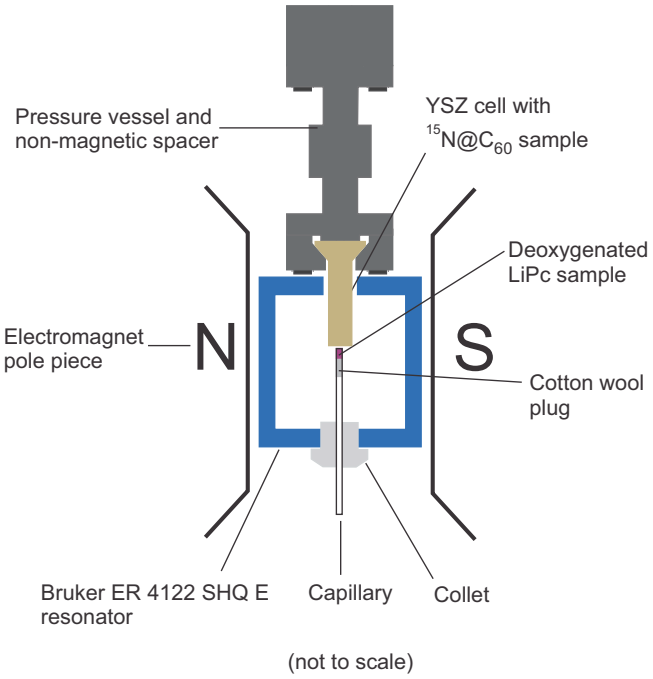

Figure 4.5: Schematic diagram of sample arrangement for g factor measurements. The pressurised $^{15}N@C_{60}$ sample is located in the yttria-stabilized pressure cell, and is subject to pressure applied by the barocycler. The LiPc powder sample is in a deoxygenated and flame-sealed capillary inserted from the bottom of the resonator and held in place with a collet. The powder sample has a small spatial extent, such that it can be considered a point-like sample in comparison to the line sample of the $^{15}N@C_{60}$ sample.

sealed. A small plug of cotton wool is used such that the sample can be inverted without the powder falling down. This was necessary since there is insufficient room to insert the capillary from the top of the resonator, so it was inserted from the bottom and held with a collet. The narrowness of the linewidth makes it suitable for use as a g marker in this experiment, since it is well resolved from the $^{15}N@C_{60}$ resonances in the EPR trace, while also being close in g factor. A representative EPR trace is displayed in Figure 4.15.

The LiPc spin system is modelled by a spin system with a single unpaired electron with spin $S = 1/2$ that interacts solely with an external magnetic field by the Zeeman interaction. The g factor is therefore given by

$$g = \frac{hf}{\mu_B B}, \tag{4.3}$$

where B is the resonant field for radiation with a frequency f.

4.3 Results

In this section, I discuss and analyse the experimental data obtained from the high pressure measurements. I observe a pressure dependent hyperfine coupling, a pressure dependent linewidth, and an apparent pressure dependent g factor. However, by measuring the g factor against a standard sample outside the pressure cell, this apparent g factor shift is shown to be a systematic error.

I consider the pressure-dependent hyperfine coupling using two different approaches. The first approach is motivated by noting the analogy with the pressure dependence of the hyperfine coupling of atomic nitrogen in the gas phase and in solid-state samples in which nitrogen is trapped within a matrix of noble gas atoms. The second approach is motivated by considering the difference in hyperfine coupling observed for nitrogen atoms confined in C_{60} and C_{70} cages. Both relate the change in hyperfine coupling with pressure to the cage radius, and permit an estimate of the bulk modulus of the cage. However, the estimated bulk modulus is much lower than theoretical estimates, and is closer to the experimentally determined bulk modulus of fullerene crystals. I also consider the possibility of solvent effects modifying the hyperfine coupling.

To understand the pressure-dependent linewidth, I focus on the effect of pressure on the viscosity of the solvent and hence on the motion of the fullerene molecules. This affects the EPR spectrum by modifying motional averaging of anisotropic interactions that may affect the linewidth. In particular, I focus firstly on translational diffusion of solvent protons and their magnetic dipole interactions with the endohedral fullerene spin system, and secondly on magnetic dipole interactions between nitrogen spins within large clusters of fullerenes. I also consider the possibility of a magnetized object moving as pressure is applied, which may lead to a pressure-dependent field inhomogeneity and hence linewidth.

4.3.1 Hyperfine coupling

The sample was measured over multiple independent runs, between which the sample was removed from the sample cell and stored at ambient temperature in a light-tight

container. The isotropic hyperfine coupling constant was fitted using an analytical expression obtained by diagonalising the Hamiltonian given in Equation 4.1 to determine A from the experimental data. Data for the hyperfine coupling constant as a function of pressure are plotted in Fig. 4.6. The error bars on the data points are the sample standard deviation of the independent measurements. The smaller error on the data points measured at high pressure may be due to increased SNR of the measured signals, and hence more reliable fits to the resonance signal. The SNR increases at high pressures due to compression of the sample, which increases the density of endohedral fullerenes in the resonator. Since the sample extends beyond the resonator, compression results in additional fullerenes moving into the resonator, where they are interrogated by the applied microwave radiation and contribute to the EPR signal. Fitting the data by a linear relationship, such that $A(P) = A_0 + A_1 P$, gives $A_0 = 22.194(4)\,\mathrm{MHz}$ and $A_1 = 3.5(3) \times 10^{-4}\,\mathrm{Hz\,Pa^{-1}}$. The bracketed number gives the statistical error in the last digit of the quoted value. The straight line fit is simply a first-order approximation to the true fit function, which has an unknown form. However, it appears that the increase in hyperfine coupling with pressure saturates at high pressures. Anticipating the discussion in the next section, this corresponds to a decrease in compressibility and increase in bulk modulus at high pressures.

Dispersive interactions between fullerene cage and nitrogen

A similar pressure-dependent hyperfine coupling has been measured previously for atomic nitrogen generated using a radio-frequency discharge plasma. Here, the hyperfine coupling is proportional to the buffer gas pressure [**HLN62**; **LP63**]. In contrast to the pressure-dependent coupling observed for atoms with unpaired s electrons, which can either be positive or negative, the magnitude of the nitrogen hyperfine coupling always increases with pressure [**Adr62**].

This observation has been explained by treating dispersive van der Waals interactions between the nitrogen atom and the buffer gas atoms as the dominant

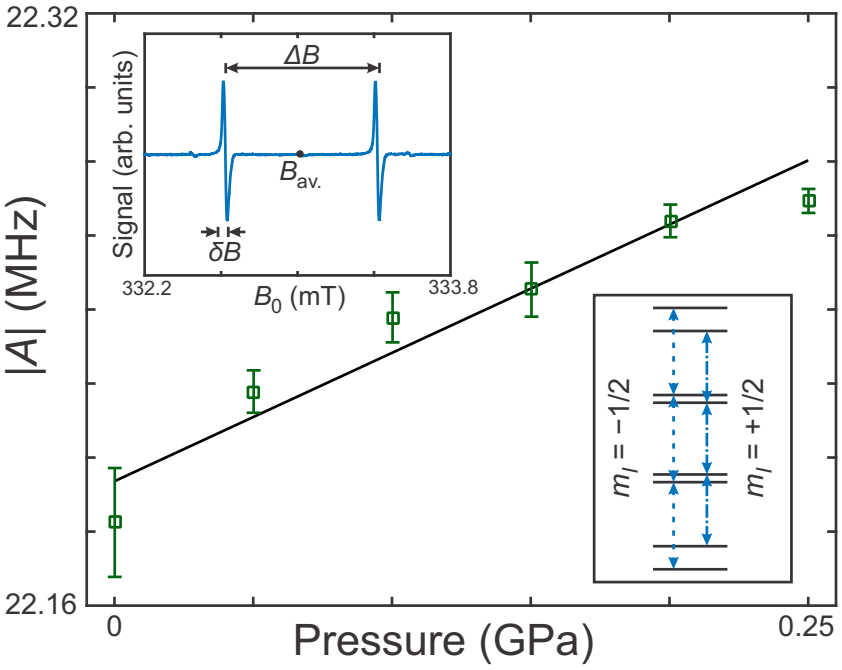

Figure 4.6: Hyperfine coupling constant A as function of pressure. The data (dark green squares with error bars) are fitted by a linear function (solid black line). The data points are the mean value of A at each pressure, and the error bars are the sample standard deviation of this measurement. Upper inset: ESR signal as function of magnetic field at frequency $f \approx 9.334\,\mathrm{GHz}$, demonstrating the hyperfine splitting ΔB, peak-to-peak linewidth δB, and the centre field B_{av}. Lower inset: schematic of high-field energy levels showing the two sets of transition frequencies corresponding to the two values of m_I.

contribution to the increased hyperfine coupling [**Adr62**]. These dispersive interactions lead to spin-dependent excitation of the s electrons from the $2s$ shell to the $2p$ shell, such that the $1s^2 2s^1 2p^4$ electronic configuration is mixed into the ground state configuration $1s^2 2s^2 2p^3$. The resulting spin polarization of the s orbital leads to an increased isotropic hyperfine coupling due to the Fermi contact interaction.

By considering the analogy between nitrogen atoms trapped in fullerene cages and noble gas solids, I test the hypothesis that the increase in hyperfine coupling for the nitrogen endohedral fullerene is due to dispersive interactions between the electrons of the incarcerated nitrogen atom and those of the fullerene cage. This significance of the dispersive interactions is supported by the prediction, obtained using density functional theory, that they are the dominant contribution to the binding energy of the endohedral fullerene system [**Par02**]. There should also be a pressure-dependent exchange coupling between the cage and the p orbitals. However,

because of spherical symmetry this does not mix p and s orbitals directly, and is therefore expected to make a weaker contribution to the hyperfine coupling [**Adr62**]. Secondly, the inner shell s electrons are screened by the outer p shell electrons, minimising their exchange interactions with the cage itself. I therefore model the shift as arising entirely from dispersive interactions.

To apply this model to the endohedral fullerene system, I consider the increase in hyperfine coupling $\Delta A = A - A_{\text{free}}$, where A_{free} is the value for free atomic nitrogen. A perturbative calculation of the van der Waals interaction between atomic nitrogen and a nearby particle predicts the relationship (Eq. (15) of Ref. [**Adr62**]):

$$\Delta A = \frac{k}{R^6}, \tag{4.4}$$

where R is the distance between the nitrogen and fullerene charge distributions. Since the nitrogen atom is located at the centre of the cage [**Pie98**], the distance R is set equal to the fullerene radius. The constant k parameterises the strength of the interaction between the two charge clouds. Performing an ab initio calculation of the value of k is beyond the scope of this work; instead, I treat it as an experimentally determined parameter.

This model is tested by using Eq. (4.4) to predict the pressure shift given theoretical estimates of the bulk modulus B, which parameterises the difficulty of compressing the fullerene cage. The cage is modelled as a sphere with volume $V = (4/3)\pi R^3$ such that the bulk modulus B defined by

$$\frac{1}{B} \equiv -\frac{1}{V}\frac{\partial V}{\partial P} \tag{4.5}$$

is given by

$$\frac{1}{B} = -\frac{3}{R}\frac{\partial R}{\partial P}. \tag{4.6}$$

Generalising Equation 4.4 to consider different power law dependencies such that $\Delta A = k/R^n$, I obtain the expression

$$\frac{d\Delta A}{dP} = \frac{-n\Delta A}{R}\frac{dR}{dP}, \tag{4.7}$$

which can be subsituted into Equation 4.6 to give

$$\frac{d\Delta A}{dP} = \frac{n\Delta A}{3B}. \tag{4.8}$$

Applying the dispersive interaction model [**Adr62**], with $n = 6$, this simplifies to

$$\left(\frac{\partial\Delta A}{\partial P}\right) = \frac{2\Delta A}{B}. \tag{4.9}$$

For ^{15}N@C$_{60}$, I take [**LP63**] $A_{\text{free}} = -14.65\,\text{MHz}$ and $A = -22.35\,\text{MHz}$ and hence $\Delta A = 7.70\,\text{MHz}$. The bulk modulus of crystalline C$_{60}$ samples has been measured experimentally [**Duc91**; **LS94**; **Pin99**; **Lev00**], but the value for an isolated C$_{60}$ molecule under conditions of hydrostatic pressure is only known via simulations [**RR91**; **Woo92**; **Kau10**; **Peó14**; **AM09**]. The simulated values range from 300 to 1200 GPa, with a grouping in the range 700 to 900 GPa [**RR91**; **Woo92**; **Peó14**]. Taking $B \sim 800\,\text{GPa}$, Eq. 4.9 predicts $\partial\Delta A/\partial P \sim 2 \times 10^{-5}$. This value is approximately eighteen times smaller than the value $\partial\Delta A/\partial P = 3.5(3) \times 10^{-4}\,\text{Hz}\,\text{Pa}^{-1}$ determined from the fit in Fig. 4.6. Explaining the measured pressure shift using Eq. 4.9 would require a value $B = 44 \pm 4\,\text{GPa}$.

The discrepancy could have at least three causes. Firstly, it may be that the electronic orbitals of the cage are modified under pressure, changing the effective interaction strength between the unpaired electrons of the nitrogen atom and the cage. Secondly, it could indicate that exchange interaction between the nitrogen and the cage, not captured by the model based on dispersive interactions, in fact contributes significantly to the nitrogen hyperfine coupling. Thirdly, the previous theoretical predictions have overestimated the fullerene's bulk modulus. The value $B = 44 \pm 4\,\text{GPa}$ estimated from the measurements presented here is outside the range of theoretical predictions for the bulk modulus of isolated fullerenes, but is closer to the value of a fullerite crystal. The bulk modulus at room temperature for fullerite crystals comprised of C$_{60}$ has previously been measured as lying within the range $5 \lesssim Blesssim20\,\text{GPa}$ [**Duc91**; **LS94**; **Pin99**; **Lev00**]. The bulk modulus of such a crystal is determined by the intermolecular forces rather than the modulus of the cage; since these forces are weaker than the rigid carbon–carbon bonds of

the cage itself, this underestimates the modulus of isolated molecules. However, the predictions for bulk modulus of an isolated C_{60} molecule themselves cover a wide range, which may indicate a need for further modelling. One source of uncertainty in the modelling is the effect of the solvent, which is expected to modify the molecule's bulk modulus [**AM09**]. In particular, the effect of toluene solvent has not yet been modelled. This may affect the modulus by changing the bond orbitals, and hence the rigidity of the cage.

Repulsive interactions

In addition to the $1/R^6$ dispersive potential discussed above, which models attractive van der Waals interactions, I also consider repulsive interactions for the sake of completeness. Intermolecular interactions are often modelled using Lennard–Jones potentials [**Jon24**], which include both attractive and repulsive terms. The most common Lennard–Jones potential is the "12–6" potential [**MR77**]. In addition to the attractive $1/R^6$ term, which is the term considered above, this potential also has a repulsive $1/R^{12}$ term that models the exchange interactions between electron clouds. If the increase in hyperfine coupling is instead proportional to this repulsive term, the relationship between $\partial\Delta A/\partial\Delta P$ and bulk modulus is therefore given by

$$\left(\frac{\partial\Delta A}{\partial P}\right) = \frac{4\Delta A}{B}. \tag{4.10}$$

Using the value of $\partial\Delta A/\partial\Delta P$ derived from the fit to the data presented in Figure 4.6, the bulk modulus is estimated to be 88 GPa. Naturally, since the power has only increased by a factor of two, the estimated value of bulk modulus remains far lower than the theoretical value. It is, however, closer to the theoretical value.

Empirical model

The endohedral fullerenes N@C_{60} and N@C_{70} provide a useful test case for investigating how hyperfine coupling varies with radius. The C_{60} cage is a truncated icosahedron, but for the purposes of this discussion I will treat it as a sphere with radius $R = 0.348$ nm [**Buc01**]. The C_{70} cage is ellipsoidal, with semi-major axis $r_M = 0.39$ nm and semi-minor axis $r_M = 0.35$ nm [**Buc01**]. Assuming that

the C_{70} cage is tumbling rapidly relative to the characteristic relaxation times of the electron spin and the time period of one microwave oscillation, the p orbitals experience an average radius

$$\bar{r} = \frac{1}{2}\sqrt{3r_m^2 + r_M^2} = 0.36\,\text{nm}. \tag{4.11}$$

The isotropic hyperfine coupling for $^{14}N@C_{60}$ and $^{14}N@C_{70}$ is $A_{60} = 15.88\,\text{MHz}$ and $A_{70} = 15.13\,\text{MHz}$, respectively [**KND03**]. These values are larger than the value for free ^{14}N, $A = 10.45\,\text{MHz}$ [**HB54**], by $\Delta A_{60} = 5.43\,\text{MHz}$ and $\Delta A_{70} = 4.68\,\text{MHz}$, respectively. This reduction in hyperfine coupling for the $N@C_{70}$ molecule relative to $N@C_{60}$ reflects the larger average radius of the C_{70} cage compared to the C_{60} cage.

By taking these values as data points in the $(r, \Delta A)$ parameter space, I estimate the bulk modulus by comparing the experimentally measured value of $d\Delta A/dP$, and hence $d\Delta A/dR$, with the change in hyperfine coupling for a known change in radius determined from the cases of $^{14}N@C_{60}$ and $^{14}N@C_{70}$. Doing this requires a function that describes how the hyperfine coupling changes with pressure between the two datapoints defined by the cage radius and hyperfine coupling of $^{14}N@C_{60}$ and $^{14}N@C_{70}$. I investigate the effect on hyperfine coupling for different test functions joining these two points. These functions include a linear function joining the two points, and functions that obey the same power law dependencies as given above.

Empirical model: linear dependence on cage radius

I start by assuming the simplest possible case, in which the hyperfine coupling is linearly related to the cage radius. Here, the increase in hyperfine coupling is given by

$$\Delta A = mr + c, \tag{4.12}$$

where the gradient

$$m = \frac{\Delta A_{70} - \Delta A_{60}}{\bar{r} - R} \tag{4.13}$$

and the intercept

$$c = \frac{R\Delta A_{70} - \bar{r}\Delta A_{60}}{R - \bar{r}}. \tag{4.14}$$

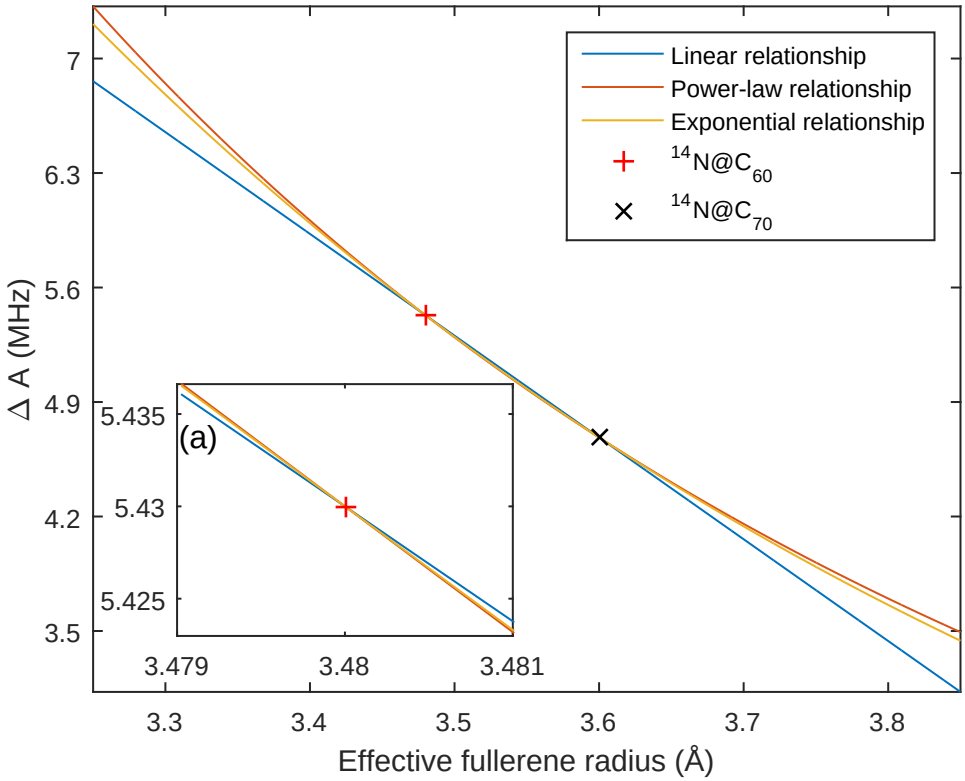

Figure 4.7: Plot showing proposed functions for increase in hyperfine coupling as a function of radius. The constant parameters used in the functions are fitted to the ^{14}N@C$_{60}$ datum (red cross) and ^{14}N@C$_{70}$ datum (black "x"). The inset (a) shows a zoom-in on the vicinity of the ^{14}N@C$_{60}$ datum, which shows that the power-law and exponential functions produce similar changes in hyperfine coupling for a given change in cage radius.

Using the parameters detailed above, the gradient $m = -6.2 \times 10^{16}\,\mathrm{Hz\,m^{-1}}$ and intercept $c = 2.7 \times 10^{7}\,\mathrm{Hz}$. By relating $d\Delta A/dr$ and dr/dP, one can estimate the bulk modulus

$$B = -\frac{R}{3} m \frac{1}{d\Delta A/dP} \tag{4.15}$$

with R the initial radius of the fullerene cage prior to compression. The hyperfine pressure shift coefficient must be adjusted to account for the difference in hyperfine coupling between ^{14}N and ^{15}N. I assume that, since the change is a relative change, this difference is given by

$$\frac{dA(^{14}\mathrm{N})/dP}{dA(^{15}\mathrm{N})/dP} = \frac{A(^{14}\mathrm{N})}{A(^{15}\mathrm{N})}. \tag{4.16}$$

Solvent	ϵ_r	μ (D)	$\lvert A\rvert$ (MHz)
Toluene	2.38	0.375	22.247(2)
Carbon disulfide	2.63	0	22.240(7)
Chlorobenzene	5.69	1.69	22.253(5)

Table 4.1: Hyperfine coupling at room temperature and pressure in solvents with different dielectric constants ϵ_r and dipole moments μ. Values of the dielectric constant are given for room temperature and atmospheric pressure [**Hay14**]. The bracketed number gives the one standard deviation error calculated by taking the sample standard deviation of six measurements.

Given the fitted of value of the pressure shift value for ^{15}N, $d\Delta A/dP = 3.5 \times 10^{-4}\,\mathrm{Hz\,Pa^{-1}}$, the pressure shift for ^{14}N should be $2.5 \times 10^{-4}\,\mathrm{Hz\,Pa^{-1}}$. Using this value, the bulk modulus $B \approx 29\,\mathrm{GPa}$.

Empirical model: power-law dependence on cage radius

I now return to the power law relationships that model the attractive van der Waals forces and the repulsive exchange forces. These are fitted to the data for ^{14}N@C$_{70}$ and ^{14}N@C$_{70}$. Here, I take

$$\Delta A_{60} = \frac{k}{R^n} \tag{4.17}$$

$$\Delta A_{70} = \frac{k}{\bar{r}^n} \tag{4.18}$$

to find the values of the numerical prefactor k and the exponent n. Solving these equations gives

$$n = \frac{\log(\Delta A_{60}/\Delta A_{70})}{\log(\bar{r}/R)} \tag{4.19}$$

$$\log(k) = \frac{\log(\Delta A_{70})\log(R) - log(\Delta A_{60})\log(\bar{r})}{\log(R) - \log(\bar{r})}. \tag{4.20}$$

Substituting in the experimental data, and replacing $d\Delta A/dP$ with the rescaled value, gives $n = 4.37$ and $\log(k) = -79.6$. Using this value of n in Equation 4.8 leads to an estimate of bulk modulus $B \approx 45\,\mathrm{GPa}$.

Solvent and solvation effects

The most direct interpretation of the pressure dependence is that the nitrogen wavefunction is modified by compression of the cage. However, for some dissolved radicals, the hyperfine coupling constant depends on the solvent due to interactions between the solvent molecules and the unpaired electrons of the radical [**Owe01**; **CR83**; **LLA64**; **Jan82**; **DW70**]. For N@C_{60}, such an effect should be small, since the fullerene cage effectively isolates the atomic nitrogen from the environment [**Din00b**]. However, changes in the electronic properties of the solvent could plausibly alter the electronic properties of the fullerene cage; considering Eq. 4.4, this would correspond to altering k. Therefore, I attempt to exclude the possibility that the pressure-dependent hyperfine coupling reflects changes in solvent properties, such as dielectric constant ϵ_r or molecular electric dipole moment μ, that are known to vary with pressure [**SCF68**; **Mop69**].

At room temperature and atmospheric pressure, toluene has dielectric constant $\epsilon_r = 2.38$ and dipole moment $\mu = 0.375\,\mathrm{D}$ [**Hay14**]. At 0.25 GPa, ϵ_r increases to $\sim$2.6 [**SCF68**], while μ is likely to vary by less than 2% [**Mop69**]. To measure the effect of changes in ϵ_r and μ, I compare the spectrum of ^{15}N@C_{60} dissolved in toluene with those of ^{15}N@C_{60} dissolved in chlorobenzene ($\epsilon_r = 5.69$ and $\mu = 1.69\,\mathrm{D}$) and carbon disulfide ($\epsilon_r = 2.63$ and $\mu = 0\,\mathrm{D}$). The ESR spectra of ^{15}N@C_{60} dissolved in these solvents were measured at room temperature and atmospheric pressure at the X band using a Bruker ER4122-SHQE-W1 resonator and EMXmicro spectrometer. Data from these experiments are presented in Table 4.1.

The data show that the effect of altering the dielectric properties of the solvent is negligible to within experimental error. Moreover, the effect of using different solvents is less than the observed change in hyperfine coupling as a function of pressure, despite varying the dielectric constant and dipole moment by considerably more than the variation achieved by pressurising toluene. The data were obtained using a different spectrometer to the data presented in Fig. 4.6, and the small difference in A between comparable values presented in Fig. 4.6 and Table 4.1 presumably reflects differences in magnet calibration. Such a systematic error does

not affect the validity of the comparison between different solvents shown here. Therefore, I believe that the increased hyperfine coupling at high pressures is likely not caused by pressure-dependent solvent properties.

The solubility of fullerenes in toluene is known to be pressure-dependent [**SF07**]. Since solubility is related to the shell of solvent molecules surrounding the molecule at atmospheric pressure [**WHC14**], it does not seem unreasonable to reverse this logic and hypothesise that applying pressure will modify the arrangement or position of molecules in the solvent shell. If the hyperfine coupling is modified directly by the solvent, or if the cage mediates some solvent molecule–nitrogen interaction, it is possible that the observed pressure shift is due to the effect of changing solvation with pressure. Up to now, I have assumed that the fullerene cage perfectly shields the endohedral nitrogen from the external environment. However, density functional theory (DFT) calculations indicate that the fullerene cage is not a perfect Faraday cage, and approximately 25% of an external electric field penetrates the cage [**DG04**]. It is therefore plausible the electrostatic fields due to the solvent molecule may change the hyperfine coupling, and the magnitude of this may be affected by pressure as it changes the molecule solvation.

It has not been possible to investigate this effect during this thesis. To investigate this possibility, the experiments should be repeated using a solvent other than toluene. If the hyperfine pressure shift is mediated by the solvent–nitrogen interactions directly, rather than via compression of the cage, the magnitude of the effect should depend on the solvent. If instead the shift is dependent solely on the nitrogen–cage interactions, its magnitude should be determined solely by the compressibility of the fullerene cage.

One possible choice of solvent would be chlorobenzene, since it is believed to solvate the C_{60} molecule differently to toluene [**WHC14**], and it can dissolve a large quantity of fullerenes [**Ruo93**]. However, chlorobenzene has a large dipole moment, and hence reduces the quality factor of the resonator, which reduces the SNR of the EPR resonance. Fortunately, this effect should not be significant in the high pressure setup because the volume of sample in the resonator is very low,

and hence little microwave energy is absorbed by the solvent. Therefore, a future experimenter may wish to investigate the hyperfine coupling of $N@C_{60}$ as a function of pressure using chlorobenzene to determine whether or not the influence of pressure on solvation is the cause of the measured pressure-dependent hyperfine coupling.

Hyperfine coupling: conclusions

The observed change in hyperfine coupling is much larger than expected given the predicted modulus of the fullerene cages. Instead, the bulk modulus of the fullerene cage given these measurements is roughly one order of magnitude less than is predicted by DFT calculations. However, it is close to that of fullerene crystals. I considered various models to explain the data. While the model based on repulsive interactions gives the highest bulk modulus, it is still much smaller than the theoretical value. On the other hand, the theoretically motivated $1/R^6$ dependency, which is typical of attractive dispersive interactions, is close to that derived by considering an empirical model based on the hyperfine coupling and radius of $^{14}N@C_{60}$ and $^{14}N@C_{70}$. This supports the hypothesis that the dispersive interaction model, made by analogy with the behaviour of nitrogen atoms in other systems, is the correct explanation for the increased hyperfine coupling in endohedral nitrogen fullerenes compared to free atomic nitrogen.

I also consider the effect of solvent on the hyperfine coupling, though without being able to draw strong conclusions. In particular, a future researcher may wish to investigate changing solvation of the fullerene molecule with pressure as the cause of the apparently pressure-dependent hyperfine.

4.3.2 Linewidth

The non-magnetic spacer made it possible to observe narrow, symmetric resonance signals similar to those previously reported in the literature. The power was adjusted to minimise power broadening, as is shown in Figure 4.8. The linewidth was measured with power $P = 3.1\,\mu$W and modulation amplitude $B_{\mathrm{mod}} = 1\,\mu$T in order to avoid broadening due to saturation and modulation broadening, respectively.

The field domain peak-to-peak linewidth δB, as shown in the upper inset of Fig. 4.6, was determined by fitting the experimental data using the derivative of a Lorentzian. The field domain linewidth for the $^{15}N@C_{60}$ sample dissolved in toluene are plotted in Fig. 4.9. The data are fitted with a straight line such that $\delta B = \delta B(0) + P\delta B'$, with $\delta B(0) = 1.68(3) \times 10^{-6}\,\mu\mathrm{T}$ and $\delta B' = 4.8(2) \times 10^{-9}\,\mu\mathrm{T\,Pa^{-1}}$, where the value and one standard deviation error for each parameter are determined from a linear fit to the data. For the sample dissolved in deuterated toluene $\delta B(0) = 1.42(4) \times 10^{-6}\,\mu\mathrm{T}$ and $\delta B' = 4.4(3) \times 10^{-9}\,\mu\mathrm{T\,Pa^{-1}}$. Given the data, it would be preferable to use a smaller modulation amplitude. However, this is not feasible due to the limitations of the experimental hardware, which sets $B_{\mathrm{mod}} = 1\,\mu\mathrm{T}$ to be the minimum possible modulation amplitude. The observed linewidth at zero pressure therefore likely contains some contribution from modulation broadening and B_0 inhomogeneity.

The linewidth contains a contribution proportional to the pressure. Pressure-dependent linewidths are typically governed by spin-exchange processes [**EKM64b**; **EKM64a**; **GPP81**; **MP15**]. However, for $N@C_{60}$ exchange interactions between the incarcerated nitrogen atoms are suppressed by the cage, which prevents overlap of the electronic wavefunctions [**Din00b**]. It is therefore unlikely that spin-exchange processes contribute significantly to the observed linewidth.

For solution samples, such as those measured in this paper, molecular motion can have a significant impact on the paramagnetic resonance linewidth. Increasing the pressure increases the viscosity of the solvent, which serves to modify the various correlation times that parameterise the motion of the molecules. This can lead to increased linewidths due to incomplete averaging of anisotropic interactions.

In this section, I consider the effect of pressure on linewidth via the solvent viscosity. I focus on models that seek to explain the pressure dependent linewidth based on the translational motion of solvent molecules relative to the endohedral fullerene molecules and incomplete averaging of anisotropic interactions in fullerene clusters. In both cases, the proposed decoherence is due to magnetic dipole interactions between spins. Dipolar decoherence due to solvent protons does not provide a satisfactory explanation of the observed pressure dependence. In contrast,

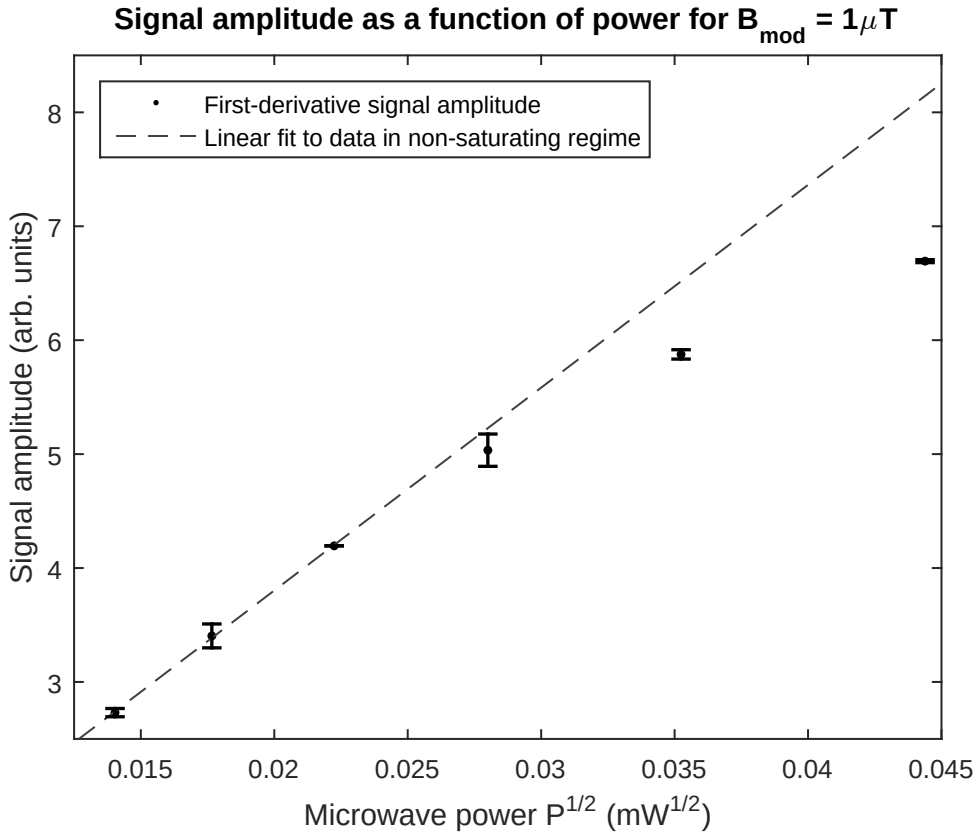

Figure 4.8: Plot of signal amplitude against power for modulation amplitude $B_{\mathrm{mod}} = 1\,\mu\mathrm{T}$. The signal amplitude was taken to be the peak-to-peak amplitude of the first derivative signal, which is calculated separately for the low- and high-field resonances of each trace. The error bars are the standard deviation of the experimental data. The data in the non-saturating regime are fitted with a linear function. This information was used to choose a suitably low applied power such that measurements presented in this thesis were not adversely affected by power saturation and linewidth broadening.

a model based on dipolar interactions between the endohedral nitrogen spins in fullerene clusters provides an excellent fit to the experimental data. However, this model provides fit parameters that represent effective values for an ensemble that is comprised of clusters that, in reality, have a wide range of possible values for cluster radius and spin–spin separation. Given the simplicity of the model, the claim that it accurately and fully represents the microscopic behaviour of the system is not tenable. Nonetheless, it indicates that the model is substantially correct, and provides additional support for observation of fullerene clusters reported in the literature, and previous observations of a concentration dependent linewidth. However, while I believe the rotational model to be in essence correct, I also outline

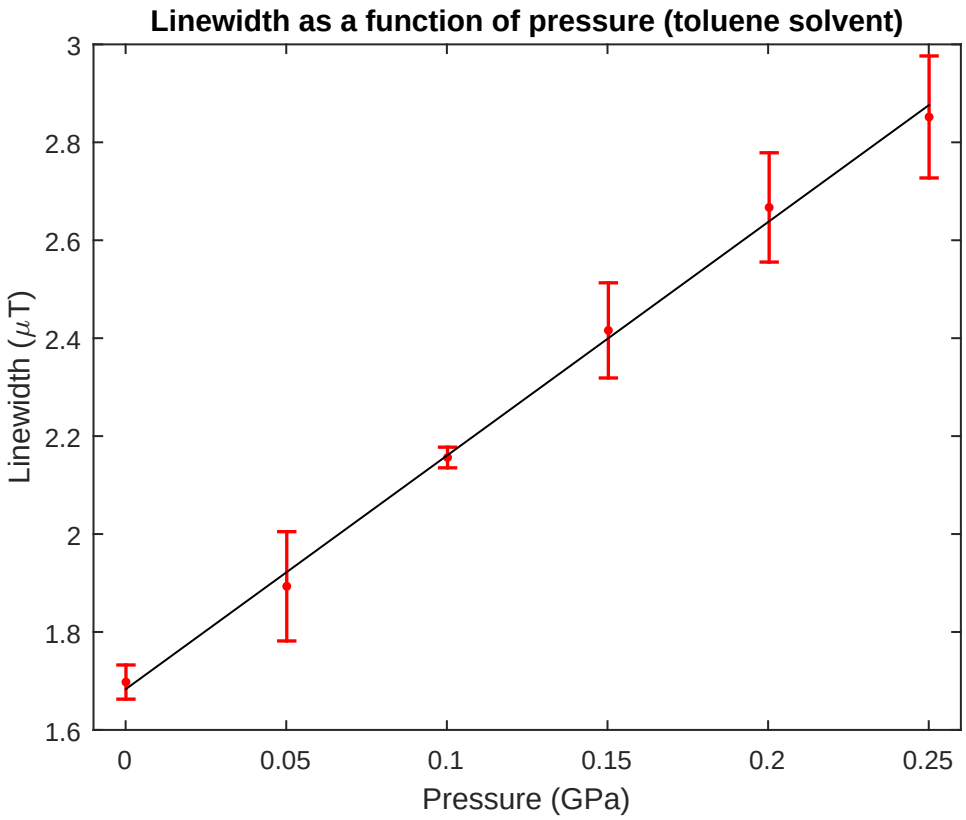

Figure 4.9: Peak-to-peak linewidth as a function of pressure for the $^{15}N@C_{60}$ sample dissolved in toluene. The linewidth was measured for the high-field resonance over two independent experimental runs, and the error bars are the standard deviation of the experimental data. The sample used in these measurements was dissolved in toluene, with a fullerene concentration $\sim 1\,\mathrm{mg\,ml^{-1}}$. The linewidth data (red crosses) displayed in this figure are the average of the linewidths measured for each run. The data are fitted with a straight line (black line).

an alternative hypothesis based on a pressure-dependent inhomogeneous magnetic field. Such a field is proposed to explain the apparent pressure-dependent g factor shift, as outlined in Section 4.3.3. If this field is inhomogeneous, it could lead to a pressure-dependent linewidth via inhomogeneous broadening. However, I have been unable to determine the physical origin of such an effect, given the care taken to ensure that all experimental apparatus in the vicinity of the sample, and particularly moving parts such as the piston, are as non-magnetic as possible.

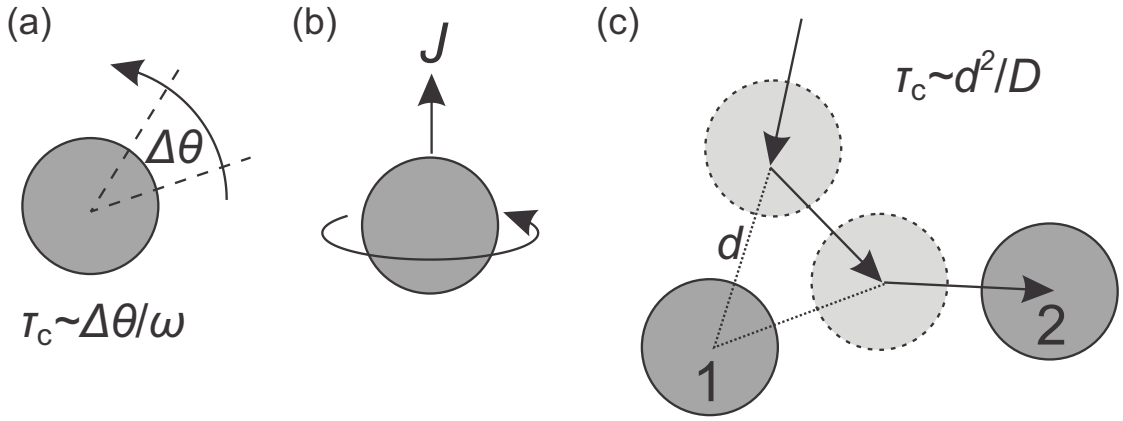

Figure 4.10: Figure explaining relevant correlation times. The fullerenes or clusters of fullerenes are represented by grey spheres. (a) The re-orientational correlation time parameterises how long the rotating system remains in one orientation. (b) The angular momentum correlation time parameterises how long the rotating system remains in a given angular momentum state J. The magnitude and orientation of the angular momentum vector is randomised each time the fullerene collides with another molecule. (c) The translational correlation time parameterises the interaction time between the endohedral fullerene spin and an external spin. This interaction time is governed by how long spin 1 remains within a given distance d of spin 2, and is affected by the diffusion cofficients D of the two objects.

Translational diffusion model

Previously, dipolar interactions between protons in the toluene solvent and the electron spins in the $^{15}N@C_{60}$ molecules have been identified as a significant source of spin decoherence [**Mor07**]. The motion of the toluene solvent protons relative to the endohedral fullerene spins cause a fluctuating magnetic field at the location of the endohedral fullerene spin. Static magnetic fields lead to dephasing of the endohedral nitrogen's electron spin, and fluctuating fields at the Larmor frequency of the protons and electrons lead to resonant transitions that relax the spin. At high temperatures, this relaxation mechanism is less significant than the Orbach mechanism because the field fluctuations induced by the protons vary rapidly over the timescale of one period. However, as the viscosity increases, either via temperature or pressure, the correlation time and decoherence rate increase. Furthermore, compression of the sample decreases the distance between spins, thereby increasing the strength of the dipole interaction. This effect is more significant than the change in spectral density associated with the pressure-dependent translational diffusion time t_D.

Following Morton et al. [**Mor07**], the spin–spin decoherence time T_2 in this model is given by

$$\frac{1}{T_2} = \kappa \frac{c(P)}{d \cdot D(P)} \left[4J(0) + 10J(\omega_e) + 6J(\omega_n)\right], \tag{4.21}$$

where the concentration of protons as a function of pressure is given by $c(P)$, the distance of closest approach between the solvent proton and the endohedral nitrogen is given by d, and the total diffusion constant is given by $D(P)$. The parameter κ parameterises the strength of the magnetic dipole interaction, and is given by

$$\kappa = \frac{16\pi}{405} \gamma_e^2 \gamma_n^2 \hbar^2 I(I+1), \tag{4.22}$$

where γ_e and γ_n are the gyromagnetic ratios of the electron spin and nuclear spin, respectively, and I is the spin of the nucleus. For a proton, $I = 1/2$ and $\gamma_n = 267.522 \times 10^6\,\mathrm{rad\,s^{-1}}$; for a deuteron, $I = 1$ and $\gamma_n = 41.065 \times 10^6\,\mathrm{rad\,s^{-1}}$. The distance of closest approach between the electron spin and solvent proton is set by the radius of the fullerene cage, such that $d = 0.35\,\mathrm{nm}$ [**Buc01**].

The proton spin concentration of the sample is estimated from the density of toluene at room temperature and pressure. Assuming the density of toluene is $0.867\,\mathrm{g\,cm^{-3}}$ [**GJ09**] and the molar mass is $92.14\,\mathrm{g\,mol^{-1}}$, the number density of toluene molecules at room temperature and pressure is $5.67{\times}10^{27}\,\mathrm{m^{-3}}$. Given the chemical composition of toluene is C_7H_8, the number density of protons in the sample is therefore $3.97{\times}10^{28}\,\mathrm{m^{-3}}$. The isothermal compressibility of toluene is used to estimate the increase in spin density with pressure.

$$c(P) = c_0 \exp(\beta(P - P_0)), \tag{4.23}$$

where the compressibility of the toluene solvent $\beta = 90.6 \times 10^{-6}\,\mathrm{atm^{-1}}$ [**RR71**]. The total diffusivity

$$D = D_{C_{60}} + D_{\mathrm{tol}}, \tag{4.24}$$

where $D = D_{C_{60}}$ and D_{tol} are the diffusivities of the C_{60} and toluene molecules respectively. The diffusivity of C_{60} molecules is estimated from the Stokes–Einstein relationship

$$D_{C_{60}} = \frac{k_B T}{6\pi d \eta(P)}, \tag{4.25}$$

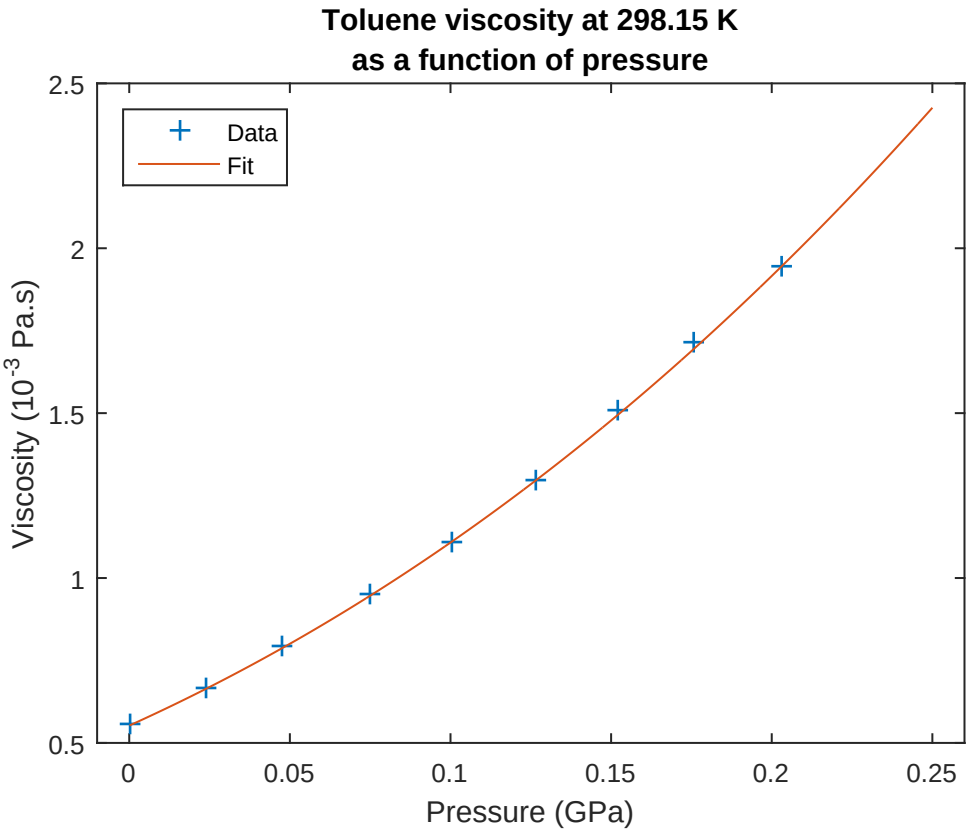

Figure 4.11: Plot of viscosity against pressure. The data, fit parameters, and fit equation are reproduced from Reference [**VC97**]. The relationship between viscosity and pressure is nearly linear over the measured range of pressures. Therefore, any quantity proportional to the viscosity may also appear to have a linear relationship with pressure given a limited signal-to-noise ratio.

given the radius of the fullerene cage $d = 0.35\,\mathrm{nm}$.

At room temperature, the viscosity of the toluene solvent as a function of pressure is given by

$$\eta = \eta_0 \left(\frac{326.146 + P[\mathrm{MPa}]}{326.146 + P_0[\mathrm{MPa}]} \right)^{2.6}, \tag{4.26}$$

where the pressure P and the initial pressure P_0 are given in megapascals [**VC97**]. The initial viscosity of the toluene solvent at room temperature and pressure $\eta_0 = 5.53 \times 10^{-4}\,\mathrm{Pa\,s}$. It can be seen from Equation 4.26 that applying pressure to the sample increases the viscosity of the toluene solvent. Therefore, the reorientational correlation time τ_c of the cluster given by Equation 4.32 increases.

The self-diffusivity of toluene at room temperature $D_0 = 2.32 \times 10^{-9}\,\mathrm{m^2 s^{-1}}$ [**Mor07**]. I estimate the diffusivity of toluene molecules as a function of pressure by assuming

$D\eta(P)/T$ constant, such that

$$D_{\mathrm{tol}} = D_0 \frac{\eta_0}{\eta(P)}, \tag{4.27}$$

assuming that the sample returns to thermal equilibrium after compression. The translational diffusion time, which parameterises the characteristic timescale over which the nitrogen electron spin and proton spin are sufficiently close to interact via the magnetic dipole interaction, is given by

$$\tau_D = 2d^2/D. \tag{4.28}$$

The spectral density functions $J(\omega)$ in Equation 4.21 are given by

$$J(\omega) = \frac{1 + 5z/8 + z^2/8}{1 + z + z^2 + z^3/6 + 4z^4/81 + z^6/648}, \tag{4.29}$$

where $z = \sqrt{2\omega\tau_D}$. Here, the spectral density term within the square brackets of Equation 4.21 decreases by about 10% over the range of applied pressure, as shown in the inset displayed in the top panel of Figure 4.12. However, this is offset by the increase in proton density $c(P)$ and decrease in diffusivity $D(P)$ as the sample is compressed, which increase by approximately 25% and decrease by approximately 80% respectively.

There are no free parameters in this model. Simulating the linewidth contribution as a function of pressure, it is therefore possible to see that the total contribution to the linewidth from the proton-related spin relaxation is less than the measured pressure dependence. If one were to assume that the translational model were the dominant cause of the the pressure dependent linewidth, fitting the data using the distance of closest approach as a fit parameter (see Figure 4.13) gives $d = 0.09\,\mathrm{nm}$, which is considerably less than the radius $R = 0.35\,\mathrm{nm}$ of the C_{60} cage. This is unphysical since the solvent proton cannot pass through the cage, and clearly indicates that this model does not satisfactorily explain the pressure-dependent linewidth.

To investigate whether or not magnetic interactions between the solvent protons and the endohedral fullerenes contribute to the linewidth, the toluene was evaporated

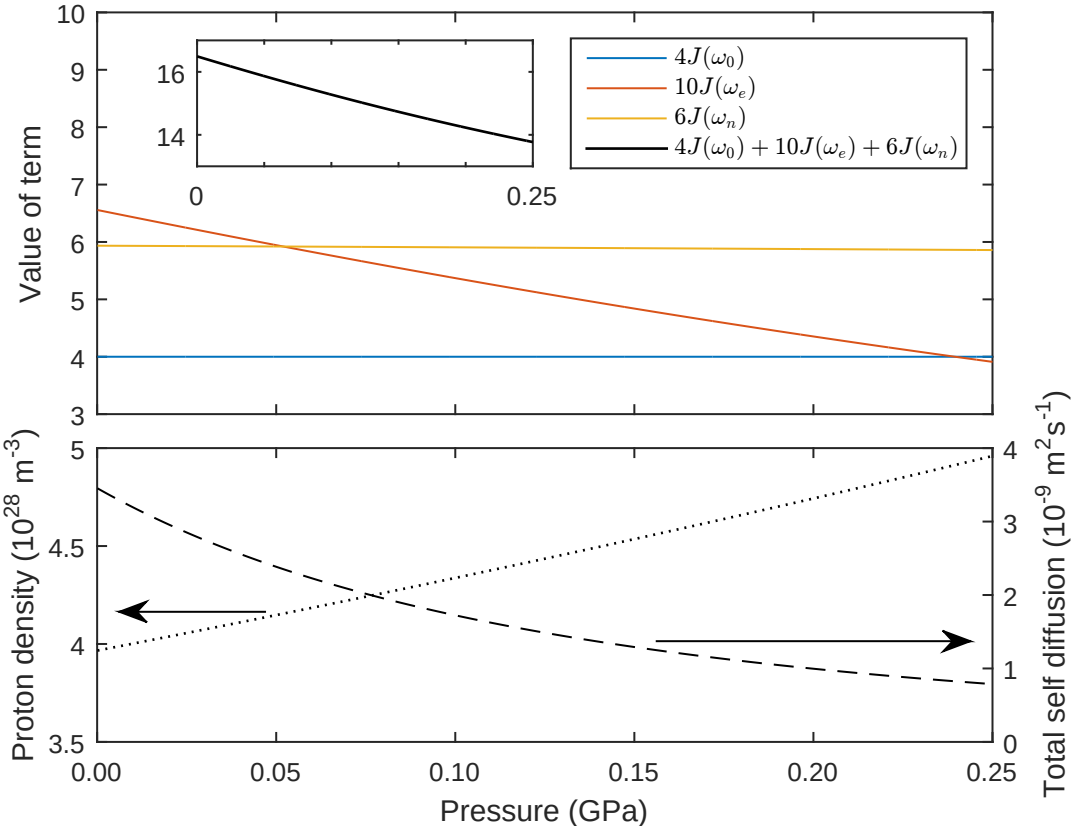

Figure 4.12: Plots of parameters used to calculate the linewidth as a function of pressure in the translational diffusion model. The top panel displays plots of the spectral density functions used in Equation 4.21 as a function of P. The static term is plotted with a solid blue line, and the terms at the electron and proton Larmor frequency are plotted with solid orange and gold lines, respectively. Inset: plot of the sum of the terms (solid black line). The lower panel plots solvent proton density (dotted black line, left axis) and total self diffusivity (dashed black line, right axis) as a function of pressure.

from the sample prior to redissolving the sample in deuterated toluene. Assuming that the number density of solvent molecules, diffusivity, and the viscosity are unaffected by this substitution, and that the spectral density terms in Equation 4.21 are dominated by the $J(0)$ and $J(\omega_e)$ terms, the main effect is on the numerical prefactor κ. Therefore, the expected linewidth due to translational diffusion for the deuterated solvent should be approximately one-fifteenth that of the toluene solvent due to the smaller gyromagnetic ratio of the deuterons compared to the protons. The contribution to the pressure-dependent linewidth

$$\Delta B(P) = \kappa(C_1 + C_2(P)), \tag{4.30}$$

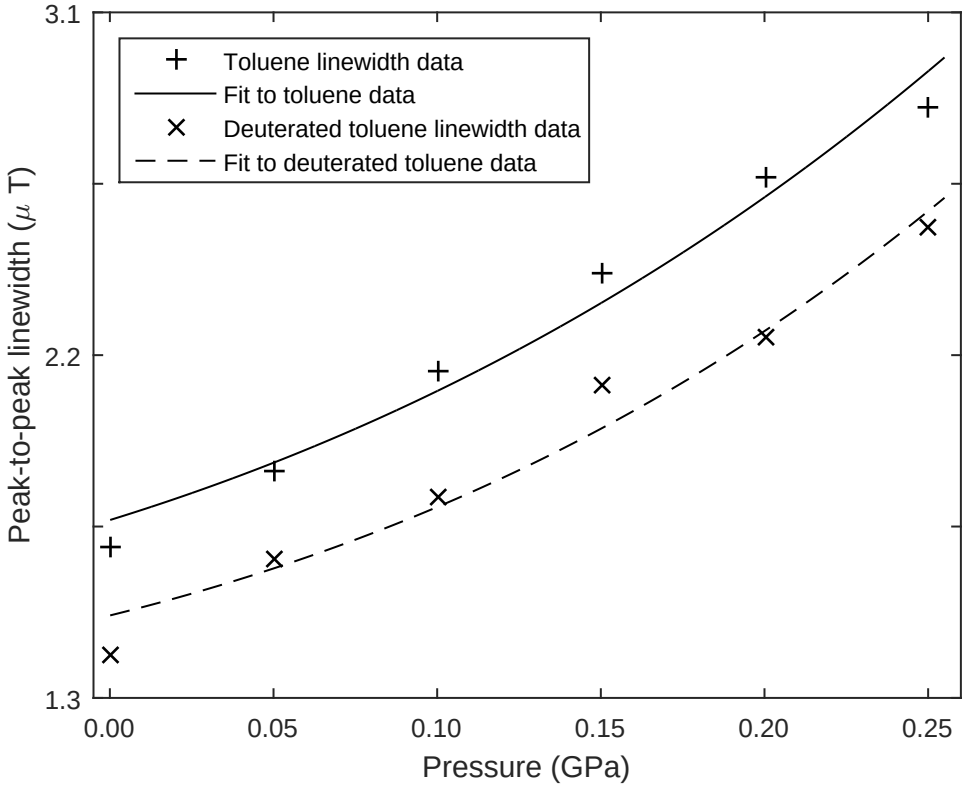

Figure 4.13: Plot of linewidth for toluene (black +) and deuterated toluene (black ×). The normal toluene data points are the average of two independent runs. The data are fitted with using the translational fit model (solid black line and dashed black line, respectively). The fitted distance of closest approach is unphysically small, so this is not a good model.

such that

$$\frac{d\Delta B}{dP} = \kappa \frac{dC_2(P)}{dP}. \tag{4.31}$$

Under the assumptions outlined above, $dC_2(P)/dP$ is the same for both normal and deuterated toluene. The gradient of the curve describing linewidth as a function of pressure should therefore be higher for samples dissolved in toluene compared to those dissolved in deuterated toluene. This is because the pressure dependent terms have the same pressure dependence for both solvents, but the numerical prefactor by which they are multiplied is different. Instead, the gradient is similar and the difference between the linewidths is better fitted by assuming a different constant offset and smaller distance of closest approach than for toluene.

The linewidth of the sample dissolved in deuterated solvents are displayed in Figure 4.13. It can be seen that there is a difference in linewidth for the two cases, but that the rate of change of linewidth with pressure is similar for both. I therefore conclude that the effect of pressure on the translational diffusion of solvent protons via the viscosity of the solvent is not the primary cause of the pressure-dependent linewidth.

Rotational dynamics of fullerenes and fullerene clusters

I also investigated a model based on magnetic dipole interactions between spins within rotating fullerene clusters. Concentrated and highly-pure endohedral fullerene samples are necessary to ensure a high signal-to-noise ratio given the low resonator filling factors. The fullerene concentration of approximately $1\,\mathrm{mg\,ml^{-1}}$ in the sample is above the $0.06\,\mathrm{mg\,ml^{-1}}$ threshold above which fullerenes form clusters rather than remaining dissolved as single fullerene molecules in solution. This reduces the distance between fullerene molecules, and hence the spin–spin separation, below that which would be naively expected given the fullerene concentration in the sample [**Guo16**; **Dat15**; **Mak16**]. Within these clusters, magnetic dipole-dipole or other spin-spin interactions between $N@C_{60}$ molecules could lead to increased relaxation rates and broadening of the resonance line. This is consistent with previous observations of reduced spin coherence times for concentrated high-purity samples compared to dilute low-purity samples [**Mor05d**].

If these clusters are sufficiently large and the purity sufficiently high that the cluster contains multiple $N@C_{60}$ molecules, magnetic dipole coupling between the spins within the cluster may lead to broadening. Since the dipolar interaction is traceless, if the cluster tumbles sufficiently rapidly the interaction will be averaged out, and the resonance will not be broadened. However, if the tumbling rate is slow, i.e. the reorientational correlation time high, the anisotropic nature of the dipolar interaction will lead to broadening of the resonance. In the extreme case, the linewidth would tend toward the rigid lattice limit imposed by dipole–dipole coupling between the spins in the cluster [**BPP48**].

In addition to magnetic dipole–dipole interactions, other anisotropic interactions may be affected by the rotational motion of the spin system. One typically assumes that the symmetry of the C_{60} molecule and the endohedral nitrogen atom ensure that the g-tensor and hyperfine coupling tensor A are isotropic, as given in Equation 4.1. This assumption is consistent with the EPR data in the literature. However, collisions with solvent molecules could plausibly distort the molecular cage such that these terms become anisotropic. In addition, such distortions of the cage have been postulated to reduce the symmetry of the cage such that the Hamiltonian acquires a zero-field splitting term [**Kna97**]. This fluctuating zero-field splitting mechanism was previously thought to be the dominant spin relaxation mechanism for $N@C_{60}$ in well-prepared samples. However, this explanation has since been replaced by an Orbach relaxation mechanism, which fits the temperature dependence of the linewidth better [**Mor06**]. This Orbach mechanism does not have an angular dependence. Therefore, I focus on the magnetic dipole–dipole interactions as the potential origin of a pressure dependent linewidth.

The reorientational correlation time of the cluster can be estimated by the Stokes–Einstein relationship

$$\tau_c = \frac{4\pi\eta a^3}{3k_B T}, \tag{4.32}$$

where η is the viscosity of the solvent, a is the effective hydrodynamic radius of the rotating molecule or supra-molecular cluster, k_B is the Boltzmann constant, and T is the temperature [**BPP48**]. This correlation time gives the characteristic time for the molecule to remain in roughly the same orientation, such that the EPR signal remains constant over the correlation time.

The tumbling rate of the cluster depends on pressure via the viscosity of the solvent. At low pressures, the viscosity of the toluene solvent is low [**Row17**; **VC97**]. The fullerene cluster therefore rotates sufficiently rapidly to average out the dipolar coupling between the spins, leading to a narrow linewidth. At high pressures, however, the viscosity increases, which reduces the rate of rotation and increases the re-orientational correlation time given in Equation 4.32.

Conversely, the increased viscosity at high pressures decreases the time the molecule spends in a given angular momentum state because angular momentum is transferred to the solvent more rapidly [**AK66**]. Therefore, if the linewidth is dominated by a spin-rotational coupling it would tend to decrease at high pressures because the spin-rotational coupling contribution to linewidth is proportional to the angular momentum correlation time. This is in contrast to the experimentally observed data, so I exclude spin-rotational coupling as the dominant source of the pressure-dependent linewidth.

The linewidth from the dipole-dipole interactions can be modeled in two ways: by considering resonant transitions due to the motion of the spins [**FB71**], or by considering dephasing due to static field inhomogeneities at the location of a given spin caused by the magnetic moment of other spins [**BPP48**]. Using the first model, I found unphysically-small fit values for the radius of the postulated fullerene cluster. I therefore focus on the latter approach.

The total linewidth is therefore modelled as the sum of a pressure-independent term $\delta B_{\text{ind.}}$ and pressure-dependent term $\delta B_{\text{dep.}}$ such that

$$\delta B(P) = \delta B_{\text{ind.}} + \delta B_{\text{dep.}}(P), \tag{4.33}$$

and where the field-dependent term

$$\delta B_{\text{dep.}}(P) = \frac{\sqrt{3}}{3}\frac{2\pi}{\gamma}\frac{1}{\pi T_2}. \tag{4.34}$$

Here, the frequency domain full-width half maximum for the Lorentzian function $\Delta f = 1/\pi T_2$, which is converted into a field uncertainty using the gyromagnetic ratio γ. The factor $\sqrt{3}/3$ converts the full-width half maximum into the linewidth as defined by the first-derivative signal peak-to-peak linewidth, which is defined by the points of inflection of the Lorentzian function.

The model developed by Bloembergen, Purcell, and Pound in the early days of nuclear magnetic resonance considers dephasing due to local magnetic field fluctuations caused by spins. [**BPP48**] The model was originally proposed to explain the linewidths of the proton nuclear magnetic resonance (NMR) signal in

water. It is derived by considering the spectral density of magnetic field fluctuations, which arise from rotation of the cluster, up to a maximum frequency defined by the spin-spin dephasing time of the spin system. Here, I apply it to understanding the behaviour of the endohedral fullerene electron spins in fullerene clusters.

In this model, henceforth referred to as the "BPP model", the dephasing time T_2^* obeys the implicit equation

$$\frac{1}{T_2^{*2}} = \frac{3}{\pi} C \tan^{-1}\left(\frac{2\tau_c}{T_2^*}\right), \tag{4.35}$$

where τ_c is the re-orientational correlation time and C is the linewidth due to dipole-dipole broadening as $\tau_c \to \infty$, i.e. the rigid lattice limit [**BPP48**]. The linewidth is initially proportional to correlation time and hence viscosity, but tends asymptotically to the rigid lattice limit as the viscosity and correlation time increase.

The data are fitted using this model, as shown in Figure 4.14. The data were first fitted using a fixed spin-spin separation $r = 3.25\,\mathrm{nm}$ calculated from the purity of the endohedral fullerene sample. The sample is approximately 1% pure. Assuming that the endohedral fullerenes are uniformly distributed among a cubic lattice of C_{60} molecules, the nearest neighbour distance $r = 2\sqrt[3]{100}R$, where R is the fullerene radius. Using this assumption, $r \approx 3.2\,\mathrm{nm}$ and the fit parameters for the $a = 0.71(3)\,\mathrm{nm}$ and $\delta B(P = 0) = 1.4(1)\,\mu\mathrm{T}$, compared to $a = 0.194(7)\,\mathrm{nm}$ and $\delta B(P = 0) = 1.4(1)\,\mu\mathrm{T}$, respectively.

Relaxing the assumption of a fixed spin-spin separation permits an excellent fit to the data. The effective hydrodynamic radius for the averaged linewidth data are $a = 9.4(2)\,\mathrm{nm}$, and the spin-spin separation $r = 11.17(7)\,\mathrm{nm}$. The constant offset linewidth is $1.21(3)\,\mu\mathrm{T}$.

The data points plotted in Figure 4.14 are the average of two independent data sets, each comprising six data points (one measurement at each value of pressure). As such, there are insufficient data to calculate a meaningful error bar. To address this objection, I fit the two data sets independently to show that they give give results that are consistent with the fitted parameters for the averaged data sets. The fit parameters for the first data set are $a = 9(1)\,\mathrm{nm}$, $r = 11.4(5)\,\mathrm{nm}$, and

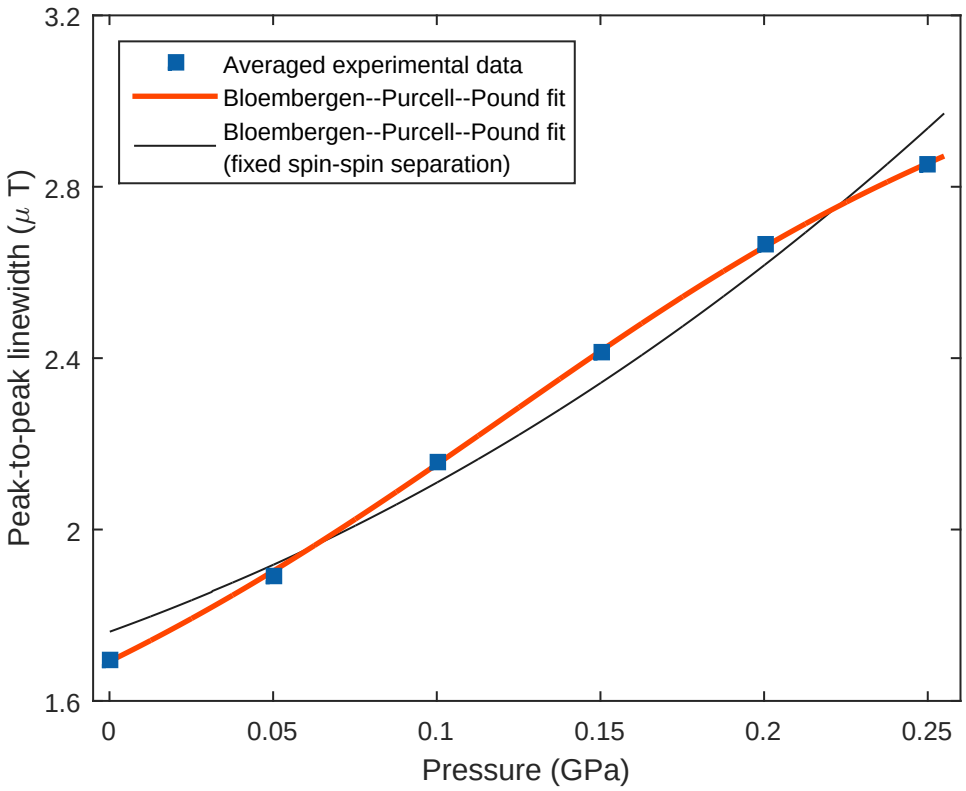

Figure 4.14: Plot of linewidth as a function of pressure and fits to the data. The linewidth data (blue squares) determined from high-resolution EPR traces are fitted using the Bloembergen–Purcell–Pound model of viscosity-dependent decoherence due to dipole–dipole interactions in rotating molecules. The data are fitted by taking either the hydrodynamic radius of the cluster and spin-spin separation as fit parameters (thick orange line), or by fixing the spin–spin separation based on the sample purity and fitting only the hydrodynamic radius (thin black line).

$\delta B(P=0) = 1.2(2)\,\mu$T; the fit parameters for the second dataset are $a = 9.3(7)\,$nm, $r = 10.9(2)\,$nm, and $\delta B(P=0) = 1.2(1)\,\mu$T. Despite the paucity of the data points, the consistence of the fit parameters between the different experimental runs reinforces my belief that this model is substantially correct.

However, the observed spin–spin separation of $r \sim 10\,$nm is larger than the separation expected if the cluster were formed of close packed fullerenes. Such a cluster would have a spin–spin separation of $r \approx 3.2\,$nm given the assumed 1% purity of the sample and the diameter of an individual fullerene. It is possible that the purity is less than assumed due to the uncertainty in the purity of the endohedral fullerene sample provided to me. The predicted spin–spin separation $r \approx 3.2\,$nm

may therefore significantly underestimate the true value. However, to achieve a spin–separation equal to the fitted value $r \approx 11.2\,\mathrm{nm}$ would require a purity $p \approx 0.02\%$, or roughly a factor of forty lower than the assumed purity. It seems unlikely that the purity is so much less than the quoted value, and hence I discount this as the primary explanation for the discrepancy between the predicted spin–spin separation value determined by fitting the data with the rotating cluster model.

The values could be explained by postulating a porous structure for the fullerene clusters, which would reduce the effective spin density in the cluster. The structure of fullerene clusters depends on the formation process [**Mak16**]. Slow aggregation leads to densely packed clusters, whereas mechanical agitation [**Mak16**] and exposure to light [**Dat15**] lead to the formation of fractal clusters. While care is taken to exclude light, due to the photosensitivity of the endohedral fullerene molecules, this is not always possible. In particular, during sample concentration using a rotary evaporator, the sample is both exposed to light and mechanically agitated by bubbling during the solvent evaporation. Furthermore, the $^{15}\mathrm{N@C_{60}}$ sample used in this work was stored under ambient atmosphere after the initial HPLC purification procedure. The fullerene molecules may have oxidised during this storage period, which further promotes the formation of large clusters by forming epoxide bonds between individual fullerenes [**Dat15**].

A plausible alternative explanation is the fact that the linewidth parameter is measured over an ensemble of fullerene clusters. Within this ensemble, there is a distribution of cluster size and cluster arrangement. Therefore, not all clusters contribute equally to the EPR signal. The probability that a cluster comprising N molecules contains n endohedral fullerenes is $P(n) = (1-p)^{N-n} p^n \frac{N!}{n!(N-n)!}$, where p is the purity of the sample. For a cluster of 100 spins with 1% pure sample, the probability of the cluster containing no $\mathrm{N@C_{60}}$ molecules $P(0) = 0.36$, the probability of a cluster containing one $\mathrm{N@C_{60}}$ molecule $P(1) = 0.36$, and the probability of a cluster containing two $\mathrm{N@C_{60}}$ molecules $P(2) = 0.18$. I neglect clusters without any endohedral fullerenes, since they do not contribute to the EPR

signal. I also neglect clusters with more than two endohedral fullerenes, since they are rare and hence contribute little to the total EPR signal.

The linewidth of clusters containing single endohedral fullerenes should approximate that of the isolated endohedral fullerenes. This is because the cage rotates rapidly at room temperature, averaging out any cage–fullerene anisotropic interactions. This also assumes that the endohedral fullerene spin does not interact with spins within the cluster, such as ^{13}C spins, other than $N@C_{60}$ spins. This is justified due to the shielding effect of the cage and the distance between spins. However, in clusters with two $N@C_{60}$ spins, dipole-dipole interactions broaden the EPR resonance signal.

Given the spin purity, it is expected that the majority of clusters therefore are unaffected by any pressure-dependent change to the rotational dynamics. since they contain only one spin-active endohedral fullerene. The contribution of two-spin clusters to the EPR signal will lead to broadening of the summed resonance signal. However, the total broadening of the summed signal will be less than that of the broadening of the two-spin contribution. As the two-spin contribution is broadened, its signal intensity decreases, since the product of amplitude and width is conserved. For this reason, the measured linewidth broadening of the ensemble average underestimates the line broadening for two-spin clusters, and hence overstimates the spin-spin separation relative to the true value. Since the fit parameters for hydrodynamic radius and spin-spin separation are not linearly independent from one another, this may also affect the fitted value of hydrodynamic radius.

Despite these shortcomings, the rotating cluster model does provide a natural explanation of the variation of linewidth with pressure, and why the minimum achievable linewidth is greater than that set by relaxation mechanisms inherent to the molecule itself, such as the Orbach process [**Mor06**]. The narrowest linewidths measured previously required careful sample preparation to inhibit clustering [**Mor07**], which occurs at concentrations above 0.06 mg/mL, and minimise paramagnetic impurities such as dissolved oxygen. Due to the low microwave power applied to the sample in the experiments presented here, power broadening does not

significantly contribute to the measured linewidth. Furthermore, care was taken to minimise any field inhomogeneity caused by the incorporating the high pressure EPR apparatus into the experimental setup. However, it is possible that inhomogeneous environmental magnetic fields, or inhomogeneities caused by imperfections in the electromagnet itself, broaden the resonance.

To further investigate the clustering model, it would be desirable to parameterise the cluster size and morphology for the samples used in these experiments. Such measurements could be performed by dynamic light scattering (DLS) [**Guo16**] and various electron microscopy techniques [**Mak16**], respectively. Alternatively, it would be desirable to perform experiments using a range of concentrations and purities to investigate the different behaviours of the ensembles. In particular, using sufficiently low concentrations that the effect of clustering is negligible, and sufficiently low purities that any clusters contain only one spin, may be of interest. In this case, the linewidth should show a much weaker pressure dependence than is observed using the samples detailed here by eliminating the dipole-dipole broadening. If such an experiment could be performed, but the same linewidth dependence were found, it would be possible to conclusively discount the proposed explanation. However, using such a low concentration in these experiments was not feasible given the small sample volume of the pressure cell and the available sample purity.

4.3.3 g-factor

The EPR spectrum shows the two $^{15}N@C_{60}$ resonances split by the hyperfine coupling, and a clipped EPR signal (central feature) from the LiPc sample. The clipping of the LiPc is because the spectrometer digitiser had insufficient dynamic range (resolution) to record faithfully both the LiPc and $^{15}N@C_{60}$ resonances. Here, I define the resonance field of the asymmetric LiPc signal by the zero-crossing of the resonance. The asymmetry of the EPR signal displayed in Figure 4.15 is consistent with previously observed LiPc EPR signals for x-LiPc crystallites, where x denotes a specific crystal structure [**BTA98**]. However, this is unimportant for this experiment, since the I am primarily interested in seeing how the g factor

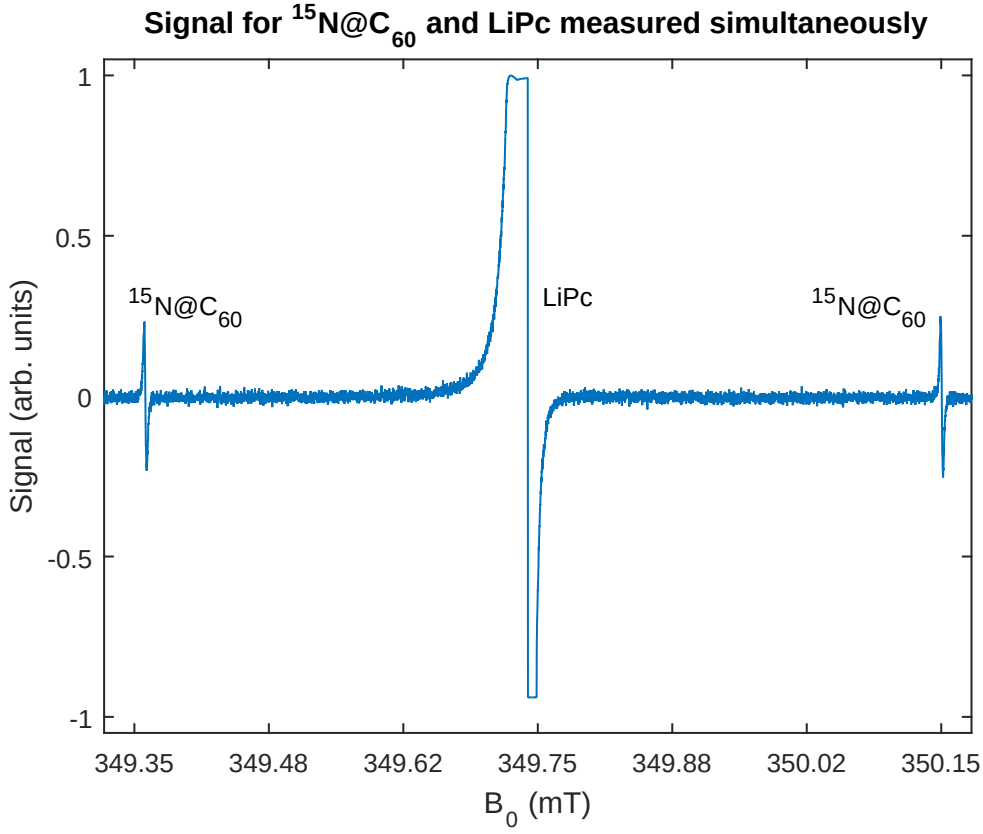

Figure 4.15: Plot of the EPR trace for a simultaneous measurement of $^{15}N@C_{60}$ and the lithium phthalocyanine (LiPc) g marker. The EPR signal from the LiPc sample is very intense due to the sample's high spin density and narrow linewidth. Given the experimental parameters, which were were chosen to optimise the EPR signal from the $^{15}N@C_{60}$ sample, the signal from the LiPc sample overwhelms the detector and is clipped. The LiPc signal is asymmetric, but this is observed even for experimental parameters optimised for the LiPc sample. For the purposes of this work, the resonance field of the LiPc signal is taken to be the zero-crossing.

changes with pressure rather than making a highly precise determination of the absolute g factor. Figure 4.16 displays the electron g factor of the endohedral fullerene sample and a lithium phthalocyanine g marker as a function of pressure applied by the barocycler. The g factor of the $^{15}N@C_{60}$ molecule is approximately 1×10^{-4} lower than that of LiPc, which is taken to be $g = 2.00214$. The measured g factor of $^{15}N@C_{60}$ is therefore in excellent agreement with the best available data for $^{14}N@C_{60}$ obtained in the literature [**Wit18**].

The data presented in Figure 4.16 show that the g factor of both the LiPc sample and the endohedral fullerene sample increase non-linearly as the system is

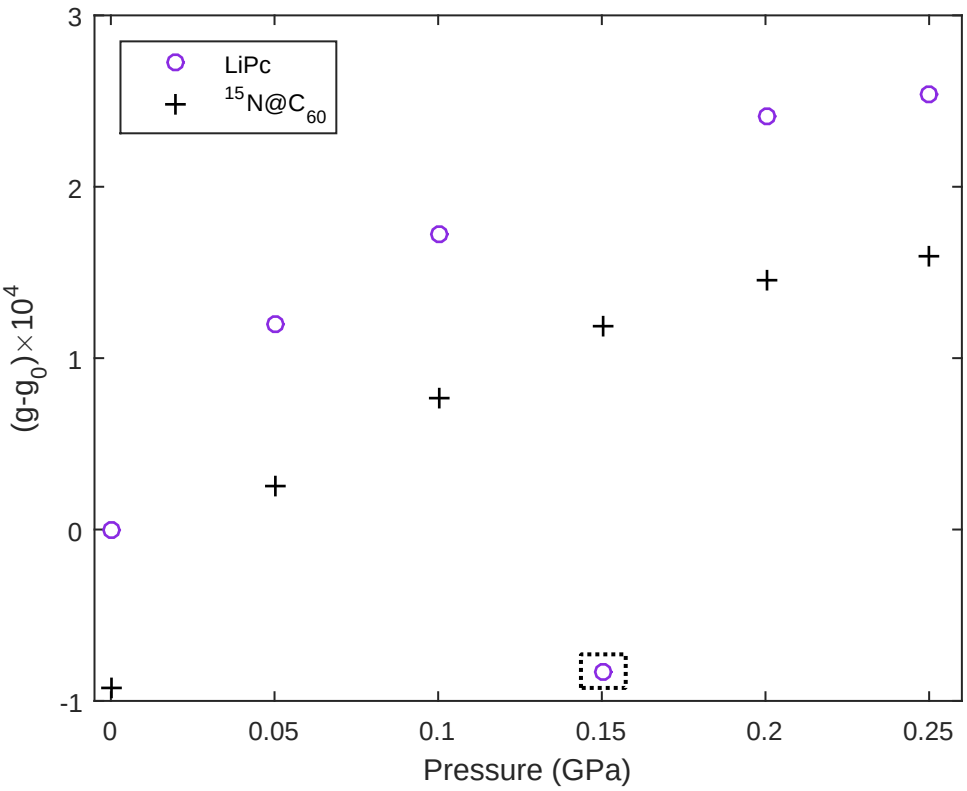

Figure 4.16: Plot of $g - g_0$ as a function of applied pressure for lithium phthalocynanine (purple circles) and $^{15}N@C_{60}$ (black crosses). An anomalous datum for the LiPc sample has been highlighted by a dashed black rectangle. The reference value g_0 is the measured g factor for the lithium phthalocynanine sample measured at zero applied pressure. Since the LiPc sample is outside the pressure chamber, and hence remains at ambient pressure, the change in g factor must be due to spurious effects, rather than modification of the g factor by compression of the fullerene cage and distortion of the unpaired electron orbitals. One candidate explanation is a pressure-dependent magnetic field shift.

pressurised. However, as shown in Figure 4.5, the LiPc sample is within a capillary rather than the YSZ pressure cell. The apparent shift in g factor is therefore not caused directly by the effect of pressure on the endohedral fullerene spin system, since I observe a similar shift for both the pressurised endohedral fullerene sample and the unpressurised LiPc sample. Moreover, the functional form of the the increase with pressure is similar for both samples, indicating that the likely share a common cause.

Assuming that the apparent shift in g is not a true shift, but is instead an artefact caused by flawed experimental design that gives rise to a systematic error in the experiment, Equation 4.3 implies the observed effect is likely caused by a

pressure-dependent magnetic field shift or error in the frequency counter.

To the best of my knowledge, there is no plausible causal link between increasing the pressure and an error in the frequency counter. However, is conceivable that a moving, magnetized object gives rise to a pressure-dependent field, and this shift is responsible for the g factor shift. If indeed there is a pressure-dependent field shift, and this field is inhomogeneous, it may also explain the pressure-dependent linewidth. The high pressure extender was specifically designed to be non-magnetic. In particular, the moving piston is fabricated from copper. It is therefore hard to find the physical origin of the pressure-dependent field. Although care was taken to ensure the mechanical stability of the apparatus by firmly clamping the extender between the pole pieces of the electromagnet used to apply the B_0 field, it remains possible that the samples moved slightly during the pressurisation process. If the field is slightly inhomogeneous, this could give rise to an effect that would look like a pressure-dependent field.

4.4 Conclusions

I have measured a pressure dependent hyperfine coupling, with $dA/dP = 3.5 \times 10^{-4}\,\mathrm{Hz\,Pa^{-1}}$, which I explain via dispersive interactions between the electrons of the nitrogen atom and the cage. Such interactions are the dominant cause of the increased hyperfine coupling for nitrogen atoms trapped in an inert lattice, which provides the closest experimental analogue for the endohedral fullerene spin system investigated in this thesis. Furthermore, density functional theory calculations predict that these dispersive interactions are the dominant contribution to the molecular binding energy. As the strongest interaction between the electrons of the encapsulated nitrogen atom and the cage, they therefore likely play a significant role in modifying the electron wavefunction and hence the hyperfine coupling. However, using the model in conjunction with theoretical predictions of the fullerene's compressibility predicts a smaller pressure shift than is observed experimentally, which may indicate that considering only dispersive interactions between the nitrogen atom and the cage is insufficient.

To understand this better, I estimate the bulk modulus of fullerene cages from the pressure-dependent hyperfine coupling coefficient using various approaches, and compare these estimates against the literature values derived from theoretical calculations. I start by estimating the bulk modulus using the dispersive interaction hypothesised to dominate the pressure shift. I also use empirical approaches based on literature values for the radius and hyperfine coupling for N@C_{60} and N@C_{70}, in conjuction with estimates of how the hyperfine coupling should change as a function of radius between these two data points. The value of bulk modulus deduced using these approaches is much less than theoretical values for the bulk modulus determined from density functional theory and molecular dynamics-based modelling of the fullerene cage's mechanical properties. This may indicate deficiencies in the modelling, systematic errors in the experiment, or that the assumption of isotropic hydrostatic equilibrium is unwarranted. For example, at the molecular scale, bending of the carbon-carbon bonds and distortion of the cage may require less force than compression. This could be due to the breakdown of the assumption that the fluid is an isotropic, homogeneous continuum. Instead, at the microcopic level, the collisions are not isotropically distributed over short time scales. Therefore, the cage may distort and bend asymmetrically, rather than experiencing isotropic compression. If bending bonds is easier than compressing them, this may allow for a greater decrease in effective radius for a given applied force, and hence a smaller apparent bulk modulus.

The estimated bulk modulus is much closer to the value measured for fullerene crystals, which raises another possibility for the low value of bulk modulus. For a fullerene crystal, the bulk modulus is dominated by the intermolecular forces. This may indicate that the hyperfine pressure shift coefficient measured in this chapter reflects the strength of the intermolecular forces between the cage and solvent molecules rather than the compressibility of the cage itself. DFT calculations indicate that, although the cage is often thought to shield the endohedral nitrogen from the external environment, electric fields may penetrate the cage. Therefore, if there is an electrostatic interaction between the solvent molecules and the endohedral

nitrogen that affects the hyperfine coupling, the observed pressure shift may reflect the strength of the repulsive interactions between the cage and the solvent molecules. It may be possible to confirm or reject this hypothesis by measuring the hyperfine coupling as a function of pressure using different solvents, since the solvation of the fullerene cage as a function of pressure is known to depend on the solvent. I tried to investigate a potential solvent dependence by measuring the hyperfine coupling at atmospheric pressure. However, the results were inconclusive, and it remains necessary to do a pressure dependent study using a different solvent. One particularly promising solvent is chlorobenzene, since it is known to have a different solvation as a function of pressure.

In addition to observing a pressure-dependent hyperfine coupling, I also measure a pressure-dependent linewidth and g factor. I investigate the linewidth by considering various different broadening mechanisms, and find that the data are well fitted by a model based on the dipole–dipole interactions between different fullerene spins within fullerene clusters. Here, the pressure modulates the linewidth via the viscosity of the solvent, which changes the rotational rate of the fullerene cluster and the degree to which the anisotropic dipolar couplings are averaged out. However, the fit parameters for this model imply a spin-spin separation that is considerably larger than that which is predicted by considering the purity of the sample and assuming that the fullerenes are densely packed. This could potentially be explained by assuming a "lacy" cluster. Future work could focus on characterising the cluster size using alternative experimental techniques, such as dynamic light scattering, or by reducing the sample concentration and spin purity to minimise clustering and mitigate its adverse effects, respectively. This latter approach would, however, be extremely challenging due to the need to achieve sufficient SNR to draw reasonable conclusions.

Another possible explanation for the observed line broadening as a function of pressure is if the sample is subject to an inhomogeneous magnetic field that is somehow related to the applied pressure. However, given the low susceptibility piston, it is hard to conceive of a moving, magnetized object near the sample that could

cause such a shift. Nonetheless, it is not possible on the basis of the measurements made in this work to fully exclude such a possibility. Moreover, it would be consistent with the observed change in g factor as a function of magnetic field.

Regardless of whether the pressure dependent linewidth arises from dipolar broadening or an inhomogeneous pressure-dependent field shift, the field-independent clock transition in the low-field spectrum of $^{15}N@C_{60}$ [**Har17**] should mitigate linewidth broadening due to magnetic interactions [**Wol13**; **Shi16**]. However, the clock transition does not protect against all dipolar decoherence mechanisms [**Wol13**]. As such, the minimum linewidth and hence maximum achievable stability of a fullerene clock may be constrained by the need to compromise between increasing spin density to increase signal intensity and avoiding line broadening due to dipolar interactions between endohedral fullerene spins. While this is true for solution samples generally, the evidence for fullerene clustering presented in this chapter means that this problem is more pressing. The dipolar broadening is sensitively dependent on the spin-spin separation, and the clusters lead to higher local spin densities than if the endohedral fullerenes were distributed homogeneously and isotropically throughout the sample volume. To successfully implement an endohedral fullerene clock may therefore require a better understanding of the processes that drive fullerene clustering, with a view to finding ways to avoiding clustering. This might be achieved by, for example, optimising the solvent since different clustering behaviours have previously been observed for different solvents. Another route to mitigating the effect of clustering would be to find a low-viscosity solvent. This would ensure that the correlation time is low and that any dipolar broadening within the cluster is minimised by rotational averaging.

From the perspective of employing endohedral fullerenes as the frequency reference within a portable atomic clock, the most important result in this chapter is the small magnitude of the change in hyperfine coupling coefficient with pressure. While the effect is too small to effectively tune the hyperfine coupling in order to compensate for temperature fluctuations and their effects on the clock frequency, it ensures that the clock will be insensitive to atmospheric pressure fluctuations.

5
Conclusions and outlook

Contents

5.1 Conclusions

In this thesis, I have investigated the EPR properties of $^{15}N@C_{60}$, focusing on those properties that are relevant to its potential use as a frequency reference in future miniaturised atomic clocks. In particular, I sought to verify the existence of a clock transition in the low-field EPR spectrum of $^{15}N@C_{60}$. Such a transition is important for the use of endohedral fullerenes to minimise sensitivity to magnetic field fluctuations, which have to potential to significantly degrade the performance of any such clock. I also look at the sensitivity of the hyperfine coupling, and hence the clock frequency, to pressure fluctuations.

To achieve this goal, I designed and built a low-field EPR spectrometer, since the instrumentation is not commercially available. Various aspects of spectrometer design are discussed in Chapter 2, with more specific details given in Chapter 3. In Chapter 3, I present low-field data confirming and characterizing the clock transition.

I confirm that the spin Hamiltonian reported previously, which is known to be valid at high fields, accurately describes the low-field EPR spectrum of $^{15}N@C_{60}$.

Using the experimental data presented in Chapter 3, I estimate the frequency-domain linewidth at the clock field. Using this linewidth ($\delta f \approx 100\,\mathrm{kHz}$), the clock transition frequency ($f_{\mathrm{clock}} \approx 38.6\,\mathrm{MHz}$), and the measured SNR (SNR≈ 2 in a 1 Hz bandwidth), I estimate the stability of a fullerene-based atomic clock. The value I obtain, assuming no further improvements, is $\sigma_y \approx 1.3 \times 10^{-3}\,\tau^{-1/2}$.

Such an atomic clock would be too unstable for practical use, and certainly not competitive with any existing technology regardless of any potential advantages with regards to miniaturisation. I therefore consider how one might improve the system to achieve better results. One approach would be to optimise the instrumentation used to interrogate the resonance. This might allow for a few orders of magnitude improvement. However, I think the scope for improvements in instrumentation necessary to make an fullerene-based frequency standard competitive with existing atomic frequency standards, even portable ones, is limited. Therefore, I also consider how the sample itself may be optimised. For example, one might try to improve the SNR by increasing the spin density in the sample. This could be achieved by using a higher purity sample, or by changing the solvent. However, it is far from clear that trying to improve the SNR in such a manner would lead to improvements in the stability of the clock. Firstly, increased spin-spin interactions may broaden the line and limit overall improvements in the SNR since, for a given number of spins, the signal amplitude is inversely related to linewidth. While the clock transition should mitigate the effect of dipolar interactions, it does not eliminate it completely. Secondly, such line broadening would also compromise the transition quality factor, which directly affects the stability. Another approach would be to pick an endohedral fullerene with a larger hyperfine coupling, such as $P@C_{60}$. However, even this is but an incremental improvement: the clock transition frequency for $P@C_{60}$ is less than one order of magnitude greater than that of $N@C_{60}$, and, as such, it is hardly likely to be a "game changer" in terms of the competitiveness of endohedral fullerene-based frequency standards.

The major limitation of the study of the low-field spectrum presented in Chapter 3 is the lack of reliable measurements of the coherence and spin-relaxation times. This is lamentable not only from a scientific perspective, but also from a technological perspective: the coherence time determines the narrowest achievable linewidth in the absence of inhomogeneous broadening that could possibly be mitigated via better engineering. The SNR was too low to permit a detailed characterization of coherence times at the clock transition using power saturation methods in a continuous-wave experiment. Furthermore, limitations were imposed by the field-swept nature of the measurements I performed. To solve these problems, future works should measure the coherence time at the clock field as a function of sample concentration and purity. This would be facilitated by developing further the low-frequency pulse spectrometer I built, such that the sensitivity is sufficient to detect the weak $^{15}N@C_{60}$ signal.

In addition to the significant experimental limitations imposed by the broad linewidth and low frequency nature of the clock transition characterised in Chapter 3, the hyperfine coupling of endohedral fullerenes is known to be strongly temperature dependent. I therefore sought to find an experimental parameter by which I could tune the hyperfine coupling to offset this effect. The temperature-dependent hyperfine is thought to be caused by the temperature-dependent mean square displacement of the nitrogen atom about the cage centre, which increases with temperature due to the increased thermal energy of the nitrogen atom. This in turn increases the strength of the nitrogen–cage interactions that increase the nitrogen hyperfine coupling above the value for a free nitrogen atom. Reversing this reasoning, I hypothesised that compressing the fullerene cage would also serve to increase the hyperfine coupling. Depending on the strength of the effect, I hoped that it might serve as a tunable parameter to compensate for temperature fluctuations. For example, one might design a sample holder with the correct thermal expansion coefficient that the thermal- and pressure-dependent contributions to the hyperfine coupling for the complete system would offset one another—a "thermal clock transition".

The experimental data and analysis for the pressure-dependent hyperfine coupling experiments are presented in Chapter 4. A limitation of this study is that the hyperfine was deduced from cw measurements, rather than directly through electron–nucleus double resonance (ENDOR). This was due to the absence of suitable high-pressure ENDOR apparatus. The observed pressure dependence is too small to be practically useful for offsetting the influence of temperature on the hyperfine coupling. However, it does enable an estimate of the bulk modulus of the C_{60} cage. This is particularly exciting since, to the best of my knowledge, there are no measurements of the bulk modulus of isolated fullerenes. The estimates of bulk modulus (B ∼40–90 GPa) presented here are much lower than the values predicted in the literature for isolated fullerene cages. It is, however, much closer to the experimentally-determined value of bulk modulus of fullerene crystals given in the literature.

The discrepancy may be a limitation of the DFT calculations, or it may be that the fullerene is not accurately represented as a single isolated fullerene. For example, the linewidth measurements are best fitted by a model that assumes the fullerenes cluster together. Nonetheless, I do not believe that the measured fullerene bulk modulus is simply another measurement of the crystal bulk modulus. The bulk modulus of a fullerene crystal reflects the strength of the interactions between the fullerene cages. In this thesis, however, I deduce the bulk modulus from the processes that depend on the radius of the fullerene cage; as such, I believe this should represent an accurate estimate of the bulk modulus of the fullerene cage itself. An alternative that I believe has some merit is that the fullerene may deform anisotropically. The theoretical estimates assume that the fullerene is compressed isotropically, and that the carbon–carbon bonds in the cage are compressed. However, it may be easier to bend the bonds than compress them; by considering an analogy with graphene, this would correspond to rolling a graphene sheet rather than compressing it in a plane. If so, this may lead to a much higher bulk modulus and bring it in line with the measurements presented in this thesis. By considering the solvent at a molecular level, we can clearly see that it is not a homogeneous, isotropic continuum. Instead, it is made up of molecules that

collide with the fullerene cage randomly. It is easy to see, therefore, how anistropic deformation of the fullerene cage could occur.

While I do strongly believe that the apparent hyperfine shift is a real effect, it is also important to note that I have not fully excluded the possibility of a systematic error in the experiment. This is of particular concern given the apparently pressure-dependent g factor derived by fitting the data, which disappears when considering the g factor shift with pressure relative to a non-pressurised standard sample. The origin of this shift remains unknown; the most likely explanation is that there is some pressure-dependent perturbation to the B_0 magnetic field. Worryingly, if this were the case, and the perturbation field were inhomogeneous, it may also explain the pressure-dependent linewidth. However, in light of the care taken to minimise the magnetic susceptibility of all components between the pole pieces of the electromagnet, I have yet to find the origin of such a field. Secondly, I have not been able to conclusively refute the possibility that the apparent change in hyperfine coupling is due to solvent effects or the effect of pressure on the solvation of the fullerene molecule.

In addition to the pressure-dependent hyperfine coupling and g factor, I also observe a pressure-dependent linewidth. The linewidth data are well fitted by a model based on dipolar interactions between spins in fullerene clusters. Physically, this is a very reasonable model: the concentration of the fullerene sample used for the experiments presented in this thesis is significant above the clustering threshold. However, the fitted spin-spin separation ($r \sim 10\,\mathrm{nm}$) is much larger than that which is to be expected by considering the purity of the sample and assuming that the clustered fullerenes are densely packed. This is not unreasonable, since there are observations in the literature of "fractal" clusters. However, I think it is more likely an artefact of the statistics of the fullerene clusters themselves. Since the pressure-dependent linewidth should only be observed for fullerene clusters containing multiple *endohedral* fullerenes, the naive model presented here will tend to overestimate the spin-spin separation. Future research could focus on refining the model to account for this fact. Furthermore, it would be good to characterize the

cluster size using an independent method such as dynamic light scattering. Finally, it is highly desirable to find a set of experiments by which the pressure-dependent field shift hypothesis may be proved or disproved.

5.2 Outlook

On the basis of the research performed in this thesis, I believe that the outlook for fullerene-based atomic frequency standards is poor. Firstly, they are fundamentally limited by a weak hyperfine interaction, which leads to a low frequency clock transition. Coupled with a large linewidth compared to that which is achievable in atomic systems, due to coupling to additional degrees of freedom inherent to a condensed matter system, this leads to a poor transition quality factor. The low frequency clock transition also leads to a small population difference between the energy levels, and consequently the signal amplitude is small. Both of these factors would compromise the short term stability of a fullerene-based atomic clock. Secondly, they are susceptible to long-term drift and instability via their temperature coefficient. Thirdly, the challenging nature of endohedral fullerene synthesis and purification limits their applicability to large-scale use.

It is worth noting that they do have some potential advantages: construction of a true single-chip atomic clock could piggyback off prior work in the field of one-chip NMR spectrometers and, as I have shown in this thesis, an endohedral fullerene clock would be reasonably insensitive to atmospheric pressure fluctuations.

However, I do not think that the advantages of a fullerene-based frequency standard outweigh the disadvantages. Furthermore, advances in CSAC technology have improved the long-term stability relative to the first generation devices and reduced the power cosumption of both the physics package and the control electronics. In addition, there are other condensed-matter frequency standards that show promise with regards to implementing low SWaP atomic clocks with good performance and high robustness. As such, I believe endohedral fullerene clocks to be an interesting concept but ultimately not viable as a practical technology.

Appendices

A

Measuring the quality factor of a resonator

Contents

The quality factor Q of a resonator is an important parameter for determining the efficiency with which the applied microwave power is converted to rf magnetic field B_1, and hence the performance of the spectrometer, as discussed in Section 2.3.2. The quality factor of a resonator can be measured using a ring-down measurement, in which the decay time of the electrical resonance is measured, or by using a network analyser to measure the power reflected from the resonator as a function of frequency. In this appendix, I show the the points at which the reflected power is 3 dB less than the off-resonance reflected power are the correct points from which to estimate the Q factor of the resonator. The quality factors reported here are the loaded quality factors, i.e. the quality factor of the system including energy lost via coupling to the measurement equipment.

A.1 Resonator Q factor

Without loss of generality, I start by modelling the resonator as a LCR lumped element circuit capacitively matched to a transmission line with a characteristic impedance $Z_0 = 50\,\Omega$. The resonant circuit comprises an inductor L, tuning capacitor C_t, and matching capacitor C_m. Losses in the circuit are modelled by a resistor R in series with the inductor. The circuit is displayed in Figure A.1(a). The impedance of the circuit

$$Z = \frac{-i}{\omega C_\mathrm{m}} + \left[\frac{1}{i\omega L + R} + j\omega C_\mathrm{t}\right]^{-1}, \tag{A.1}$$

where i is the imaginary unit. The impedance of the circuit is therefore frequency dependent. The voltage reflection coefficient

$$S_{11} = \frac{Z - Z_0}{Z + Z_0}, \tag{A.2}$$

and the power reflection coefficient

$$\frac{P_\mathrm{ref.}}{P_\mathrm{inc.}} = |S_{11}|^2 = \left|\frac{Z - Z_0}{Z + Z_0}\right|^2, \tag{A.3}$$

where $P_\mathrm{inc.}$ is the power incident on the resonator and $P_\mathrm{ref.}$ is the power reflected from the resonator. In this thesis, I determine the quality factor of the resonator by measuring the power reflection coefficient as a function of frequency. A schematic diagram of the experimental setup is given in Figure A.1(b).

For high-Q (i.e. $Q \gg 1$) resonators, the quality factor

$$Q = \frac{f}{\Delta f}, \tag{A.4}$$

where f is the centre frequency of the resonator and Δf is the full-width at half-maximum (FWHM) of the resonance. In practice, Δf can be determined from the "$-3\,$dB points". The $-3\,$dB points are the frequencies at which the reflected power is $3\,$dB below the off-resonance reflected power. To illustrate this, I have simulated an arbitrary resonator to illustrate the correspondence between the $-3\,$dB points and the FWHM of the power absorbed by the resonance. The results of this simulation are shown in Figure A.2. As can be seen from this simulation, the

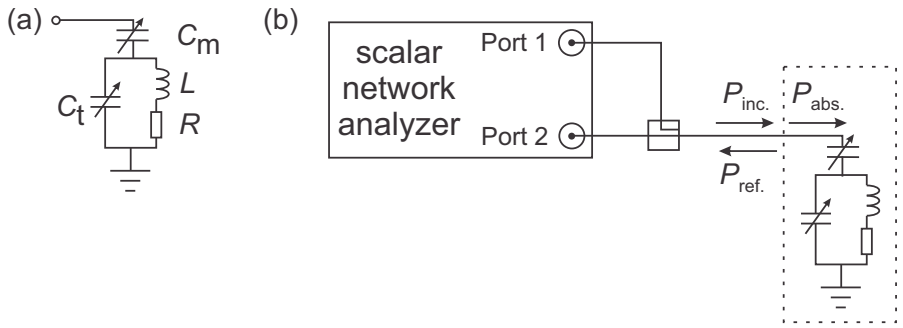

Figure A.1: (a) shows a lumped element model of the resonator, comprising tuning capacitor C_r, inductance L, and resistance R. The impedance of the resonant circuit is set to $50\,\Omega$ using the capacitor C_m in order to match it to the characteristic impedance of the transmission line. The setup used to measure the Q factor of the resonator is displayed in panel (b). A scalar network analyser applies a power $P_{inc.}$ to the resonator, and measures the reflected power $P_{ref.}$ as a function of the frequency of the applied rf radiation. In this thesis, I assume that the applied power $P_{inc.}$ is either reflected from the resonator or dissipated in the resonator, which is denoted by $P_{abs.}$, with no power lost to the environment otherwise.

FWHM of the absorbed power $\mathrm{FWHM}_{P_{abs.}}$, which is analogous to, for example, the FWHM of an atomic resonance, corresponds closely to the value $\mathrm{FWHM}_{-3\,dB}$ determined from a measurement of the $-3\,$dB points. In contrast, defining Δf using the $3\,$dB points obtained by identifying the frequencies at which the reflected power is $3\,$dB greater than the on-resonance minimum in reflected power would underestimate the linewidth and overestimate Q. Furthermore, as the resonator approaches critical coupling, the linewidth measured using this approach would tend towards unphysically small values as sides of the dip become steeper.

By altering the parameters of the simulation, it can be seen that the degree of similarity between the two measures increases as resonator approaches critical coupling. Figure A.3 shows a simulation using the same parameters used to generate the plots displayed in Figure A.2 except for the matching capacitor, which is adjusted to bring the resonator closer to critical coupling. This demonstrates very good agreement between $\mathrm{FWHM}_{P_{abs.}}$ and $\mathrm{FWHM}_{-3\,dB}$. Due to the near-critical coupling achieved for the resonators used in this thesis, with $P_{ref.}/P_{inc.} \lesssim -50\,$dB, the discrepancy between the two measures is negligible.

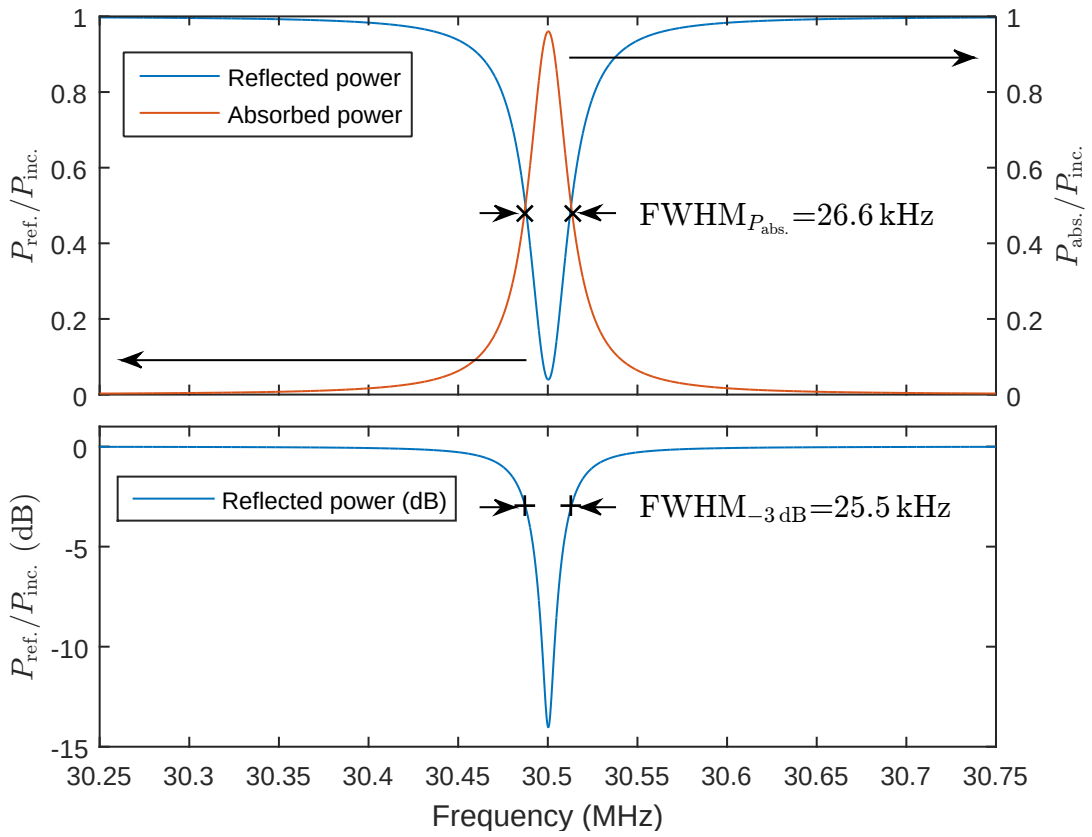

Figure A.2: Simulated plots of power absorbed and reflected by a model resonator. The resonator is modelled as a capacitively-coupled LCR circuit, as shown in Figure A.1. The values used in this simulation are $L = 10\,\text{nH}$, $C_\text{t} = 2.713\,\text{nF}$, $R = 0.001\,\Omega$, and $C_\text{m} = 10\,\text{pF}$. The resonant frequency is 30.5003(1) MHz, where the uncertainty is given by the precision of the simulation. The top panel displays the power reflected from the resonator $P_{\text{ref.}}$ (blue line) and power absorbed by the resonator $P_{\text{abs.}}$ (orange line) relative to the incident power $P_{\text{inc.}}$ as a function of frequency. The black $\times$ symbols in the top panel indicate the points from which $\text{FWHM}_{P_{\text{abs.}}}$ is determined, and the black $+$ symbols in the lower panel indicate the points from which $\text{FWHM}_{-3\,\text{dB}}$ is determined. The minimum power reflection coefficient is -14.03 dB, and $\text{FWHM}_{P_{\text{abs.}}}/\text{FWHM}_{-3\,\text{dB}} = 1.043$.

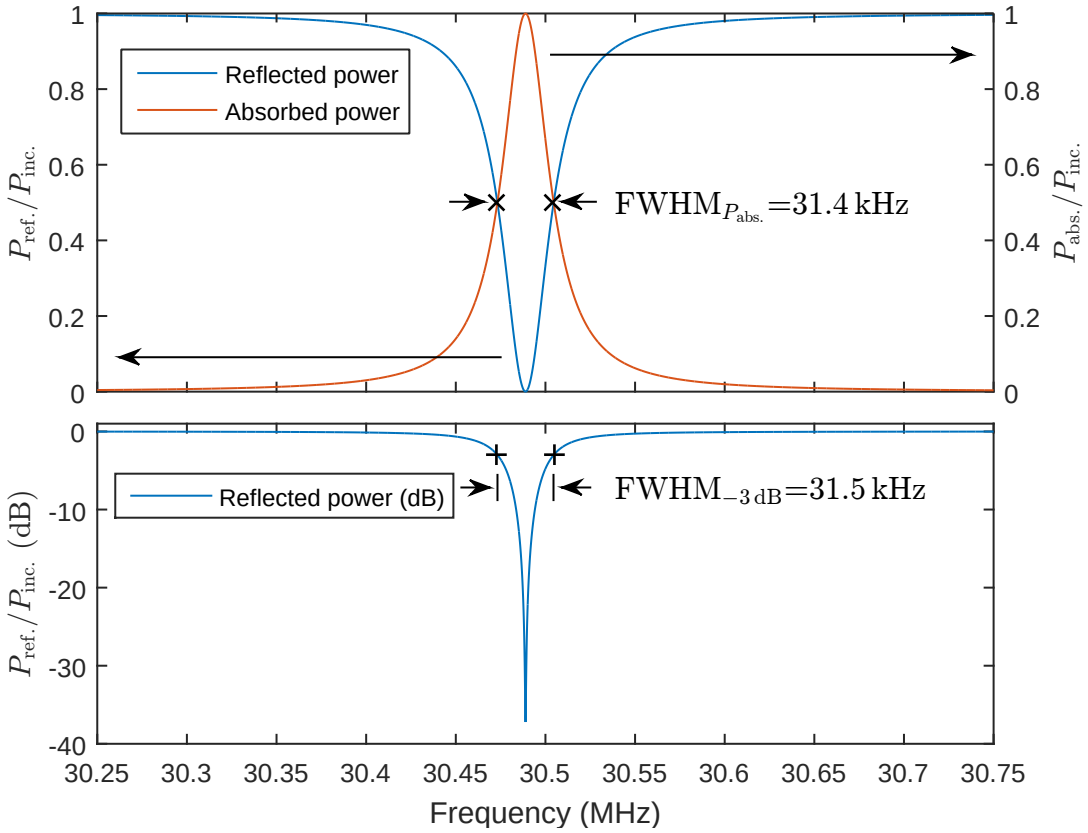

Figure A.3: Simulated plots of power absorbed and reflected by a model resonator. The values used in this simulation ($L = 10\,\mathrm{nH}$, $C_\mathrm{t} = 2.713\,\mathrm{nF}$, $R = 0.001\,\Omega$) are the same as for the resonator displayed in Figure A.2, with the exception of the matching capacitor. Here, $C_\mathrm{m} = 12.1\,\mathrm{pF}$ to better match the resonator to the transmission line. The linewidth has increased, as is to be expected when going towards critical coupling from the under-coupling regime, since more energy is coupled back out to the rf circuitry used to measure the resonator. The minimum power reflection coefficient is -37.21 dB, and $\mathrm{FWHM}_{P_\mathrm{abs.}}/\mathrm{FWHM}_{-3\,\mathrm{dB}} = 0.997$ demonstrating the better correspondence between $\mathrm{FWHM}_{P_\mathrm{abs.}}$ and $\mathrm{FWHM}_{-3\,\mathrm{dB}}$ closer to critical coupling.

B

Explanation of the lineshape observed using the low-field cw EPR spectrometer

Contents

The lineshape for the spin resonances displayed in Figures 3.10 and 3.11 of Chapter 3 differ considerably from the lineshapes observed in most EPR experiments. The lineshape is described by the second derivative of a Lorentzian. This is surprising, since I tuned the local oscillator phase such that the double-balanced mixer was sensitive to amplitude rather than the phase of the rf signal reflected from the cavity; in this case, one would typically expect to observe the a first-derivative lineshape given that I was measuring the first harmonic output from the lock-in amplifier. In this appendix, I explain how the observed lineshape arises; in short, it is due to the lack of automatic frequency control (AFC) in the spectrometer. The rf signal generator therefore does not track the resonant frequency of the cavity, and frequency pulling of the cavity by the spin ensemble on resonance modulates the amplitude of the reflected signal. This is because the source frequency stays fixed, and hence moves in the frequency domain relative to the minimum reflection from the resonator. The amplitude of the reflected signal therefore changes on

resonance. When using a modulation approach, this naturally gives rise to the observed second derivative lineshape.

This appendix is based on the supplementary information of Harding et al. [**Har17**].

B.1 Lineshape

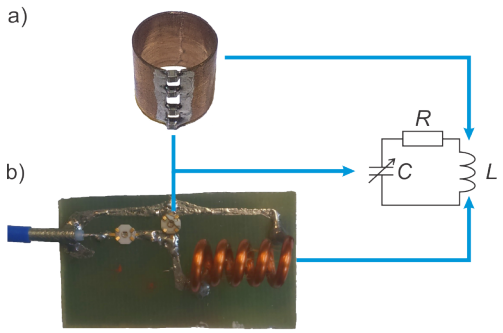

Figure B.1: Lumped element model of loop gap resonator, comprising inductance L (loop), capacitance C, and resistance R.

As shown in Chapter 2, the magnetic susceptibility $\chi = \chi' - i\chi''$ perturbs the inductance of the resonator such that

$$L_0 \to L_0(1 + \eta\chi' - i\eta\chi''). \tag{B.1}$$

By considering the impedance

$$Z = \left[i\omega C + \frac{1}{i\omega L + R}\right]^{-1} \tag{B.2}$$

of the resonant circuit, and by treating the effect of the sample magnetic susceptibility as a perturbation, such that $\eta\chi(\omega) \ll 1$, one can derive the expression

$$\omega_{\text{res}} = \omega_0 \left[1 - \frac{1}{2}\eta\chi'\right], \tag{B.3}$$

where

$$\omega_0 = \frac{1}{\sqrt{L_0 C}}\left(1 - \frac{CR^2}{2L}\right) \tag{B.4}$$

is the resonant frequency of the bare resonator. These calculations assume that the quality factor of the resonator $Q \gg 1$.

In the absence of saturation, the value of χ' is given by

$$\chi'(\omega_{\text{spin}}, \omega_{\text{rad}}) = \overline{\chi}(\omega_{\text{spin}}) \frac{(\omega_{\text{spin}} - \omega_{\text{rad}})}{(\delta\omega/2)^2 + (\omega_{\text{rad}} - \omega_{\text{spin}})^2}, \tag{B.5}$$

where ω_{spin} is the resonant frequency of the spin ensemble at a field B_0, ω_{rad} is the frequency of applied radiation, and $\delta\omega$ is the width of the resonance in the angular frequency domain for a given value of ω_{rad}. The quantity $\overline{\chi}$, with dimension s^{-1}, parameterises the magnitude of the magnetic susceptibility for a given energy splitting between the clock states.

In general, ω_{spin} is a non-linear function of magnetic field B_0 as can be seen from the transition frequency diagram in Figure 3.1. However, when the ensemble is near resonance such that $\omega_{\text{spin}} \approx \omega_{\text{rad}}$, it can be approximated as linear function. In this case, $\omega_{\text{spin}} - \omega_{\text{rad}} = \gamma_{\text{eff}} \Delta B$, where γ_{eff} is the effective gyromagnetic ratio at the predicted resonant field B_{rad} for which $\omega_{\text{spin}} = \omega_{\text{rad}}$, and $\Delta B = B_0 - B_{\text{rad}}$. Furthermore, I assume that the susceptibility parameter $\overline{\chi}(\omega_{\text{spin}}) \approx \overline{\chi}(\omega_{\text{rad}})$ is constant over the small frequency difference between ω_{spin} and ω_{rad}. In this case, Equation (B.5) reduces to

$$\chi'(\Delta B, \omega_{\text{rad}}) = \frac{\overline{\chi}(\omega_{\text{rad}})}{\gamma_{\text{eff}}} \cdot \frac{(\Delta B)}{(\delta B/2)^2 + (\Delta B)^2}, \tag{B.6}$$

where the field domain linewidth $\delta B = \delta\omega/\gamma_{\text{eff}}$. Substituting Equation (B.6) into Equation (B.3), one can see that the sample introduces a field-dependent frequency shift of the resonator $\Delta\omega_{\text{res}}$ that is described by the derivative of a Lorentzian.

In the experiments presented here, the rf source was deliberated detuned from the resonant frequency of the resonator. This was to ensure that the spectrometer behaved predictably even if the resonator or source frequencies drifted slightly over the duration of an experiment, which could take up to one day. However, the reflection coefficient depends on the relative frequency difference between the source and the resonator. Therefore, as the cavity resonant frequency is modified by the magnetic susceptibility of the spin ensemble on resonance, the measured signal

voltage is therefore described by a Lorentzian-derivative lineshape $S \propto \chi'(\Delta B, \omega_{\mathrm{rad}})$, and hence the observed signal after field modulation and phase-sensitive detection

$$S_{\mathrm{obs}} \propto \frac{\partial}{\partial(\Delta B)}\left[\chi'(\Delta B, \omega_{\mathrm{rad}})\right] \tag{B.7}$$

is described the second-derivative of a Lorentzian in the field domain.

In practice, the experiment will also be sensitive to absorption of energy within the spin ensemble. This is parametrised by the real magnetic susceptibility χ, and would give rise to a Lorentzian derivative lineshape. While the observed signal likely includes components of both, the fact that the lineshape is well fitted by the second derivative of a Lorentzian indicates that the experimental procedure presented here is primarily sensitive to the imaginary component χ' of the rf magnetic susceptibility.

C

Non-magnetic spacer for high-pressure EPR experiments

Contents

In this appendix, I discuss the mechanical design and pressure sealing of the non-magnetic spacer described in Chapter 4.

C.1 Mechanical design

The spacer must withstand significant mechanical stress due to the pressure of the sample. A schematic cross-section of the spacer is given in Fig. C.1. Modelling the spacer as a thick-walled tube, I calculate the safety factor at the maximum applied pressure $P = 0.25\,\mathrm{GPa}$. This safety factor parameterises the strength of the spacer compared to the bursting force applied by the fluid to which it is subject. The safety factor

$$s = \frac{\sigma_u(r_o^2 - r_i^2)}{P(r_o^2 + r_i^2)} \tag{C.1}$$

is determined by the ultimate tensile strength σ_u of the material used to fabricate the spacer and the spacer's inner and outer radii r_i and r_o, respectively. This is derived by assuming a thick-walled pipe and considering the mechanical stress in the pipe walls, which are modelled by the Lamy equation [**Bro73**].

The spacer is effectively a thick-walled pipe with internal diameter $r_i = 1\,\text{mm}$ and external diameter $r_0 = 3.4\,\text{mm}$. The inner radius of $r_i \approx 1\,\text{mm}$ is determined by the wire EDM machine used to drill the hole, and the outer radius $r_o \approx 3.1\,\text{mm}$ is fixed by the placement of the UNC#4-40 screws that mate the spacer to the pressure vessel. The safety factors for spacers fabricated from various different low-susceptibility metals are listed in Table C.1. The safety factor parameterises the safety margin compared to the design pressure $P = 0.25\,\text{GPa}$. A safety factor of less than 1 corresponds to mechanical failure at the design pressure.

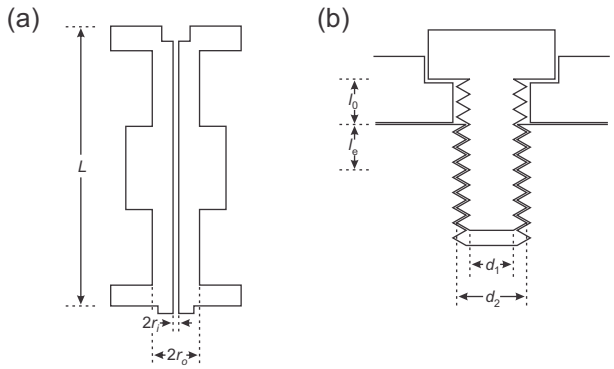

Figure C.1: Schematic diagram showing the relevant dimensions of (a) the spacer and (b) the screws that attach the sample cell clamp to the spacer. The spacer is essentially a thick walled pipe with internal radius $r_i = 1\,\text{mm}$, external radius $r_o = 3.4\,\text{mm}$, and length $L = 112\,\text{mm}$. The screws are M3 socket cap head screws, with pitch minor diameter $d_1 = 2.4\,\text{mm}$ and pitch major diameter $d_2 = 3\,\text{mm}$. The engaged thread length $l_e \approx 2\,\text{mm}$, and the distance between the spacer and the screw head $l_0 = 3.4\,\text{mm}$.

These safety factors are computed from the ultimate tensile strength of the material. The mechanical properties of a metal strongly depend on its microstructure, which can be influenced by various processes such as heat treatment and cold working. This is reflected in the range of tensile strengths for each metal given in Table C.1. Some of the listed materials would be suitable when highly tempered due to the increase in tensile strength. However, titanium was selected since it was the only candidate with sufficient tensile strength to achieve an acceptable

Material	Ultimate tensile strength (MPa)	Safety factor s
Copper (C10100)	221–455	0.72–1.48
Aluminium alloy (7075)	230–570	0.75–1.85
Brass (C26000)	303-896	0.98–2.91
Titanium alloy (Ti–6Al–4V)	993–1172	3.22–3.80

Table C.1: Safety factors for spacer fabricated from various materials at an internal pressure $P = 0.25\,\mathrm{GPa}$. The specific alloy considered is denoted by the unified numbering system (UNS) code given in brackets. The tensile strengths listed are taken from reference [**SA01**]. The range of tensile strengths is due to different metallurgical techniques that can modify the tensile strength of the alloy by altering its microstructure.

safety factor even in the annealed condition. This eliminates the need for further processing of the spacer after fabrication.

C.2 Pressure sealing

It is necessary to seal the joints between the pressure vessel, spacer, and sample cell such that the pressurised fluids does not leak. In the initial setup, sealing between the sample cell and the pressure vessel was achieved using a flat kapton washer. However, this solution was not satisfactory for the apparatus incorporating the spacer: the joint between the spacer and pressure vessel leaked. This could be due to either surface imperfections on the sealing surface of the spacer caused by the manufacturing process, or due to the difficulty in ensuring perfect alignment of the sealing surfaces. At the sample cell–spacer interface, the cone shaped cross-section of the YSZ sample cell ensures good alignment of the sealing surfaces by evenly distributing the axial load applied by the screws. However, the spacer–pressure vessel interface does not benefit from this effect, and did not seal well using kapton washers.

Pressure sealing was achieved using an indium wire gasket in a partially-trapped seal configuration. Indium is a very soft metal that, under compression, fills in the surface imperfections of the sealing faces. Furthermore, due to its thickness, the wire gasket is tolerant of sealing face mis-alignment. The indium wire was cleaned

with acetone prior to use in order to remove dirt and grease that could provide leakage pathways. The screws at each joint were then tightened to compress the indium wire. The seal is capable of withstanding the 2500 bar pressure applied to the sample by the barocycler. Some pressure runs failed at lower pressures. This could be due to, for example, inadequate cleaning of the indium wire. Due to its low magnetic susceptibility $\chi = -5.1 \times 10^{-5}$, [**Hay14**] the indium does not significantly impair the homogeneity of the B_0 field.

The screws used to mate the various parts of the low magnetic susceptibility setup were made from the same titanium alloy as the spacer to ensure a combination of high strength and low magnetic susceptibility. Vacuum grease was applied to the threads to prevent galling, since titanium–titanium interfaces are susceptible to cold welding under pressure.

The screws are subject to an axial force due to the pressure of the sample applied to the end caps of the pipe. I consider three possible mechanical failure modes: stripped threads, and extension or tensile failure of the screw. The axial force $F = PA$, where $A = \pi r_i^2$ is the cross-sectional area of the interior of the spacer. At a pressure of 0.25 GPa the force $F = 790$ N, which I assume to be equally distributed over all six screws such that the force on a single screw $F_1 = 130$ N. The resultant shear and tensile stresses experienced by the thread and screw, respectively, are much lower than the failure stresses of the Ti–6Al–4V alloy, which ensures that the threads will not be stripped, and the screw will not fail under tension.

The extension of the screws $\Delta L = F_1 l_0/(EA)$, where $A = \pi d_1^2/4$ and l_0 is the distance between the head of the screw and where the threads engage. For a Young's modulus $E = 114$ GPa [**SA01**] and $l_0 = 3.4$ mm, the expected extension is $\Delta L = 0.9\,\mu$m. A gap due to this extension would cause loss of pressure due to sample leakage. Since this was not observed, it seems likely that the indium wire elastically rebounds from the initial compression applied by the screws, or that radial pressure applied to the indium wire by the toluene deforms the confined indium wire such that it expands in the axial direction.

D
Pulse spectrometer

Contents

I designed and built a low-frequency pulse EPR spectrometer, but did not manage to measure the EPR signal from $N@C_{60}$ using this spectrometer. For this reason, I have not included it in the thesis, but wish to record it as a useful starting point for anyone who follows me. In this appendix, I include a brief overview of the design and some preliminary results obtained from a lithium phthalocyanine (LiPc) standard sample.

D.1 Pulse spectrometer

The low-frequency pulse spectrometer used inductive pickup of the spin ensemble's oscillating magnetization, which induces a voltage in the resonator. This rf voltage is coupled out of the resonator and detected using a double balanced mixer similarly to the cw spectrometer. However, there are significant differences in the rf circuitry

between the cw and pulse spectrometers. A diagram of the spectrometer configured for use at $f \sim 360\,\mathrm{MHz}$ is given in Figure D.1.

In contrast to the cw spectrometer, the pulse spectrometer uses a single source. The phase of each pulse can be controlled electronically using IQ modulation of the rf source to maximise the absorption and dispersive components of the signal in the I and Q output channels, respectively, and to implement phase cycling.

D.1.1 Phase cycling

In the cw spectrometer, I reduce noise by minimising the measurement bandwidth of the experiment through signal averaging. I also perform signal averaging in the pulse spectrometer to mitigate noise a white frequency spectrum. However, signal averaging cannot eliminate coherent signals such as ring down from the resonator. The ring down signal and other instrumental artefacts, such as imbalance in the gain of the IQ arms or the receiver, can be eliminated by phase cycling of the excitation and local oscillator pulses. Phase cycling the phase of the rf pulses can be used to control the position of the spin state on the Bloch sphere relative the coherent instrumental artefact. Using this approach, one can sum the spin signals while cancelling the coherent artefacts by choosing an appropriate pulse sequence.

In this spectrometer, I used two-step phase cycling to remove the cavity ringdown due to the second pulse in the Hahn echo sequence. Using phase cycling requires adding and subtracting the digitised spin signal depending on the phase of the excitation pulses. This can be achieved in software or in hardware. The latter approach is faster, since there is no processing time. It may be achieved by using an inverter controlled by the pulse-sequencing AWG to modify the polarity of the spin signal. The signal is then averaged as normal. Alternatively, the phase of the local oscillator pulse can be used to invert the spin signal if necessary. In practice, however, I manipulate the data in software. At the same time the pulse sequence is generated for transfer to the AWG, the programme produces a matrix comprising values either $+1$ or -1. This matrix is subsequently used to multiply the digitised spin signal conditional on the phase of the pulse in order to sum the spin echo

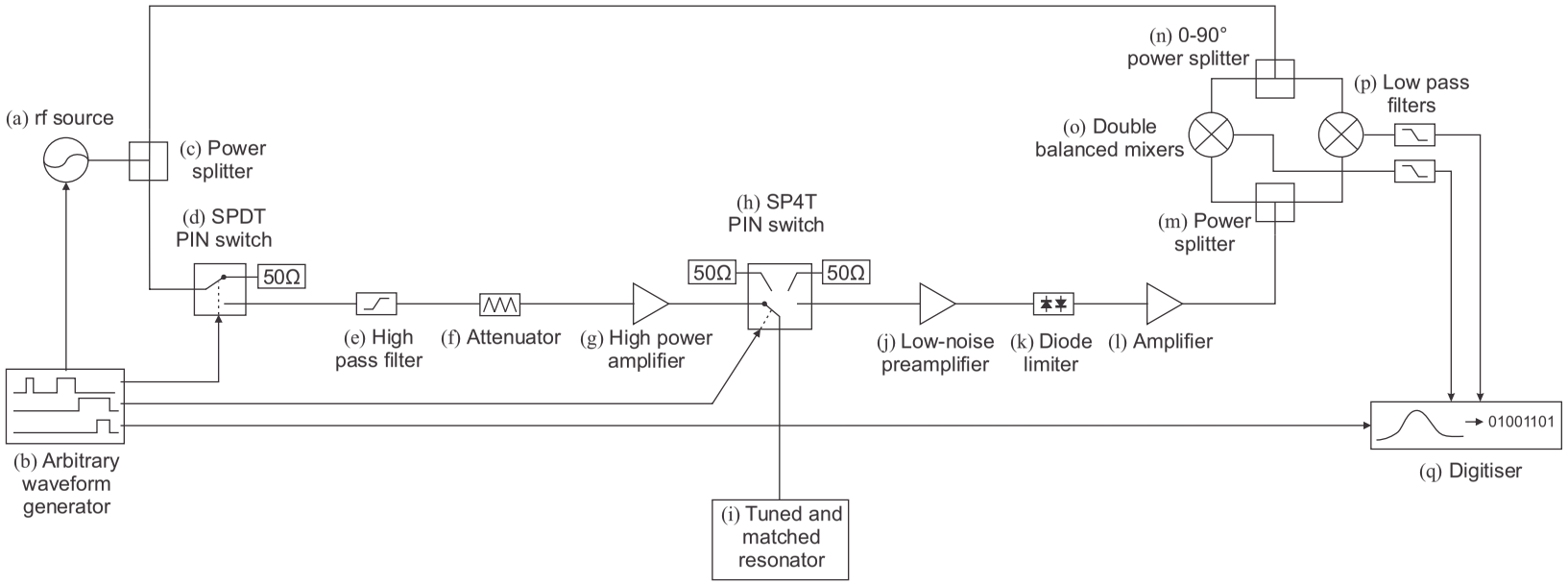

Figure D.1: Schematic diagram of the low-frequency pulse spectrometer. The rf source (a) is a Rohde & Schwarz SMW200A vector signal generator. The amplitude and phase of the rf signal from the source is controlled by a Tektronix AWG 5014C arbitrary waveform generator (b) using IQ-modulation inputs on the front panel of (a). The rf output from (a) is split using a Minicircuits ZESC-2-11 power splitter. The power in the transmit arm first passes through a Minicircuits ZASWA-2-50DR+ single-pole, double-throw (SPDT) PIN diode switch (c). This switch is controlled by the AWG (b). The amplitude from the rf source is fixed to ensure that the mixers in the receiver arm are driven with the correct power. The excitation pulse power therefore set using an attenuator (f) before the ENI 503L high power amplifier (g). The output from the power amplifier is directed into the resonator (i) using a Minicircuits ZSWA4-63DR+ single-pole, four-throw (SP4T) PIN diode switch (h) controlled by the AWG. During the receive period, this switch disconnects the resonator from the transmit arm, and closes the contact linking the resonator to the Minicircuits ZX60-P103LN+ low noise preamplifier (j). The output from this amplifier passes through a Minicircuits VLM-33S+ diode limiter (k) before being further amplified by a Minicircuits ZX60-33LN+ (l). The signal is then split with a Minicircuits ZESC-2-11 power splitter (m). The split signal is the rf input to two Minicircuits ZP-3MH double balanced mixers (p). The local oscillator signal for these mixers is derived from the same source (a) as the excitation signal. To obtain both inphase and quadrature information, the local oscillator is split using a 0–90° splitter (n). The 0–90° splitter has a narrow bandwidth such that it is necessary to choose an appropriate device based on the desired frequency. Here, for the $f \sim 360\,\mathrm{MHz}$ measurements of LiPC, I used a Minicircuits ZX10-5-2-S+. The output from the mixers is low-pass filtered using Minicircuits SBLP-39 filters (p) before digitisation using an AlazarTech ATS9440 digitiser, with each measurement triggered by (b). The SBLP-39 filters were selected due to minimal ringing in response to a pulsed signal.

while subtracting the background signal. In addition to pulses to the rf source and switches, the AWG provides a separate pulse to the digitiser that determines whether the measured signal should be summed or subtracted.

The spin signal is digitised using an Alazartech ATS9440. The digitiser has four analogue inputs, a trigger input, and an external clock input. The analogue inputs are used to measure the in-phase and quadrature output channels from the mixer, and the trigger input initiates digitisation of the analogue inputs. The trigger input is provided by the AWG used to gate the rf source and the switches in the circuit, which ensures that the timing of the trigger relative to the spin echo remains stable. The local oscillators of the AWG pulse sequencer, rf source, and ADC are locked via a 10 MHz reference signal to ensure that the spin echoes can be coherently added to achieve signal averaging.

D.1.2 RF switches

One of the most significant experimental challenges in building the pulse spectrometer was finding suitable switches. In particular, I struggled to find an acceptable balance between switching speed and video noise: the high speed switches used to in the spectrometer to route pulses through the spectrometer circuitry output large voltage spikes on switching ("video leakage") that cause amplifier overloading. This is particularly problematic at the low frequencies used in this thesis due to the difficulty of separating the desired rf signal from the video leakage since they occur at similar frequencies.

The pulse spectrometer requires fast, electrically controlled switches for forming rf pulses used to excite the spin system, routing the pulses through the spectrometer, and protecting the low-noise preamplifier from the high power pulse used to drive the spins. These switches should switch rapidly, possess high isolation, and have little dc video leakage.

The rapid switching time is necessary to maximise the bandwidth of the excitation pulse. High isolation is necessary to prevent leakage of the rf excitation pulses into the receiver arm of the spectrometer, since this would lead to large offset

signals. The same rf source is used to provide the rf pulses and local oscillator signal. A high isolation switch is therefore placed between the source and the high power amplifier to prevent the local oscillator pulse from reaching the transmit arm. The duplexer that switches the resonator between the transmit and receive arms is also implemented using a high isolation switch to prevent broadband noise in the pulse amplifier output from being coupled into the receiver arm. It also prevents residual noise in output from transmit side being coupled into receiver.

Switch video leakage can lead to the low-noise amplifiers in the receiver arm overloading, which may block rf signals from passing or affect the gain such that the signals do not provide reliable experimental data. If the rf signal is sufficiently separated in frequency from the video leakage, high-pass filtering of the switch outputs can be used to block the video leakage while passing the desired rf, which prevents amplifier overloading. Capacitive dc blocks did not work to block the video leakage and prevent overloading and transient changes in the amplifier gain.

The video leakage causes the filters to start ringing, which appears as a decaying rf voltage at the input to any subsequent amplifier. The frequency of this signal is approximately equal to the cutoff frequency of the filter. The time constant of the decay is inversely proportional to the filter frequency for a given filter quality factor. This leads to a conflict between minimising the filter frequency to maximise the separation between filter ringing and the spin signal, and maximising the filter frequency to minimise ringdown time. This is a very significant problem at low frequencies where that spin signal may decay before the filter ringing. I have yet to find a satisfactory solution to this problem. It is possible to use a slow speed duplexer, which permits using a switch with low video leakage and removes the need for filters. It is not possible to use a slow switch as the pulse forming switch, since it would increase the minimum spacing between pulses and make it impossible to measure short coherence time samples.

D.1.3 Pulse sequences

I implemented the following pulse EPR experiments:

- Two pulse Hahn echo seqeuence $[\frac{\pi}{2} - \tau - \pi - \tau]$ with two-step phase cycling applied to the first pulse to eliminate the background signal due to ringdown of the resonator.

- Inversion pulse calibration experiment. The pulse sequence is the same as the Hahn echo pulse sequence detailed above, but the interpulse separation τ is fixed and the duration of the first pulse is incremented.

- Three pulse inversion recovery $[\pi - \tau_1 - \frac{\pi}{2} - \tau_2 - \pi - \tau_2]$. The amplitude of the spin echo is measured as τ_1 is incremented. Two-step phase cycling was applied to the $\frac{\pi}{2}$ pulse.

D.2 Results

Here, I present some preliminary results for the characterization of LiPc at $f \sim 360\,\mathrm{MHz}$. Figure D.2 plots the decay of a spin echo from LiPc in a Hahn echo experiment. Figure D.3 plots the inversion pulse calibration experiment. Figure D.4 plots the decay of a spin echo from LiPc in an inversion recovery experiment.

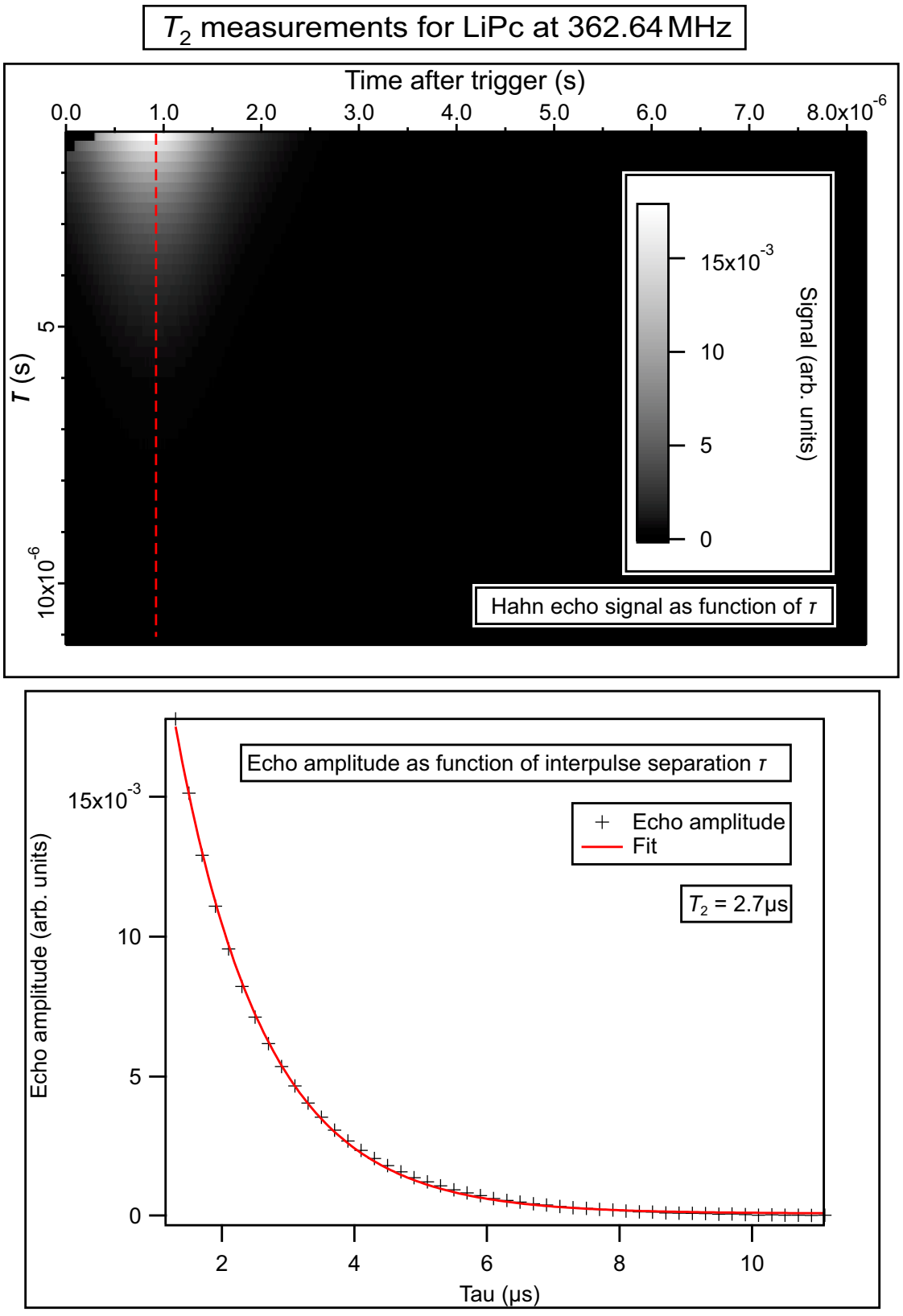

Figure D.2: Measurement of lithium phthalocyanine T_2 made using the low-field pulse spectrometer

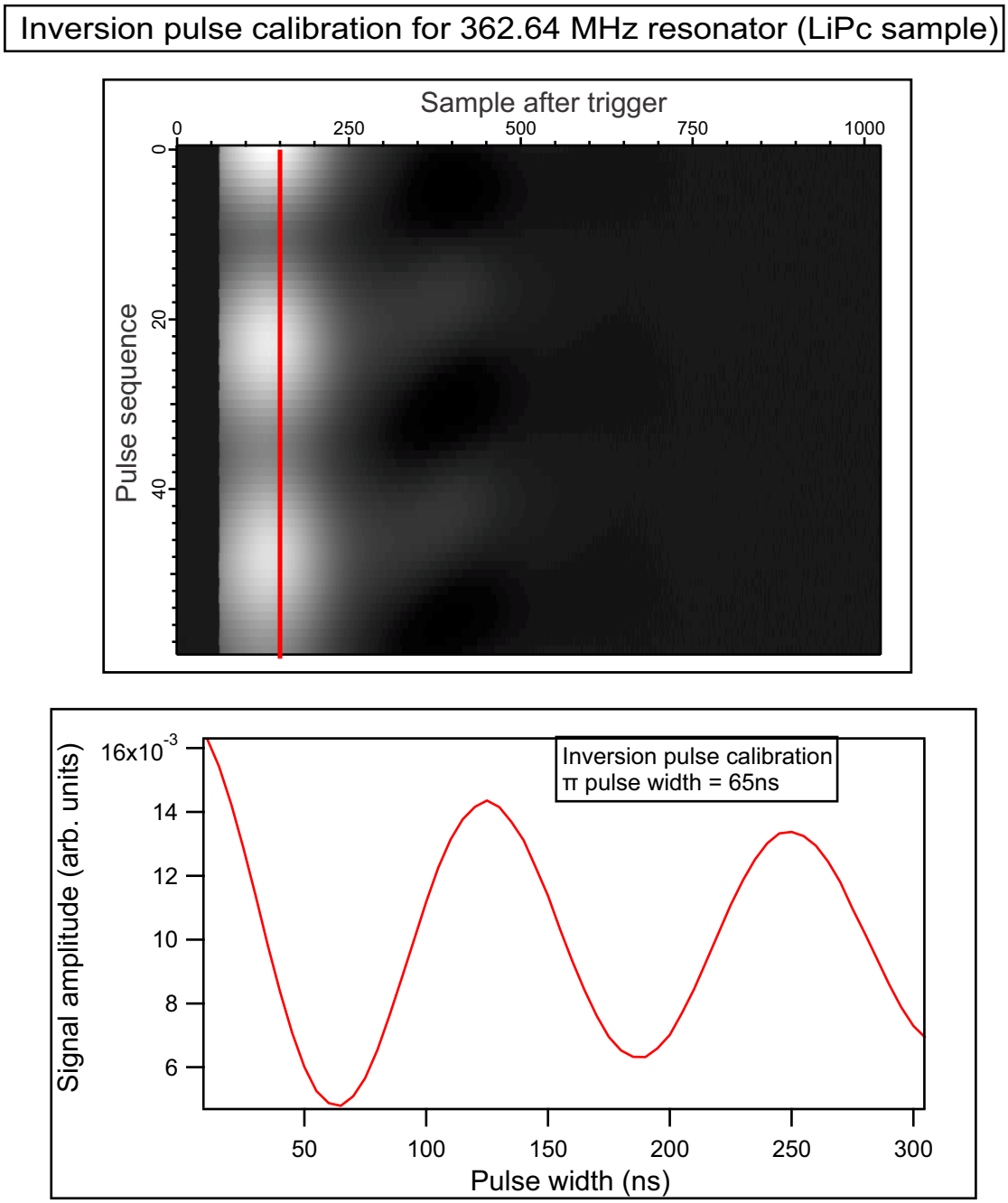

Figure D.3: Calibration of the inversion pulse length.

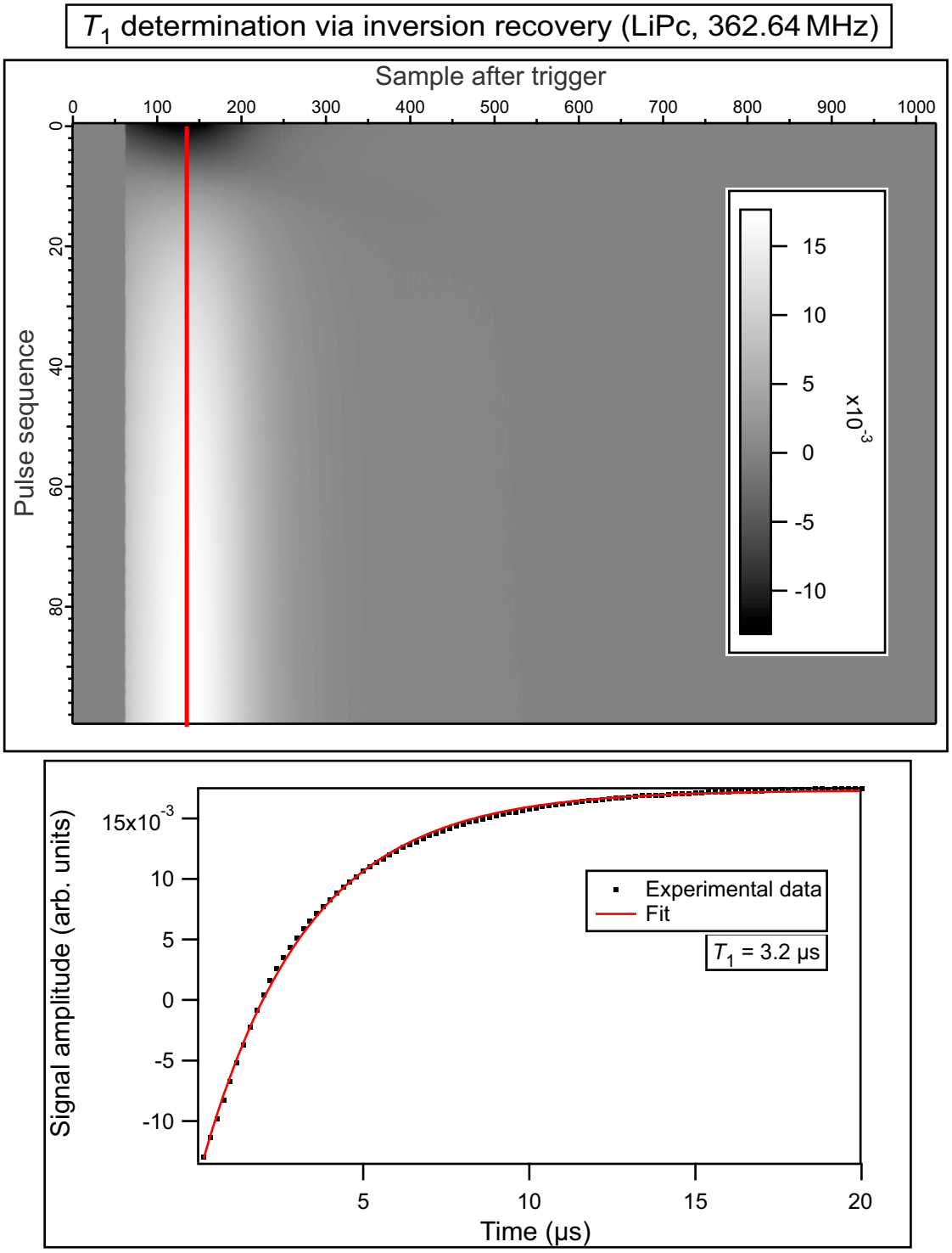

Figure D.4: Measurement of lithium phthalocyanine T_1 made using the low-field pulse spectrometer.

References

[**Adr62**] Frank J. Adrian. "Effect of Matrix Interactions and Buffer Gases on the Atomic Nitrogen Hyperfine Splitting". In: *Physical Review* 127.3 (Aug. 1962), pp. 837–843.

[**AFI59**] J. M. Andres, D. J. Farmer, and G. T. Inouye. "Design Studies for a Rubidium Gas Cell Frequency Standard". In: *IRE Transactions on Military Electronics* MIL-3.4 (1959), pp. 178–183.

[**AK66**] P. W. Atkins and Daniel Kivelson. "ESR Linewidths in Solution. II. Analysis of Spin-Rotational Relaxation Data". In: *The Journal of Chemical Physics* 44.1 (Jan. 1966), pp. 169–174.

[**All66**] D.W. Allan. "Statistics of atomic frequency standards". In: *Proceedings of the IEEE* 54.2 (1966), pp. 221–230.

[**Alm96**] T. Almeida Murphy et al. "Observation of Atomlike Nitrogen in Nitrogen-Implanted Solid C_{60}". In: *Phys. Rev. Lett.* 77.6 (1996), pp. 1075–1078.

[**AM09**] Maher S. Amer and John F. Maguire. "On the compressibility of C_{60} individual molecules". In: *Chemical Physics Letters* 476.4-6 (July 2009), pp. 232–235.

[**AN09**] D.P. Arnold and Naigang Wang. "Permanent Magnets for MEMS". In: *Journal of Microelectromechanical Systems* 18.6 (Dec. 2009), pp. 1255–1266.

[**Ash07**] N Ashby et al. "Testing Local Position Invariance with Four Cesium-Fountain Primary Frequency Standards and Four NIST Hydrogen Masers". In: *Physical Review Letters* 98.7 (Feb. 2007), p. 070802.

[**Atk67**] P.W. Atkins. "Relaxation studies". In: *Molecular Physics* 12.3 (Jan. 1967), pp. 201–209.

[**AV76**] C Audoin and J Vanier. "Atomic frequency standards and clocks". In: *Journal of Physics E: Scientific Instruments* 9.9 (Sept. 1976), pp. 697–720.

[**Ave93**] Nimrod Averbuch. *Base-site synchronization in a communication system.* US Patent 5,245,634. 1993.

[**BA12**] G. A. D. Briggs and A. Ardavan. *Atomic clock.* US Patent 8,217,724. 2012.

[**BA99**] M. Brinkmann and J.-J. André. "Electrodeposited lithium phthalocyanine thin films. Part II: magnetic properties and mesoscopic effects". In: *Journal of Materials Chemistry* 9.7 (1999), pp. 1511–1520.

[**Bal62**] John D Baldeschwieler. "Double Resonance Spectra of N^{14} and N^{15} Ammonium Ion". In: *The Journal of Chemical Physics* 36.1 (Jan. 1962), pp. 152–158.

[**Bar71**] James A. Barnes et al. “Characterization of Frequency Stability”. In: *IEEE Transactions on Instrumentation and Measurement* IM-20.2 (May 1971), pp. 105–120.

[**Bel02**] Joseph J. BelBruno. “Computational study of N@C_{60}, P@C_{60}, and As@C_{60}”. In: *Fullerenes, Nanotubes and Carbon Nanostructures* 10.1 (Apr. 2002), pp. 23–35.

[**Ben06**] Simon C Benjamin et al. “Towards a fullerene-based quantum computer”. In: *Journal of Physics: Condensed Matter* 18.21 (May 2006), S867–S883.

[**Ber17**] Lawrence J. Berliner. “The evolution of biomedical EPR (ESR)”. In: *Biomedical Spectroscopy and Imaging* 5.1 (June 2017), pp. 5–26.

[**Bet93**] D S Bethune et al. “Atoms in carbon cages: the structure and properties of endohedral fullerenes”. In: *Nature* 366.6451 (Nov. 1993), pp. 123–128.

[**BG09**] Marina Brustolon and Elio Giamello. *Electron Paramagnetic Resonance: A Practitioner’s Toolkit*. Ed. by Marina Brustolon and Elio Giamello. Hoboken, NJ: John Wiley & Sons, Inc., 2009.

[**BG47**] D. M. S. Bagguley and J. H. E. Griffiths. “Paramagnetic Resonance and Magnetic Energy Levels in Chrome Alum”. In: *Nature* 160.4068 (Oct. 1947), pp. 532–533.

[**BHP46**] F. Bloch, W. W. Hansen, and M. Packard. “The Nuclear Induction Experiment”. In: *Physical Review* 70.7-8 (Oct. 1946), pp. 474–485.

[**Blo14**] B. J. Bloom et al. “An optical lattice clock with accuracy and stability at the 10^{-18} level”. In: *Nature* 506.7486 (2014), pp. 71–75.

[**Blu58**] Richard J. Blume. “Electron Spin Relaxation Times in Sodium-Ammonia Solutions”. In: *Physical Review* 109.6 (Mar. 1958), pp. 1867–1873.

[**BMM07**] M. Bloch, O. Mancini, and T. McClelland. “Mass-Produced Quartz Oscillators as Low-Cost Replacement of Passive Rubidium Vapor Frequency Standards”. In: *Frequency Control Symposium, 2007 Joint with the 21st European Frequency and Time Forum. IEEE International*. 2007, pp. 1235–1240.

[**BP48**] B. Bleaney and R. P. Penrose. “Paramagnetic Resonance at Low Temperatures in Chromic Alum”. In: *Proceedings of the Physical Society* 60.4 (Apr. 1948), pp. 395–396.

[**BPP48**] N Bloembergen, E. M. Purcell, and R. V. Pound. “Relaxation Effects in Nuclear Magnetic Resonance Absorption”. In: *Physical Review* 73.7 (Apr. 1948), pp. 679–712.

[**BR14**] Chris Bonebrake and Lori Ross O’Neil. “Attacks on GPS Time Reliability”. In: *IEEE Security & Privacy* 12.3 (May 2014), pp. 82–84.

[**Bro10**] Richard M. Brown et al. “Electron spin coherence in metallofullerenes: Y, Sc, and La@C_{82}”. In: *Physical Review B* 82.3 (July 2010), p. 033410.

[**Bro73**] James McD. Baxter Brown. *Introductory Solid Mechanics*. London, New York: J. Wiley, 1973.

[**Bro77**] K. L. Brower. “EPR techniques for studying defects in silicon”. In: *Review of Scientific Instruments* 48.2 (Feb. 1977), pp. 135–141.

[**BTA98**] M. Brinkmann, P. Turek, and J.-j. André. "EPR study of the x,α and β structures of lithium phthalocyanine". In: *Journal of Materials Chemistry* 8.3 (1998), pp. 675–685.

[**Buc01**] A. L. Buchachenko. "Compressed Atoms". In: *The Journal of Physical Chemistry B* 105.25 (June 2001), pp. 5839–5846.

[**BY02**] John Burnett and Patrick Du Yaping. "Mitigation of extremely low frequency magnetic fields from electrical installations in high-rise buildings". In: *Building and Environment* 37.8-9 (Aug. 2002), pp. 769–775.

[**Car60**] R. J. Carpenter et al. "A Prototype Rubidium Vapor Frequency Standard". In: *IRE Transactions on Instrumentation* I-9.2 (1960), pp. 132–135.

[**Cas59**] T. G. Castner. "Saturation of the Paramagnetic Resonance of a V Center". In: *Physical Review* 115.6 (Sept. 1959), pp. 1506–1515.

[**CF15**] David Calero and Enric Fernandez. "Characterization of Chip-Scale Atomic Clock for GNSS navigation solutions". In: *2015 International Association of Institutes of Navigation World Congress (IAIN)*. 10. IEEE, Oct. 2015, pp. 1–8.

[**CH46**] Robert L. Cummerow and David Halliday. "Paramagnetic Losses in Two Manganous Salts". In: *Physical Review* 70.5-6 (Sept. 1946), pp. 433–433.

[**Cha91**] Yan Chai et al. "Fullerenes with metals inside". In: *The Journal of Physical Chemistry* 95.20 (Oct. 1991), pp. 7564–7568.

[**Col19**] Charles Collett et al. "A Clock Transition in the Cr_7Mn Molecular Nanomagnet". In: *Magnetochemistry* 5.1 (Jan. 2019), p. 4.

[**CR83**] Malcolm D Cook and Brian P Roberts. "Liquid xenon as a solvent for e.s.r. studies". In: *Journal of the Chemical Society, Chemical Communications* 0.6 (1983), p. 264.

[**CTB93**] Normand Cyr, Michel Tetu, and Marc Breton. "All-optical microwave frequency standard: a proposal". In: *IEEE Transactions on Instrumentation and Measurement* 42.2 (Apr. 1993), pp. 640–649.

[**Dat15**] Rajeev Dattani et al. "Fullerene oxidation and clustering in solution induced by light". In: *Journal of Colloid and Interface Science* 446 (May 2015), pp. 24–30.

[**DG04**] P. Delaney and J. C. Greer. "C_{60} as a Faraday cage". In: *Applied Physics Letters* 84.3 (Jan. 2004), pp. 431–433.

[**DG15**] Pierre Danhier and Bernard Gallez. "Electron paramagnetic resonance: a powerful tool to support magnetic resonance imaging research". In: *Contrast Media & Molecular Imaging* 10.4 (July 2015), pp. 266–281.

[**Din00a**] K.-P. Dinse. "FT-EPR and pulsed ENDOR studies of encapsulated atoms and ions". In: *Electron Paramagnetic Resonance: Volume 17*. Ed. by B.C. Gilbert, M.J. Davies, and K.A. McLauchlan. Vol. 17. The Royal Society of Chemistry, 2000, pp. 78–108.

[**Din00b**] K.-P Dinse et al. "EPR investigation of atoms in chemical traps". In: *Carbon* 38.11-12 (2000), pp. 1635–1640.

[**Dor94**] H. C. Dorn et al. “Endohedral Metallofullerenes: Isolation and Characterization”. In: *MRS Proceedings*. MRS Proceedings 359 (Jan. 1994), pp. 123–135.

[**Duc91**] Steven J. Duclos et al. “Effects of pressure and stress on C_{60} fullerite to 20 Pa”. In: *Nature* 351.6325 (May 1991), pp. 380–382.

[**DW70**] Joseph A. D’Anna and James H. Wharton. “Electron Spin Resonance Spectra of α-Nitronylnitroxide Radicals; Solvent Effects; Nitrogen Hyperfine Tensor; g Anisotropy”. In: *The Journal of Chemical Physics* 53.10 (Nov. 1970), pp. 4047–4052.

[**EE04**] Gareth R. Eaton and Sandra S. Eaton. “EPR Spectrometers at Frequencies Below X-band”. In: *EPR: Instrumental Methods*. Ed. by Lawrence J. Berliner and Christopher J. Bender. Boston, MA: Springer US, 2004, pp. 59–114.

[**EE95**] S. S. Eaton and G. R. Eaton. “The Future of EPR”. In: *Bulletin of Magnetic Resonance* 16 (1995), pp. 149–192.

[**EFR04**] M. Epstein, G. Freed, and J. Rajan. “GPS IIR rubidium clocks: In-orbit performance aspects”. In: *Proceedings of the 35th Annual Precise Time and Time Interval (PTTI) Meeting*. 2004, pp. 117–134.

[**EKM64a**] N. Edelstein, A. Kwok, and A. H. Maki. “Effects of Hydrostatic Pressure and Temperature on Spin Exchange between Free Radicals in Solution”. In: *The Journal of Chemical Physics* 41.11 (Dec. 1964), pp. 3473–3478.

[**EKM64b**] N. Edelstein, A. Kwok, and A. H. Maki. “Effects of Hydrostatic Pressure on Linewidths of Free Radicals in Solution. I. Anisotropic Region”. In: *The Journal of Chemical Physics* 41.1 (July 1964), pp. 179–183.

[**EWH15**] Michael Eckardt, René Wieczorek, and Wolfgang Harneit. “Stability of C_{60} and $N@C_{60}$ under thermal and optical exposure”. In: *Carbon* 95 (Dec. 2015), pp. 601–607.

[**FB71**] Thomas C. Farrar and Edwin D. Becker. “Chapter 4 - Relaxation Mechanisms”. In: *Pulse and Fourier Transform NMR*. Ed. by Thomas C. Farrar and Edwin D. Becker. San Diego: Academic Press, 1971, pp. 46–65.

[**Fer30a**] E. Fermi. “Magnetic Moments of Atomic Nuclei”. In: *Nature* 125.3140 (Jan. 1930), pp. 16–16.

[**Fer30b**] Enrico Fermi. “Uber die magnetischen Momente der Atomkerne”. In: *Zeitschrift fur Physik* 60.5-6 (May 1930), pp. 320–333.

[**FH82**] W. Froncisz and James S. Hyde. “The loop-gap resonator: a new microwave lumped circuit ESR sample structure”. In: *Journal of Magnetic Resonance (1969)* 47.3 (1982), pp. 515–521.

[**Flu88**] E Fluck. “New notations in the periodic table”. In: *Pure and Applied Chemistry* 60.3 (Jan. 1988), pp. 431–436.

[**FZA10**] D. M. Farkas, A. Zozulya, and D. Z. Anderson. “A compact microchip atomic clock based on all-optical interrogation of ultra-cold trapped Rb atoms”. In: *Applied Physics B* 101.4 (Dec. 2010), pp. 705–721.

[**GA74**] J.E. Gray and D.W. Allan. "A Method for Estimating the Frequency Stability of an Individual Oscillator". In: *28th Annual Symposium on Frequency Control*. IEEE, 1974, pp. 243–246.

[**Gae06**] Torsten Gaebel et al. "Room-temperature coherent coupling of single spins in diamond". In: *Nature Physics* 2.6 (June 2006), pp. 408–413.

[**GB42**] C.J. Gorter and L.J.F. Broer. "Negative result of an attempt to observe nuclear magnetic resonance in solids". In: *Physica* 9.6 (June 1942), pp. 591–596.

[**GC11**] Alan T Gardner and John A Collins. "A Second Look at Chip Scale Atomic Clocks for Long Term Precision Timing Four Years in the Field". In: (2011), pp. 1–9.

[**GC12**] A. T. Gardner and J .A. Collins. "Advancements in high-performance timing for long term underwater experiments: A comparison of chip scale atomic clocks to traditional microprocessor-compensated crystal oscillators". In: *2012 Oceans*. IEEE, Oct. 2012, pp. 1–8.

[**GGB15**] M. Grisi, G. Gualco, and G. Boero. "A broadband single-chip transceiver for multi-nuclear NMR probes". In: *Review of Scientific Instruments* 86.4 (2015), p. 044703.

[**GJ09**] Norman F. Glen and Andy I. Johns. "Determination of the Density of Toluene in the Range from (293 to 373) K and from (0.1 to 30) MPa †". In: *Journal of Chemical & Engineering Data* 54.9 (Sept. 2009), pp. 2538–2545.

[**Gon94**] W. D. Gonzalez et al. "What is a geomagnetic storm?" In: *Journal of Geophysical Research* 99.A4 (1994), p. 5771.

[**Gor36a**] C.J Gorter. "Negative result of an attempt to detect nuclear magnetic spins". In: *Physica* 3.9 (Nov. 1936), pp. 995–998.

[**Gor36b**] C.J. Gorter. "Paramagnetic relaxation". In: *Physica* 3.6 (June 1936), pp. 503–514.

[**Gor36c**] C.J. Gorter. "Paramagnetic relaxation in a transversal magnetic field". In: *Physica* 3.9 (Nov. 1936), pp. 1006–1008.

[**GPP81**] W. C. Gardiner, H M Pickett, and M H Proffitt. "Collisional linewidths of the EPR spectrum of molecular oxygen". In: *The Journal of Chemical Physics* 74.11 (June 1981), pp. 6037–6043.

[**Guo16**] Rong-Hao Guo et al. "Mesoscale aggregation properties of C_{60} in toluene and chlorobenzene". In: *Soft Matter* 12.29 (2016), pp. 6300–6311.

[**Hah50**] E. L. Hahn. "Spin Echoes". In: *Physical Review* 80.4 (Nov. 1950), pp. 580–594.

[**Har02a**] W. Harneit et al. "Architectures for a Spin Quantum Computer Based on Endohedral Fullerenes". In: *physica status solidi (b)* 233.3 (Oct. 2002), pp. 453–461.

[**Har02b**] Wolfgang Harneit. "Fullerene-based electron-spin quantum computer". In: *Physical Review A* 65.3 (2002), p. 032322.

[**Har17**] R. T. Harding et al. "Spin Resonance Clock Transition of the Endohedral Fullerene $^{15}N@C_{60}$". In: *Physical Review Letters* 119.14 (Oct. 2017), p. 140801.

[**Har18**] M. Hara et al. "Micro atomic frequency standards employing an integrated FBAR-VCO oscillating on the 87 RB clock frequency without a phase locked loop". In: *2018 IEEE Micro Electro Mechanical Systems (MEMS)*. Vol. 2018-Janua. 1. IEEE, Jan. 2018, pp. 715–718.

[**Hay14**] William M. Haynes, ed. *CRC Handbook of Chemistry and Physics*. 95th ed. Boca Raton, FL, USA: CRC Press, 2014.

[**HB06**] E.C. Hannah and M.A. Brown. *Atomic clock*. US Patent 7,142,066. 2006.

[**HB54**] Mark A. Heald and Robert Beringer. "Hyperfine Structure of Nitrogen". In: *Physical Review* 96.3 (Nov. 1954), pp. 645–648.

[**Hea14**] Thomas P. Heavner et al. "First accuracy evaluation of NIST-F2". In: *Metrologia* 51.3 (June 2014), pp. 174–182.

[**Hic15**] D Hicks et al. *NPL time disseminated through the UBS infrastructure*. Tech. rep. Teddington: National Physical Laboratory, 2015.

[**Hin13**] N. Hinkley et al. "An Atomic Clock with 10^{-18} Instability". In: *Science* 341.6151 (Sept. 2013), pp. 1215–1218.

[**HK72a**] J. C. Hafele and Richard E. Keating. "Around-the-World Atomic Clocks: Observed Relativistic Time Gains". In: *Science* 177.4044 (1972), pp. 168–170.

[**HK72b**] J. C. Hafele and Richard E. Keating. "Around-the-World Atomic Clocks: Predicted Relativistic Time Gains". In: *Science* 177.4044 (1972), pp. 166–168.

[**HLC01**] B. Hofmann-Wellenhof, H. Lichtenegger, and J. Collins. *Global positioning system: theory and practice*. Vienna, Austria: Springer-Verlag, 2001.

[**HLN62**] W. W. Holloway, E. Lüscher, and R. Novick. "Hyperfine Structure of Atomic Nitrogen". In: *Physical Review* 126.6 (June 1962), pp. 2109–2115.

[**Hod13**] J. S. Hodges et al. "Timekeeping with electron spin states in diamond". In: *Physical Review A* 87.3 (Mar. 2013), p. 032118.

[**HR76**] D.I Hoult and R.E Richards. "The signal-to-noise ratio of the nuclear magnetic resonance experiment". In: *Journal of Magnetic Resonance (1969)* 24.1 (Oct. 1976), pp. 71–85.

[**HSF89**] James S Hyde, Pawel B. Sczaniecki, and Wojciech Froncisz. "The Bruker lecture alternatives to field modulation in electron spin resonance spectroscopy". In: *Journal of the Chemical Society, Faraday Transactions 1: Physical Chemistry in Condensed Phases* 85.12 (1989), p. 3901.

[**HW81**] W. N. Hardy and L. A. Whitehead. "Split-ring resonator for use in magnetic resonance from 200-2000 MHz". In: *Review of Scientific Instruments* 52.2 (Feb. 1981), pp. 213–216.

[**Iij91**] Sumio Iijima. "Helical microtubules of graphitic carbon". In: *Nature* 354.6348 (Nov. 1991), pp. 56–58.

[**Jak03**] Peter Jakes et al. "Purification and optical spectroscopy of $N@C_{60}$". In: *Physical Chemistry Chemical Physics* 5.19 (2003), pp. 4080–4083.

[**Jan82**] Edward G. Janzen et al. "Solvent effects on the nitrogen and β-hydrogen hyperfine splitting constants of aminoxyl radicals obtained in spin trapping experiments". In: *Canadian Journal of Chemistry* 60.21 (Nov. 1982), pp. 2725–2733.

[**Jau12**] Y. Y. Jau et al. "Low-power, miniature ^{171}Yb ion clock using an ultra-small vacuum package". In: *Applied Physics Letters* 101.25 (2012).

[**Jon24**] J. E. Jones. "On the Determination of Molecular Fields. II. From the Equation of State of a Gas". In: *Proceedings of the Royal Society A: Mathematical, Physical and Engineering Sciences* 106.738 (Oct. 1924), pp. 463–477.

[**KA99**] John A. Kusters and Charles A. Adams. "Performance requirements of communication base station time standards". In: *RF Design* 5 (1999), pp. 28–38.

[**Kan04**] M. Kanai et al. "Purification by HPLC and the UV/Vis absorption spectra of the nitrogen-containing *incar*-fullerenes $i\mathrm{NC}_{60}$, and $i\mathrm{NC}_{70}$". In: *Chemical Communications* 0 (2 2004), pp. 210–211.

[**Kar14**] Denis Karaiskaj. *Silicon-based atomic clocks*. US Patent 8,816,784 B1. 2014.

[**Kar15**] Denis Karaiskaj. *Atomic clock using a photodetector*. US Patent 9,052,698 B1. 2015.

[**Kau10**] Narinder Kaur et al. "Pressure induced transformations in condensed and molecular phases of C_{60}". In: *Carbon* 48.3 (Mar. 2010), pp. 744–755.

[**KL95**] G. W. C. Kaye and T. H. Laby, eds. *Tables of Physical and Chemical Constants*. 16th ed. Harlow, Essex, United Kingdom: Longman, 1995.

[**Kna04**] S. Knappe et al. "A microfabricated atomic clock". In: *Applied Physics Letters* 85.9 (2004), pp. 1460–1462.

[**Kna05a**] S Knappe et al. "A chip-scale atomic clock based on ^{87}Rb with improved frequency stability". In: *Optics Express* 13.4 (2005), p. 1249.

[**Kna05b**] S Knappe et al. "Atomic vapor cells for chip-scale atomic clocks with improved long-term frequency stability". In: *Optics Letters* 30.18 (Sept. 2005), p. 2351.

[**Kna97**] C. Knapp et al. "Fourier transform EPR study of $N@C_{60}$ in solution". In: *Chemical Physics Letters* 272.5-6 (July 1997), pp. 433–437.

[**Kna98**] C. Knapp et al. "Electron paramagnetic resonance study of atomic phosphorus encapsulated in [60]fullerene". In: *Molecular Physics* 95.5 (Dec. 1998), pp. 999–1004.

[**KND03**] Kaoru Kobayashi, Shigeru Nagase, and Klaus-Peter Dinse. "A theoretical study of spin density distributions and isotropic hyperfine couplings of N and P atoms in $N@C_{60}$, $P@C_{60}$, $N@C_{70}$, $N@C_{60}(CH_2)_6$, and $N@C_{60}(SiH_2)_6$". In: *Chemical Physics Letters* 377.1-2 (Aug. 2003), pp. 93–98.

[**Kro85**] H. W. Kroto et al. "C_{60}: Buckminsterfullerene". In: *Nature* 318.6042 (Nov. 1985), pp. 162–163.

[**Lem09**] N. D. Lemke et al. "Spin-1/2 optical lattice clock". In: *Physical Review Letters* 103.6 (2009), pp. 10–13.

[**Ler15**] Michael T. Lerch et al. "High-Pressure EPR and Site-Directed Spin Labeling for Mapping Molecular Flexibility in Proteins". In: *Methods in Enzymology*. 1st ed. Vol. 564. Elsevier Inc., 2015, pp. 29–57.

[**Lev00**] V.M. Levin et al. "Elastic modules of solid C_{60} : measurement and relationship with nanostructure". In: *Journal of Physics and Chemistry of Solids* 61.7 (July 2000), pp. 1017–1024.

[**LGS11**] Ruoxin Li, Kurt Gibble, and Krzysztof Szymaniec. "Improved accuracy of the NPL-CsF2 primary frequency standard: evaluation of distributed cavity phase and microwave lensing frequency shifts". In: *Metrologia* 48.5 (Oct. 2011), pp. 283–289.

[**Li16**] Lin Li et al. "Automatic compensation of magnetic field for a rubidium space cold atom clock". In: *Chinese Physics B* 25.7 (July 2016), p. 073201.

[**Lie04**] Li-Anne Liew et al. "Microfabricated alkali atom vapor cells". In: *Applied Physics Letters* 84.14 (Apr. 2004), pp. 2694–2696.

[**Lin15**] Thomas Lindvall. *MAC Theory Report*. Unpublished. Dec. 2015.

[**Lip00**] K Lips et al. "Atomic Nitrogen Encapsulated in Fullerenes: Realization of a Chemical Faraday Cage". In: *physica status solidi (a)* 177.1 (Jan. 2000), pp. 81–91.

[**Liu11**] Guoquan Liu et al. "Photochemical stability of $N@C_{60}$ and its pyrrolidine derivatives". In: *Chemical Physics Letters* 508.4-6 (May 2011), pp. 187–190.

[**Liu15**] Chao Liu et al. "Effect of magnetic field fluctuation on ultra-low field MRI measurements in the unshielded laboratory environment". In: *Journal of Magnetic Resonance* 257 (Aug. 2015), pp. 8–14.

[**LLA64**] Peter. Ludwig, Thomas. Layloff, and Ralph N. Adams. "Solvent Effects on Hyperfine Coupling Constants in Electron Paramagnetic Resonance Spectra". In: *Journal of the American Chemical Society* 86.21 (Nov. 1964), pp. 4568–4573.

[**LP63**] R. H. Lambert and F. M. Pipkin. "Pressure Shifts of the Hyperfine Structure of Atomic Nitrogen". In: *Physical Review* 129.3 (Feb. 1963), pp. 1233–1239.

[**LS94**] A Lundin and B Sundqvist. "Compressibility of C_{60} between 150 and 335 K and up to 1 GPa". In: *Europhysics Letters (EPL)* 27.6 (Aug. 1994), pp. 463–466.

[**Lu12**] Xing Lu et al. "Current status and future developments of endohedral metallofullerenes". In: *Chemical Society Reviews* 41.23 (2012), p. 7723.

[**Lud08**] A. D. Ludlow et al. "Sr Lattice Clock at 1×10^{-16} Fractional Uncertainty by Remote Optical Evaluation with a Ca Clock". In: *Science* 319.5871 (Mar. 2008), pp. 1805–1808.

[**Lut04**] R. Lutwak et al. "The Chip-Scale Atomic Clock - Low-Power Physics Package". In: *Proceedings of the 36th Annual Precise Time and Time Interval Systems and Applications Meeting*. Institute of Navigation. Dec. 2004, pp. 339–354.

[**Lut07**] R. Lutwak et al. "The Chip-Scale Atomic Clock - Prototype Evaluation". In: *Proceedings of the 39th Annual Precise Time and Time Interval Systems and Applications Meeting*. Institute of Navigation. Long Beach, CA, Nov. 2007, pp. 269–290.

[**Lut16**] R. Lutwak. *Broad Agency Announcement Atomic Clock with Enhanced Stability (ACES)*. Tech. rep. Arlington, VA: Defence Advanced Research Projects Agency (DARPA), 2016, pp. 1–40.

[**Mak16**] Urol Makhmanov et al. "Features of self-aggregation of C_{60} molecules in toluene prepared by different methods". In: *Physics Letters A* 380.24 (May 2016), pp. 2081–2084.

[**Mis11**] Sushil K. Misra et al. "Spectrometers". In: *Multifrequency Electron Paramagnetic Resonance*. John Wiley & Sons, Ltd, 2011. Chap. 4, pp. 115–228.

[**MLV05**] M.J. Mescher, Robert Lutwak, and Mathew Varghese. "An ultra-low-power physics package for a chip-scale atomic clock". In: *The 13th International Conference on Solid-State Sensors, Actuators and Microsystems, 2005. Digest of Technical Papers. TRANSDUCERS '05.* Vol. 1. IEEE, 2005, pp. 311–316.

[**Mop69**] Frederick I Mopsik. "Dielectric Properties of Slightly Polar Organic Liquids as a Function of Pressure, Volume, and Temperature". In: *The Journal of Chemical Physics* 50.6 (Mar. 1969), pp. 2559–2569.

[**Mor05a**] G. W. Morley. "Designing a quantum computer based on pulsed electron spin resonance". PhD thesis. University of Oxford, 2005.

[**Mor05b**] G. W. Morley et al. "Hyperfine structure of $Sc@C_{82}$ from ESR and DFT". In: *Nanotechnology* 16.11 (Nov. 2005), pp. 2469–2473.

[**Mor05c**] John J L Morton et al. "A new mechanism for electron spin echo envelope modulation". In: *The Journal of Chemical Physics* 122.17 (May 2005), p. 174504.

[**Mor05d**] John J. L. Morton. "Electron spins in fullerenes as prospective qubits". PhD thesis. University of Oxford, 2005.

[**Mor06**] John J. L. Morton et al. "Electron spin relaxation of $N@C_{60}$ in CS2". In: *The Journal of Chemical Physics* 124.1 (Jan. 2006), p. 014508.

[**Mor07**] John J. L. Morton et al. "Environmental effects on electron spin relaxation in $N@C_{60}$". In: *Physical Review B* 76.8 (Aug. 2007), p. 085418.

[**Mor14**] Igor Morić et al. "Hysteresis prediction inside magnetic shields and application". In: *Review of Scientific Instruments* 85.7 (July 2014), p. 075117.

[**MP15**] Matthias Mendt and Andreas Pöppl. "The Line Width of the EPR Signal of Gaseous Nitric Oxide as Determined by Pressure and Temperature-Dependent X-band Continuous Wave Measurements". In: *Applied Magnetic Resonance* 46.11 (2015), pp. 1249–1263.

[**MR77**] Frank M. Mourits and Frans H. A. Rummens. "A critical evaluation of Lennard–Jones and Stockmayer potential parameters and of some correlation methods". In: *Canadian Journal of Chemistry* 55.16 (Aug. 1977), pp. 3007–3020.

[**MSC17**] *Quantum*^{TM} *SA.45s CSAC chip scale atomic clock*. Microsemi Corporation. Aliso Viejo, California, USA, 2017.

[**Nar12**] Mitch Narins et al. "The Need for a Robust Precise Time and Frequency Alternative to Global Navigation Satellite Systems". In: *Proceedings of the 25th International Technical Meeting of the Satellite Division of The Institute of Navigation (ION GNSS 2012)*. Nashville, TN, 2012, pp. 2057–2062.

[**NC00**] Michael A. Neilsen and Isaac L. Chuang. *Quantum Computation and Quantum Information*. 1st ed. Cambridge University Press, 2000.

[**ND95**] O. M. Namoos and R. S. DiEsposti. "Direct-Y : Fast Acquisition of the GPS PPS Signal". In: *27th Annual Precise Time and Time Interval (PTTI) Applications and Planning Meeting*. 1995, pp. 419–431.

[**Nov04**] K. S. Novoselov et al. "Electric Field Effect in Atomically Thin Carbon Films". In: *Science* 306.5696 (Oct. 2004), pp. 666–669.

[**NPL16**] National Physical Laboratory (NPL). *Time Traceability for the Finance Sector - Fact Sheet*. Tech. rep. Teddington, UK: National Physical Laboratory, 2016, pp. 1–14.

[**Owe01**] Rikard Owenius et al. "Influence of Solvent Polarity and Hydrogen Bonding on the EPR Parameters of a Nitroxide Spin Label Studied by 9-GHz and 95-GHz EPR Spectroscopy and DFT Calculations". In: *The Journal of Physical Chemistry A* 105.49 (Dec. 2001), pp. 10967–10977.

[**Par02**] Jung Mee Park et al. "Nature of the interaction of paramagnetic atoms (A=4N,4P,3O,3S) with π systems and C_{60}: A theoretical investigation of AC6H6 and endohedral fullerenes A@C_{60}". In: *The Journal of Chemical Physics* 116.24 (June 2002), pp. 10684–10691.

[**Peó14**] R. Peón-Escalante et al. "The bond force constant and bulk modulus of C_{60}". In: *Computational Materials Science* 83 (2014), pp. 120–126.

[**PF99**] Charles P. Poole and Horacio A. Farach. "Lineshapes". In: *Handbook of Electron Spin Resonance*. Ed. by Charles P. Poole and Horacio A. Farach. 1st ed. Vol. 2. Springer-Verlag New York, 1999. Chap. 4.

[**Phi01**] D. F. Phillips et al. "Limit on Lorentz and *CPT* violation of the proton using a hydrogen maser". In: *Physical Review D* 63.11 (Apr. 2001), p. 111101.

[**Pie02**] B. Pietzak et al. "Group V Endohedral Fullerenes: N@C_{60}, N@C_{70}, and P@C_{60}". In: *Endofullerenes: A new family of carbon clusters*. 1st ed. Vol. 3. Springer Netherlands, 2002. Chap. 2.

[**Pie97**] B. Pietzak et al. "Buckminsterfullerene C_{60}: a chemical Faraday cage for atomic nitrogen". In: *Chemical Physics Letters* 279.5-6 (Nov. 1997), pp. 259–263.

[**Pie98**] B. Pietzak et al. "Properties of endohedral N@C_{60}". In: *Carbon* 36.5-6 (1998), pp. 613–615.

[**Pin99**] L Pintschovius et al. "Bulk modulus of C_{60} studied by single-crystal neutron diffraction". In: *Physical Review B* 59.16 (Apr. 1999), pp. 11020–11026.

[**Poo83**] C. P. Poole. *Electron Spin Resonance: A Comprehensive Treatise on Experimental Techniques*. 2nd ed. Wiley-Interscience, 1983.

[**Por53**] A. M. Portis. "Electronic Structure of F Centers: Saturation of the Electron Spin Resonance". In: *Physical Review* 91.5 (Sept. 1953), pp. 1071–1078.

[**Poz12**] David M. Pozar. *Microwave engineering*. 4th ed. Hoboken, NJ: John Wiley & Sons, Inc., 2012.

[**PP14**] Simon R. Plant and Kyriakos Porfyrakis. "Using electron paramagnetic resonance to map N@C_{60} during high throughput processing". In: *The Analyst* 139.18 (June 2014), pp. 4519–4524.

[**PP19**] *0505C/P Series capacitor datasheet*. Passive Plus Inc. Huntington, NY, USA, 2019.

[**PRM01**] Thomas Prisner, Martin Rohrer, and Fraser MacMillan. "Pulsed EPR Spectroscopy: Biological Applications". In: *Annual Review of Physical Chemistry* 52.1 (Oct. 2001), pp. 279–313.

[**PTM95**] John D. Prestage, Robert L. Tjoelker, and Lute Maleki. "Atomic Clocks and Variations of the Fine Structure Constant". In: *Physical Review Letters* 74.18 (May 1995), pp. 3511–3514.

[**RE99**] George A. Rinard and Gareth R. Eaton. "Loop-Gap Resonators". In: *Biomedical EPR, Part B: Methodology, Instrumentation, and Dynamics*. Ed. by Sandra S. Eaton, Gareth R. Eaton, and Lawrence J. Berliner. Springer US, 1999. Chap. 2, pp. 19–52.

[**Rei07**] Sascha Reinhardt et al. "Test of relativistic time dilation with fast optical atomic clocks at different velocities". In: *Nature Physics* 3.12 (2007), pp. 861–864.

[**Rie04**] F. Riehle. *Frequency standards: basics and applications*. Weinheim, Germany: WILEY-VCH Verlag GmbH & Co. KGaA, 2004.

[**Ril81**] William J. Riley. "A Rubidium Clock for GPS". In: *Proceedings of the 13th Precise Time and Time Interval Meeting* (1981), pp. 609–630.

[**Ril90**] William J. Riley. "Rubidium atomic frequency standards for GPS block IIR". In: *Proceedings of the 22nd Precise Time and Time Interval Meeting*. 1990, pp. 221–230.

[**Ril92**] William J. Riley. "The physics of the environmental sensitivity of rubidium gas cell atomic frequency standards". In: *IEEE Transactions on Ultrasonics, Ferroelectrics and Frequency Control* 39.2 (Mar. 1992), pp. 232–240.

[**Ril94**] William J. Riley. *Handbook of Frequency Stability Analysis*. Vol. 31. 1. US Department of Commerce, 1994, A49.

[**Rin04**] George A. Rinard et al. "Frequency Dependence of EPR Sensitivity". In: *EPR: Instrumental Methods*. Ed. by Lawrence J. Berliner and Christopher J. Bender. Boston, MA: Springer US, 2004, pp. 115–154.

[**Rob80**] F. N. H. Robinson. "A bi-symmetric Zeeman modulator for nuclear quadrupole resonance". In: *Journal of Physics E: Scientific Instruments* 13.9 (Sept. 1980), pp. 961–963.

[**Row17**] Aaron J. Rowane et al. "High-temperature, high-pressure viscosities and densities of toluene". In: *The Journal of Chemical Thermodynamics* 115 (Dec. 2017), pp. 34–46.

[**RR71**] Alfred J. Richard and Kenneth S. Rogers. "The Isothermal Compressibility of Organic Liquids by Ultracentrifugation. Correlation with Surface Tension". In: *Canadian Journal of Chemistry* 49.24 (Dec. 1971), pp. 3956–3959.

[**RR91**] Rodney S. Ruoff and Arthur L. Ruoff. "The bulk modulus of C_{60} molecules and crystals: A molecular mechanics approach". In: *Applied Physics Letters* 59.13 (Sept. 1991), pp. 1553–1555.

[**RS18**] Maxie M. Roessler and Enrico Salvadori. "Principles and applications of EPR spectroscopy in the chemical sciences". In: *Chemical Society Reviews* 47.8 (2018), pp. 2534–2553.

[**RU18**] United Kingdom Research and Innovation (UKRI). *QFC: Quantum Fibre Clock*. 2018. URL: `https://gtr.ukri.org/projects?ref=EP/S000232/1` (visited on 04/22/2019).

[**Rub06**] Enrico Rubiola. "Tutorial on the double balanced mixer". In: *ArXiv* (Aug. 2006), physics/0608211. arXiv: `0608211 [physics]`.

[**Ruo93**] R. S. Ruoff et al. "Solubility of fullerene C_{60} in a variety of solvents". In: *The Journal of Physical Chemistry* 97.13 (1993), pp. 3379–3383.

[**SA01**] James F. Shackelford and William Alexander, eds. *CRC Materials Science and Engineering Handbook*. 3rd ed. Boca Raton, FL, USA: CRC Press, 2001.

[**SCF68**] James F Skinner, Edward L. Cussler, and Raymond M Fuoss. "Pressure dependence of dielectric constant and density of liquids". In: *The Journal of Physical Chemistry* 72.3 (Mar. 1968), pp. 1057–1064.

[**Sch06**] Michael Scheloske et al. "Synthesis and Functionalization of Fullerenes Encapsulating Atomic Phosphorus". In: *Israel Journal of Chemistry* 46.4 (Dec. 2006), pp. 407–412.

[**SF07**] Seiji Sawamura and Nobuyuki Fujita. "High-pressure solubility of fullerene C_{60} in toluene". In: *Carbon* 45.5 (Apr. 2007), pp. 965–970.

[**Sha14**] Li Shao-Liang et al. "Integrated physics package of chip-scale atomic clock". In: *Chinese Physics B* 23.7 (2014), pp. 1–6.

[**Shi00**] H Shinohara. "Endohedral metallofullerenes". In: *Reports on Progress in Physics* 63.6 (June 2000), pp. 843–892.

[**Shi16**] Muhandis Shiddiq et al. “Enhancing coherence in molecular spin qubits via atomic clock transitions”. In: *Nature* 531.7594 (Mar. 2016), pp. 348–351.

[**Shi92**] Hisanori Shinohara et al. “Mass spectroscopic and ESR characterization of soluble yttrium-containing metallofullerenes YC_{82} and Y_2C_{82}”. In: *The Journal of Physical Chemistry* 96.9 (Apr. 1992), pp. 3571–3573.

[**Shi93**] Hisanori Shinohara et al. “Isolation and spectroscopic properties of scandium fullerenes ($Sc_2@C_{74}$, $Sc_2@C_{82}$, and $Sc_2@C_{84}$)”. In: *The Journal of Physical Chemistry* 97.17 (Apr. 1993), pp. 4259–4261.

[**SJ01**] Arthur Schweiger and Gunnar Jeschke. *Principles of pulse electron paramagnetic resonance*. 2nd ed. Oxford University Press, 2001.

[**Sli90**] C. P. Slichter. *Principles of Magnetic Resonance*. 3rd ed. Springer-Verlag, 1990.

[**SRS11**] *Model SR830 DSP Lock-In Amplifier*. Stanford Research Systems. Sunnyvale, California, USA, 2011.

[**Sto05**] N. J. Stone. “Table of nuclear magnetic dipole and electric quadrupole moments”. In: *Atomic Data and Nuclear Data Tables* 90.1 (2005), pp. 75–176.

[**Stu83**] Mark A. Sturza. “GPS Navigation Using Three Satellites and a Precise Clock”. In: *Navigation* 30.2 (1983), pp. 146–156.

[**Sun11**] N. Sun et al. “Palm NMR and 1-Chip NMR”. In: *IEEE Journal of Solid-State Circuits* 46.1 (Jan. 2011), pp. 342–352.

[**Suy11**] Suyalatu et al. “Effects of phase constitution on magnetic susceptibility and mechanical properties of Zr-rich Zr–Mo alloys”. In: *Acta Biomaterialia* 7.12 (Dec. 2011), pp. 4259–4266.

[**Suz92**] Shinzo Suzuki et al. “Isomers and carbon-13 hyperfine structures of metal-encapsulated fullerenes $M@C_{82}$ (M = Sc, Y, and La)”. In: *The Journal of Physical Chemistry* 96.18 (Sept. 1992), pp. 7159–7161.

[**TJ10**] Joel A. Tang and Alexej Jerschow. “Practical aspects of liquid-state NMR with inductively coupled solenoid coils”. In: *Magnetic Resonance in Chemistry* 48.10 (Oct. 2010), pp. 763–770.

[**Tur87**] Philippe Turek et al. “Preparation and study of a lithium phthalocyanine radical: optical and magnetic properties”. In: *Chemical Physics Letters* 134.5 (Mar. 1987), pp. 471–476.

[**VA89**] J. Vanier and C. Audoin. *The Quantum Physics of Atomic Frequency Standards*. A. Hilger, 1989.

[**VC05**] L. M. K. Vandersypen and I. L. Chuang. “NMR techniques for quantum control and computation”. In: *Reviews of Modern Physics* 76.4 (Jan. 2005), pp. 1037–1069.

[**VC97**] F. J. Vieira dos Santos and C. A. Nieto de Castro. “Viscosity of toluene and benzene under high pressure”. In: *International Journal of Thermophysics* 18.2 (Mar. 1997), pp. 367–378.

[**Ves80**] R. F. C. Vessot et al. "Test of Relativistic Gravitation with a Space-Borne Hydrogen Maser". In: *Physical Review Letters* 45.26 (Dec. 1980), pp. 2081–2084.

[**Vig93**] J.R. Vig. "Military applications of high accuracy frequency standards and clocks". In: *IEEE Transactions on Ultrasonics, Ferroelectrics and Frequency Control* 40.5 (Sept. 1993), pp. 522–527.

[**Vio14**] Maddalena Violetti et al. "The Microloop-Gap Resonator: A Novel Miniaturized Microwave Cavity for Double-Resonance Rubidium Atomic Clocks". In: *IEEE Sensors Journal* 14.9 (Sept. 2014), pp. 3193–3200.

[**Wai01**] M. Waiblinger et al. "Corrected Article: Thermal stability of the endohedral fullerenes N@C_{60}, N@C_{70} and P@C_{60}". In: *Physical Review B* 64.15 (2001), p. 159901.

[**Wal01**] William J Walsh. *Apparatus and method for providing synchronization of base-stations in a communication system.* US Patent 6,308,077 B1. 2001.

[**Wan18**] Cheng Wang et al. "An on-chip fully electronic molecular clock based on sub-terahertz rotational spectroscopy". In: *Nature Electronics* 1.7 (July 2018), pp. 421–427.

[**Wat99**] G D Watkins. "EPR of defects in semiconductors: Past, present, future". In: *Physics of the Solid State* 41.5 (May 1999), pp. 746–750.

[**Wei00**] N. Weiden et al. "Squeezing of nitrogen atomic orbitals in a chemical trap". In: *Physical Review Letters* 85.7 (2000), pp. 1544–1547.

[**Wei98a**] A. Weidinger et al. "Atomic nitrogen in C_{60}: N@C_{60}". In: *Applied Physics a-Materials Science & Processing* 66 (1998), pp. 287–292.

[**Wei98b**] A. Weidinger et al. "Study of N@C_{60} and P@C_{60}". In: *AIP Conference Proceedings* 363 (1998), pp. 363–367.

[**WH05**] C.J. White and Ali Hajimiri. "Solid-state atomic frequency standard". In: *Proceedings of the 2005 IEEE International Frequency Control Symposium and Exposition, 2005.* Vol. 2005. IEEE, 2005, pp. 940–946.

[**WHC14**] Chun I. Wang, Chi C. Hua, and Show A. Chen. "Dynamic Solvation Shell and Solubility of C_{60} in Organic Solvents". In: *The Journal of Physical Chemistry B* 118.33 (Aug. 2014), pp. 9964–9973.

[**Whi05**] Christopher J. White. "A solid-state atomic frequency standard". PhD thesis. California Institute of Technology, 2005.

[**Whi48**] C. A. Whitmer et al. "Magnetic Resonance Absorption in the Chrome Alums". In: *Physical Review* 74.10 (Nov. 1948), pp. 1478–1484.

[**Wil67**] T. H. Wilmshurst. *Electron Spin Resonance Spectrometers.* Springer US, 1967, pp. 1–280.

[**Wit18**] J. J. Wittmann et al. "High-precision measurement of the electron spin g factor of trapped atomic nitrogen in the endohedral fullerene N@C_{60}". In: *Journal of Magnetic Resonance* 290 (May 2018), pp. 12–17.

[**WM16**] Gary Wolfowicz and John J. L. Morton. "Pulse Techniques for Quantum Information Processing". In: *eMagRes.* Vol. 5. 4. Chichester, UK: John Wiley & Sons, Ltd, Dec. 2016, pp. 1515–1528.

[**Wol13**] Gary Wolfowicz et al. "Atomic clock transitions in silicon-based spin qubits". In: *Nature Nanotechnology* 8.8 (Aug. 2013), pp. 561–564.

[**Wol98**] Robert Wolfert et al. "Direct P(Y)-code acquisition under a jamming environment". In: *IEEE 1998 Position Location and Navigation Symposium (Cat. No.98CH36153)*. IEEE, 1998, pp. 228–235.

[**Woo92**] S.J. Woo et al. "Bulk modulus of the C_{60} molecule via the tight binding method". In: *Physics Letters A* 162.6 (Mar. 1992), pp. 501–505.

[**Wu14**] Weiping Wu et al. "The design and fabrication of a low-field NMR probe based on a multilayer planar microcoil". In: *Microsystem Technologies* 20.3 (Mar. 2014), pp. 419–425.

[**Yam03**] K. Yamazaki et al. "Analysis of magnetic disturbance due to buildings". In: *IEEE Transactions on Magnetics* 39.5 (Sept. 2003), pp. 3226–3228.

[**Zad15**] Joseph M. Zadrozny et al. "Millisecond Coherence Time in a Tunable Molecular Electronic Spin Qubit". In: *ACS Central Science* 1.9 (Dec. 2015), pp. 488–492.

[**Zak10**] Mujtaba Zaka et al. "Exchange interactions of spin-active metallofullerenes in solid-state carbon networks". In: *Physical Review B* 81.7 (Feb. 2010), p. 075424.

[**Zav45**] E. Zavoisky. "Paramagnetic relaxation of liquid solutions for perpendicular fields". In: *Journal of Physics (U.S.S.R.)* 9.2 (1945), pp. 211–216.

[**Zha16**] Lingwei Zhan et al. "Utilization of Chip-Scale Atomic Clock for Synchrophasor Measurements". In: *IEEE Transactions on Power Delivery* 31.5 (Oct. 2016), pp. 2299–2300.